TIDAL DISTORTION IN SHALLOW ESTUARIES

by

Paul Edward Speer

B.A., 1978 Williams College

SUBMITTED IN PARTIAL FULFILLMENT

OF THE REQUIREMENTS FOR THE DEGREE OF

DOCTOR OF PHILOSOPHY

at the

MASSACHUSETTS INSTITUTE OF TECHNOLOGY
and the
WOODS HOLE OCEANOGRAPHIC INSTITUTION

March 1984

Signature of Author. .....
Department of Earth and Planetary Sciences, Massachusetts Institute of Technology and the Joint Program in Oceanography, Massachusetts Institute of Technology/Woods Hole Oceanographic Institution, March, 1984.

Certified by.....
Thesis Supervisor

Accepted by.....
Chairman, Joint Committee for Marine Geology and Geophysics, Massachusetts Institute of Technology/Woods Hole Oceanographic Institution.

TIDAL DISTORTION IN SHALLOW ESTUARIES

by

PAUL EDWARD SPEER

Submitted to the Massachusetts Institute of Technology -
Woods Hole Oceanographic Institution
Joint Program In Oceanography
on March, 1984 in partial fulfillment of the
requirements for the Degree of Doctor of Philosophy

ABSTRACT

The offshore tide becomes distorted as it propagates into shallow inlet/estuarine systems. Time asymmetries develop in the rise and fall of sea surface with consequent time and magnitude asymmetries in tidal currents. Flood-dominant estuaries are characterized by longer falling tides and stronger flood currents while ebb-dominant estuaries have longer rising tides and stronger ebb currents. The asymmetries are reflected in the non-linear growth of harmonics and compound tides of the principal equilibrium tidal constituents. This dissertation consists of three papers which examine the development of tidal asymmetries in shallow estuarine systems: a study of the recent migration history of Nauset Inlet (MA), a shallow estuarine system located on Cape Cod; an analysis of the results of a series of field experiments conducted at Nauset; a numerical model study of the types of estuarine characteristics controlling tidal asymmetry. The analysis of field results focuses on sea surface measurements. Non-linear distortion of the tide at Nauset is characterized by the strong growth of harmonics and compound constituents particularly in the quarter-diurnal band. Phase relationships between the forced constituents and their parents produce a flood-dominant estuary. Numerical modeling of M_2 tidal propagation in shallow estuarine channels utilizes the one-dimensional equations of motion. Shallow, frictionally dominated channels with moderate tidal flat area develop a flood-dominant asymmetry while deeper channels with extensive tidal flats develop an ebb-dominant asymmetry. Model results are supported by observations of tidal asymmetry in natural estuaries. Implications of non-linear tidal distortion on bedload and suspended material transport are profound. Flood-dominant estuaries tend to import sediment if the supply is adequate whereas ebb-dominant estuaries can flush entering sediment effectively. Over long time periods, flood-dominant estuaries may eventually fill. Ebb-dominant estuaries may represent more stable long-term configurations.

Thesis Supervisor: Dr. David G. Aubrey

Title: Associate Scientist
Woods Hole Oceanographic Institution

ACKNOWLEDGEMENTS

This study was supported by the Department of Commerce, NOAA Office of Sea Grant under Grant numbers NA79AA-D-00102 and NA80AA-D-00077, the U.S. Army Research Office under Grant DAAG 29-81-K-0004, the Woods Hole Oceanographic Institution's Coastal Research Center and the W.H.O.I. education program.

I would like to express my appreciation to Dave Aubrey for his support, guidance and friendship over the past five and one half years. His enthusiasm and dedication to students made this an enjoyable experience despite some occassionally difficult moments.

I thank Bill Grant for many useful discussions and also for his help in learning fluid mechanics my first two years in the program. Keith Stolzenbach, Dale Haidvogel and John Milliman provided valuable advice and also read and commented on this thesis.

Steve Gegg and Wayne Spencer were primarily responsible for collection of the field data (under conditions which were sometimes less than ideal). Pam Barrows typed the manuscript.

I thank the members and friends of the WHMC especially Paul, Kenny, Scott, Larry, John, Mike, Betsey and Char for their friendship. We had some good times. I especially thank Susan for her love and support through the past three years.

I thank the students and staff of G & G for their friendship, advice and support.

Finally, I thank my parents. This work would have been difficult to complete without their constant encouragement and support.

TABLE OF CONTENTS

CHAPTER I

INTRODUCTION

Shallow estuarine/tidal marsh systems connected to the ocean by a narrow inlet are ubiquitous features along barrier beach coastlines. Barrier beaches and their associated tidal inlets comprise approximately 13% of the world's coastline (King, 1972), most occurring in areas with low to moderate tidal range. The longest stretch of barrier beaches and tidal inlets in the world is located along the U.S. East and Gulf of Mexico coasts, affording protection to over 5000 km of navigable waters. Inlet/estuarine systems along these coastlines play important roles in the biological cycles of many organisms and in nutrient exchange with coastal waters. In addition, many are used, or are intended for use, as navigational channels. As the offshore tide propagates into these systems, it can become distorted as a result of non-linear fluid mechanical processes. The tidal distortion takes the form of time asymmetries in the rise and fall of sea surface and consequent time/magnitude asymmetries in tidal currents. Patterns of sediment transport and nutrient/pollutant exchange can be strongly affected by the tidal distortion. The long term stability and evolution of these estuaries are partly controlled by their response to tidal forcing.

Coastal geologists have focused on the velocity asymmetries frequently observed in the tidal inlet channel and classified inlets as either "ebb dominant" or "flood dominant" (eg., Hayes, 1975). Many inlet channels are termed "ebb dominant" because it is observed that ebb currents continue to flow even after the ocean tide has turned to rise. As a result, flood currents are confined to shallow channels on either side of the main inlet channel during early stages of rising tide (see figure 1 for inlet morphology). This situation is caused by lags in low water from the ocean to the far reaches of the estuary. The terms "ebb dominant" and "flood dominant"

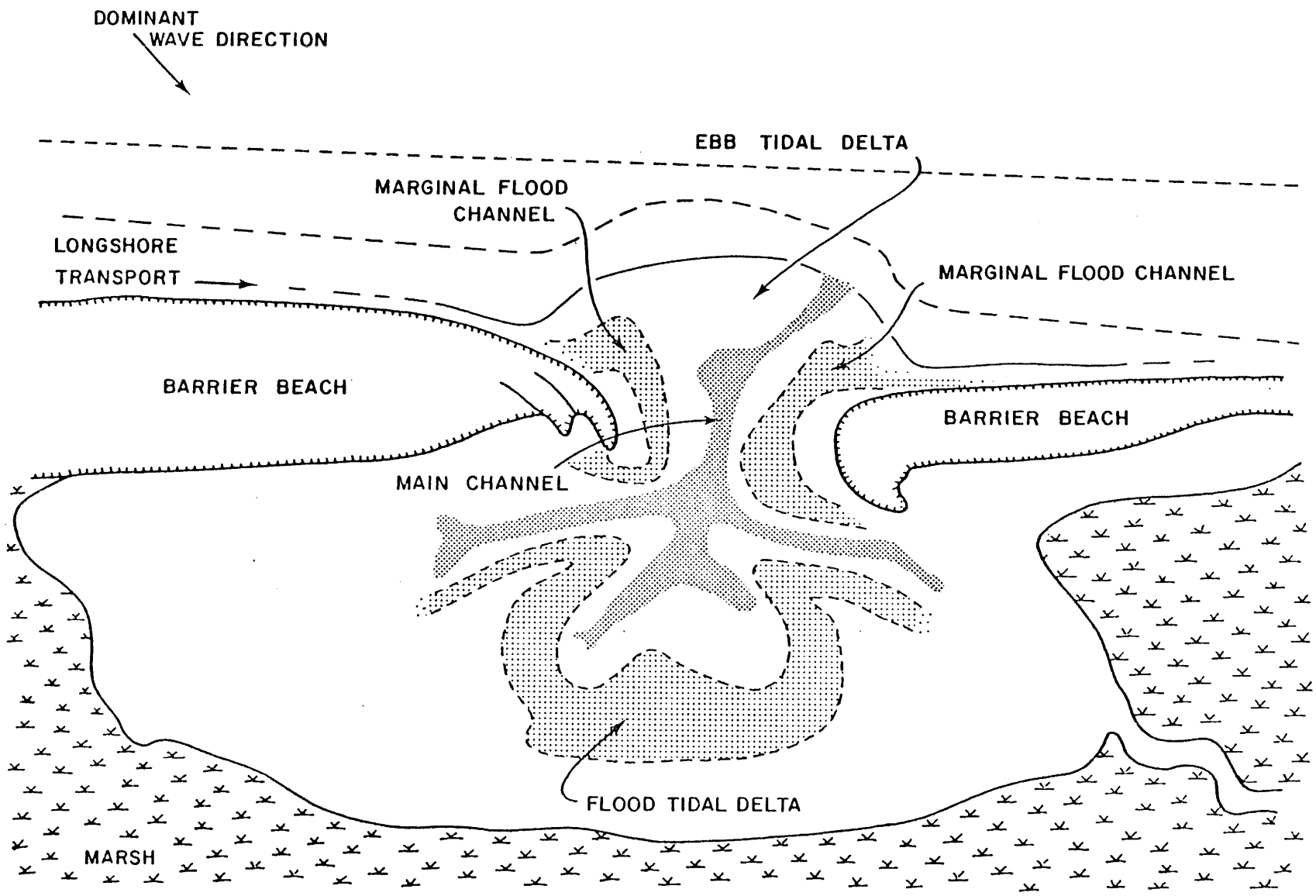

Figure 1. Sketch of dominant morphologic features in a tidal inlet.

have generally been applied to currents at the inlet as opposed to further within the estuary. Although most work has focused on the time-velocity asymmetry of tidal currents investigators have noted the time asymmetry present in sea surface (eg., Byrne et al., 1975; Boon and Byrne, 1981; FitzGerald and Nummedal, 1983). The duration asymmetry in rising and falling tide can impart an ebb or flood dominance to the estuary as a whole. For example, an estuary characterized by a longer rising tide will tend to have stronger ebb currents ("ebb dominant"). Estuaries of both types occur along the U.S. East coast (Table 1).

The importance of tidal asymmetries to processes such as sediment transport (eg., Postma, 1967; Pingree and Griffiths, 1979) has long been recognized. The presence of a distorted tidal velocity signal can produce a net suspended and bed load transport. Within estuaries, net patterns of sediment transport can have important implications for inlet/estuarine stability. An estuary characterized by a longer falling tide and hence stronger flood currents may show a pattern of net up-estuary sediment transport. Such an estuary may be unable to flush effectively sediments entering the system through the inlet. As a result, the estuary could be expected to gradually fill, with consequent reduction of tidal prism and development of channel shoaling problems. The tidal response of these systems, therefore, may play an important role in their geological development. Some investigators, in fact, have hypothesized that an inlet/estuarine system could evolve from a flood-dominant transport pattern in its early stages to ebb-dominant as the estuary filled (Byrne and Boon, 1976). Such a development implies a feedback between estuarine geometry and tidal forcing.

Table 1

Examples of Tidal Asymmetry along U.S. east coast

Longer falling tide ("flood dominant")	Reference
Murrells Inlet, S.C.	Boon and Byrne, 1981
Nauset Inlet, MA	Aubrey and Speer, 1983
Ogunquit River Inlet, ME	Fitzgerald et al. (in press)
Longer rising tide ("ebb dominant")	
Wachapreague Inlet, VA	Boon and Byrne, 1981
North Inlet, S.C.	Nummedal and Humphries, 1978
Price Inlet, S.C.	Fitzgerald and Nummedal, 1983

Over shorter time scales, many investigators have been interested in patterns of net suspended material transport. This is particularly important for biologists concerned whether inlet/marsh systems export dissolved and particulate nutrients into coastal waters (Valiela et al., 1978; Teal, 1983). Nutrient circulation depends in part on transformations which occur in the tide as it propagates into these shallow systems. Net patterns of suspended material transport have been explained by means of the time-velocity asymmetries developed in estuarine channels (eg. Boon, 1975; Ward, 1981).

Despite the large number of problems studied in shallow estuaries, few have focused on the tidal propagation problem itself. However, it is the interaction of estuarine geometry and tidal forcing which produces the observed asymmetries in tidal currents and the rise and fall of sea surface. A number of investigators have utilized numerical models to investigate the role of estuarine hypsometry in distorting the tide (Mota-Oliveira, 1970; Seelig and Sorensen, 1978; Boon and Byrne, 1981). These studies have not been sufficiently systematic. In addition, they did not focus on the spectral response of the model estuaries to tidal forcing. This is important because the non-linear process of tidal distortion observed in the field reveals itself in the growth of harmonics of the principal astronomic constituents.

Data sets obtained in the field have largely consisted of 12 or 24 hour cycles of velocity measurements typically sampled at hourly intervals. These measurements frequently have been concentrated near the inlet channel (eg., Boothroyd and Hubbard, 1975; Finley, 1975; Hine, 1975; Nummedal and Humphries, 1978; FitzGerald and Nummedal, 1983). Long-term records of sea surface measurements (sufficient for harmonic analysis) are sparse, with

only a few comprehensive surveys (e.g., NOS experiment, Murrells Inlet, SC, Boon and Byrne, 1981). A comprehensive field program supported by modeling is required to understand tidal propagation in these shallow systems. The key questions are: What are the kinematics and mechanics of the non-linear distortion of the tide within a shallow estuary? What are the geometry and friction characteristics of estuaries which produce the different types of asymmetry? The present study addresses these questions. It has involved a field study at Nauset Inlet, MA, a tidal inlet/marsh complex representative of many such features along the U.S. east coast. In addition, numerical modeling was employed as a diagnostic tool to investigate the important aspects of tidal propagation identified by the field experiments.

The thesis consists of three papers (co-authored with D. Aubrey): a study of the recent migration history of Nauset Inlet; an analysis of the results of a series of field experiments conducted at Nauset; a numerical model study of the types of estuarine characteristics responsible for producing different tidal asymmetries. The first paper places the field experiments within the framework of the recent history of the inlet/estuarine system. The Nauset estuary/marsh complex is serviced by an unstable inlet which has migrated as much as 2 km over the past 30 years. The inlet is presently moving north at approximately 100 m/yr and is more than 2 km from an historically preferred location. Such large-scale migration changes the lengths of estuarine tidal channels and can affect its tidal response. This paper examines the migration episodes and formulates three hypotheses explaining the observed behavior.

The second paper discusses results from field experiments designed to examine tidal propagation in this shallow estuary. The analysis focuses on sea surface elevation measurements, supplementing them with velocity

records which illustrate the type of tidal asymmetry developed at Nauset. The non-linear distortion of the tide is characterized by the growth of harmonics and compound constituents of the primary astronomic frequencies. Sea surface records of sufficient length to examine this problem spectrally are far easier to obtain than velocity records. In fact, difficult environmental conditions (shallow water, strong flows, extreme sediment transport rates) preclude long velocity records from most regions of the estuary. Hence velocity is used as supplementary information to a detailed investigation of sea surface records.

The numerical section presents results from one-dimensional (cross-sectionally averaged) modeling of estuarine characteristics contributing to different forms of tidal asymmetry. The modeling is diagnostic and does not attempt to predict or hindcast conditions at Nauset. These systems are physically complex and require two-dimensional models to hindcast sea surface and depth-mean velocity. Such models exist (eg., Masch et al., 1977; Butler, 1980) but they do not explain what drives estuaries to different tidal responses. In addition, their ability to represent non-linear estuarine dynamics accurately is unclear since investigators have not provided spectral comparisons of field data with model solutions. The one-dimensional models are used to examine the role of channel cross-section shape, tidal flats and variable levels of friction in distorting the estuarine tide. Model results indicate systems with strongly time-variable channel cross-section and moderate extent of tidal flats tend to be flood-dominant. Conversely, estuaries with extensive tidal flats and less time-variability in channel geometry are ebb-dominant. Results of the field experiments at Nauset Inlet and observations of tidal asymmetry in other shallow estuaries support the findings of the model study.

REFERENCES

Boon, J.D., 1975. Tidal discharge asymmetry in a salt marsh drainage system. Limnol. Oceanog., v. 3, p. 71-80.

Boon, J.D. and R.J. Byrne, 1981. On basin hypsometry and the morphodynamic response of coastal inlet systems. Marine Geology, v. 40, p. 27-48.

Boothroyd, J.C. and D.K. Hubbard, 1975. Genesis of bedforms in mesotidal estuaries. In L. Eugene Cronin (ed.), Estuarine Research, v. 2, Academic Press, p. 217-234.

Butler, H.L., 1980. Evolution of a numerical model for simulating long-period wave behavior in ocean-estuarine systems. Estuarine and Wetland Processes with Emphasis on Modeling, Marine Science Series, v. 11, Plenum Press, p. 147-182.

Byrne, R.J., P. Bullock and D.G. Tyler, 1975. Response characteristics of a tidal inlet: A case study. In L. Eugene Cronin (ed.), Estuarine Research, v. 2, p. 201-216.

Byrne, R.J. and J.D. Boon, III, 1976. Speculative hypothesis on the evolution of barrier island - inlet - lagoon systems. Geol. Soc. Am., NE/SE Sect. Ann. Meet., Abstr., v. 8, p. 159.

Finley, R.J., 1975. Hydrodynamics and tidal deltas of North Inlet, South Carolina. In L. Eugene Cronin (ed.), Estuarine Research, v. 2, p. 277-292.

FitzGerald, D.M. and D. Nummedal, 1983. Response characteristics of an ebb-dominated tidal inlet channel. Jour. Sed. Pet., v. 53, p. 833-845.

Hayes, M.O., 1975. Morphology of sand accumulation in estuaries: An introduction to the symposium. In L. Eugene Cronin (ed.), Estuarine Research, v. 2, p. 3-22.

Hine, A.C., 1975. Bedform distribution and migration patterns on tidal deltas in the Chatham harbor estuary, Cape Cod, Mass. In L. Eugene Cronin (ed.), Estuarine Research, v. 2, p. 235-252.

King, C.A.M., 1972. Beaches and Coasts, Edward Arnold Ltd., London, 570 pp.

Masch, F.D., R.J. Brandes and J.D. Reagan, 1977. Comparison of numerical and physical hydraulic models, Masonboro Inlet, North Carolina. Appendix 2, v. 1, Numerical simulation of hydrodynamics (WRE). GITI Report 6, U.S. Army Coastal Eng. Res. Cent., 123 pp.

Mota-Oliveira, I.B., 1970. Natural flushing ability in tidal inlets. In Am. Soc. Civ. Eng., Proc. 12^{th} Coastal Eng. Conf., p. 1827-1845.

Nummedal, D. and S.M. Humphries, 1978. Hydraulics and dynamics of North Inlet, South Carolina, 1975-1976. GITI Report 16, U.S. Army Coastal Eng. Res. Cent., 214 pp.

Pingree, R.D. and D.K. Griffiths, 1979. Sand transport paths around the British Isles resulting from M_2 and M_4 tidal interactions. J. Mar. Biol. Assoc. v. 59, p. 467-513.

Postma, H., 1967. Sediment transport and sedimentation in the estuarine enviroment. In G.H. Lauff (ed.), Estuaries, Am. Assoc. Adv. Sci., p. 158-179.

Seelig, W.N. and R.M. Sorensen, 1978. Numerical model investigation of selected tidal inlet-bay system characteristics. In Am. Soc. Civ. Eng., Proc. 16^{th} Coastal Eng. Conf., p. 1302-1319.

Teal, J.M. (ed.), 1983. The coastal impact of groundwater discharge: an assessment of anthropogenic nitrogen loading in Town Cove, Orleans, Massachusetts. Report to Board of Selectmen, Orleans, Mass. Woods Hole Oceanographic Institution.

Valiela, I., J.M. Teal, S. Volkmann, D. Shafer and E.J. Carpenter, 1978. Nutrient and particulate fluxes in a salt marsh ecosystem: tidal exchanges and inputs by precipitation and groundwater. Limnol. Oceanogr., v. 23, p. 798-812.

Ward, L.G., 1981. Suspended-material transport in marsh tidal channels, Kiawah Island, South Carolina. Mar. Geology, v. 40, p. 139-154.

CHAPTER II

UPDRIFT MIGRATION OF TIDAL INLETS

ABSTRACT

Three mechanisms are responsible for tidal inlet migration in an updrift direction (counter to net longshore transport): 1) attachment of distal ebb tide delta bars to the downdrift barrier spit; 2) storm-induced breaching and subsequent stabilization to form a new inlet; and 3) ebb tide discharge around a channel bend creating a three-dimensional flow pattern which erodes the outer channel bank and accretes on the inner channel bank. The last two mechanisms can result in either updrift or downdrift inlet migration, depending on channel geometry in the bay and barrier beach configuration. The last mechanism is discussed here for the first time. Analysis of historical charts and aerial photographs, combined with an historical storm synthesis, shows that all three mechanisms are active at a natural tidal inlet along a sandy coast (Nauset Inlet, Cape Cod, MA). On a time scale of ten years, these mechanisms were effective in producing an updrift migration of more than two kilometers. Initiation of updrift migration coincided with a marked increase in storm frequency perturbing the historically stable inlet position. Subsequent updrift migration resulted from ebb-delta bypassing and channel bend flows.

INTRODUCTION

Migration of tidal inlets and the associated changes in adjacent barrier beaches have profound implications on both the geological evolution of inlet/estuary systems and the short-term stability of these features. Past studies have documented many instances of inlets migrating in the direction of net littoral drift along sandy shores, but have uncovered few cases (e.g., Indian River Inlet, Delaware, and Thorsminde Inlet, Denmark) where inlets appear to migrate in directions opposed to the dominant longshore transport direction (Bruun, 1978). Migration of tidal inlets in any direction accelerates inlet-induced changes in the estuary. The estuary may fill in with littoral sands derived from updrift sources, as flood tide delta growth accompanies the migration of the inlet, and marsh development (colonization and plant emergence) becomes more variable and less permanent.

Previous attempts to explain a reversal in direction of inlet migration suggest a change in direction of net littoral drift, causing a change in migration direction. This explanation is not realistic for some inlets where wave forcing and nearshore bathymetry have remained constant through time. This study presents three alternatives to explain the tendency of some inlets to migrate updrift, each supported by historical observations at a site with a large-volume, directionally-biased littoral drift.

The study site is located on the Atlantic coast of Cape Cod, Massachusetts (figure 1), exposed to open ocean waves from the east and a two-meter ocean tide. Offshore bathymetry and sediments are described elsewhere (Aubrey, Twichell and Pfirman, 1982). Longshore transport rates and directions were studied by Zeigler (1954, 1960), and net littoral drift has been estimated at 250,000 m^3 per year towards the south (U.S. Army Corps of Engineers, 1969). Sediment is derived from erosion of sea cliffs

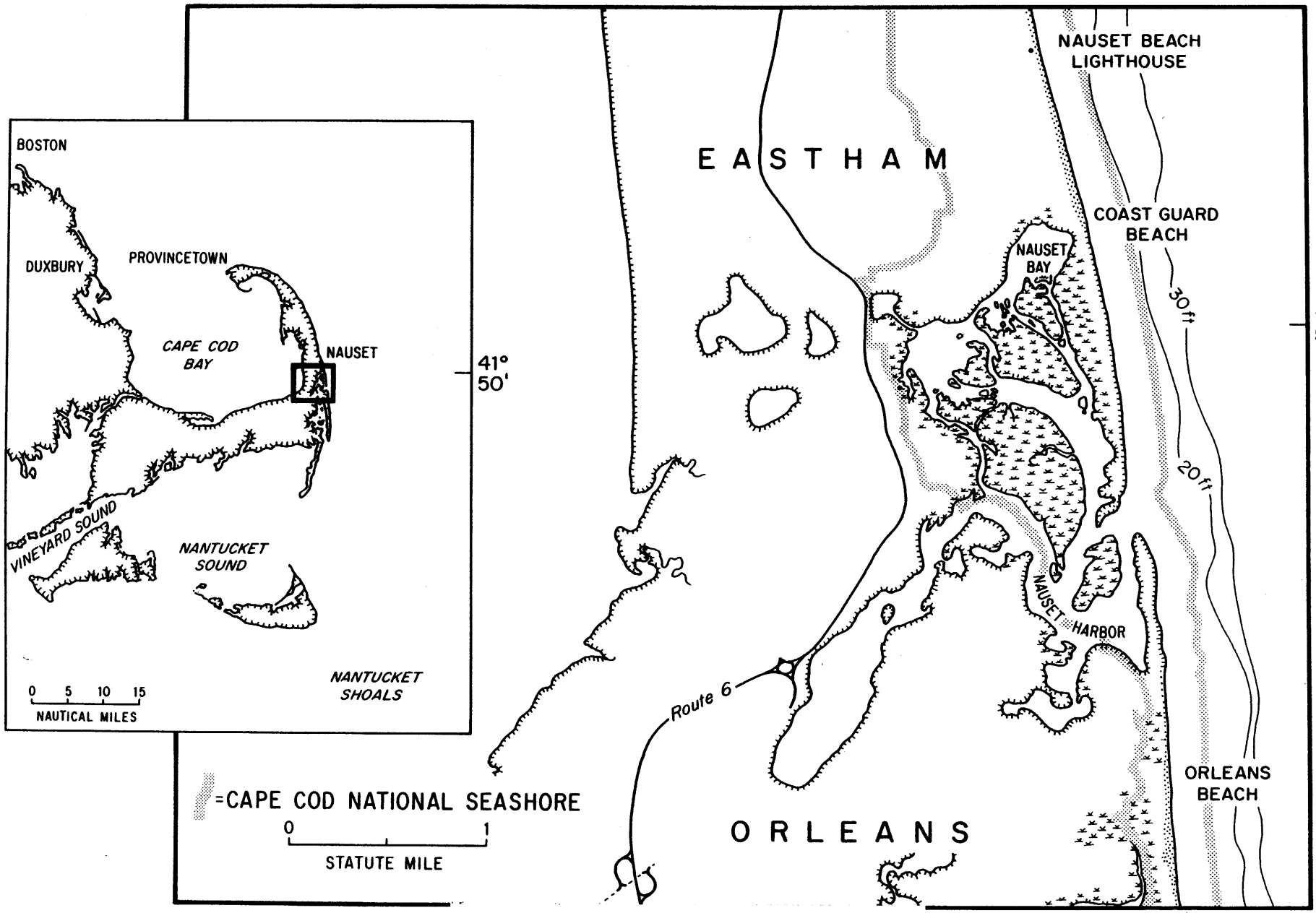

Figure. 1. Location map for study.

bordering Nauset Inlet to the north. Overwash processes along Nauset barrier beaches are described in Zaremba and Leatherman (1979). Aubrey and Speer (1983, 1984) discuss tidal flows and sediment transport in the bay and inlet. Other sedimentologic studies of the region are found in a summary volume by Leatherman (1979).

Sea level here has risen an average of about 3.5 mm/year. This rate is three times greater than the mean sea level rise of one mm/year over the past 2100 years established from measurements of salt marsh peat accumulation at Barnstable Harbor, Cape Cod (Redfield and Rubin, 1962). As discussed by Aubrey and Emery (1983) and others, although short-term mean sea level records exhibit considerable oscillations about a mean trend, the mean rate over the past 100 years has not changed significantly. Sea-level rise favors landward migration of evolving barrier beaches.

METHODS

Historical charts and aerial photographs of the Nauset Inlet area dating from 1670 and 1938, respectively, were examined to define and (where possible) quantify changes in inlet position and morphology. Historical data (figure 2) were obtained from a variety of sources including government agencies, the National Archives, the Library of Congress, the Woods Hole Oceanographic Institution, and private industry (Speer, Aubrey and Ruder, 1982; Appendices 1 and 2). Chart coverage is dense from 1790 to present (coverage was sparse before 1790), and good aerial photographic coverage exists from 1951 to present (only one aerial photo sequence was available prior to 1951, taken in 1938). Small scale and uncertain mapping techniques used in pre-1846 historical charts make it difficult to quantify changes in inlet morphology during this period, but these charts were valuable in depicting general trends in inlet morphology. Care was required in

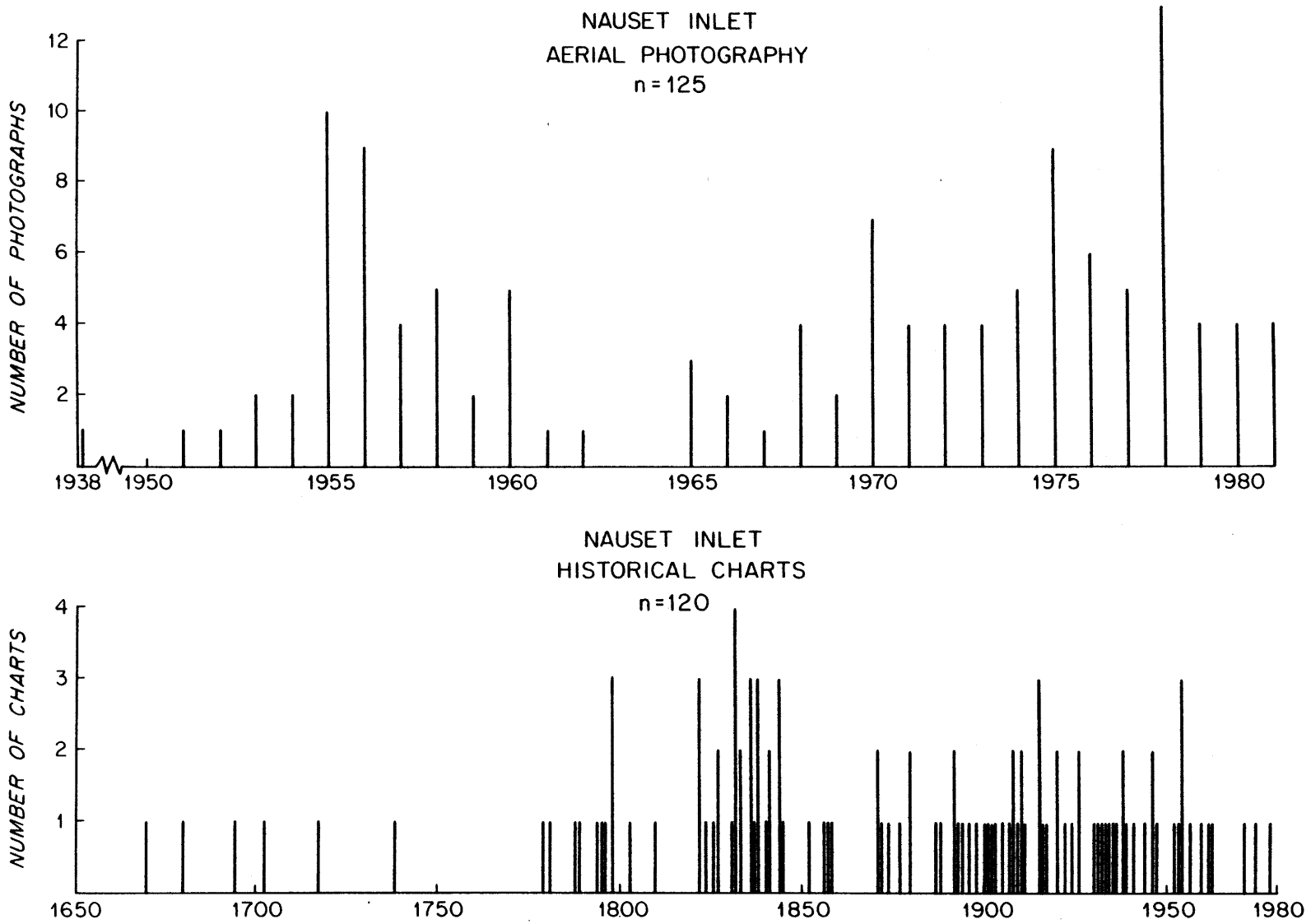

Figure 2. Summary of Nauset Inlet aerial photography (125 sets since 1938) and historical charts (120 sets since 1670).

interpreting the charts because several of the charts from the 1800's did not specify survey dates, and were merely reproductions of earlier and perhaps outdated surveys. Also, in the case of U.S. Coast and Geodetic Survey (USC&GS) charts, only limited shoreline segments were updated between editions.

Aerial photographs provide more detailed information than the charts because they are generally larger in scale (allowing resolution of shoreline features such as bars and marshes). They also provide more comprehensive temporal coverage for a limited period (1951 to 1981) than do the charts, and the dates of coverage are unambiguous. Fifty vertical sets of the 125 photographs available were measured to quantify inlet and spit migration at Nauset. The remaining photographs were not measured because they were taken at oblique angles, were poorly fitted mosaic series, or lacked sufficient ground control to assure measurement accuracy. However, they were instrumental in providing a continuous record of relative changes in inlet and spit locations during the past 30 years.

Measurements of spit and inlet locations are relative to a baseline, sub-parallel to the shoreline, established between well-defined, permanent features identified on each set of aerial photographs (figure 3). The known length of this baseline provided a consistent determination of scale for all photos. Uncertainty in some measurements resulted when one of the two primary reference points was absent from a particular photo mosaic. In these cases, secondary landmarks were used along with geometrical relations to define the baseline from the one available endpoint. As a result of such variations in the photographs, overall accuracy of measurements is estimated to be $\pm$ 15 m, despite a measurement resolution of 5 m.

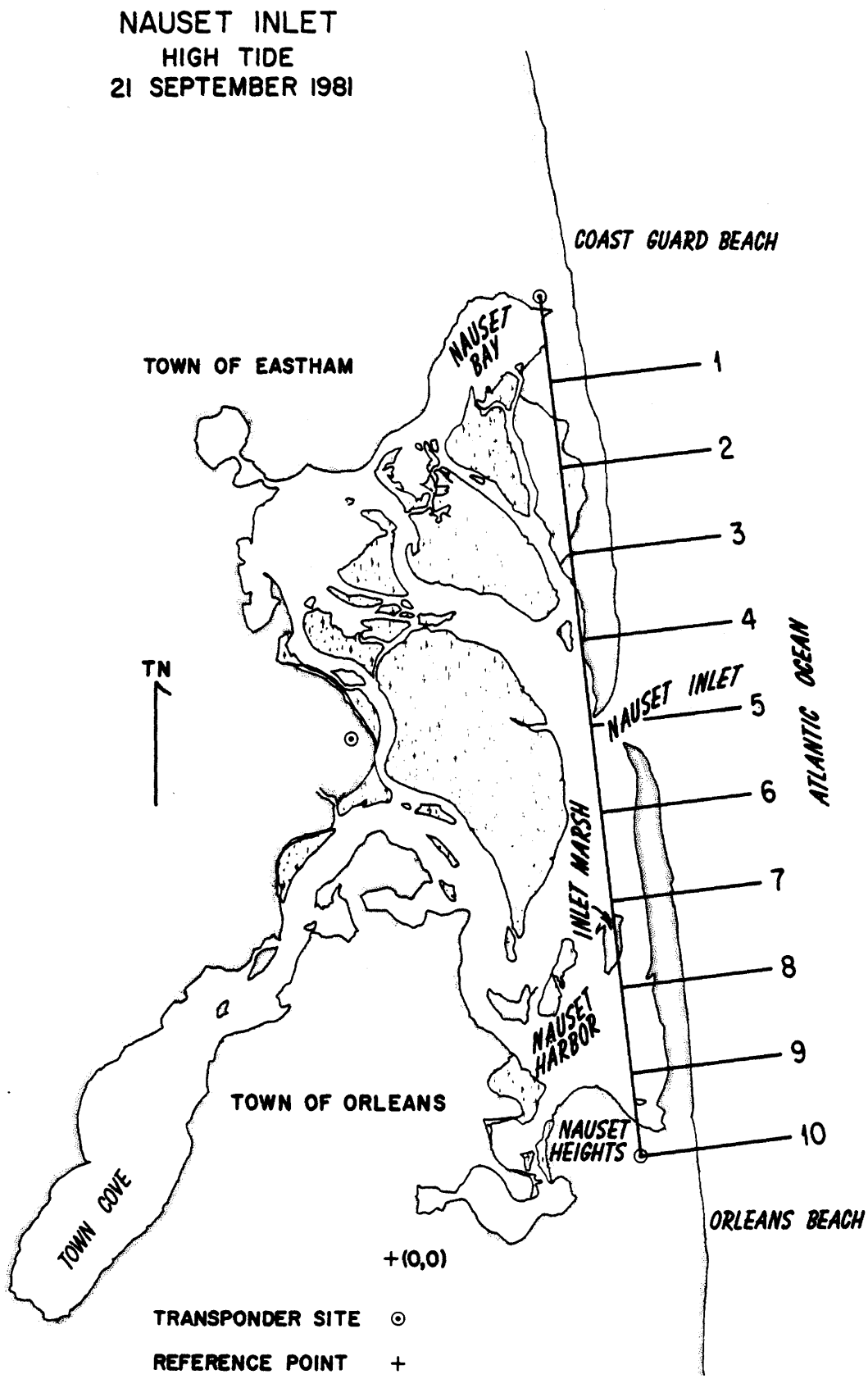

Figure 3. Baseline location for inlet migration measurements. The northern reference point adjacent to Coast Guard beach is Coast Guard Station. Distance between adjacent reference lines (1-10) is 535 m.

RESULTS

Analysis of historical charts and photographs reveals patterns of inlet migration and barrier beach elongation/shortening at Nauset. Nauset Inlet has migrated extensively over the past 30 years, related in part to an increase in storm frequency, as discussed below.

INLET/BARRIER BEACH MIGRATION

Historical charts (dating from 1779) and aerial photography (dating from 1938) show the preferred inlet location to have been just north of Nauset Heights, at the southern (downdrift) extremity of the bay drainage system (figure 4). None of the charts (up to 1946) depict a significant south spit. Although aperiodic historical coverage might have undersampled previous episodes of inlet migration, the persistence of a southern location suggests this was an historically stable inlet configuration.

Aerial photographs from 1938 and a 1946 USGS chart confirm an inlet location just north of Nauset Heights, with no south barrier apparent (figures 5 and 6). From the 1950's into the early 1980's, the inlet has been active with three distinct cycles of northward (updrift) movement. The first two of these (figure 5; 1952-1957; 1965-1972) resulted in a pattern of overlapping spits. In both cases, the length of the north spit remained approximately stable while the south spit continually grew north. The third cycle (figure 5; 1972-1984) has involved substantial erosion of the north spit along with northward growth of the south spit.

The first cycle of northward growth was initiated by storm activity. The north barrier was breached and a remnant of the barrier located south of the new breach attached to the south barrier. Subsequent southward growth of the north barrier through attachment to an island in the marsh (Inlet Marsh), and northward growth of the south spit, resulted in the over-

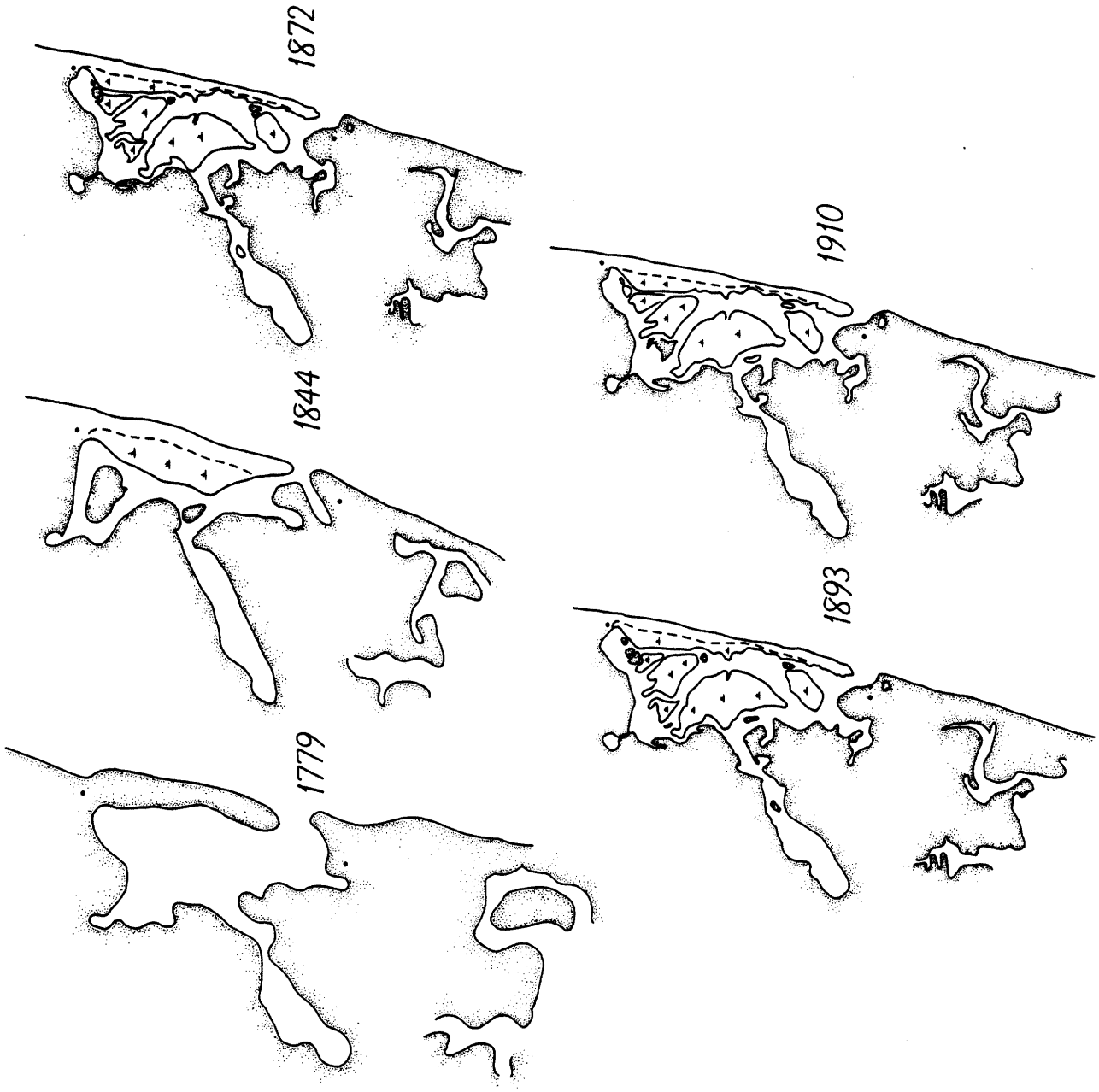

Figure 4. Five representative historical charts depicting variability of Nauset Inlet from 1779-1910.

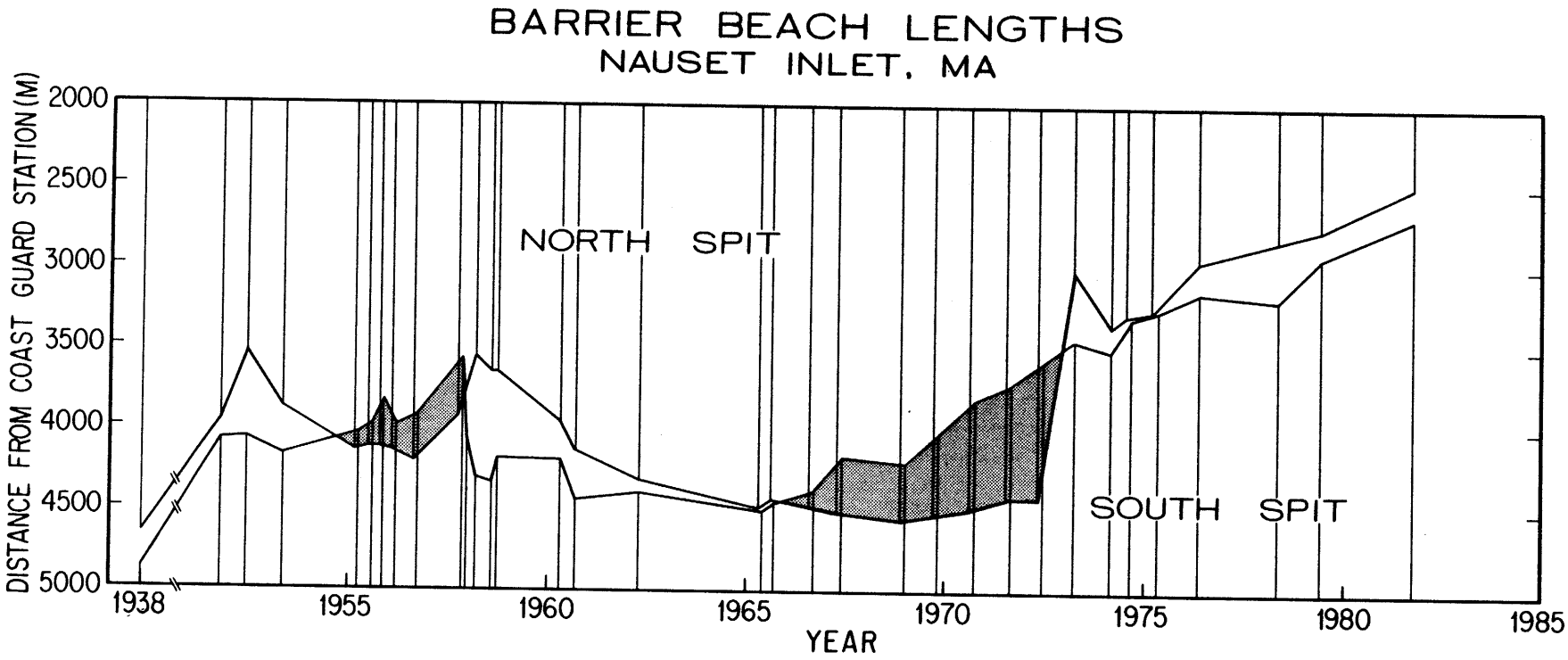

Figure 5. Location of North Spit and South Spit termini, measured along the baseline from Coast Guard Station (see figure 3 caption). Stippled patterns indicate periods when South Spit overlapped North Spit, and extended farther north. Vertical lines indicate periods for which measurements were made.

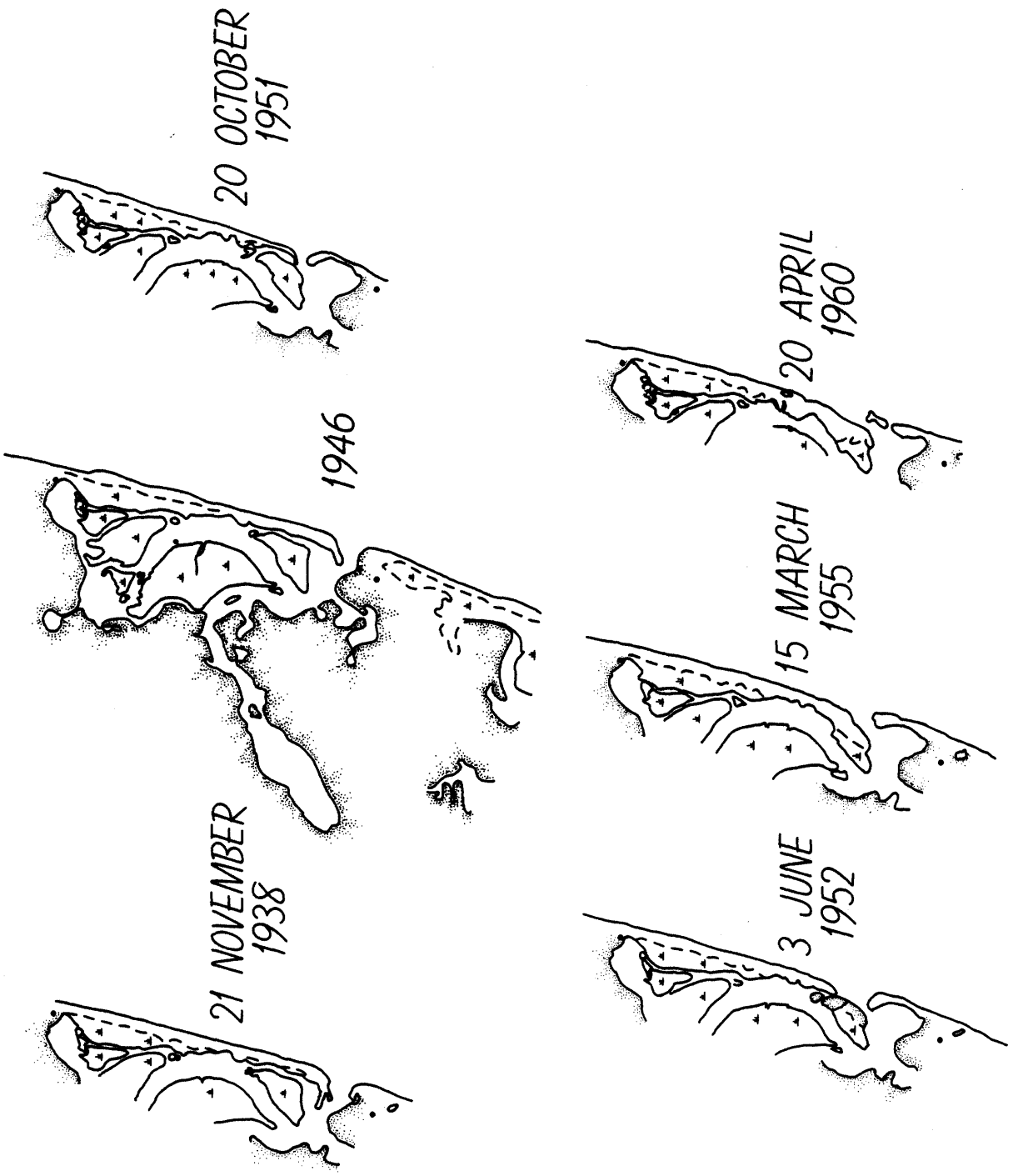

Figure 6. Tracings of vertical aerial photographs of Nauset Inlet between 1938 and 1960.

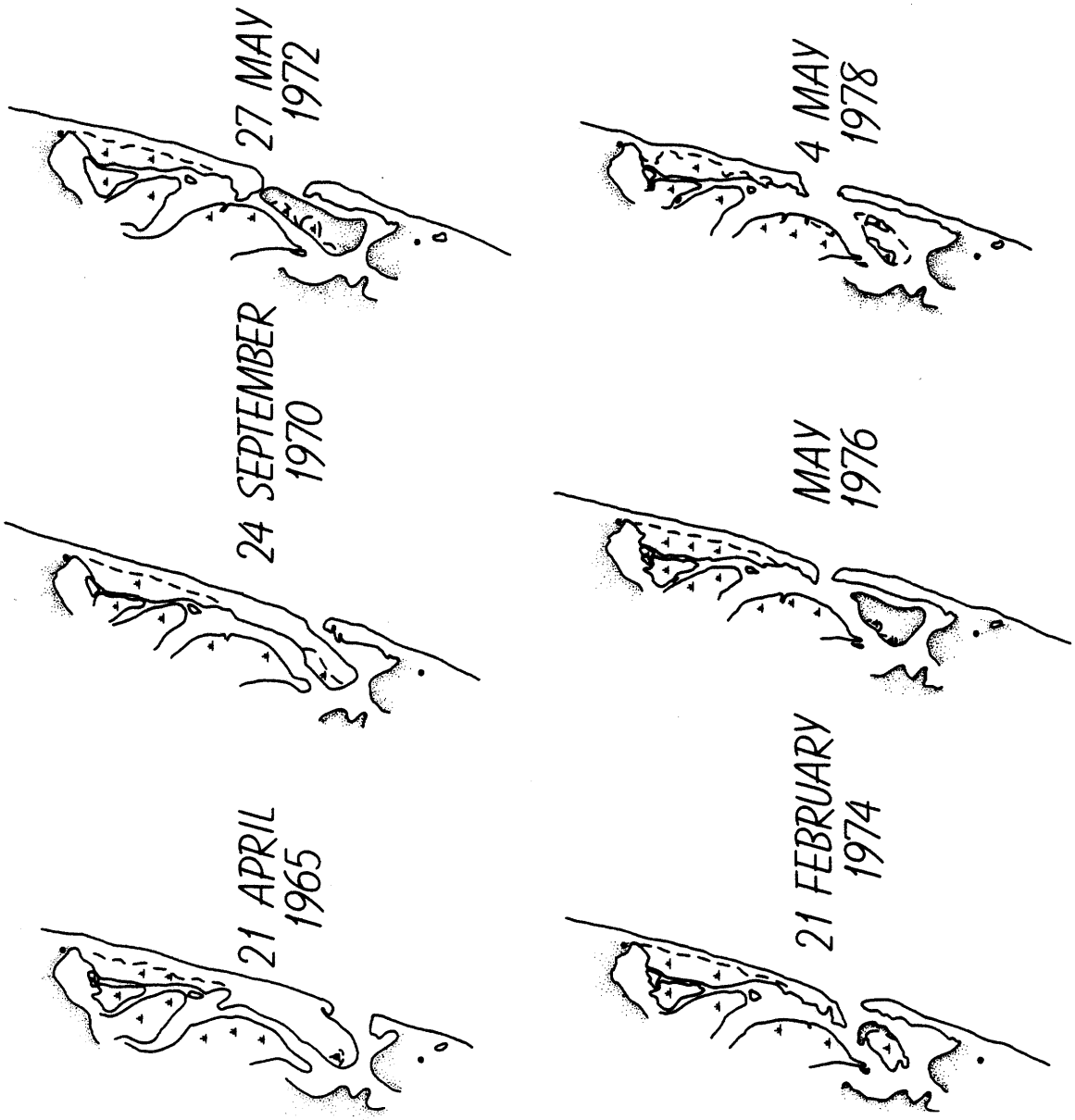

Figure 7. Tracings of vertical aerial photographs of Nauset Inlet between 1965 and 1978.

lapping pattern of the mid-1950's (figure 6). During this period of barrier growth, the elongated inlet channel extended to the north from its original southern location. A series of storms in the late 1950's and early 1960's re-established the inlet to its southernmost position immediately adjacent to Nauset Heights (figure 6f, 7a). By April 1965, the inlet/barrier beach configuration was similar to that in 1938, with the sole major difference being landward migration of the north spit due to repeated storm overwashes (Zaremba and Leatherman, 1979). The second cycle of northward migration was characterized by extension of the south barrier while the north barrier remained in approximately the same location. Between 1965 and 1972, the south spit extended nearly 900 m to the north (figure 7b, 7c). As in the mid-1950's, the inlet channel also extended north, accompanying this barrier growth.

The final cycle of northward movement was initiated by a storm breach in the north spit in the spring of 1972 (figure 7c). This resulted in the present phase of northward migration which is qualitatively different from the previous two episodes. In this third instance, the main inlet channel stabilized in the location of the newly formed breach with the former inlet closing off. Since 1972, the inlet channel and the south barrier have been growing northward at a rate of approximately 100 m/yr. Unlike previous cycles, the north spit is steadily eroding and the main inlet channel is actually moving north, instead of simply extending to the north from a southern location (figure 7d-7f). No major breaches affecting the stability of the south spit have occurred during this latest period. A large overwash occurred at the northernmost part of the north spit during the 6 February 1978 blizzard. Since this overwash emptied into a shallow

(<1 m deep), broad bay (Nauset Bay), the overwash did not evolve into a permanent breach. Such an overwash occurring on the south spit would probably result in a new inlet position.

STORM ANALYSIS

The Atlantic shore of Cape Cod is frequently buffeted by storms which have the potential to cause dramatic changes in shoreline configuration. A U.S. Army Corps of Engineers report (1979) cites 160 gales with wind speeds greater than 32 mph between 1870-1975. Half of these were northeasters. Both tropical and extra-tropical (including northeasters) cyclones produce dramatic changes at Nauset Inlet because of the geographical orientation of the outer Cape.

Three types of storm data were collected for comparison with large-scale morphologic changes at Nauset Inlet:

a) Hayden and Smith (1982) compiled a monthly list of cyclone occurrences off the east coast between 1885 and 1982, using as a data base the "Tracks of the Centers of Cyclones at Sea Level" published by Monthly Weather Review and in recent years by Mariners Weather Log. Cyclone statistics (both tropical and extra-tropical) are available on 2.5° latitude by 5° longitude grid cells. The four grid cells bordering the Cape Cod region to the east and southeast (total area covered is 60°W to 70°W, $37\frac{1}{2}$°N to $42\frac{1}{2}$°N) are used as the region of storm influence for the study area. For generation of year-by-year and monthly mean statistics, storm values for the four grid cells are summed. Although this yields an overestimate of the number of storms (the same storm may pass more than one grid cell), it will still provide a qualitative indication of storm duration and persistence, since on the average a storm tracking through two grid cells generates waves in the study area for a longer period of time than one passing a single grid cell.

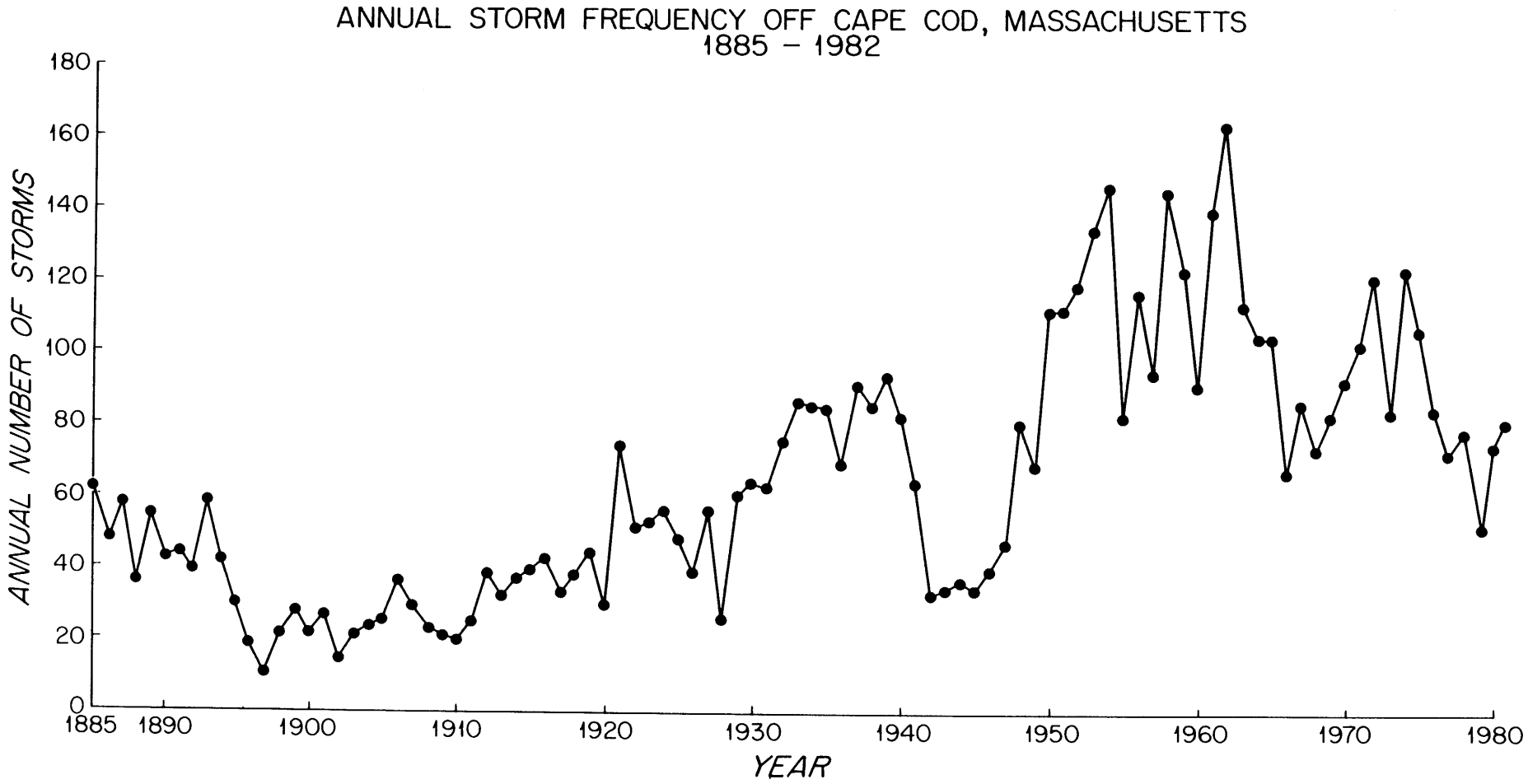

Figure 8. Number of cyclones affecting Cape Cod, Massachusetts (including area 60°W to 70°W, 37½° to 42½°N) from 1885 to 1981. Storm count is indicative of storm duration, and not individual cyclone events. Data derived from Hayden and Smith (1982).

Cyclone statistics resulting from the averaging serve as a crude indicator of wave activity. Large cyclone counts suggest high wave activity; a small cyclone count represents low wave activity. Persistence and frequency of storms are our criteria for wave intensity. Clearly, storm intensity or magnitude would be a useful weighting factor for linking waves and storms; unfortunately, this information is not available.

The period from 1885 through 1949 experienced a relatively low incidence of storm activity (figure 8). Within this low background level, the periods from 1885-1893, 1921-1924, and 1930-1941 have local maxima in cyclone frequency. The last thirty years of the record show consistently higher cyclone frequency, with local maxima at 1950-1954, 1961-1962, 1972 and 1974. Although the absolute number of storms may be sensitive to the quality and quantity of weather observation stations, local trends (minima and maxima) are valid indicators of relative storm occurrence.

b) Another source of storm incidence data was the U.S. Army Waterways Experiment Station (WES) wave hindcast program (data provided by W. Birkemeier). This program computes nearshore wave height statistics based on weather observations and local bathymetry. The study identified the 157 largest storm events from 1956 to 1976 (inclusive). These storms were assigned recurrence intervals according to their rankings, allowing for weighting of storms by severity. The WES compilation (figure 9) correlates well with cyclone data. W.E.S. data show high storm activity in 1956, 1962, and 1972; however, it also indicates a high level of storm activity in 1969 which does not appear in cyclone data. Differences between the two data sets are the result both of weighting procedures and different representations of the data base.

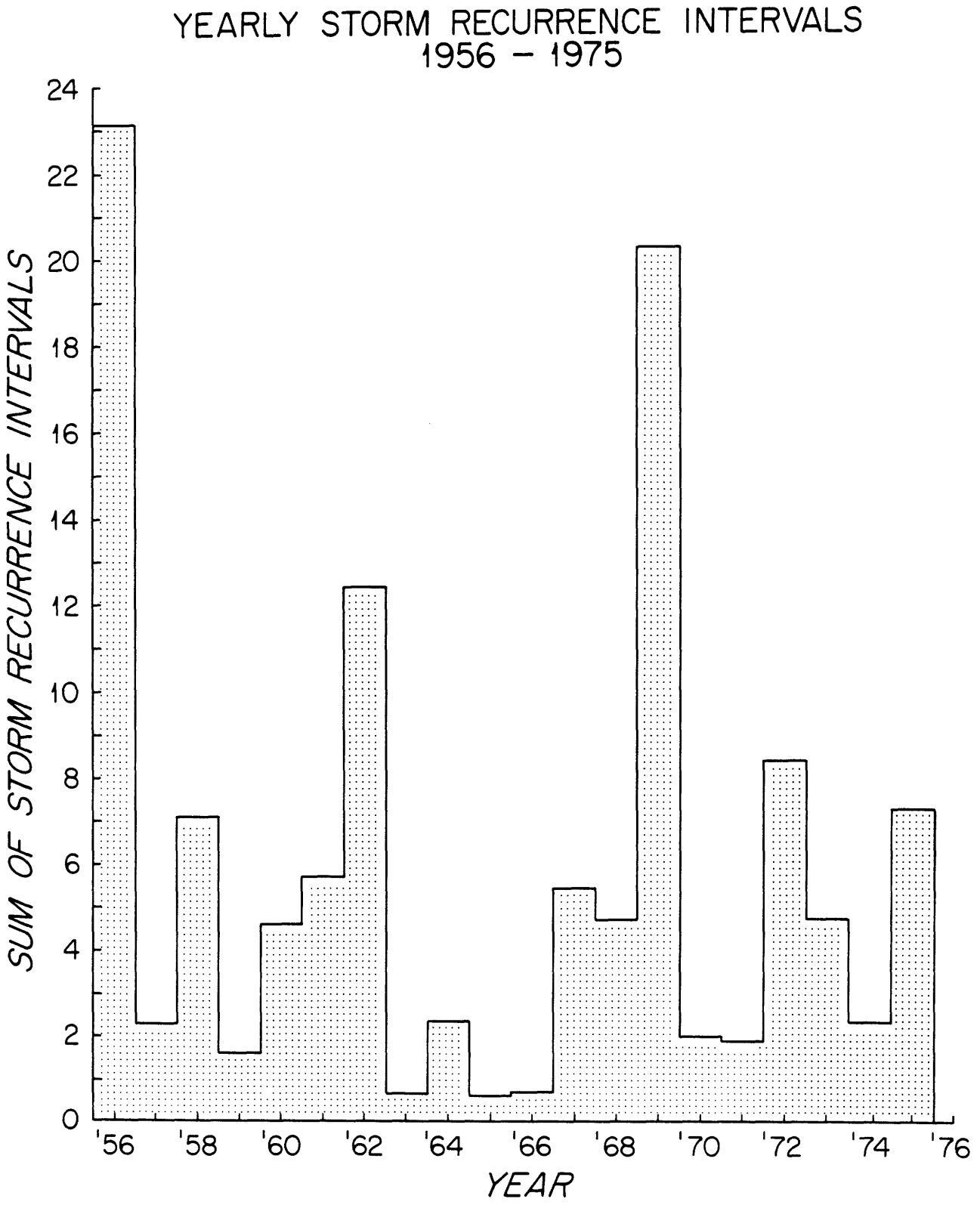

Figure 9. Yearly storm activity from 1956-1976 off Cape Cod, Massachusetts, determined by W.E.S. hindcast.

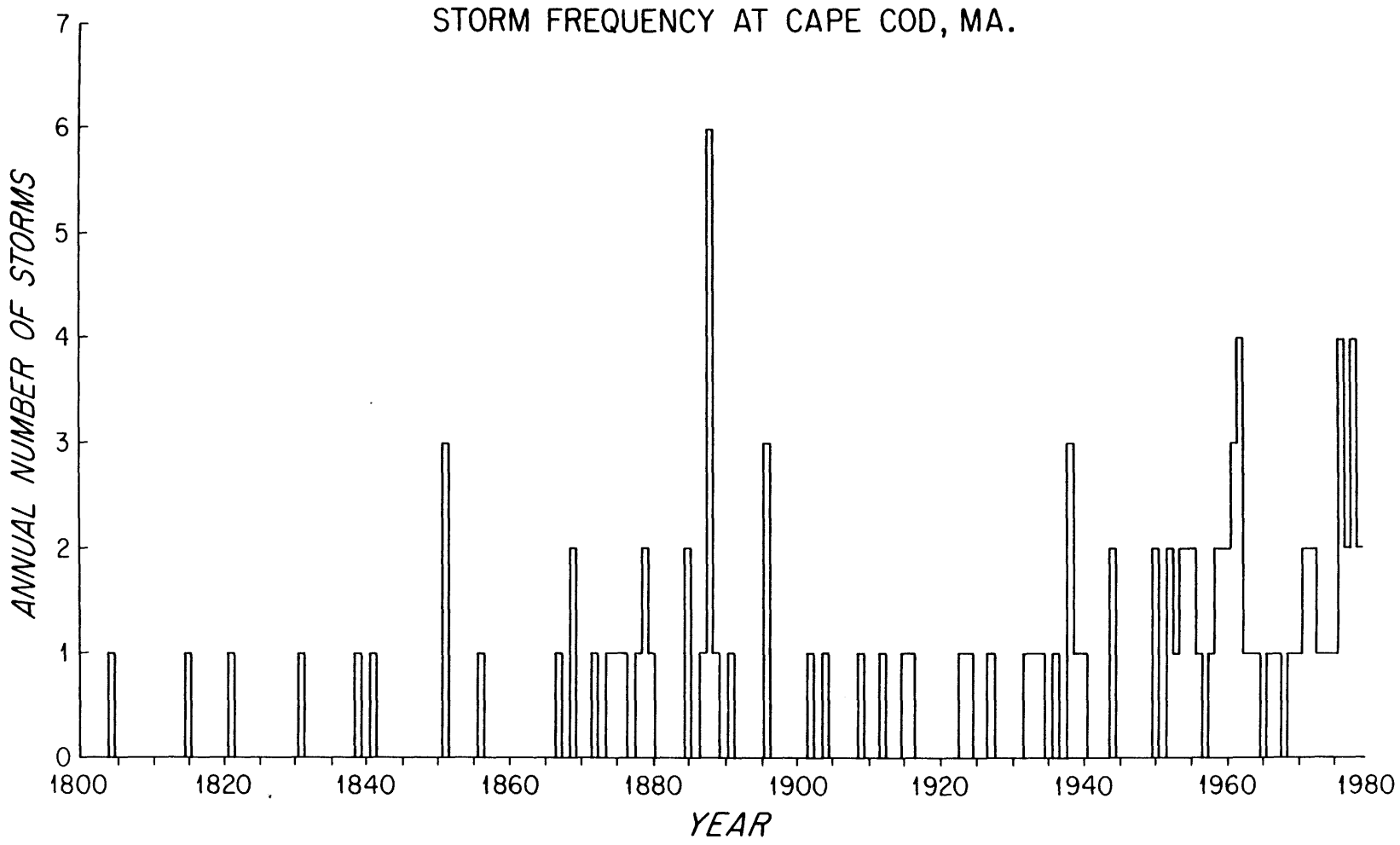

Figure 10. Compilation of storm events on an annual basis from 1800 through 1980. Sources are newspapers, historical descriptions, and published tropical storm tracks.

c) Finally, a list of major storms affecting the outer Cape was compiled from newspapers, historical descriptions, and published tropical storm tracks (figure 10). This list is incomplete since prior to 1948 it only includes hurricanes and storms of historical significance. It is possible to identify specific storms which are likely to cause changes at Nauset Inlet, although irregular sampling afforded by aerial photography (figure 2) makes direct correlation difficult. Through this method, ten significant storms were found that were not hindcast in the WES study.

DISCUSSION

Aerial photographs and historical charts reveal patterns of inlet/barrier beach change with which conceptual models must be consistent. The important features of Nauset Inlet's migration patterns are: the historical stability of the southernmost inlet entrance; the role of storms in initiating major changes in the inlet/barrier beach system; and the recent tendency for the inlet to move in a direction opposite the predominant longshore drift. Migration of the inlet with accompanying changes in the barrier beaches takes place on essentially two different time scales. Major relocations of the inlet, involving longshore movements of hundreds of meters in several days, occur episodically during large storms, and have a recurrence on the order of a decade. The other important time scale is associated with the recent steady migration of the inlet in a general northward direction, responding to the combined effects of wave activity, tidal flows, and longshore sand transport. The magnitude of this movement is on the order of 100 m/yr. Northward migration of the inlet is accompanied by extension of the southern barrier and generally by shortening of the northern barrier (especially from 1973-1983).

The general stability of a southern inlet location in this system is not surprising. Most of the tidal prism passes through the deeper southernmost channels of the marsh, therefore a southern inlet provides the most direct link to the ocean. Frictional dominance in this shallow inlet/estuary system (Aubrey and Speer, in prep.; Speer and Aubrey, in prep.) makes this an energetically favorable location for the inlet. The 1983 location of the inlet requires that long (~2 km) shallow channels carry most of the tidal prism to the south. A large fraction of the total tidal energy is dissipated in these channels; consequently development of an energetically more favorable inlet location further south is probable in the near future (order of a decade).

The southernmost location places constraints on barrier beach configuration. In general, the northern barrier is not strongly eroded by the ebb tidal flows when the inlet is in a southerly location as compared to a more northerly one (reasons for this are presented later). A short, slowly-growing southern spit can develop without catastrophic storm influence. However, large-scale growth of a southern barrier spit is dependent on storm activity and breaching of the northern barrier.

Three mechanisms appear responsible for observed updrift tidal inlet migration at Nauset (figure 11): a) attachment of distal ebb tide delta bars to the downdrift barrier spit; b) storm-induced breaching and subsequent stabilization to form a new inlet; and c) ebb tide discharge around the inlet channel bend. The last two mechanisms can result in either updrift or downdrift migration. The first two mechanisms have been observed widely at other inlets; the third mechanism is described here for the first time.

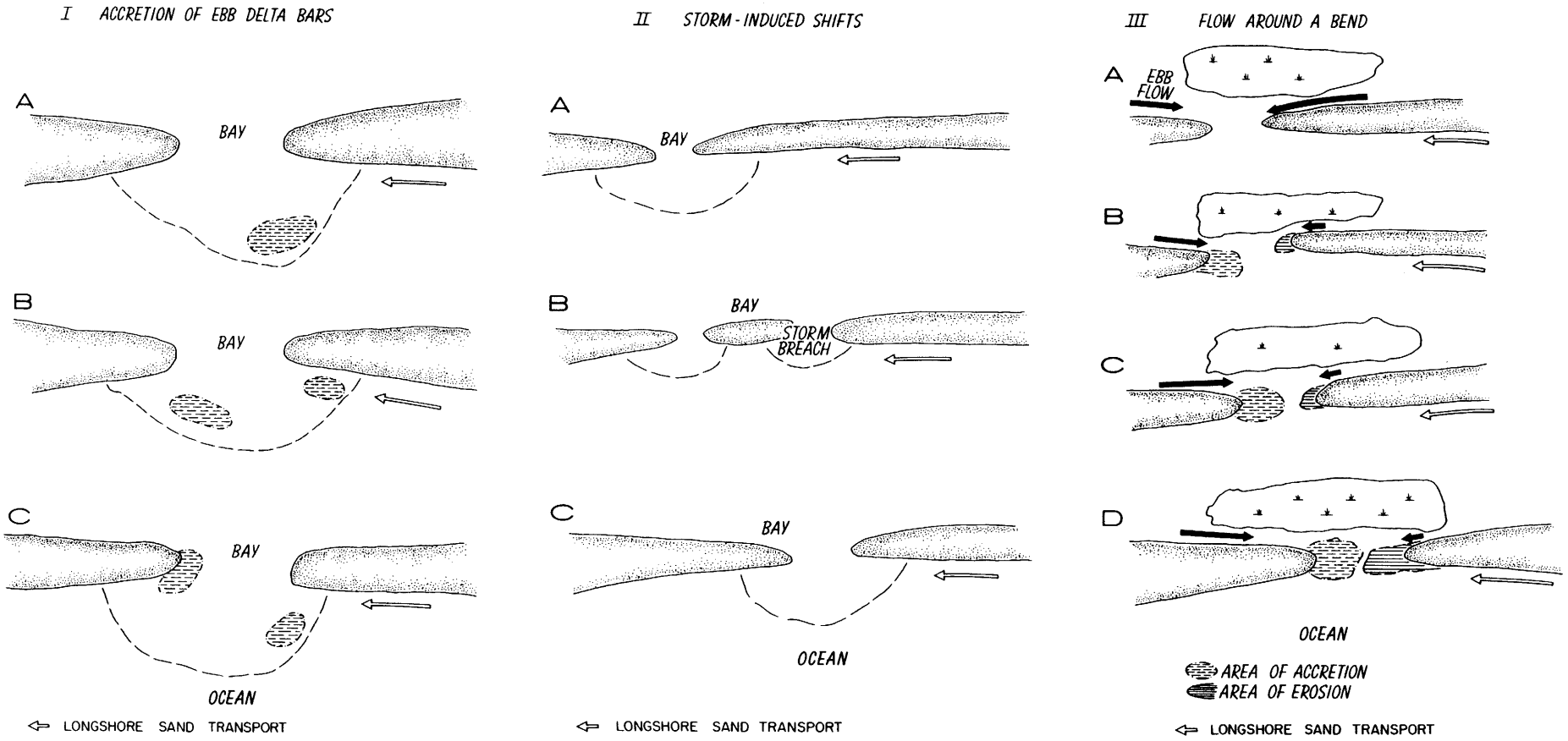

Figure 11. Three modes of updrift inlet migration responding to different combinations of waves, tides and storms. All three modes have been observed at Nauset Inlet, Cape Cod, Massachusetts.

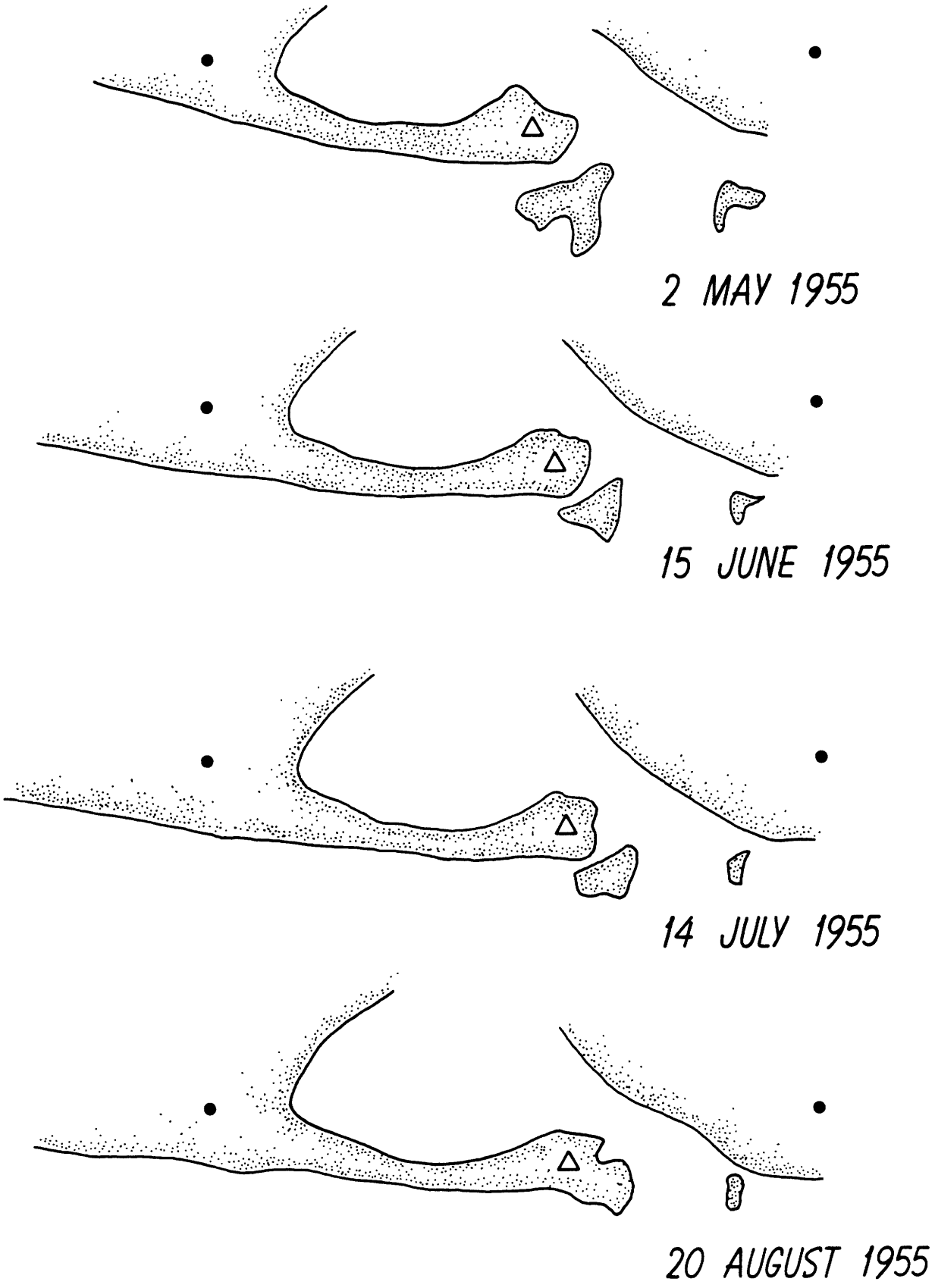

Figure 12. Four month bar-bypassing event observed at Nauset Inlet, Massachusetts.

a) Any model of Nauset Inlet's migration must include mechanisms for longshore bypassing of sediment past the inlet, since the volume rate of longshore sand transport is a primary factor controlling inlet stability (e.g., Brunn and Gerritsen, 1959; Bruun, 1978). Large net longshore transport rates, estimated to be about 250,000 m^3/yr to the south (U.S. Army Corps of Engineers, 1969), occur at Nauset Inlet. Consequently, shallow overwashes are typically filled quickly, and the tidal prism seems capable of supporting only a single stable inlet.

A common mode for sediment bypassing of tidal inlets is through formation and migration of distal ebb delta bars, which are predominantly wave-driven. For many wave-influenced tidal inlets throughout the world, ebb delta bar migration is the dominant bypassing mode (Bruun, 1978; Fitzgerald, 1983; Nummedal, 1983), while bypassing through the inlet proper (Galvin, 1983) appears less important. Bar bypassing results in episodic accretion of sand on the downdrift barrier, often increasing encroachment of the downdrift barrier into the inlet throat.

Bar bypassing has been documented several times at Nauset Inlet (figure 12), increasing the length of the southern (downdrift) barrier. The existence of active bar bypassing at Nauset causes south spit to grow to the north, <u>against</u> the influence of predominant longshore transport, since the migrating bars weld to the spit terminus instead of escaping the inlet influence (figure 11). Although not shown on the figure, the accreted sand remains on the downdrift spit, increasing its length, and forcing the inlet to migrate northwards. Contrary to the observations of Fitzgerald (1983), these accretionary episodes occur on time scales of months, not years.

b) The importance of storm activity to major changes in inlet/barrier beach configuration is illustrated by comparison of inlet migration rates with storm frequency. Historical data (figures 8, 9 and 10) show three periods of high storm activity since 1933, preceded by a 48 year period of relative quiescence. The first period of intense activity lasted from 1933 until 1939. Unfortunately, inadequate chart and photo coverage prevents full documentation of inlet response to this stormy period. The second stormy period covered the years 1950 to 1962. Large scale inlet migration, together with overwash and breaching of the barrier beaches, occurred during this time. The north barrier breached in May 1953 and January 1956, while the south barrier breached in December 1957 and early spring 1960. Storm-induced changes in barrier beach length of as much as 780 m have been observed. A third period of intense storm activity existed in the early 1970's. One of the peak years, 1972, coincides with a breach in the north spit, which initiated the current phase of steady northward inlet migration.

c) Casual observation of tidal inlet and estuarine flows shows that these channels often are not straight, but rather have pronounced curvature. This curvature has dramatic effects on flow through these channels, affecting near-bed shear stress distributions and resultant sediment transport. Complexity of channel geometry ranges from long, straight channels with occasional bends, to nearly continuous, sinuous geometry reminiscent of river channel meanders. Channel curvature within an inlet mouth provides a mechanism for inlet migration, as discussed below. An extensive literature discusses the effects of channel curvature on flow structure and sediment transport, largely resulting from an interest in river channel meanders and open channel flow. Much of the work to date has been done by engineers interested in channel scour and deposition (e.g., Nouh and Townsend, 1979), or by geologists studying riverine processes (e.g., Dietrich

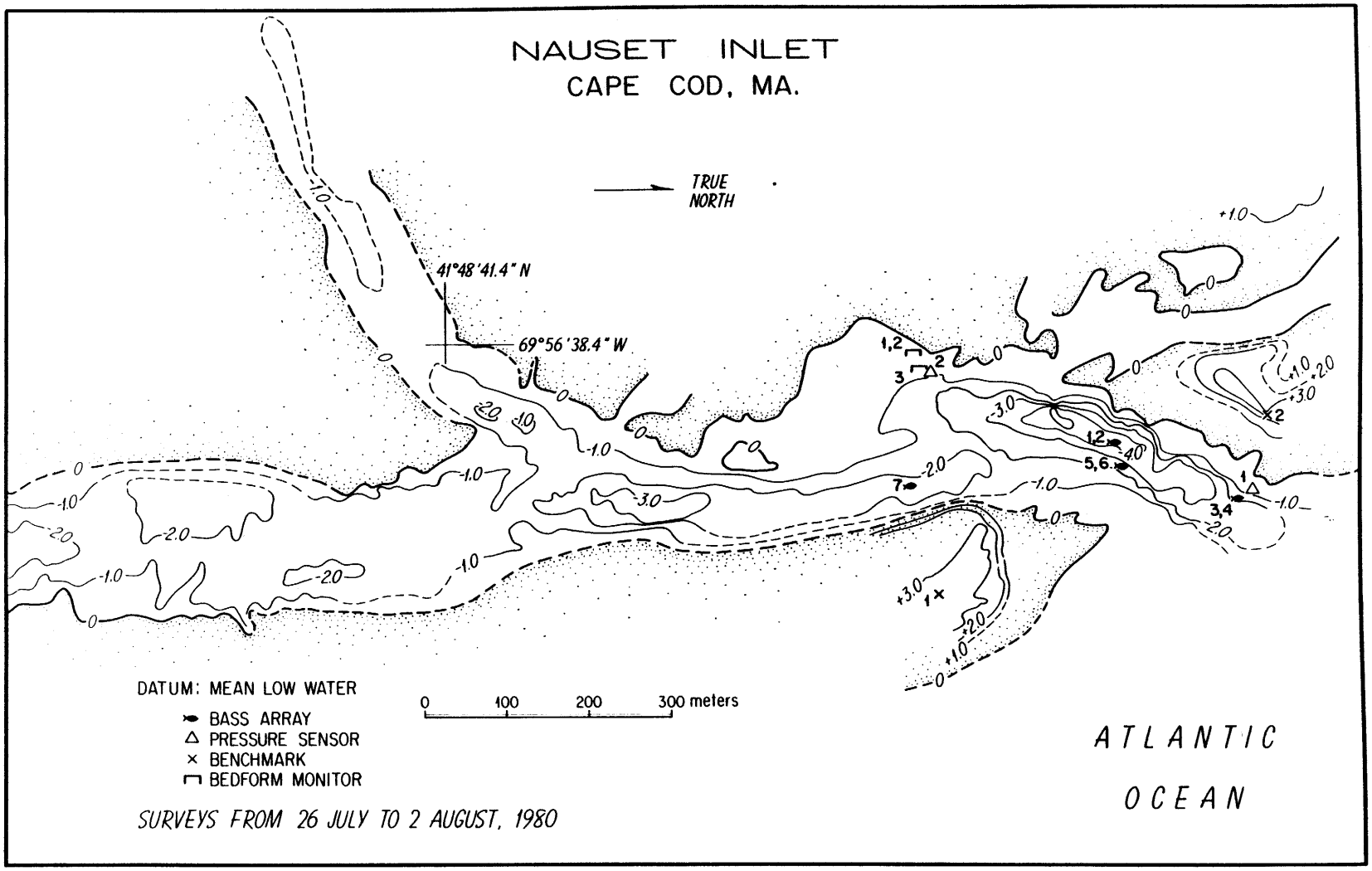

Figure 13. Nauset Inlet in summer of 1980 shows the strong channel curvature responsible for 'river-bend' flow structure. Primary tidal channels in the estuary are to the south (left), causing this curved flow.

et al., 1982). Recently, more complete numerical models have quantified aspects of channel bend flow which had been described qualitatively by previous researchers (e.g., Smith and McLean, 1983).

Since the inlet mouth at Nauset has considerable curvature (figure 13), sediment transport patterns are modified by resulting bed shear stress gradients. To examine the magnitude of flow curvature at Nauset Inlet and evaluate its effect on sediment transport, simple theory was developed and tested by field observations (Aubrey and Speer, 1983). Since flow curvature induces gradients in water level through a channel bend, and water level is relatively easy to monitor compared to velocity or shear-stress distribution, modeling and measurement efforts concentrated on surface gradients across the inlet mouth.

For simple geometry and quasi-steady channel flows, the along-channel (n) momentum equation reduces to a simple balance between the bottom stress (τ_b) and the sea surface gradient ($\partial\eta/\partial n$):

$$\tau_b = -\rho g h \, \partial\eta/\partial n \qquad (1)$$

where h = mean water depth, ρ is density of water, and g is gravitational acceleration. If the downstream set-down is measured, an estimate of total bottom friction is obtained. The lowest order equation for cross-stream flow reduces to:

$$\frac{U^2}{gR} = \frac{\partial}{\partial r}(\eta) \qquad (2)$$

for the case of small channel half-width (b) compared to radius of curvature (R). U is the depth-averaged velocity. For a sinusoidal channel, the cross-stream gradient reduces to:

$$(\eta_b - \eta_{-b}) = \left(\frac{2b}{gR_o}\right) U^2 \qquad (3)$$

The depth-averaged velocity required for solving for cross-channel gradient is obtained from equation (1) and

$$\tau_b = \rho C_f U^2, \tag{4}$$

where C_f is a friction coefficient. Then the cross-channel set-up is given by

$$(\eta_b - \eta_{-b}) = \left(\frac{2bh}{R_o C_f}\right) \partial\eta/\partial n \tag{5}$$

This simple depth-averaged model can be improved using a complete perturbation solution (similar to that used by Smith and McLean, 1983), but the difficulty of obtaining high quality field data within a tidal inlet with which to evaluate such theory caused us to use the simple theory outlined above.

Field experiments covering five days (described in detail by Aubrey and Speer, 1983) examined the magnitude of sea surface gradients, and checked their consistency with channel bend theory. Maximum instantaneous down-channel gradient over the five-day period during ebb tide was 0.0007 (thirty centimeters over the channel length separating the two sensors), while maximum flood tide gradients were 0.0005 (twenty centimeters over the same separation). Average maximum gradients over the five-day period are the same for flood and ebb tide (18.5 cm over the instrument separation). From these gradients, a maximum shear stress of approximately 140 dynes/cm^2 was calculated, where these shear stress estimates include not only near-bed friction but also form drag, wave/current interaction, and sediment transport effects (e.g., Grant and Madsen, 1982). Bed shear stress is not easily separated from this total shear stress. Maximum cross-channel set-up of approximately 5 cm was calculated from the down-channel gradients, using equation (5), which represents a slope of 0.0009, similar

to the down-channel gradient. Field measurements show a cross-channel set-up of complicated structure, with a magnitude of five-to-eight cm, most of which is consistent with the simple model presented above. The remainder of the observed set-up is of unknown hydrodynamic origin and not explained by our simple theory.

Theory and observation are consistent with the analogy between Nauset Inlet flow structure and river-bend flows, although neither the measurements nor theory allow for in-depth comparison of the flow fields. Resulting inlet morphology is also consistent with the hypothesis that channel bends are responsible for inlet migration. Nauset Inlet has both a steep outer (northern) channel bank, and an accreting point bar on the inner (southern) bank, similar to sedimentation patterns in river bends. Observation of Nauset Inlet since 1972 shows a migration pattern consistent with the river bend analogy, with the south spit elongating and the north spit shortening due to erosion. Although analogies between inlet bends and river bends based on simple theory and observations of flow patterns and sedimentation are incomplete, they indicate the potential importance of curvature in inlet geometry on migration history of tidal inlets.

A conceptual model of inlet migration (figure 11) based on the three mechanisms described above explains the unusual northward movement of Nauset Inlet, opposite the longshore transport direction. When the inlet is at its southernmost location, the estuary channels empty directly into the ocean. There is no curvature to the flow (which could result in complex flow non-uniformity), and the north barrier is not preferentially eroded. Tidal flows are strong enough, however, to prevent material trans-

ported past the north spit from filling in the inlet channel. Bar bypassing of littoral drift leads to accretion along the downdrift spit. If storms do not halt this growth, the south spit can extend to the north and eventually overlap the north spit, as occurred in the late 1960's and early 1970's. The base of the inlet channel retains its southerly location, and the channel simply elongates to the north. In this configuration, the north barrier remains essentially unchanged. This particular pattern has been observed once in the last 30 years.

A different mechanism was responsible for the barrier overlap pattern observed in the 1950's. In this instance, the northern barrier was breached during a storm. The barrier remnant south of the breach attached to Nauset Heights to form a relatively long southern spit. The base of the inlet channel retained its southern location and extended through the breach. Subsequently, the northern barrier lengthened by attachment to a marshy island in the bay. The south spit further elongated through bar bypassing, resulting in a pattern of overlapping spits. As in the 1965-1972 pattern, the inlet channel lengthened as the south spit grew to the north. The north spit remained relatively stable after attachment to the bay island. Neither of these patterns is representative of the present migration phase. The past ten years of movement have been characterized by actual northward migration of the inlet channel and shortening of the north spit, with no barrier overlap.

A storm breaching the north spit in 1972 caused this new migration pattern to develop. The main inlet channel stabilized further north than in previous storm breaches. As a result, the dominant ebb tidal flow was constrained to flow to the north, and then east through the inlet channel, setting up a channel bend flow pattern with erosion on the outer part of

the bend (north), and accretion on the inside of the bend (south). The north wall of the inlet channel is presently eroding while a large sand deposit is forming on the south bank of the channel. This "flow around a bend" has existed for approximately ten years, leading to nearly 1 km of northward inlet movement. This migration will probably continue until either the inlet encounters an erosion-resistant substrate or a major storm changes the inlet location. In the case of Nauset, the former is unlikely (see Aubrey et al., 1982) since inlet tidal flows are currently eroding peat deposits underneath the sandy barrier spits. Nothing more erosion-resistant is likely to be encountered. Storm-induced inlet relocation is a strong possibility. The long, frictionally dominated channels presently carrying the tidal prism would probably be abandoned if a more southerly breach were created by a storm. In that case, the large long-shore transport could quickly close off the present inlet, which is nearly clogged by the extensive ebb-tide delta. A more northerly breach created by storm overwash is not likely to persist (as the February, 1978 blizzard demonstrated) because the northern depths and tidal prism are too small. An additional factor increasing the likelihood of breaching near Nauset Harbor is the narrow width of the barrier at this point. This narrowing is caused by erosion on the bay side of the barrier during ebb tide, as the easterly-flowing tide is redirected northwards towards the present inlet (resulting in another complex, channel-bend flow pattern).

The long-term fate of this estuary is affected by two dominant trends: inlet migration (which contributes sediment to the estuary via flood tide delta growth) and westward spit migration. Both of these factors reduce the tidal prism, and consequently reduce the equilibrium cross-sectional area of the inlet. The first factor has been discussed in detail. The

second factor, net onshore migration of the Nauset barrier beach, is apparent in spite of large, higher frequency fluctuations (Speer et al., 1982). The steady shoreward migration is a result of sea level rise combined with overwash and inlet processes (barrier roll-over). Higher frequency oscillations superimposed on this steady retreat result from inlet migration episodes, seasonal beach changes, bar bypassing events, and large, nearshore bedform generation (Aubrey, 1980). The effect of the onshore migration is a reduction in tidal prism (specifically by reduction of the area of the back bay). Tidal prism is also reduced by deposition of sand as a flood tide delta, an important factor since 1972, as the inlet has steadily migrated northwards approximately 1 km. Vestiges of the former flood tidal deltas are visible on recent aerial photographs of the area. As a result of overwash and bay infilling, the stable inlet configuration will become narrower and shallower with time (reduced equilibrium cross-sectional area). This filling trend currently exceeds back-barrier deepening attributable to sea-level rise, but anticipated increased rates of sea-level rise (Aubrey and Emery, 1983) may reverse this trend.

SUMMARY

Three distinct patterns of natural inlet migration have been identified from historical data (figure 11), and their underlying causes hypothesized. These mechanisms explain the rare case where an inlet migrates in a direction opposite the dominant longshore sand transport, such as at Nauset Inlet. Large variability in barrier spit length across a baymouth can also be a reflection of these mechanisms. This rapid, spatially variable, inlet migration contributes to infilling of some inlet/estuary complexes on a geological time scale, as the continually enlarging flood tide delta evolves at each inlet location. The result is an accelerated shrinkage of

some estuaries, with consequent reduction in inlet channel depth and width (the decreased channel area responding to a reduced tidal prism). Whether or not this flood tide delta growth significantly alters the fate of the estuary depends on the hydraulic characteristics of the inlet and estuary (flood tide delta growth is a function of flood/ebb flow dominance), as well as long-term trends in sea-level rise.

The three distinct patterns of inlet migration are (figure 11):

1) Growth of the downdrift spit by addition of sediment from ebb tide delta distal bars: some of these distal bars weld onto the downdrift spit without escaping the inlet environment. The time scale of these growth episodes is months, with an associated spit growth on a scale of 100 m. Resultant spit change are relatively small compared to the other two growth mechanisms. This mechanism can cause only updrift inlet migration.

2) Storm-induced shifts in inlet position associated with superelevated water levels: these changes are rare but significant, with time scales of tens of years and spatial scales of hundreds of meters. Storm breaches will remain stable and replace previous inlets if they are hydraulically more efficient than alternative breaches. These major inlet relocations have played an important role at Nauset Inlet, by shifting the inlet position to the north (against the sense of net littoral drift) and allowing the flow characteristics to set up a stable, steady northward inlet migration independent of storm influences.

Storm effects in the future are expected to influence the Nauset barriers significantly, and shift the inlet to the south. Since the southernmost limit of the estuary/inlet system has historically been the preferred position (because it is the most efficient location for tidal exchanges

between the ocean and bay), a breach at this narrow part of the barrier will likely become the preferred inlet position. At present, a stable dune-line is inhibiting storm overwash and breaching at this location.

3) Steady northward migration characterized by flow around a bend (erosion on outside of bend, accretion on inside of bend) during ebb tides: this migration has occurred since 1972 when a storm breach rapidly shifted the inlet location, setting up a long, confined southern barrier-parallel channel through which most tidal exchange takes place. Ebb flow through this barrier-parallel channel must make a sharp bed through the inlet to exit into the ocean. This bend creates a distinctive three-dimensional flow pattern similar to river bend flows, eroding the north spit and accreting to the south. The result is a steady northward migration which will cease when a storm opens a breach further south of the present inlet; this new breach will likely become the preferred inlet position. Flow curvature resulting from complex inlet/tide channel geometry may be responsible for both updrift and downdrift inlet migration at other locations, playing an important role in barrier beach evolution.

REFERENCES

Aubrey, D.G., 1980. Our dynamic coastlines. Oceanus, v. 23, no. 4, p. 4-13.

Aubrey, D.G. and P.E. Speer, 1983. Sediment transport in a tidal inlet. Woods Hole Oceanographic Institution Techincal Report WHOI-83-20, 110 pp.

Aubrey, D.G. and P.E. Speer, in prep. A study of non-linear tidal propagation in shallow inlet/estuarine systems, Part I: Observations.

Aubrey, D.G., D.C. Twichell and S.L. Pfirman, 1982. Holocene sedimentation in the shallow nearshore zone off Nauset Inlet, Cape Cod, Massachusetts, Marine Geology, v. 47, p. 243-259.

Aubrey, D.G. and K.O. Emery, 1983. Eigenanalysis of recent United States sea levels. Continental Shelf Research, v. 2, p. 21-33.

Bruun, P., 1978, Stability of Tidal Inlets. Elsevier, New York, 506 pp.

Bruun, P. and F. Gerritsen, 1960, Stability of Coastal Inlets. Amsterdam, North Holland Pub. Co., 124 pp.

Dietrich, W.E., J.D. Smith and T. Dunne, 1979. Flow and sediment transport in a river meander. Jour. Geology, v. 87, p. 305-315.

Emery, K.O., 1980. Relative sea levels from tide gage records. Proc. of the National Academy of Sciences, v. 77, p. 6968-6972.

Fitzgerald, D.M., 1983. Sediment bypassing at mixed energy tidal inlets. ASCE 18th Coastal Engineering Conference, Cape Town, South Africa.

Galvin, C., 1983. Shoaling with bypassing for channels at tidal inlets. ASCE Coastal Engineering Conference, Cape Town, South Africa.

Grant, W.D. and O.S. Madsen, 1982. Moveable bed roughness in unsteady oscillatory flow. Jour. Geophys. Res., v. 87, p. 469-481.

Hayden, B.P. and W. Smith, 1982. Season-to-season cyclone frequency prediction. Monthly Weather Review, v. 110, p. 239-253.

Leatherman, S.P., 1979. Environmental geologic guide to Cape Cod National Seashore. S.E.P.M. Field Guide Book, 249 pp.

Leatherman, S.P., A.J. Williams, and J.S. Fisher, 1977, Overwash sedimentation associated with a large scale northeaster. Marine Geology, v. 24, p. 109-121.

Nouh, M.A. and R.D. Townsend, 1979. Shear-stress distribution in stable channel bends. Jour. Hydr. Div., ASCE, v. 105, No. HY10, p. 1233-1245.

Nummedal, D., 1983. Barrier Islands. In Handbook of Coastal Processes and Erosion, P.D. Komar (ed.), CRC Press, Boca Raton, FL, p. 77-121.

Redfield, A.C., and M. Rubin, 1962, The age of salt marsh peat and its relation to recent changes in sea level at Barnstable, MA. Proc. Nat. Acad. of Sciences, v. 48, p. 1728-1735.

Smith, J.D. and S.R. McLean, in prep. A model for meandering streams.

Speer, P.E., D.G. Aubrey and E. Ruder, 1982. Beach changes at Nauset Inlet, Cape Cod, Massachusetts 1670-1981. Woods Hole Oceanographic Institution Technical Report No. WHOI-82-40, 92 pp.

Speer, P.E. and D.G. Aubrey, in prep. A study of non-linear tidal propagation in shallow inlet/estuarine systems, Part II: Theory.

U.S. Army Corps of Engineers, 1969. Nauset Harbor, Orleans and Eastham, Massachusetts, Survey Report, Department of the Army, New England Division, Corps of Engineers, Waltham, Mass., 13 pp. + appendices.

U.S. Army Corps of Engineers, 1979, Cape Cod easterly shore beach erosion study, v. 1, 11, 111. New England Division, Corps of Engineers, Waltham, MA.

Zaremba, R., and S.P. Leatherman, 1979, Overwash processes and barrier dynamics: Nauset Spit, Cape Cod, MA., U. MA-N.P.S.-C.R.U. Progress Report, 245 p.

Zeigler, J.M., 1954. Beach Studies in the Cape Cod area conducted during the period January 1, 1954 - June 30, 1954. Woods Hole Oceanographic Institution, unpublished manuscript, reference number 54-59, 14 pp.

Zeigler, J.M., 1960, Cape Studies, Cape Cod, Aug. 1953 - April 1960. Woods Hole Oceanographic Institution, unpublished report No. 60-20, 32 pp.

CHAPTER III

A STUDY OF NON-LINEAR TIDAL PROPAGATION IN SHALLOW INLET/ESTUARINE SYSTEMS

PART I: OBSERVATIONS

ABSTRACT

The offshore tide becomes strongly distorted as it propagates into shallow estuarine systems. Observations of sea surface elevation and horizontal currents over periods ranging from three days to one year, at nine stations within Nauset inlet/estuary, document the non-linear interaction of the offshore equilibrium tidal constituents. Despite strong frictional attenuation within the estuary, the overtides and compound tides of M_2, S_2 and N_2, in particular, reach significant amplitude, resulting in strong tidal distortion. High frequency forced constituents in sea surface are phase-locked, consistently leading the forcing tides by 60°-70°, resulting in a persistent distortion with falling tide longer than rising tide. Forced constituents in currents are more nearly in phase with equilibrium constituents, producing flood currents which are shorter but more intense than ebb currents. A compound fortnightly tide, MS_f, modulates the mean water level such that lowest tides occur during Neap phase instead of Spring phase. This fortnightly tide can be contaminated by storm surge, changing the phase characteristics of this constituent. Implications of the overtides, compound tides, and lower frequency tides on near-bed and suspended material transport are profound.

I. INTRODUCTION

The astronomical tide is strongly distorted during its propagation from offshore into shallow inlet/estuarine systems common to the U.S. East and Gulf Coasts. Time asymmetries develop in the rise and fall of the surface tide with resulting time and amplitude asymmetries in the velocity field (e.g., Boon and Byrne, 1981). This distortion can be represented as the non-linear growth of harmonics of the principal ocean astronomical constituents (e.g., Dronkers, 1964; Pingree and Griffiths, 1979). Harmonic growth is a result of finite amplitude effects entering through friction, non-linear advection, and interactions with channel geometry as the tide oscillates within the estuary. In the inlet/estuarine systems of interest to this study, the water column is well mixed throughout most of the tidal cycle and freshwater inflow forms a negligible part of the tidal prism.

The astronomical tide spectrum is composed of a large number of constituents whose mutual non-linear interactions represent a complex physical problem (e.g., Munk and Cartwright, 1966; Gallagher and Munk, 1971). Primary frequencies of interest are integral linear combinations of six basic components related to celestial mechanics of the Earth-Moon-Sun system:

f_1^{-1} = 1 day = period of Earth's rotation relative to the Sun
f_2^{-1} = 1 lunar month = period of Moon's orbital motion
f_3^{-1} = 1 year = period of Sun's orbital motion
f_4^{-1} $\simeq$ 8.85 years = period of lunar perigee
f_5^{-1} $\simeq$ 18.61 years = period of regression of lunar nodes
f_6^{-1} $\simeq$ 20,900 years = period of solar perigee

Interactions between these basic frequencies result in other energetic tidal frequencies, such as the inverse lunar day (f_2^{-1}), where:

$$f_2 = f_1 - f_2 + f_3 \simeq 0.966\ f_1$$

Tidal frequencies are divided into species which are separated by one cycle/lunar day, into groups which are separated by one cycle/month, and constituents which are separated by one cycle/year. Here we are concerned with various predominant species and associated groups (table 1).

Compound constituents, which are linear combinations of basic frequencies, can be generated through non-linear celestial and fluid mechanics. For example, MSf consists of both a weak astronomical term and a potentially larger hydrodynamic term arising from $M_2 - S_2$ interactions, while MS_4 is a constituent arising solely from non-linear hydrodynamic interaction of M_2 and S_2. Similarly M_4, M_6, and M_8 have no equilibrium tidal argument, but reflect non-linear generation in oceanic basins of various scales. Magnitude and phase of each observed constituent provides insight into hydrodynamic processes.

The present study, along with its companion study (Speer and Aubrey, 1984), focuses on the distortion of the offshore tide as it propagates through shallow estuarine systems connected to the ocean by a narrow tidal inlet. Frictional decay of the offshore tide and harmonic growth of forced constituents form the basis for examination of non-linear processes. Diagnostic numerical modeling examines the most important and representative interactions observed in the field. Robinson, Warren, and Longbottom (1983) reported a similar, but less comprehensive, study conducted in the Fleet, on the south coast of England.

Along the US northeast coast, the principal tidal constituents of interest are the M_2 tide and its harmonics. The magnitude of M_2 results in it dominating non-linear processes during tidal propagation through the estuary, although compound tides are also generated. In particular, M_2 and its first harmonic, M_4, can be used to illustrate the dominant features of

TABLE 1

TIDAL SPECIES AND CONSTITUENTS OF INTEREST

Species	Constituent	
Fortnightly	MS_f	1.4 solar days
Diurnal	O_1	25.8 solar hours
	K_1	23.93 solar hours
Semi-Diurnal	N_2	12.66 solar hours
	M_2	12.42 solar hours
	S_2	12.00 solar hours
Ter-Diurnal	MK_3	8.18 solar hours
Quarter-Diurnal	MN_4	6.27 solar hours
	M_4	6.21 solar hours
	MS_4	6.10 solar hours
Sixth-Diurnal	M_6	4.14 solar hours
	S_6	4.00 solar hours

tidal asymmetries in these systems (fig. 1). Two (arbitrary) phase relationships between M_2 and M_4 constituents (sea surface or velocity), can be defined:

$$A_{M2} = a_1 \cos(\omega t - \theta_1)$$
$$A_{M4} = a_2 \cos(2\omega t - \theta_2)$$

For the case of sea surface, when M_4 leads M_2 by 90°, falling tide exceeds rising tide in duration (fig. 1A). The phase relationship in this situation is:

$$2\theta_1 - \theta_2 = 90°$$

If we let the constituents refer to tidal velocity, with M_2 and M_4 in phase, the case of shorter, enhanced flood currents is demonstrated. This phase relationship can be expressed as:

$$2\theta_1 = \theta_2$$

The cases of symmetrical and enhanced ebb currents can be shown in a similar manner.

The development of tidal asymmetries can have important effects on both the geological evolution of shallow estuaries as well as on the short term navigability of estuarine channels. An estuary characterized by shorter, more intense flood then ebb currents (flood dominant) may be unable to flush entering sediments effectively. Conversely, an estuary with stronger ebb than flood currents (ebb dominant) may represent a more stable configuration. The magnitude of the velocity asymmetry depends on the non-linearity of the tide. Both flood- and ebb-dominated inlet/ estuarine systems are found along the U.S. east coast (e.g., Nauset Inlet, flood dominant; Wachapreague Inlet, ebb dominant). In addition to the different types of asymmetry, these estuaries also exhibit varying degrees of non-linear response to tidal forcing as measured by the ratio of amplitudes of M_4 to

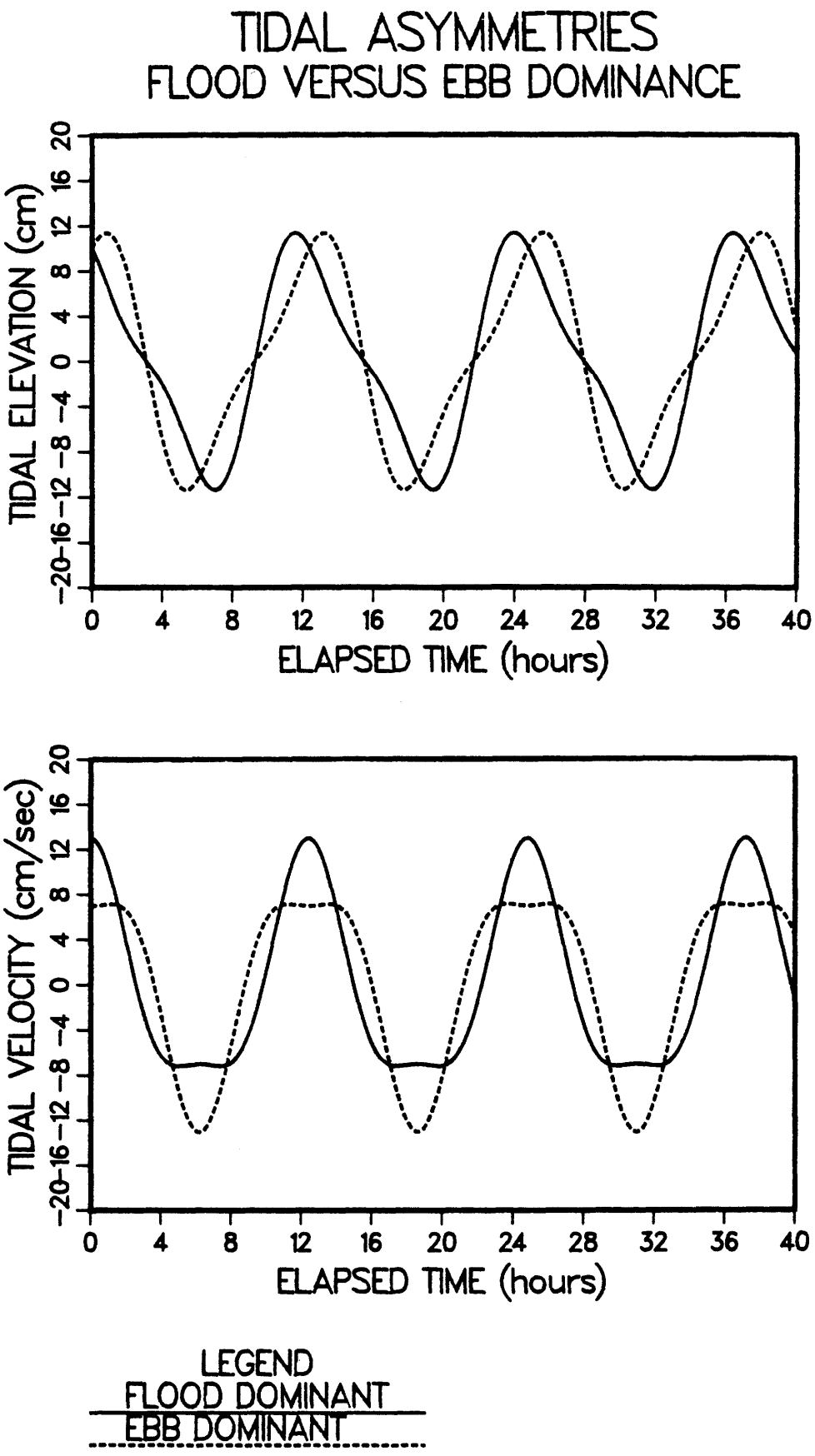

Figure 1. Examples of tidal asymmetries for the case of $M_4/M_2=0.3$. 1a) M_4 is 90° out of phase with M_2. 1b) M_4 in phase and 180° out of phase with M_2.

M_2 (the M_4/M_2 ratio). To better understand the problem of tidal propagation in a shallow inlet/estuarine complex, a field program and a numerical modeling study were initiated at Nauset Inlet, Cape Cod, MA (fig. 2). This paper details results of the field experiments examining the tidal response of this estuary. Part II (Speer and Aubrey, 1984) focuses on diagnostic models of the M_2, M_4 interactions.

The Nauset Inlet system is a salt marsh intersected by three major tidal channels and connected to the ocean by a natural, unstabilized inlet (fig. 3). The offshore tide is predominantly semi-diurnal with a range of approximately two meters. The northern channel has extensive tidal flats and mean depths less than one meter (fig. 3). Middle and south channels have regions of tidal flats, channel depths of 2-3 m, and terminate in a deeper body of water, Town Cove (4-6 m). The channels are well-mixed over most of the tidal cycle and fresh water inflow is negligible. Nauset was chosen for study because in terms of both channel geometries and tidal asymmetry it is representative of many such systems on the US east coast.

II. FIELD METHODS

Two field experiments were undertaken at Nauset to examine the characteristics of tidal propagation and to provide a data set against which to test diagnostic numerical models of tide interactions. A two-week experiment in September 1981 emphasized measurement of currents near the inlet channel, some month-long measurements of tidal elevation throughout the estuary, and measurement of sea surface gradients through the inlet proper. The second field experiment, extending from August-October 1982, included velocity and sea surface measurements to estimate local momentum balances and a three month deployment of an array of tide gages. Experimental instrumentation for 1982 (fig. 3) consisted of Steven's tide gauges

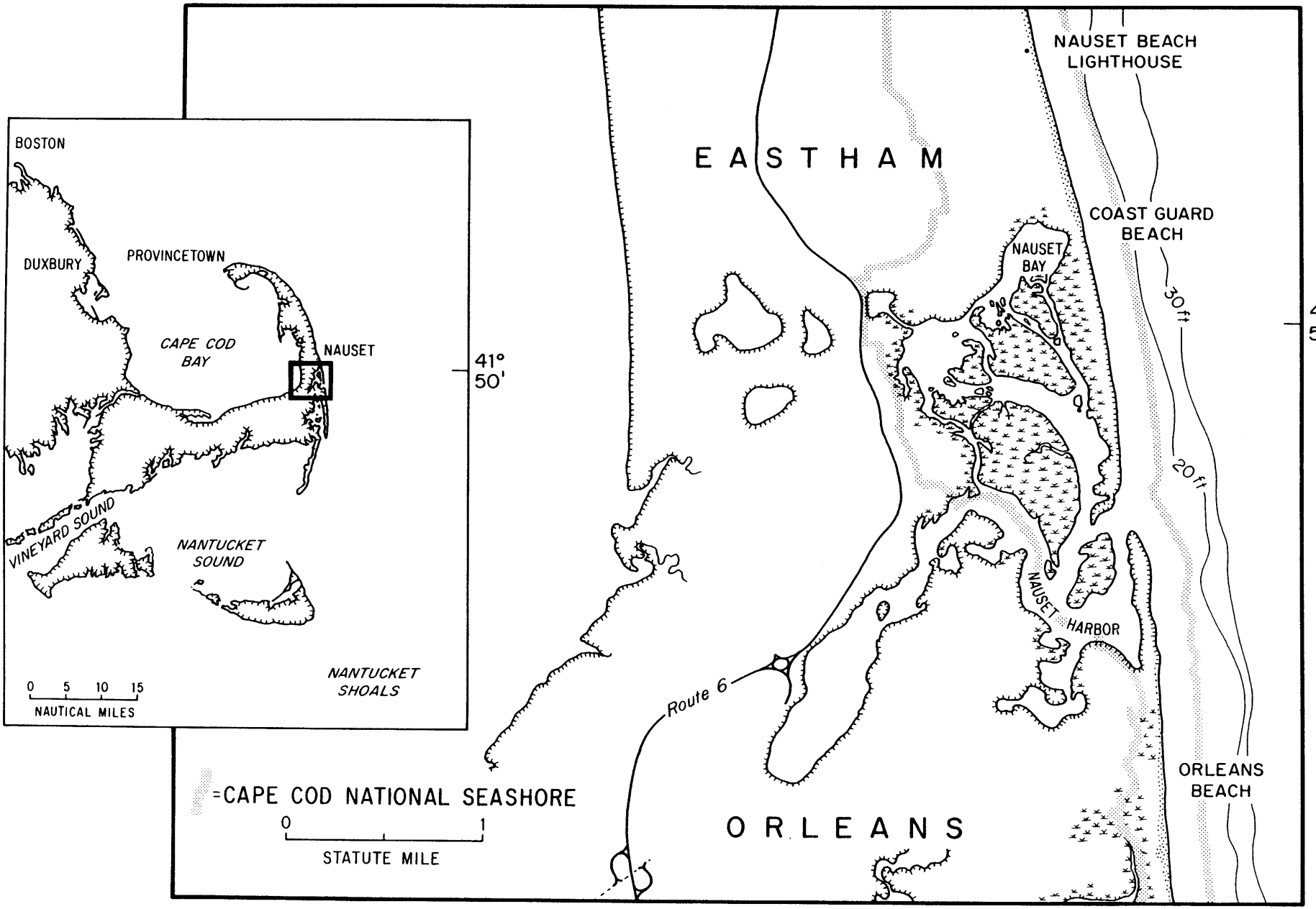

Figure 2. Location map of Nauset Inlet/estuary.

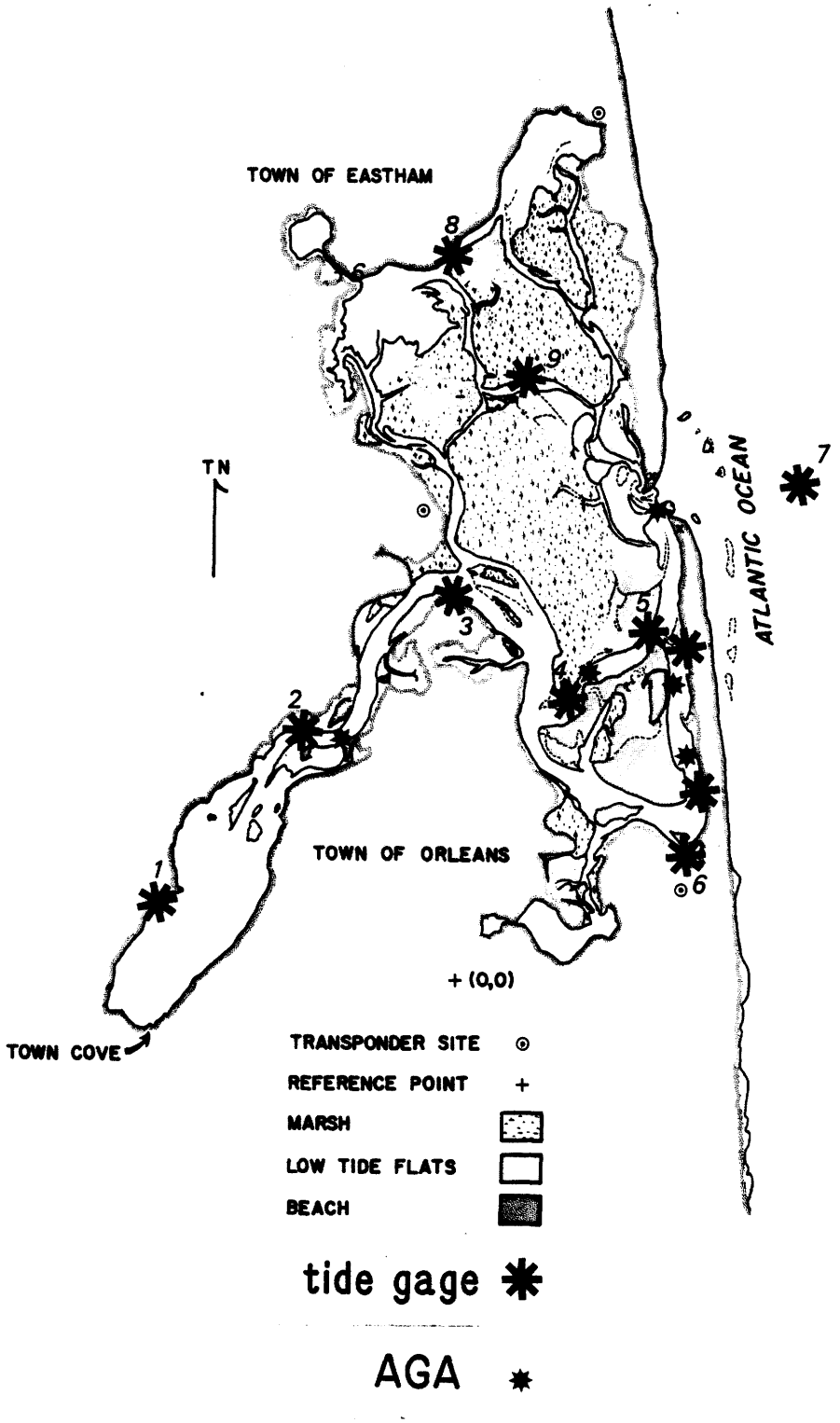

Figure 3. Location map for Nauset Inlet experiment of August through October, 1982. Numbered locations: 1-Goose Hummock (GH), 2-Mead's Pier (MP), 3-Snow Point (SP), 4-Middle Channel West (MCW), 5-Middle Channel East (MCE), 6-Nauset Heights (NH), 7-Ocean site, 8-Nauset Bay (NB), and 9-North Channel (NC). AGA refers to locations of four-day long deployments of an electromagnetic current meter array.

(model nos. 71-A and 7030, made available by the NOAA National Ocean Survey), a five-element array of electromagnetic current meters deployed on a tripod (deployments typically lasting 2-4 days with sampling rates of 1 Hz), and numerous 2-7 day deployments of pressure sensors (Sea Data Model TDR-1a). The inlet was instrumented with four-day deployments of pressure sensors in 1980 and 1981. These latter measurements yielded insight into the interaction of tide and the narrow inlet channel, a region where long term tide gauging is impractical. Further details of these experiments may be found in Aubrey and Speer (1983).

Because of the sensitivity of estimates of harmonic tidal constituents to errors in time base, attention was focused on annotating tide gage records with precise time codes. Data from these tide gages were reduced to a standard format either under contract to NOS at their facilities (with either a one minute or six minute sample interval), or using a Calcomp model 9000 coordinate digitizer to convert analog records to digital form at the Woods Hole Oceanographic Institution. In both cases, proper quality control on the time base was provided. Other data types were internally recording on magnetic tape, with later processing at W.H.O.I.

III. STATISTICAL METHODS

Statistical analysis of the data sought to extract the amplitudes and phases of major tidal constituents from both sea surface elevation (tide gages and pressure sensors) and velocity (current meter) records. Experimental logistics and instrument peculiarities produced data records of varying duration at different areas of the estuary, making Fourier harmonic analysis of limited use. Conventional fourier analysis requires 15- or 29-day record lengths to separate major harmonic components (M_2 from S_2 and M_2 from N_2, respectively). Our records were either longer than this

(in which case we wanted to utilize all the data and not just some subset) or shorter than this, in which case we still wanted to extract tidal components.

For records of 15-days or more duration, initial analysis utilized standard power spectral techniques to determine the structure of the tide at various points within the ocean/inlet/estuary system. Vector velocity data was analysed via rotary component spectral analysis (Gonella, 1972) to extract both frequency content as well as any tendency for rotary tidal motion (negligible in long, straight channels, but potentially appreciable near channel bends). Error analysis for this method is well-established, with power spectral values following a chi-squared distribution, and phase and coherence confidence limits described in Gonella (1972) following the work by Goodman (1957).

Quantitative estimates of harmonic content were derived from least-square harmonic analysis, a variant of the standard Fourier harmonic analysis technique developed by Schureman (1971). The goal of harmonic analysis is to extract amplitudes and phases of the primary tidal harmonic constituents and their compound tides. Finite record lengths and contamination of tidal signals by noise introduced by storms and other sources, combine to make harmonic analysis inexact, rendering estimation of confidence intervals for these estimates of utmost importance. Methods for performing harmonic analysis include: Fourier Harmonic Analysis (Schureman, 1971), the response or admittance method (Munk and Cartwright, 1966; Cartwright, Munk and Zetler, 1969), and least-squares harmonic analysis (Boon and Kiley, 1978). The techniques vary in their mathematical approach, with consequent differences in error estimates. A thorough

review of the three techniques along with an intercomparison is provided in Aubrey, Speer, and Boon (in prep.); a brief discussion of the techniques is provided here.

Fourier Harmonic Analysis is performed on integral multiples of 15- or 29-day records of sea surface elevation or velocity. Record length is determined by the need to resolve adjacent energetic tidal frequency bands. Spectral estimates yield two degrees of freedom when the minimum record length for maximum resolution is used. These estimates have confidence limits given by a chi-square distribution, and suffer from the internal aliasing due to finite record length (gate function in the time domain, sinc function in the frequency domain), since the tidal constituents are not integral multiples of elemental frequency bands. Low frequency and unresolved tidal constituents must be inferred using formulae such as those presented in Schureman (1971). Shorter record lengths are difficult to quantitatively examine using Fourier Harmonic Analysis, because of the resolution restrictions associated with this method. In particular, separation of the many constituents within semi-diurnal, quarter-diurnal, and sixth-diurnal species from a short record is not possible. These restrictions led us away from the Fourier Harmonic Analysis in favor of other schemes.

The response or admittance method was developed by Munk and Cartwright (1966) as an alternative to the Fourier Harmonic Analysis method. The method is based on spectrally relating a time series of long duration and hence of excellent accuracy to an arbitrary length series at the same or nearby location. The nomenclature arises from the admittance function, or transfer function, relating two quantities in a spectral sense. The Fourier transform of the admittance function is the impulse response func-

tion, which is convolved with the input series in the time domain to yield an output function. Alternatively, the admittance (or transfer) function is multiplied by the input transform to obtain the transform of the output function. Ideally, the input function is derived from a suitably long record of tidal data at a reference station, generated either from equilibrium tidal theory, or lacking this, from a long time series of tides at that coastal station. In the former case, the admittance function yields a relationship between the measured tide over the period of interest and the equilibrium tidal arguments. Infinite frequency resolution is possible if the admittance function is assumed to be smoothly varying on the premise that (barring resonance) the response of the ocean to similar frequencies is similar. For harmonic analysis purposes, the tide record examined is related through this admittance procedure to a noise-free predicted tide for the same period. The part of the measured tide that is coherent with the predicted tide is expressed in terms of a new admittance function, whose statistical uncertainties have been derived in Munk and Cartwright (1966). Relative amplitudes and phases for the admittance function derived from this analysis have simple confidence limits for the case of small relative noise levels.

The admittance technique is useful for extracting that part of an observed tide which is coherent with the reference station series, with the remaining incoherent part of the signal interpreted as noise. To be useful, the reference station and data station must have a similar response to ocean tides. An admittance function relating tides in the middle of the ocean to tides within an embayment has limited value, and does not appreciably improve a prediction generated by an alternate harmonic analysis method. The extra work involved with the admittance procedure is not

justified in this situation. For the present study of non-linear tidal harmonic generation in shallow estuaries, the admittance procedure was not used for several reasons. First, there is no long time series of tides in the estuarine system from which to extract response functions suitable for generating noise-free reference series. Second, no local station is available from an environment physically similar to the estuarine system of interest. A suitable reference station would require similar non-linear response to discrete harmonic input; such a station is not available. This points out the limited utility of the admittance technique in many shallow-water coastal regions. The additional work required for a complete admittance procedure represents another shortcoming compared to alternate techniques. As a result, the procedure may not be justified except for certain scientific studies where additional precision is made possible with an appropriate long-term reference station.

The least squares harmonic analysis method provides several attractive features which resulted in its adoption in this study. The least squares method can be applied to any length time series, extracting tidal constituents without the resolution restrictions imposed by Fourier Harmonic Analysis, and reducing internal aliasing by extracting the exact constituent frequency from the series, not the nearest integral multiple of the fundamental frequency. The nearly infinite resolution of this technique, termed super-resolution by Munk and Hasselman (1964), is attributable to the least-square requirement that to determine phase and amplitude of a signal of known frequency, only two data points are needed. For n frequencies, then, only 2n data points are needed. No requirements are placed on length of record or sample interval. The paradox between least-squares analysis and Fourier harmonic analysis is resolved by proper analysis of

noise levels in the data series. In particular, noise (defined as energy due to non-tidal sources) at frequencies adjacent to tidal harmonic frequencies limits the accuracies of harmonic least squares analysis, such that a longer record will improve the estimates. Munk and Hasselman (1964) first analysed the effect of noise on least-squares estimates of two neighboring spectral lines. Filloux and Snyder (1979) extended the algorithm for the noise analysis, deriving a form for estimating phase and amplitude errors arising from least squares analysis.

Following Filloux and Snyder (1979), the sea surface elevation, ζ, at tidal and lower frequencies is separated into harmonic, ζ_H, and residual, ζ_R, components:

$$\zeta = \zeta_H + \zeta_R$$

Harmonic components are represented by real variables:

$$\zeta_H = \sum_{n=1}^{\infty} {}_n\zeta_I \; I_n \; = \zeta_I$$

and residuals become:

$$\zeta_R' = \zeta - \sum_{n=1}^{2N} {}_n \zeta_I' \; I_n$$

where primes indicated estimated quantities, the ${}_n\zeta_I$ represents the complex amplitude corresponding to the $n^{\underline{th}}$ harmonic frequency, and I_n can be defined as:

$$I_{2n-1} = \cos(\omega_n t + \Phi_n)$$
$$I_{2n} = \sin(\omega_n t + \Phi_n)$$

Φ_n is the phase of the corresponding constituent of the equilibrium tide evaluated at time zero. The phase of ${}_n\zeta_I$ is relative to the equilibrium tide at Greenwich, equivalent to G in Schuremann (1971). A scalar product is defined:

$$(\alpha,ß) = \int_{t_o}^{t_o+T} \alpha ß \; dt$$

where T is the record length. Conditions for solution of the least-squares problem are set by differentiating $\zeta_R'^2$ with respect to the ${}_n\zeta_I'$'s:

$$\sum_{m=1}^{2N} (I_n, I_m)\ {}_m\zeta_I' = (I_n, \zeta) \qquad n=1,2,\ldots 2N$$

Inverted, this becomes:

$${}_m\zeta_I' = \sum_{n=1}^{2N} {}_{mn}S_I^{-1}\ (I_n, \zeta)$$

where ${}_{mn}S_I = (I_n, I_m)$, and S_I^{-1} is the inverse of S_I. These estimates can be decomposed into three parts:

$${}_m\zeta_I' = {}_m\zeta_I + \sum_{\ell=2N+1}^{\infty} {}_{m\ell}E_I\ {}_\ell\zeta_I + \sum_{n=1}^{2N} {}_{nm}S_I^{-1}\ (I_n, \zeta_R)$$

where ${}_{m\ell}E_I = \sum_{n=1}^{N} {}_{mn}S_I^{-1}\ {}_{n\ell}S_I$.

The first term is the true complex amplitude, the second represents errors arising from tidal amplitudes not included in the analysis, and the third term represents errors due to residual fluctuations. The second term can be reduced by including a sufficient number of constituents in the analysis; however these additional constituents adversely affect the third term. This study includes twenty-nine terms in the analysis, with only four (MS_f, M_2, M_4, M_6) of primary interest. Consequently, the second error term is small; the third term is the larger error source. Using a definition of

$$E_R(\omega) = \frac{1}{2\pi} \int_{-\infty}^{\infty} d\tau\ C_{\zeta_R^2}(\tau) \cos\omega\tau$$

as the two-sided spectrum of ζ_R, calculated from the covariance:

$$C_{\zeta_R^2}(\tau) = \langle \zeta_R(x,t)\ \zeta_R(x,t+\tau) \rangle$$

where angle brackets represent ensemble averaging, a co-variance matrix can be calculated,

$$\langle {}_n\zeta_I^{\,|}\ {}_m\zeta_I^{\,|}\rangle - \langle {}_n\zeta_I^{\,|}\rangle\ \langle {}_m\zeta_I^{\,|}\rangle$$

where the summation is over adjacent constituents within the same tidal species. Using appropriate assumptions of quasi-stationarity in ζ_R and length of record T, Filloux and Snyder (1979) show:

$$\langle {}_n\zeta_I^{\,|}\ {}_m\zeta_I^{\,|}\rangle - \langle {}_n\zeta_I^{\,|}\rangle\ \langle {}_m\zeta_I^{\,|}\rangle$$

$$\simeq \pi T E_R\ (\omega_n) \sum_p\ {}_{np}S_I^{-1}\ {}_{mp}S_I^{-1}$$

where p,m,n refer to constituents of the same species. If

$${}_n\Phi_H^{\,|} = -\arg\ {}_n\zeta_H^{\,|} = -\tan^{-1}\ ({}_{2n-1}\zeta_I^{\,|}/{}_{2n}\zeta_I^{\,|})$$

$$|{}_n\zeta_H^{\,|}| = \mathrm{mod}\ {}_n\zeta_H^{\,|} = ({}_{2n-1}\zeta_I^{\,|2} + {}_{2n}\zeta_I^{\,|2})^{1/2},$$

and a covariance, V, is defined for brevity

$$V(\alpha,\beta) = \langle\alpha\beta\rangle - \langle\alpha\rangle\ \langle\beta\rangle$$

then the variances of $|{}_n\zeta_H^{\,|}|$ and ${}_n\Phi_H^{\,|}$

are given as:

$$|{}_n\zeta_H^{\,|}|^2\ V(|{}_n\zeta_H^{\,|}|,|{}_n\zeta_H^{\,|}|) =$$

$${}_{2n-1}\zeta_I^{\,|2}\ V({}_{2n-1}\zeta_I^{\,|},\ {}_{2n-1}\zeta_I^{\,|})$$

$$+ 2\,{}_{2n-1}\zeta_I^{\,|}\ {}_{2n}\zeta_I^{\,|}V({}_{2n-1}\zeta_I^{\,|},\ {}_{2n}\zeta_I^{\,|})$$

$$+ {}_{2n}\zeta_I^{\,|2}\ V({}_{2n}\zeta_I^{\,|},\ {}_{2n}\zeta_I^{\,|})$$

$$|n\zeta_H^{\,|}|^4\ V({}_n\Phi_H^{\,|},{}_n\Phi_H^{\,|}) =$$

$${}_{2n-1}\zeta_I^{\,|2}\ V({}_{2n-1}\zeta_I^{\,|},{}_{2n-1}\zeta_I^{\,|})$$

$$- 2\,{}_{2n-1}\zeta_I^{\,|}\ {}_{2n}\zeta_I^{\,|}\ V({}_{2n-1}\zeta_I^{\,|},\ {}_{2n}\zeta_I^{\,|})$$

$$+ {}_{2n}\zeta_I^{\,|2}\ V({}_{2n}\zeta_I^{\,|},{}_{2n}\zeta_I^{\,|})$$

Errors can be presented as standard deviations, or

$V(|{}_n\zeta_H^{\,|}|,\ |{}_n\zeta_H^{\,|}|)^{1/2}$ and $V({}_n\Phi_H^{\,|},\ {}_n\Phi_H^{\,|})^{1/2}$.

Although algebraically complex, these expressions show the direct dependence of errors on the noise spectrum, E_R, while the $\Delta\omega$ dependence shown by Munk and Hasselman (1964) is implicit in the matrix S_I^{-1}.

For this study, twenty-nine tidal constituents were extracted in a least-squares sense, fourteen calculated directly with the remainder inferred using formulae provided in Schureman (1971). Of these, six species were of particular interest (table 1), with all species except diurnal and semi-diurnal containing considerable forced constituents. Once these constituents were eliminated, the residual signal (regenerated from the original series less the harmonic components) was analysed with a fast Fourier transform, to generate estimates of the noise spectrum, E_R. These noise estimates were used to calculate errors in phase and amplitude presented in tables 2, 3, and 4.

IV. RESULTS AND DISCUSSION

Harmonic analyses of 29-day records of sea surface elevation indicate that Nauset is a strongly non-linear as well as frictionally dominated inlet/estuarine system. The non-linear response to tidal forcing is reflected in growth of high frequency M_2 overtides, compound tides and a forced low frequency MS_f constituent throughout the estuary. The frictional nature of the estuary is demonstrated both by large phase changes in the tide (~76° in 2 km for the M_2 constituent) and by amplitude decay of the total spectrum (as much as 57 percent of the ocean range in 2 km).

Nine stations provide tidal data for examination of tidal distortion in Nauset estuary (fig. 3). Presentation of these results is divided into three sections: a) decay of the primary diurnal and semi-diurnal constituents, and generation of the overtides of M_2 (table 2); b) generation of compound tides at frequencies greater than semi-diurnal (table 3); and c) generation of the forced MS_f, or fortnightly, compound tide (tables 3 and 4).

TABLE 2: FUNDAMENTAL TIDES AND OVERTIDES
(amplitude in cm, Greenwich phase in degrees,
confidence limits of one standard deviation)

Station	t_o	O_1		K_1		N_2		M_2		S_2		M_4		M_6		M_8	
		a	θ	a	θ	a	θ	a	θ	a	θ	a	θ	a	θ	a	θ
(OTG) 7	29/09/82	11.4	263	9.0	272	17.3	228	98.2	265	20.0	298	0.7	253	0.5	273	0.2	335
	30/10/82	11.7	258	12.9	264	21.0	240	98.7	263	16.7	287	0.7	254	0.2	231	0.1	42
(MCE) 5	23/09/82	8.4 ±3.5	300 ±24	7.6 ±3.5	310 ±26	10.1 ±3.2	244 ±18	66.4 ±3.3	273 ±3	10.2 ±3.2	309 ±18	5.2 ±0.3	121 ±3	2.0 ±0.2	166 ±7	0.5	316
	06/10/82	8.4 ±3.2	298 ±22	7.8 ±3.2	302 ±23	11.5 ±3.0	25 ±15	66.1 ±3.0	271 ±3	9.8 ±3.0	305 ±17	5.8 ±0.3	122 ±3	2.1 ±0.3	161 ±7	0.6	316
(MCW) 4	18/10/82	7.4 ±3.1	309 ±24	8.2 ±3.1	307 ±22	9.6 ±3.0	259 ±17	58.9 ±3.0	281 ±3	9.3 ±3.0	308 ±18	7.0 ±0.3	138 ±2	1.9 ±0.3	169 ±8	0.8	4
(NH) 6	30/09/82	8.1 ±3.2	294 ±22	7.1 ±3.2	301 ±26	10.2 ±3.2	233 ±18	61.6 ±3.2	259 ±3	9.4 ±3.1	296 ±19	6.9 ±0.3	86 ±3	1.4 ±0.2	119 ±7	0.6	267
	18/10/82	7.5 ±3.3	309 ±25	8.5 ±3.3	307 ±22	10.1 ±3.0	258 ±16	60.1 ±3.0	280 ±3	9.7 ±3.0	308 ±17	7.4 ±0.3	128 ±2	1.3 ±0.2	196 ±9	0.7	348
(SP) 3	25/08/82	9.1 ±3.0	307 ±19	7.0 ±3.0	331 ±25	9.0 ±2.0	242 ±13	53.5 ±2.0	293 ±2	8.4 ±2.0	330 ±14	7.4 ±0.3	160 ±2	1.2 ±0.1	187 ±7	0.7	38
	23/09/82	8.3 ±3.0	311 ±21	7.2 ±3.0	328 ±24	9.8 ±3.0	255 ±17	56.0 ±3.0	292 ±3	8.2 ±3.0	329 ±21	7.6 ±0.4	160 ±3	1.2 ±0.1	172 ±6	0.7	33
	18/10/82	7.6 ±2.9	316 ±22	8.0 ±2.9	327 ±22	8.9 ±2.6	270 ±17	53.8 ±2.7	292 ±3	8.6 ±2.7	335 ±18	8.1 ±0.4	162 ±3	1.0 ±0.2	176 ±9	0.7	34

TABLE 2: FUNDAMENTAL TIDES AND OVERTIDES (continued)
(amplitude in cm, Greenwich phase in degrees,
confidence limits of one standard deviation)

Station	t_o	O_1		K_1		N_2		M_2		S_2		M_4		M_6		M_8	
		a	θ	a	θ	a	θ	a	θ	a	θ	a	θ	a	θ	a	θ
(NC) 9	13/09/81	7.2	305	5.3	333	10.9	277	45.0	290	9.5	330	8.5	160	0.3	358	0.2	34
(NB) 8	25/08/82	8.4 ±2.5	322 ±17	6.4 ±2.4	346 ±22	7.4 ±1.2	265 ±9	40.2 ±1.2	319 ±2	6.9 ±1.2	350 ±10	10.3 ±0.5	215 ±3	1.3 ±0.2	130 ±7	0.4	99
	18/10/82	8.0 ±2.9	331 ±21	7.6 ±2.9	340 ±22	7.3 ±2.5	286 ±20	41.2 ±2.5	317 ±4	7.4 ±2.5	348 ±19	10.9 ±0.8	221 ±4	1.7 ±0.3	116 ±10	0.4	90
(MP) 2	17/03/83	7.5	302	5.9	330	13.1	240	57.0	302	10.9	358	8.8	185	0.9	141	0.7	65
	26/06/83	8.6	328	8.9	347	11.3	282	56.0	321	2.2	41	7.2	224	1.7	240	1.1	134
(GH) 1	22/07/82	8.1	309	7.1	354	8.1	266	51.9	307	7.7	8	11.8	191	1.9	91	0.6	36
	17/03/83	7.8	303	6.3	333	14.4	236	57.1	305	11.8	359	10.7	188	1.1	90	0.4	65

TABLE 3: COMPOUND TIDES
(amplitude in cm, Grenwich phase in degrees,
confidence limits of one standard deviation)

Station	t_o	MS_f		MK_3		MN_4		MS_4	
		a	θ	a	θ	a	θ	a	θ
(OTG) 7	29/09/82	7.8	214	0.1	107	0.1	262	0.5	290
	30/10/82	4.3	59	0.1	349	0.3	313	0.2	331
(MCE) 5	23/09/82	10.4	254	1.4 ±0.7	101 ±27	2.3 ±0.2	89 ±6	2.7 ±0.2	162 ±5
	06/10/82	9.0	297	1.6 ±0.6	96 ±23	2.3 ±0.3	92 ±7	2.8 ±0.3	157 ±6
(MCW) 4	18/10/82	7.3	29	2.0 ±0.8	126 ±22	2.8 ±0.3	113 ±6	2.7 ±0.3	173 ±6
(NH) 6	30/09/82	12.1	255	1.5 ±0.7	86 ±28	2.6 ±0.3	53 ±7	3.0 ±0.3	125 ±6
	18/10/82	7.5	30	2.1 ±0.9	119 ±24	3.1 ±0.3	106 ±6	2.7 ±0.3	164 ±7
(SP) 3	25/08/82	6.0	33	1.5 ±0.8	182 ±32	2.8 ±0.3	110 ±6	2.4 ±0.3	210 ±7
	23/09/82	9.5	254	1.7 ±0.8	152 ±27	2.8 ±0.4	122 ±7	3.0 ±0.4	199 ±7
	18/10/82	7.7	32	2.3 ±0.8	150 ±20	3.0 ±0.4	138 ±8	2.9 ±0.4	190 ±9

TABLE 3: COMPOUND TIDES (continued)
(amplitude in cm, Grenwich phase in degrees,
confidence limits of one standard deviation)

Station	t_o	MS_f		MK_3		MN_4		MS_4	
		a	θ	a	θ	a	θ	a	θ
(NC) 9	13/09/81	3.0	338	1.4	178	3.7	146	3.6	207
(NB) 8	25/08/82	6.2	31	2.2	237	3.4	161	3.1	264
				±1.1	±28	±0.5	±8	±0.5	±9
	18/10/82	9.5	37	3.2	200	3.6	178	3.7	224
				±1.4	±25	±0.8	±12	±0.8	±12
(MP) 2	17/03/83	8.4	44	1.3	176	4.5	121	3.6	235
	26/06/83	6.3	71	2.2	208	2.8	192	0.9	351
(GH) 1	22/07/82	6.6	54	2.7	218	3.7	150	3.5	255
	17/03/83	8.3	48	1.5	184	5.9	114	5.1	235

TABLE 4 MS_f TIDAL DATA

STATION/DATE		25/8/82	30/9/82	18/10/82
(OTG) 7	Amplitude (m)	0.043*****	0.078	
	%Total Tide	0.2	0.6	
	Relative Phase	-37°	177°	
(MCE) 5	Amplitude (m)		0.104	0.090
	% Total Tide		2.0	1.5
	Relative Phase		141°	4°
(MCW) 4	Amplitude (m)			0.073
	% Total Tide			1.3
	Relative Phase			-4°
(NH) 6	Amplitude (m)		0.121	0.075
	% Total Tide		3.0	1.3
	Relative Phase		140°	-4°
(SP) 3	Amplitude (m)	0.060	0.095	0.077
	% Total Tide	1.1	2.2	1.7
	Relative Phase	12°	141°	-9°
(NC) 9	Amplitude (m)	0.030****		
	% Total Tide	0.3		
	Relative Phase	60°		
(NB) 8	Amplitude (m)	0.062		0.095
	% Total Tide	1.8		3.8
	Relative Phase	7°		-26°
(MP) 2	Amplitude (m)	0.084*	0.063***	
	%Total Tide	1.6	1.0	
	Relative Phase	9°	7°	
(GH) 1	Amplitude (m)	0.083*	0.066**	
	% Total Tide	1.5	1.2	
	Relative Phase	5°	5°	

---

* Starts 17/3/83
** Starts 22/7/82
*** Starts 26/6/83
**** Starts 13/9/81
***** Starts 30/10/82

Table 4

Nonlinearity in the tides can be illustrated by comparing the offshore tide with the estuary tide (figs. 4a and 4b, table 2). The equilibrium diurnal and semi-diurnal tides decay in their propagation through the estuary, both through friction and through non-linear transfers of energy. Non-linear, forced tides are negligible in the ocean station, but are significantly enhanced within the estuary. In terms of sea surface elevation, phase relationships between the equilibrium and forced constituents cause a definite asymmetry in estuary tides, with rising tide shorter than falling tide (fig. 5). Duration and magnitude asymmetries also exist in velocity records, with stronger flood currents than ebb currents.

The dominant diurnal tides are the K_1 and O_1 constituents, with roughly equivalent amplitudes (fig. 4). M_2 is the dominant semi-diurnal constituent, with an amplitude six times greater than both the N_2 and S_2 constituents. These relative amplitudes caused us to focus theoretical modeling on overtides of M_2, rather than overtides of N_2 or S_2, or compound tides between M_2 and either S_2 or N_2 (e.g., MN_4, MS_4), although the physics of interactions are identical. The principal overtide is M_4, with smaller forced constituents arising from MK_3, MN_4, and MS_4. The forced MS_f (fortnightly) tide is the largest compound constituent.

a) Decay of diurnal and semi-diurnal tides, and generation of M_2 overtides: The behavior of the diurnal and semi-diurnal tides as they propagate through the estuary reflects dissipation due to friction and non-linear spectral energy transfer. Friction reduces the amplitude of the tide and creates phase lags, while other non-linear transfers reduce tidal amplitude with characteristic phase change signatures.

The frictional nature of the estuary is demonstrated by the significant decay of all semi-diurnal and diurnal constituents, with associated large phase lags (table 2 and fig. 6). The amplitude decay of M_2 from the ocean

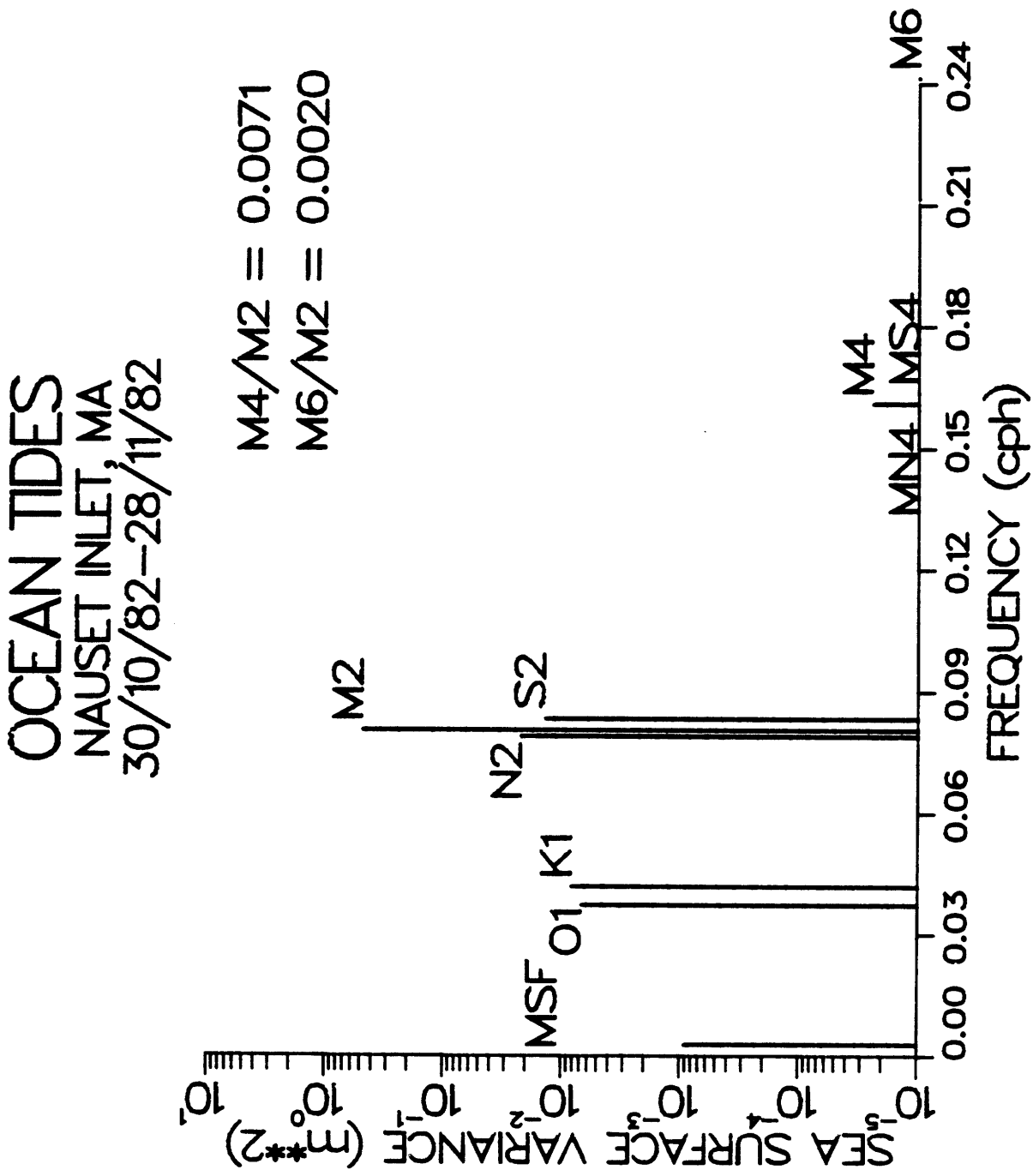

Figure 4a. Periodogram of offshore tides (10 m water depth) outside of Nauset Inlet, showing selected (out of 35) tidal constituents calculated with least-squares harmonic analysis procedures. Overtides and compound tides are clearly negligivle here.

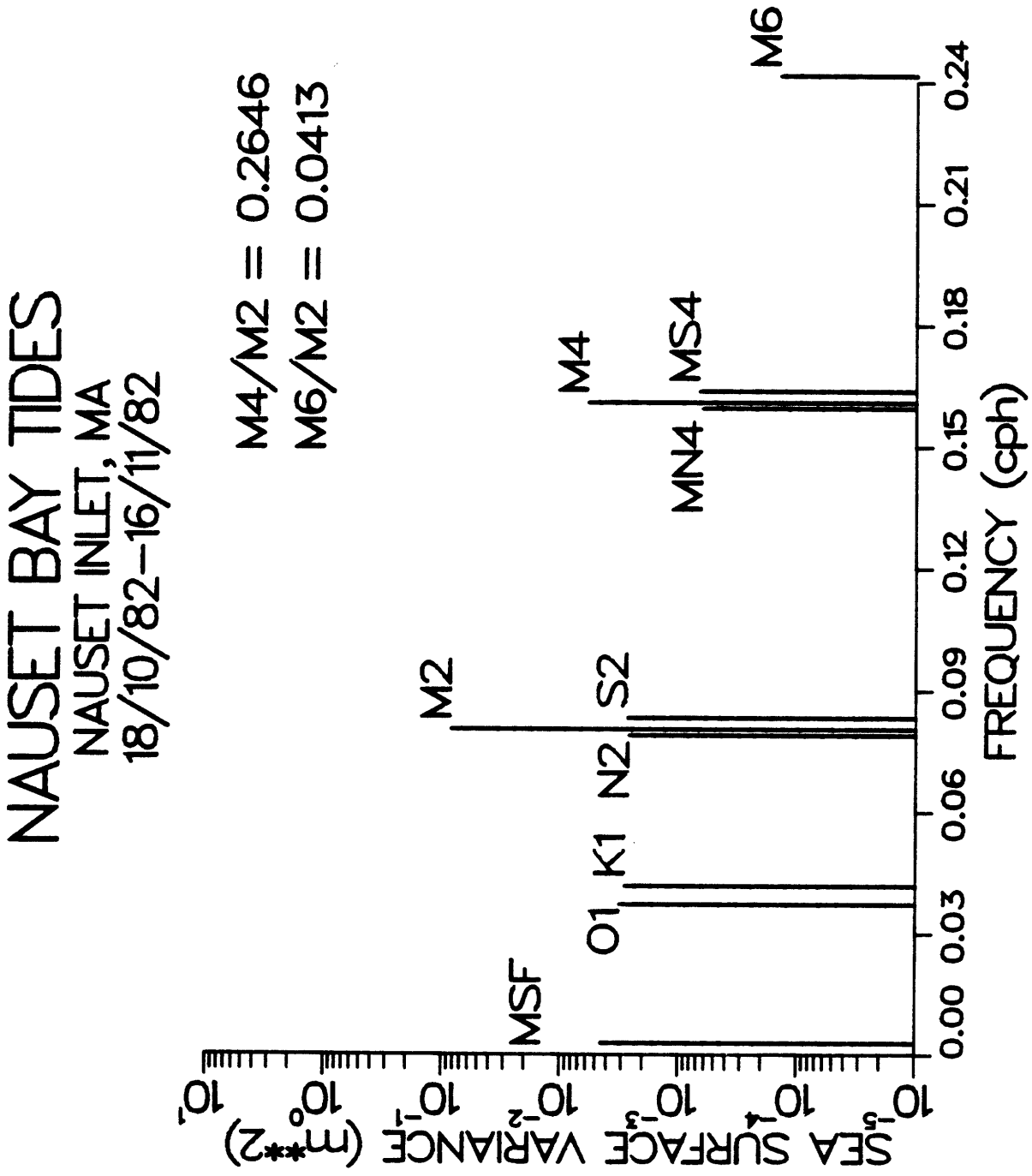

Figure 4b. Periodogram of sea surface tides within Nauset Inlet at Nauset Bay, showing the distinct growth of overtides and compound tides, compared with the offshore tides of figure 4a. Only selected (10 of 35) constituents are depicted. Both figures 4a and 4b are estimates based on 29-days of data.

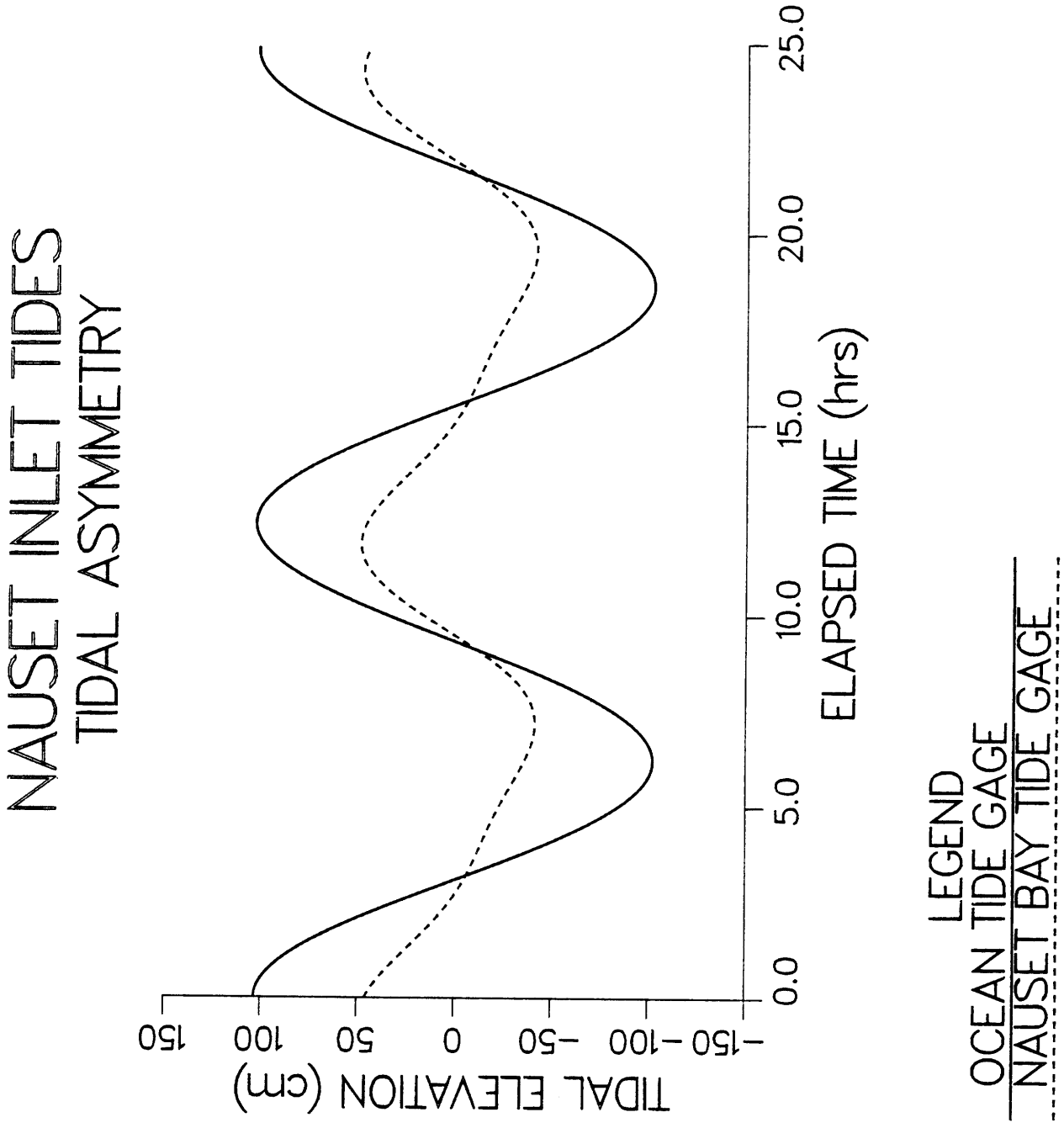

Figure 5. The effect of tidal distortion on sea surface, shows as a 24-hour reconstruction of tides consisting of the M_2 constituent and its first overtide, M_4, with their proper phase relationships. The offshore tide is nearly a pure sinusoid, whereas the Nauset Bay tide is distorted by overtides, leading to shorter flood tides and longer ebb tides.

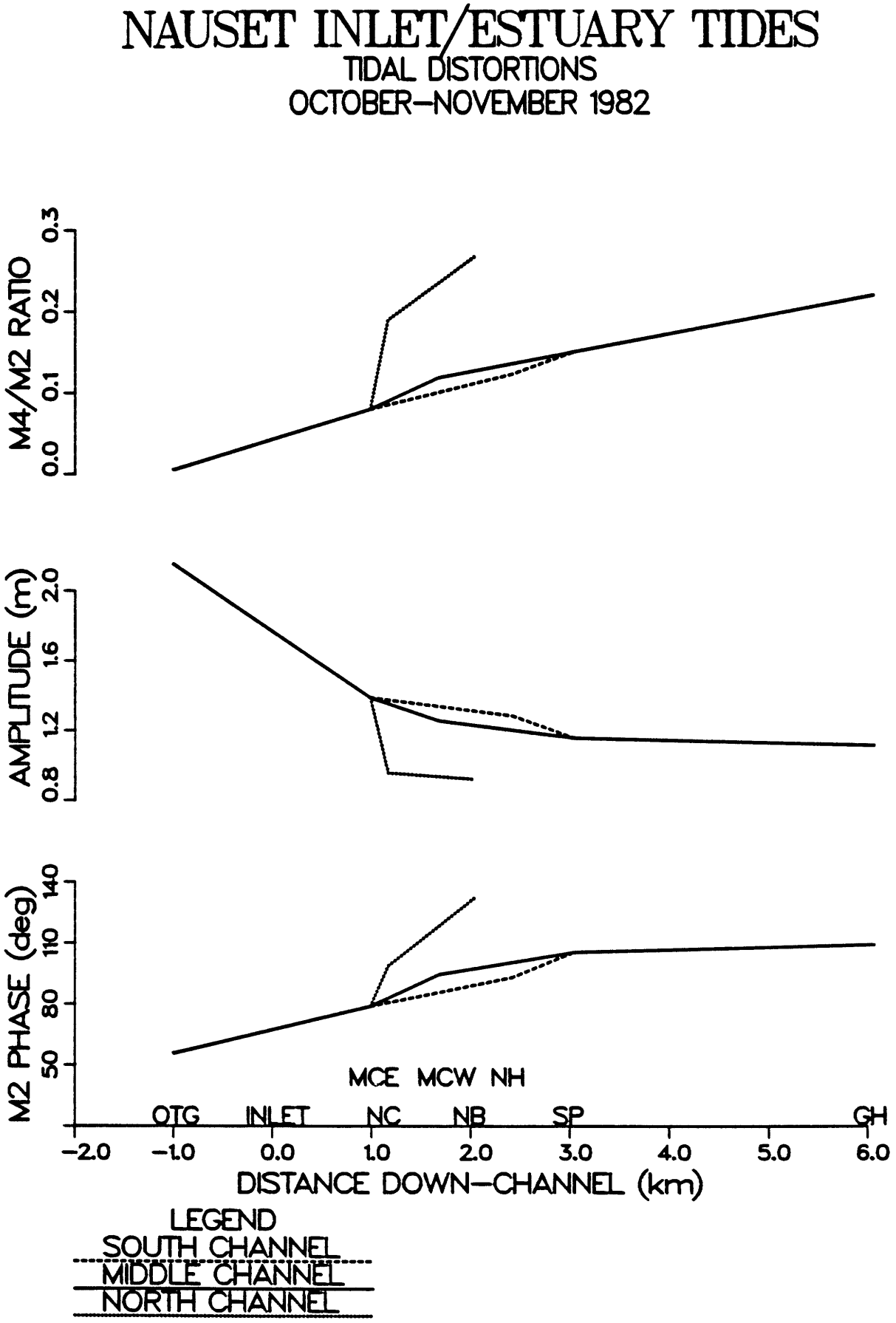

Figure 6. Tidal distortion changes as a function of distance into the estuary for each of the primary drainage channels. Top panel shows sea surface M_4/M_2 ratios; middle panel shows tidal amplitude and bottom panel, M_2 phase. Tide gage stations are indicated on the abscissa.

to the far reaches of the estuary is approximately 60% to the north and 50% to the south. Tidal dissipation occurs at different rates along different reaches of the estuary (fig. 6), and is largest in shallow channels and in channel reaches where tidal flats are developed. Along middle channel, the greatest decline in amplitude is in the short (0.7 km) reach between stations 5 (MCE) and 4 (MCW). This reach is characterized by large tidal flats and extremely variable channel geometry over a tidal cycle. Amplitude decay down the rest of the channel to Town Cove, a reach characterized by less time variable geometry and no large regions of tidal flats, is much less. North channel, with extremely shallow depths and extensive flats has the highest rate of M_2 and total tide amplitude decay. Phase changes in M_2 (table 2 and fig. 6) display the same pattern as frictional decay with greatest lags occurring in shallow channels and channels bordered by tidal flats.

The pattern of tidal dissipation shows the estuary acts as a low pass filter, with larger decay rates for semi-diurnal than diurnal constituents. At Goose Hummock (station 1), the semi-diurnal energy (averaged over N_2, M_2 and S_2) is only 27% of that at the ocean gage, whereas the diurnal energy (averaged over K_1, O_1) is 43% of that at the ocean gage. At Nauset Bay (station 8), the semi-diurnal energy (averaged over N_2, M_2 and S_2) is only 21% of that at the ocean gage, whereas the diurnal energy (averaged over K_1, O_1) is 36% of that at the ocean gage. From a phase standpoint, the semi-diurnal tides have larger lags through the estuary than do diurnal tides. Because of non-linear growth of higher frequency compound tides, and lack of suitable directly calculated (not inferred) lower frequency elementary tidal constituents, the complete filter characteristics (cutoff frequency, reject-band dropoff rate, phase behavior, etc.) cannot be defined.

Non-linear growth of the harmonics of M_2 follows a consistent pattern through the estuary. The primary indicator of non-linearity used here is the M_4/M_2 ratio, which reflects the combined effects of spectral energy transfer from M_2 to M_4 and frictional dissipation through the estuary. As discussed earlier, the estuary tends to act as a low pass filter in the absence of non-linear effects; the nonlinear effects selectively enhance specific high frequency (>2cpd) compound constituents. If nonlinearities were absent, therefore, the ocean magnitudes of M_4, M_6, and M_8 would rapidly decrease within the estuary from their small offshore values. In fact, the general pattern in all three channels is a steady increase in the amplitude of M_4 with distance into the estuary. The amplitude of M_4 within the estuary can be contrasted with the offshore tide (table 2) which has an M_4 amplitude less than 1 cm. The rate of growth of M_4 differs in the three channels. In a distance of 2 km through north channel, where M_4 reaches 11 cm in amplitude, the M_4/M_2 ratio reaches 0.27. Middle channel, with extensive tidal flats but greater mean depths than north channel, has a slower rate of non-linear growth. M_4 has an amplitude of 7 cm at a distance of 1.7 km from the inlet mouth. The slowest rate of non-linear growth is found along south channel where M_4 attains an amplitude of 7 cm in 2.4 km. Proceeding along middle channel into Town Cove, M_4 grows steadily to 11 cm a distance of 6 km from the inlet. At this location, M_4 is the second largest constituent behind M_2. The higher harmonics, M_6 and M_8, are not an important part of the sea surface spectrum, with amplitudes typically 1 cm or less. They do not display any systematic pattern of growth through the estuary, a result of both limited tide gauge accuracy and the large high-frequency attenuation characteristics of the estuary.

Throughout the estuary, M_4 is phase locked to M_2 with M_4 leading by 63° (standard deviation of 1.3°). The largest deviation from this phase relationship is at Nauset Heights, located in a shallow embayment off the main channel (fig. 3), where M_4 leads M_2 by 71°. The result of this pattern of increasing M_4 amplitude and M_4 phase lead of 63° is a distorted surface tide with falling tide exceeding rising tide in duration (fig. 5). The duration asymmetry due to the M_2, M_4 interaction becomes more pronounced far from the inlet and in shallow regions with extensive flats. It reaches extreme values in Town Cove and in north channel where ebb averages more than 7.5 hours in duration (Table 5).

The non-linear spectral transfer from M_2 to M_4 accounts for only a small fraction of the total decay in M_2, the larger portion attributable to frictional dissipation. At Goose Hummock (station 1), potential energy contained in M_4 represents only about 2% of the total decrease in M_2 potential energy from the ocean. Although the transfer to M_4 is important for water and sediment transport purposes, it is not the major contributor to decay of M_2.

Despite gradual changes in the geometry of the estuary caused by northward movement of the inlet (Aubrey et al., 1984), the monthly averaged pattern of tidal propagation appears consistent over a 1-2 year period (Table 2). Data from Snow Point (station 3) demonstrate similar phase relationships, amplitude decay and non-linear growth despite the occurrence of a large storm during October, 1982. If one examines individual neap/spring cycles at five stations within a month, however, the non-linear distortion of the tide varies considerably. During spring tides, the increased tidal amplitude due to the in-phase nature of S_2 and M_2 enhances finite amplitude effects on the propagating tide. This is indicated by the

TABLE 5

TIDAL DURATION ASYMMETRY AT NAUSET

STATION	DISTANCE FROM INLET	AVERAGE EBB	AVERAGE FLOOD
Ocean	----	6 hrs. 13 min.	6 hrs. 13 min.
Inlet	----	6 hrs. 30 min.	5 hrs. 57 min.
North Channel	1.2 km	7 hrs. 24 min.	5 hrs. 01 min.
Nauset Bay	2.0 km	7 hrs. 43 min.	4 hrs. 42 min.
Middle Channel East	0.99	6 hrs. 46 min.	5 hrs. 39 min.
Middle Channel West	1.7	7 hrs. 00 min.	5 hrs. 25 min.
Nauset Heights	2.4	7 hrs. 03 min.	5 hrs. 22 min.
Snow Point	3.0	7 hrs. 12 min.	5 hrs. 13 min.
Goose Hummock	6.1	7 hrs. 32 min.	4 hrs. 53 min.

change in the ratio, a/h, where a = amplitude of semi-diurnal tide; h = mean water depth. Typically, the amplitude of the semi-diurnal tide is 1.5 times larger at spring than neap tide. As a result of enhanced non-linear effects during spring tide, the M_4 constituent is 2.5 to 5 times larger than at neap (Table 6), such that at some stations the time asymmetry of the tide virtually disappears during neap tides (fig. 7). This, in turn, should cause considerable variability in patterns of sediment transport over the spring/neap cycle.

The strong non-linear effects visible in the surface tide are also present in tidal currents within the estuary. Spectral energy transfer is, in fact, more pronounced in the velocity field with friction directly removing energy from the primary semi-diurnal constituent. A velocity spectrum from a week-long current meter deployment in south channel (1.5 km from inlet) illustrates the content of tidal velocities (fig. 8). This harmonic generation particularly of the quarter-diurnal constituent, again results in a distortion of the tide. The type of distortion is dependent on the relative phasing of semi- and quarter-diurnal constituents. Unlike the case of the surface tide, M_2 and its first harmonic are more nearly in phase. Considerably shorter velocity records prevent us from defining the phase as carefully as for the surface tide.

The in-phase nature of M_2 and M_4 produces a velocity signal generally characterized by more intense flood than ebb currents. Depending on channel geometry, this effect becomes pronounced further in the estuary where the tide is more non-linear (fig. 9). Continuity arguments support the observation that a long ebb flow must be balanced by a shorter, more intense flood flow. This simple picture is complicated in certain regions of the estuary by large changes in channel geometry which occur over a tidal cycle. Ebb velocities in South Channel exceed flood velocities

TABLE 6 Spring/Neap Response

	M_4/M_2			$2M_2 - M_4$ Phase		
Station	Spring	Monthly	Neap	Spring	Monthly	Neap
5 (MCE)	0.116	0.079	0.023	52°	65°	69°
4 (MCW)	0.156	0.117	0.044	52°	64°	69°
6 (NH)	0.150	0.121	0.061	61°	71°	85°
3 (SP)	0.197	0.149	0.083	54°	62°	62°
8 (NB)	0.334	0.266	0.205	60°	63°	70°

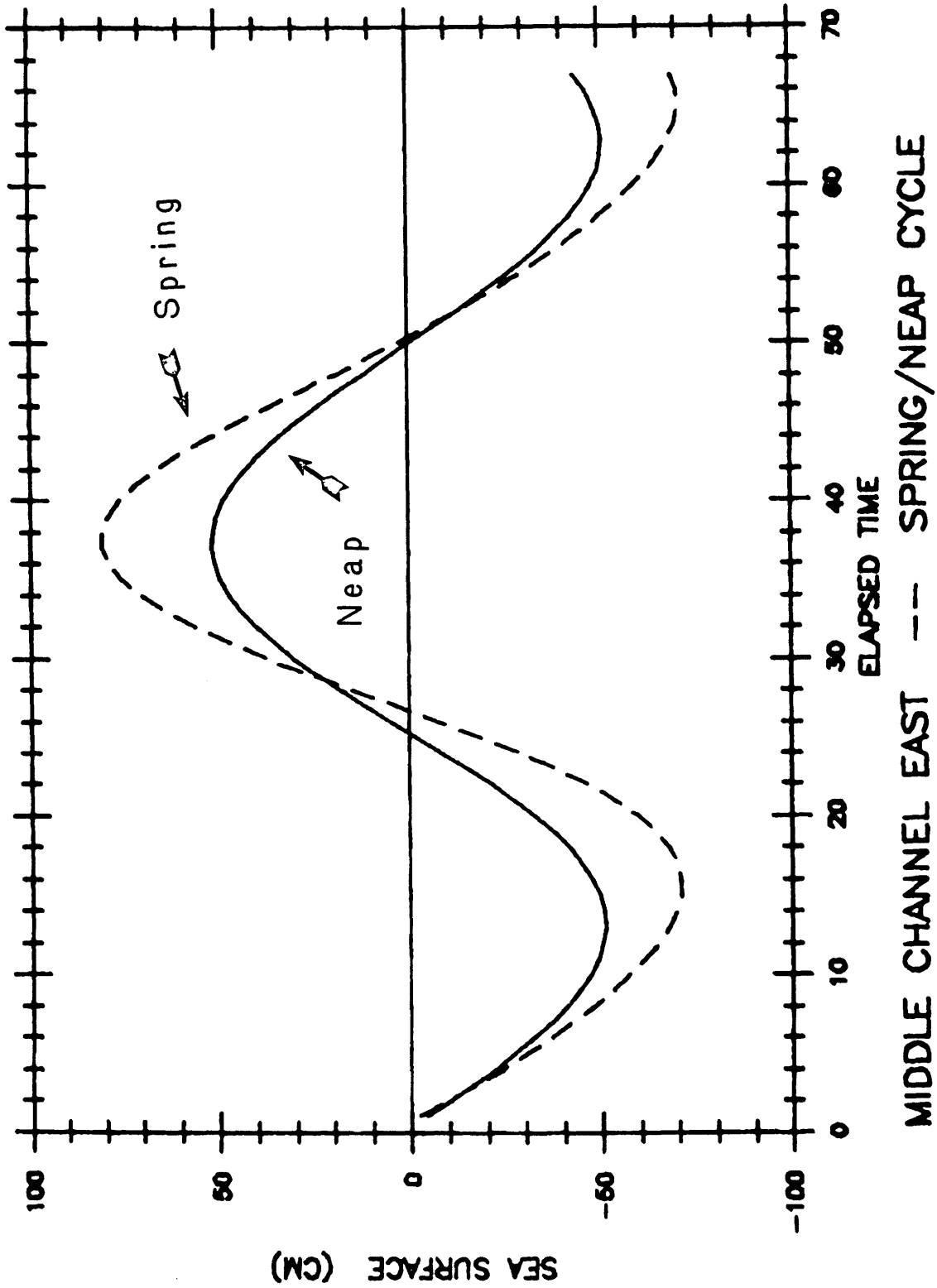

Figure 7. Differences in harmonic growth and tidal distortion are shown for Spring and Neap cycles (4-day periods within each). During neap tides, tidal distortion is much less, as flood and ebb duration are approximately equal. In Spring tides, flood tide is markedly shorter than ebb.

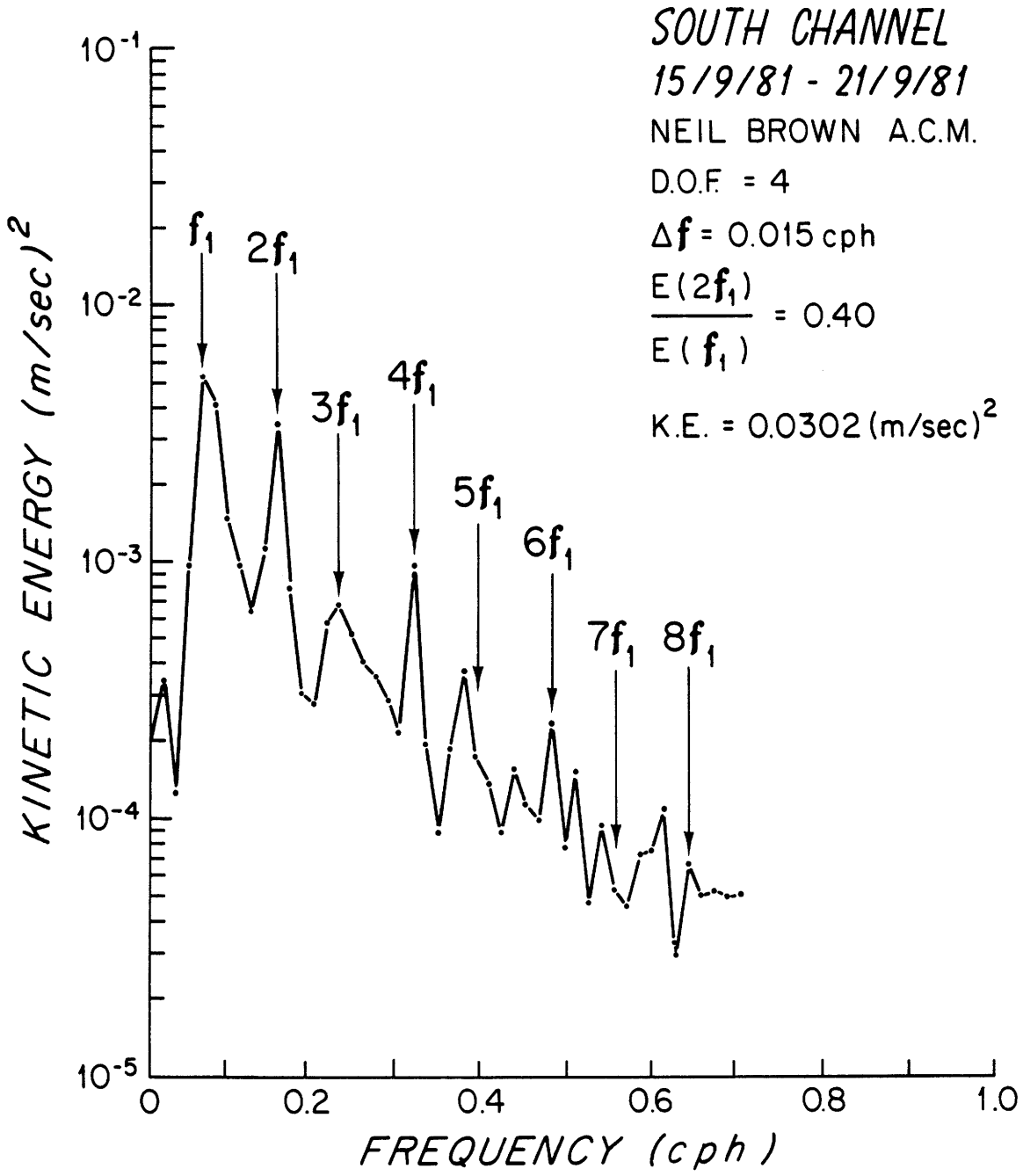

Figure 8. Periodogram (using Fourier analysis) of tidal velocities in South Channel for a week-long period. f_1 is the M_2 tide, with overtides (and compound tides which are not resolved with this short record) shown at higher frequencies. Velocity is clearly more non-linear than sea surface.

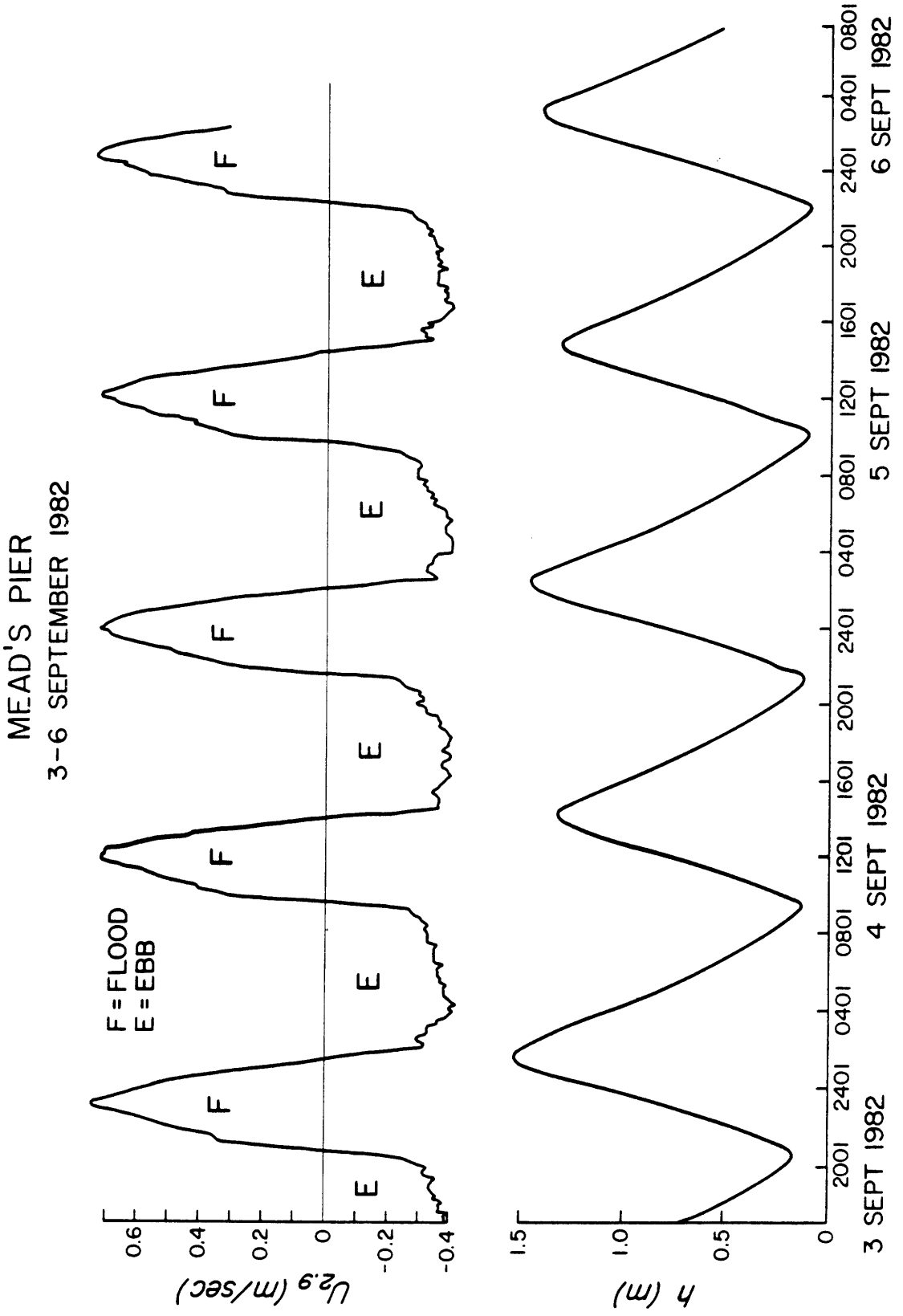

Figure 9. Three-day records of velocity (top panel-taken 2.9 m above bottom in 3.5 m water depth) and sea surface at Mead's Pier (location 2, figure 3).

despite the time asymmetry favoring ebb. This pattern occurs because peak ebb flow is confined to a much smaller channel at this location.

b) Generation of compound tides at frequencies greater than semi-diurnal other than pure harmonics of M_2: Tides resulting from interactions of various diurnal and semi-diurnal constituents were examined. Although results show pure harmonics of M_2 to be the strongest overtides generated within Nauset Inlet, other forced tides are energetic. The compound tides discussed here include ter-diurnal (MK_3) and quarter-diurnal (MN_4 and MS_4). Additional forced tides at these and other frequencies exist, but were smaller than those listed.

The rationale for examining only specific forced tides and not the full spectrum of possible constituents arises from both observation and theory. Fourier analysis of residual tide data indicates the compound tides selected for analysis by the least squares procedure contain most of the energy in any particular species. More constituents can be selected because of the "super resolution" characteristics of least-squares analysis. However, the low residual energy remaining after removal of the major compound constituents indicates additional ones would not have statistical significance at Nauset. The tides selected in this study represent first order non-linear interactions between equilibrium constituents with largest relative energy levels. In fact, as Munk and Gallagher (1971) demonstrate, each of the forced frequency bands includes a large number of constituents involving 2nd and 3rd order interactions between forced and equilibrium constituents. Non-linear processes produce strong frequency splitting in the non-astronomical or forced bands. The strength of these constituents in the resulting spectrum depends a great deal on the relative energy level of the constituents from which they were formed. Energy levels are low for

all but five astronomical frequencies (M_2, S_2, N_2, O_1, K_1) and drop off rapidly past the quarter-diurnal band. This fact along with the dissipative tendency of Nauset to attenuate higher frequency components of the spectrum explains why most of the residual energy is found in relatively few compound tides.

The ter-diurnal tide (MK_3) arises from interaction of M_2 and K_1 constituents. Other possible ter-diurnal constituents not considered here include $2MK_3$ (arising from $2M_2$-K_1), SK_3 (arising from S_2 and K_1), and SO_3, (arising from S_2 and O_1). Offshore, MK_3 is negligible (table 2), but once inside the inlet it increases progressively from a value of 1.5 cm near the inlet, to a maximum of 3 cm at the far reaches of the estuary. It is roughly a factor of three less in amplitude than the M_4 overtide. The phase of the forced MK_3 tide uniformly leads the phase of the sum of the M_2 and K_1 tides by 101° ($\pm$ 15° standard deviation), so it too is phase locked to the forcing function, although not as narrowly as the M_4 overtide. Another ter-diurnal constituent of equal magnitude is MO_3, resulting from the (M_2+O_1) interaction. This was not examined in detail because its response was similar to MK_3. The MK_3 constituent does not produce time asymmetry in the surface tide, but does have a minor effect on the diurnal inequality.

The quarter-diurnal compound tides include the major constituents MN_4 and MS_4, which are derived from interactions of (M_2+N_2) and (M_2+S_2), respectively. Other quarter-diurnal tides exist, including MK_4 (M_2+K_2), and S_4 ($2S_2$), these have not been considered because of arguments similar to those of Gallagher and Munk (1971). MN_4 and MS_4 are approximately of equal magnitude, increasing uniformly from a value of about 2.3 cm near the inlet proper, to about 3.5 cm near the extremes of the estuary. The amplitudes of

both are negligible offshore. Although non-linear growth is slower than for M_4, reaching only about one-tenth its potential energy in the far reaches of the estuary, non-linear transfer into compound tides exceeds frictional decay. Phasing of these two constituents follows that of the other compound tides and overtides. MN_4 leads the sum of the forcing tides (M_2+N_2) by 68° (standard deviation error of five degrees), while MS_4 leads the sum of the forcing tides (M_2+S_2) by 61° (standard deviation error of four degrees). These phase relationships enhance the time asymmetry favoring ebb. The consistency of the phase lead in all overtides and compound tides throughout the estuary, and for different periods of time, suggests it is a property of the estuary as a whole, and not just of local channel characteristics.

c) Generation of the forced MS_f, or fortnightly, compound tide: The MS_f tide consists of both an elementary component which is part of the equilibrium tide, and a possible forced component arising from the interaction of M_2 and S_2 (S_2-M_2). At the offshore gage, MS_f is smaller than within the estuary, with different phase relationships, suggesting that the more energetic MS_f found in the estuary itself is partly a forced component. Although other longer-term, less energetic constituents with similar frequencies exist, this study concentrated on the MS_f constituent with appropriate error analysis, as it is the largest of these fortnightly constituents. Once inside the estuary, MS_f grows from a value of near zero to between five and ten centimeters. There is no consistent pattern of growth of MS_f within the estuary, rather its amplitude depends in part on atmospheric conditions, suggesting it is not a simple compound tide (table 4). Of three periods of observation, the second period uniformly had the largest relative amplitudes of MS_f (compared to the total tide), and it was the most energetic period from a storm perspective. The first and third periods were characterized

by lower wind stress. As an illustration, the tidal residual which included fortnightly components shows relatively low amplitude in the first period, more energetic storm super-elevation during the second period, and relatively less energy during the third period (fig. 10). In each of these residuals a clear fortnightly structure is apparent, with superimposed oscillations of various frequencies. Fourier analysis of residuals shows the fortnightly band to be cuspate, particularly during periods of large wind stress events, illustrating the complexity of the interactions among tidal and non-tidal forcing.

The MS_f phase provides some insight into the nature of the observed fortnightly tide, although phase information is more complex than for other compound tides. During the two periods of lower mean wind stress the forced fortnightly tide is in phase with the forcing tide (S_2-M_2) with little scatter about the mean phase difference (table 4). During these periods, MS_f is fairly small (except at Nauset Bay). During the middle period, which included a large storm event, MS_f phase locking is still excellent (values of 140°, 141°, and 141° for the three estimates), although MS_f leads the forcing by a significantly different amount than during the other two periods. This anomalous phase relationship is related to the superelevation corresponding to the 9 October 1982 storm event, which increased water levels by approximately 0.75m within the estuary. The inconsistency in phase relationships, and apparent dependence on meteorological events, suggests that prediction of the MS_f fortnightly tide is tenuous, with consequent poorly forecasted mean water level deviations of 10 cm or so on a fortnightly cycle.

The phase locking between MS_f and the forcing components results in a low water level which is lower during neap tides, higher during spring tides (fig. 11). This behavior has been observed previously in rivers

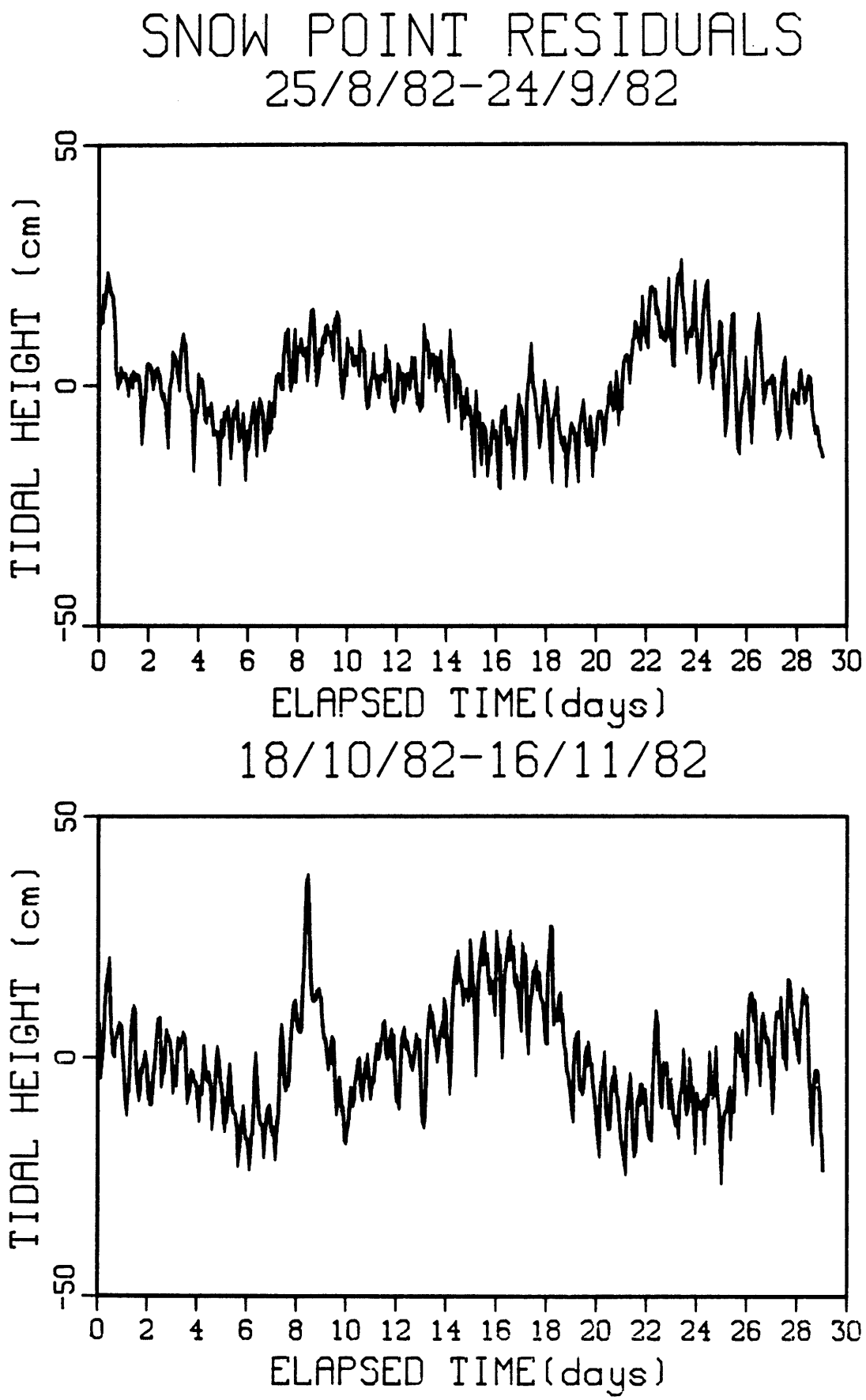

Figure 10. The fortnightly tide (MS_f) is both an astronomic and forced constituent (figure 10a, top panel) and can contain energy from storm surge (figure 10b, bottom panel). These two examples show the residual tide when diurnal and higher frequency constituents are removed.

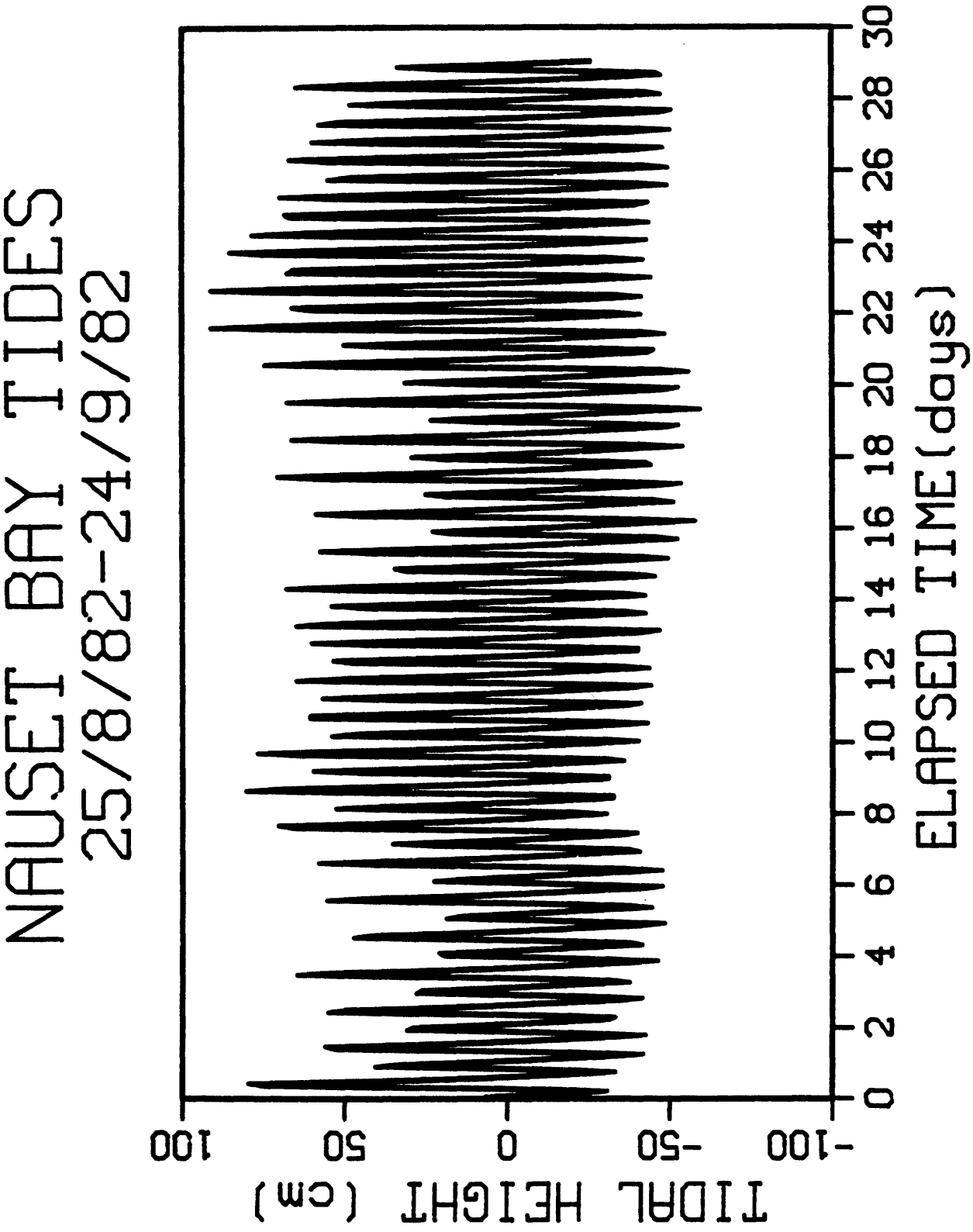

Figure 11. Fortnightly modulation of the tide is demonstrated by a 29-day plot of the tide. During Neap tides, low waters are lower than during Spring tides, the effect of the forced fortnightly tide (MS_f).

(e.g., LeBlond, 1979), and has been ascribed to a fortnightly modulation of the frictional forces due to fortnightly variations in the velocity field. A similar mechanism may be responsible for the observed fortnightly relationship in Nauset and similar estuaries, although the response of Nauset is complicated by its response to wind stress. This fortnightly component is under further investigation by the authors.

V. IMPLICATIONS FOR SEDIMENT TRANSPORT

Tidal asymmetries generated in estuaries through non-linear interactions, and represented as overtides and compound tides, can have profound effects on sediment transport in these systems. For the shelf around the British Isles, Pingree and Griffiths (1979) found sand transport directions coinciding with asymmetries in the tide caused by the M_2, M_4 interaction. Boon and Byrne (1981) discussed the potential importance of inlet/estuarine tidal response to long-term sedimentation trends, as well as the different types of asymmetry present in shallow inlet/estuarine systems.

For Nauset Inlet, the observed asymmetry favors flood transport of sediment, and promotes infilling of the estuary. This trend is depicted in the phase relationship between the overtides and compound tides with the dominant elementary tidal constituents, where the higher frequency induced tides always lead the elementary constituents in sea surface. This phase lead in sea surface results in flood flows which are shorter in duration, and consequently stronger, than ebb flows. Since sediment transport is proportional to the excess shear stress raised to some power, the higher flood velocities may result in a net up-estuary (flood) transport of material, providing the drag coefficient remains nearly equal over the tidal cycle. In the distal reaches of tidal channels at Nauset, the increase in magnitude of flood flow is sufficient that the transport is

greater despite the longer duration of the less intense ebb flow. The balance between increased flow velocity and lesser duration for other estuaries may not be as clear-cut, so each asymmetrical tide must be evaluated given its peculiar geometry and dynamical characteristics. Although this study has emphasized sea surface elevation instead of velocity as an indicator of asymmetry, the flow records available are consistent with this flood asymmetry, and verify the landward transport tendency.

The existence of a landward transport of coarse, near-bed material is reflected in the geometry of the far reaches of the estuary. In the north (Nauset Bay, station 8), the mean water depth is much less than in other parts of the estuary. Although partly a result of barrier overwash, the geometry of the flood-tide deltas shows a clear up-estuary transport. Even more clearly, the channels leading into Town Cove in the southern part of the estuary are shoaling, with a well-defined flood-tide delta encroaching on the deeper waters of Town Cove. Local measurements of the flow structure near this delta demonstrate the dominance of up-estuary transport. Unless conditions change drastically, the estuary will continue to fill, with the lower mean water depths resulting from this filling process accelerating the rate of fill.

On a time scale of decades or a century, the increase in sea-level along this region may also affect the estuarine response to tidal forcing. Sea-level rise in this region has been approximately 2.5 mm/yr over the past 40 years (Aubrey and Emery, 1983). Predictions of increased rate of sea-level rise over the next century due to the global increase in atmospheric carbon dioxide will modify this pattern significantly, perhaps even in as short a time as a few decades. If sea-level rise exceeds the rate of filling of the estuary, the system may develop a more linear response

to tidal forcing. The decreasing rate of infilling could lead to a more stable estuary in the future. These trends are presently under study to evaluate the effects of increased sea-level rise on estuarine physics.

Fine suspended sediment transport will be affected by the nonlinear tidal distortion as well. In particular, for suspended particulate material consisting of plant matter or fine inorganic sediment, an increased tendency exists at Nauset for up-estuary transport, a result of the flood asymmetry. Larger flood currents exert higher near-bed shear stresses, and hence entrain larger quantities of material. Sufficiently small or light material can be transported in the suspended mode. The tidal asymmetry has strong implications for other aspects of mass flux calculations commonly attempted in estuarine systems. Many investigators (e.g., Boon, 1978; Valiela et al., 1978; Kjerfve et al., 1981; Ward, 1981) have attempted to measure, with varying degrees of success, dissolved and particulate organic and inorganic species over tidal cycles to determine net influx or efflux of this material from the estuary. Because of the volume and complexity of sampling required, and logistical considerations, these experiments generally last 30 hours or less. To perform mass balances, the water flux must be balanced; that is, the net volume of water flowing from the estuary must be equal to the sum of freshwater inflow and evapo-transpiration terms (which sum can be near zero). Since these latter terms are difficult to quantify independently, a tidal cycle of 12.4 or 24.8 hours is often imposed. Results commonly show a net influx or efflux of water over the tidal period, which must be accounted for in the chemical balances. Primary contributors to this net water flux are diurnal inequality, meteorological events and the MS_f (fortnightly) compound tide. MS_f at Nauset can have a 10 cm amplitude (total range of 20 cm), accounting

for an appreciable difference in water storage within the estuary system between Spring and Neap tides. If measurements of mass flux are made during periods between Spring and Neap tides, much of this water overburden will be transported either into or out of the estuary, resulting in potentially large net water fluxes. MS_f can also affect estimates of residual flows. The period from neap to spring tides will correspond to a period of net landward flowing residual currents, and spring to neap will correspond to net seaward flowing currents. If experiments are performed over peak Spring or peak Neap tides, this effect will be reduced. Storm surge associated with wind stress events can also dominate the net flux calculations, as superelevations of 1 m or more are not uncommon during large storms. The timing of these storms can severely bias mass flux calculations. In summary, lower frequency tidal and non-tidal motions limit the accuracy of mass balances in estuaries. Since these lower frequency flows contribute significant water fluxes through an estuary, they must be properly sampled to obtain an accurate estimate of mass balances, a difficult criterion to satisfy.

VI. CONCLUSIONS

Observations of sea surface elevation and horizontal currents in a shallow inlet/estuarine system demonstrate the nature of the tidal distortion and suggest implications for sediment transport. The major findings supported by these observations include:

i) Overtides and compound tides derived from the dominant equilibrium tidal constituents offshore can be important in estuaries such as Nauset which are relatively shallow, with large tidal amplitudes, and moderate tidal flat extent. The primary interaction is with the M_2 tide, whose overtides dominate the non-linear signature of the estuary. Growth of the M_2

overtides as well as the compound tides demonstrates the degree of non-linearity, since these constituents continue to grow within the estuary in spite of strong frictional dissipation. Because of the filtering characteristics of the estuary, the M_4 tide is the dominant overtide, since dissipation at higher frequencies is greater than at lower frequencies (the estuary is a low pass filter, to first order).

ii) The overtides and compound tides at frequencies higher than semi-diurnal are phase locked to their forcing tides, with the forced tides consistently leading their forcing by 60-70° in phase. This phase lead appears to be a characteristic of the overall geometry and dissipation characteristics of the inlet/estuarine system, and does not reflect any offshore phase relationship. The relative phase is maintained throughout the estuary, even as the amplitude of the forced tides increases. Reasons for this phase-locking are discussed in a companion paper by Speer and Aubrey (1984).

iii) The sense of the phase locking (with forced tides leading the forcing in sea surface) imparts a flood dominance to Nauset Inlet, such that flood tides are shorter but more intense than ebb tides. This characteristic can be inferred from the sea surface records, where flood tide is shorter and ebb tide is longer, as well as from direct observations of currents within the estuary. Estuaries with different phase relationships can have ebb dominance, where ebb tides are shorter but more intense than flood tides. Watchapreague Inlet, Virginia, an example of an ebb-dominated estuary (sea surface M_4 to M_2 phase of approximately -140° to -160°; Boon and Byrne, 1981), is used as a case example in the companion theory paper by Speer and Aubrey (1984).

iv) A fortnightly compound tide is found consistently within the estuary. The MS_f constituent is partly generated within the estuary by interaction of the S_2 and M_2 tides, perhaps modulated by frictional effects, as suggested by LeBlond (1979) for riverine flow. This 10 cm overtide causes lowest water levels at Neap tides rather than at Spring tides, since MS_f is in phase with its forcing (for two of the three periods of observation). The amplitude and phase relationships are consistent throughout the estuary for any given observation period, so the estuary appears to respond as a system. During one of three observation periods, a large storm induced a 0.75 meter superelevation within the estuary, with a decay time of approximately one week. This energetic event swamped the non-linear component of MS_f, such that the storm surge dominated estimates of MS_f. Even though estuarine response was uniform at the two working tide stations within the estuary, phase relationships and amplitudes were much different than for non-storm periods. This latter observation provided estimates of MS_f which were therefore dynamically unrelated to the compound (S_2-M_2) tide.

v) From a sediment transport standpoint, the overtides and compound tides at frequencies greater than semi-diurnal cause net import of near-bed material at Nauset. More intense flood flows transport more sediment than less intense ebb flows of longer duration (aided by the threshold criterion). This causes filling of the estuary, as evidenced by shoaling in the extreme parts of the estuary (notably Town Cove). Over a long-time frame, decreased depths may accentuate the filling tendency, although the effects of increased sea level rise due to increased global atmospheric carbon dioxide may reverse this trend. For suspended particulate transport, the asymmetry experienced by the Nauset inlet/estuary system favors

up-estuary transport, as higher flood shear stresses (on the average) will entrain more fine sediment and light particulate material for subsequent transport.

vi) The effects of the MS_f fortnightly tide are more subtle, as MS_f has a longer period and does not directly affect the tidal asymmetry. MS_f makes accurate estimates of mass balances more difficult, as the superimposed low-frequency flow can impart a significant bias to water flux estimates over a 25 hour period. Mixing is substantially influenced as well, since MS_f can account for a large volume of water (given its 20 cm range). Estimates of residual currents must consider the effects of these lower frequency flows.

REFERENCES

Aubrey, D.G. and K.O. Emery, 1983. Eigenanalysis of recent United States sea levels. Continental Shelf Research, v. 2, p. 21-33.

Aubrey, D.G. and P.E. Speer, 1983. Sediment transport in a tidal inlet. Woods Hole Oceanographic Institution Technical Report, WHOI 83-20, 130 pp.

Aubrey, D.G., P.E. Speer and J.D. Boon III, in prep. Tidal spectroscopy in shallow water - a review of methods.

Boon, J.D., III, 1978. Suspended solids transport in a salt marsh creek - An analysis of errors. In B. Kjerfve (ed.), Estuarine Transport Processes, Univ. of South Carolina, p. 147-159.

Boon, J.D. III and K.P. Kiley, 1978. Harmonic analysis and tidal prediction by the method of least squares. Spec. Report No. 186, Virginia Institute of Marine Science, Gloucester Pt., VA, 49 pp.

Boon, J.D. and R.J. Byrne, 1981. On basin hypsometry and the morphodynamic response of coastal inlet systems. Marine Geology, v. 40, p. 27-48.

Cartwright, D., W.H. Munk and B. Zetler, 1969. Pelagic tidal measurements. EOS, v. 50, p. 472-477.

Daifuku, P.R. and R.C. Beardsley, 1983. The K_1 tide on the continental shelf from Nova Scotia to Cape Hatteras. Jour. Phys. Ocean., v. 13, p. 3-17.

Dronkers, J.J., 1964. Tidal Computations in Rivers and Coastal Waters. North-Holland Publishing Company, Amsterdam, The Netherlands. 516 pp.

Filloux, J.H. and R.L. Snyder, 1979. A Study of tides, set up and bottom friction in a shallow semi-enclosed basin. Part I: Field experiment and harmonic analysis. Jour. Phys. Ocean., v. 9, p. 158-169.

Gallagher, B.S. and W.H. Munk, 1971. Tides in shallow water: spectroscopy. Tellus, v. 23, p. 346-363.

Gonella, J., 1972. A rotary-component method for analyzing meteorological and oceanographic vector time series. Deep-Sea Research, v. 19, p. 833-846.

Goodman, N.R., 1957. On the joint estimation of the spectra, cospectrum and and quadrature spectrum of a two-dimensional stationary Gaussian process. Scientific Paper no. 10, Engineering Statistics Laboratory, New York University.

Kjerfve, B., L.H. Stevenson, J.A. Proehl, T.H. Chrzanowski, and W.M. Kitchens, 1981. Estimation of material fluxes in an estuarine cross section: A critical analysis of spatial measurement density and errors. Limnology and Oceanography, v. 26, p. 325-335.

LeBlond, P.H., 1979. Forced fortnightly tides in shallow rivers. Atmosphere-Ocean, v. 17, p. 253-264.

Munk, W.H. and D.E. Cartwright, 1966. Tidal spectroscopy and prediction. Phil. Trans. Royal Soc. of London, v. 259, p. 533-581.

Munk, W.H. and K. Hasselmann, 1964. Super-resolution of tides. Studies in Oceanography, Univ. of Washington Press, p. 339-344.

Pingree, R.D. and D.K. Griffiths, 1979. Sand transport paths around the British Isles resulting from M_2 and M_4 tidal interactions. J. Mar. Bio. Ass. U.K., v. 59, p. 497-513.

Robinson, I.S., L. Warren and J.F. Longbottom, 1983. Sea-level fluctuations in the Fleet, an English tidal lagoon. Estuarine, Coastal and Shelf Science, v. 16, p. 651-668.

Schureman, P., 1971. "Manual of Harmonic Analysis and Prediction of Tides," U.S. Dept. of Commerce, Coast and Geodetic Survey, Special Publ. No. 98, Revised 1940 Edition, Published 1971.

Speer, P.E. and D.G. Aubrey, in prep. A study of non-linear tidal propagation in shallow inlet/estuarine systems. Part II: theory.

Valiela, I., J.M. Teal, S. Volkmann, D. Shafer and E.J. Carpenter, 1978. Nutrient and particulate fluxes in a salt marsh ecosystem: tidal exchanges and inputs by precipitation and groundwater. Limnology and Oceanography, v. 23, p. 798-812.

Ward, L.G., 1981. Suspended material transport in marsh tidal channels, Kiawah Island, South Carolina. Marine Geology, v. 40, p. 139-154.

CHAPTER IV

A STUDY OF NON-LINEAR TIDAL PROPAGATION IN SHALLOW INLET/ESTUARINE SYSTEMS

PART II: MODELING TIDAL ASYMMETRIES

Abstract

The development of tidal asymmetries is studied via numerical integration of the one-dimensional equations for channel geometries characteristic of those in shallow estuaries located on the U.S. east coast. Channels without tidal flats develop a time asymmetry characterized by a longer falling than rising tide. This behavior is enhanced by strong friction and large channel area variability over a tidal cycle. The resulting tidal currents have a shorter, intense flood and a longer, weak ebb (flood dominant). Addition of tidal flats to the channels can produce a longer rising tide and stronger ebb currents (ebb dominant), if the area of tidal flats is large enough to overcome the effects of time-variable channel geometry. Weaker friction with flats can also produce this asymmetry. The general features of tidal channels in shallow estuaries can be represented with simple geometries. Despite the physical complexity of these systems, essential features of the estuarine tidal response can be recovered from simple models. This is illustrated by modeling idealized representations of tidal channels at Nauset Inlet, MA and Wachapreague Inlet, VA.

1. Introduction

The tidal response of shallow inlet/estuarine systems commonly found on the U.S. east coast is frequently characterized by the development of asymmetries in the estuarine tide. The asymmetries take the form of unequal duration and/or unequal magnitude of ebb and flood. This distortion of the estuarine tide can be represented by the non-linear growth of harmonics of the astronomical constituents. A particularly important type of tidal distortion is the duration inequality in the rise and fall of the surface tide. Some inlet/estuarine systems (e.g., Murrels Inlet, SC, Boon and Byrne, 1981; Nauset Inlet, MA, Aubrey and Speer, 1983) are characterized by longer ebbs than floods and consequently a tendency for higher current velocities during flood (flood dominant). Other systems (e.g. Wachapreague Inlet, VA, Boon and Byrne, 1981; North Inlet, SC, Nummedal and Humphries, 1978; Price Inlet, SC, FitzGerald and Nummedal, 1983) show the opposite duration asymmetry and hence a tendency for stronger ebb currents (ebb dominant). The different types of asymmetry have important implications for estuarine sediment transport, dispersal of water column contaminants, and (over long time scales) estuarine/inlet stability. An important question, therefore, is what processes are responsible for different forms of tidal asymmetry. This paper describes a series of numerical experiments, based on idealized estuarine geometries, which examine the problem of estuarine tidal distortion.

2. Physical Description of the Problem

Before proceeding to the numerical solutions, a description of physical aspects of the problem is presented. For representative systems, (fig. 1.), the estuary is serviced by a narrow inlet and consists of a number of channels generally terminating in bays. The bays may consist

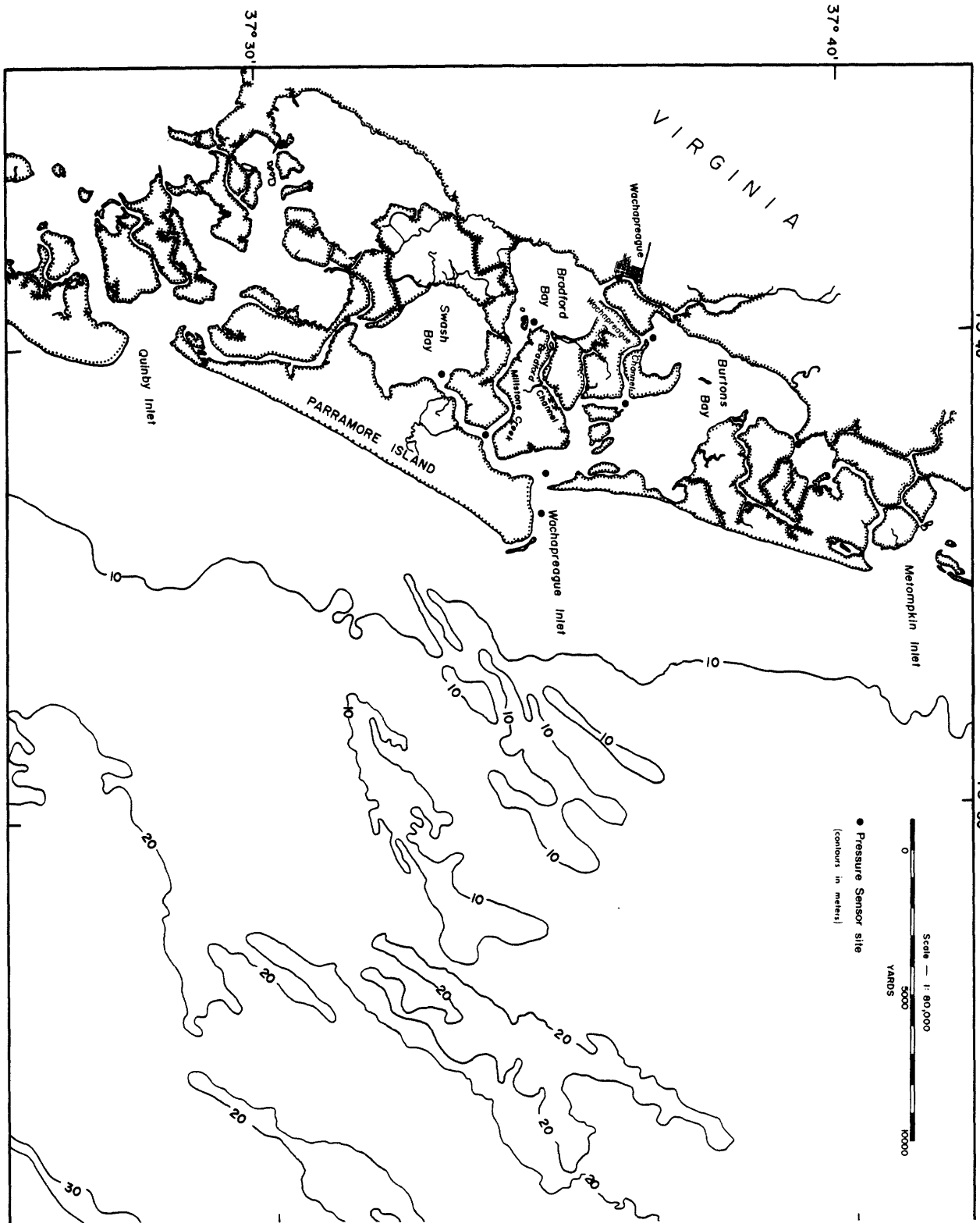

Figure 1a. Wachapreague Inlet/estuary system, VA. The estuary is serviced by a deep (18 m.), stable inlet. Channel depths are 4-5 m. and terminate in shallow bays consisting of extensive tidal flats.

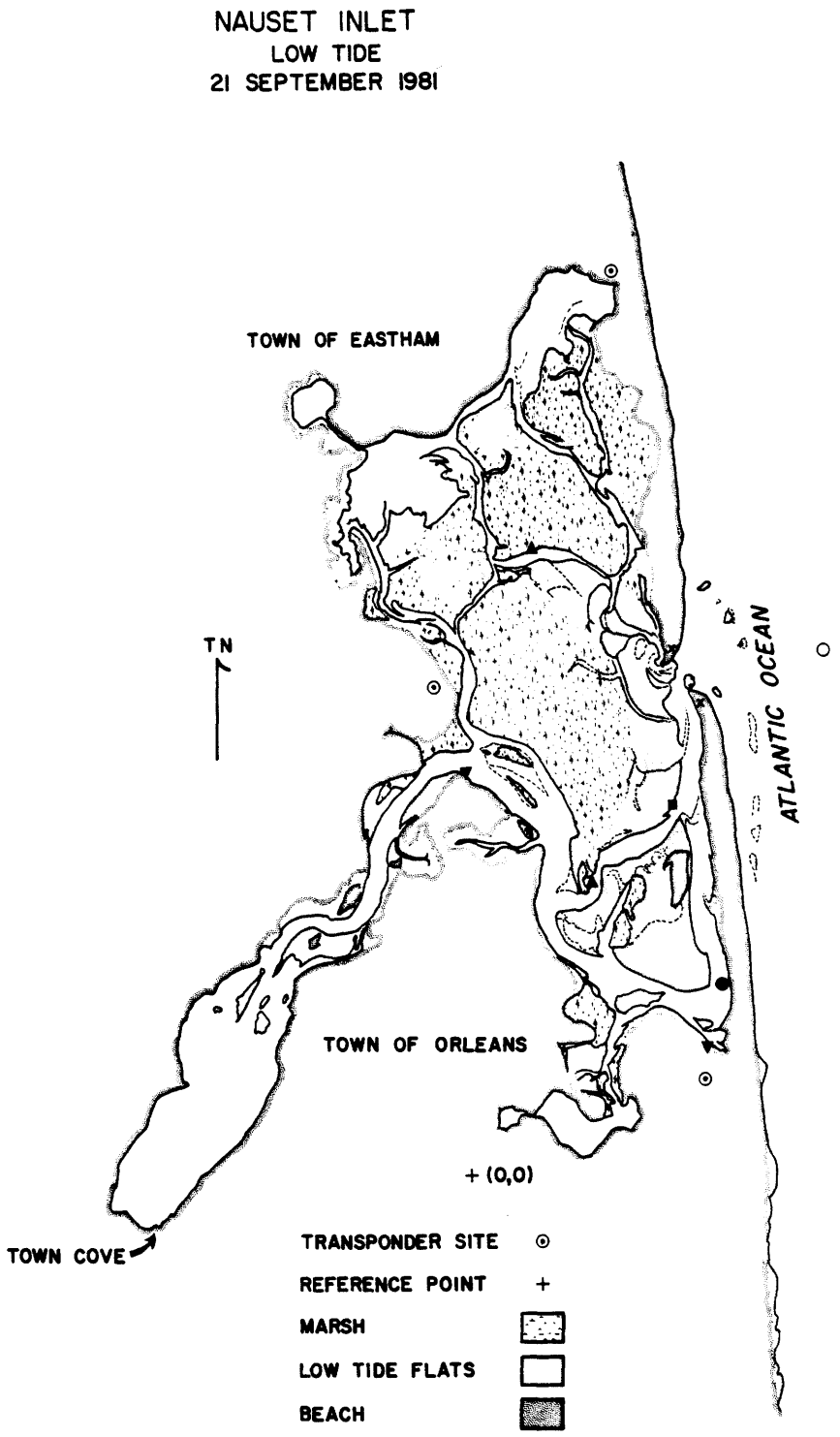

Figure 1b. Nauset Inlet/estuary system, MA. Nauset is a shallow (3-4 m.), unstable inlet. Estuarine channels are shallow (>3 m.) with tidal flat deposits located near the inlet.

largely of tidal flats (fig. 1a) or may be basins deeper than the connecting tidal channels (fig. 1b). Separating the tidal channels are regions of flats exposed at low tides and islands of marsh grass which are occasionally overtopped at high tide. Typical channel depths, h, are 1-10 meters and lengths, L, are on the order of 1-10 km. Characteristic values for the tidal amplitude, a, suggest that finite amplitude effects as indicated by the ratio, a/h, can be important in these systems. Since the tidal wavelength, $2\pi/k$, is much greater than L, characteristic length scales are determined by estuarine geometry. The channels are also long compared to their width, $b/L \ll 1$, and the horizontal aspect ratio, h/b, is small. The flow may therefore be termed one-dimensional although channel bends visible in Figure 1 will produce locally two-dimensional effects (e.g., Aubrey and Speer, 1984).

Estuarine systems of interest to this study are also characterized by a well-mixed water column and negligible freshwater inflow. Mixing is promoted by the strong currents (order 1 m/s) often found in estuarine channels and by interaction of currents with a rough bed. In deeper basins at channel terminations, a weak stratification develops during summer months.

The offshore astronomical tide spectrum is composed of a number of important constituents (fig. 2a). A complex interaction between these constituents is possible in a non-linear system. At Nauset, field observations of estuarine tides indicate a rich spectrum of forced motions (fig. 2b) ranging from high frequency (i.e., greater than semi-diurnal) to low frequency (e.g., fortnightly). The M_2 constituent, however, as the major constituent along the northeast U.S. coast dominates non-linear processes within the estuary. This domination can be shown from theoretical arguments (e.g., Gallagher and Munk, 1971) as well as field observations

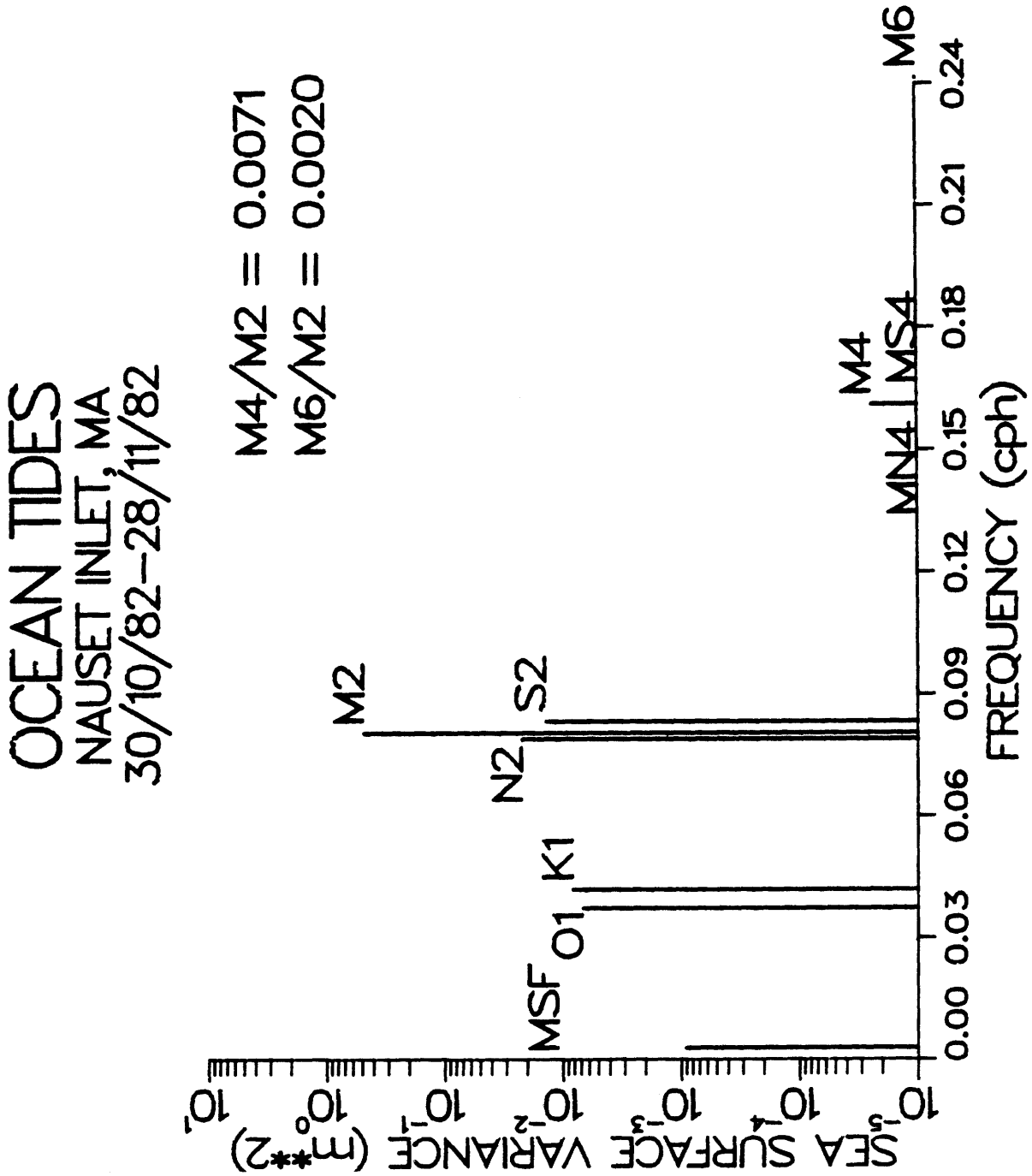

Figure 2a. Periodogram derived from tidal harmonic analysis of pressure sensor located in 10 m. water depth outside Nauset Inlet. Subscripted letters refer to tidal constituents with M_2 the dominant constituent. Relative size of the ratios M_4/M_2 and M_6/M_2 specifies the degree of non-linearity of the tides. In this case ratios are low indicating a weakly non-linear tide. Ratios are for amplitudes not energy.

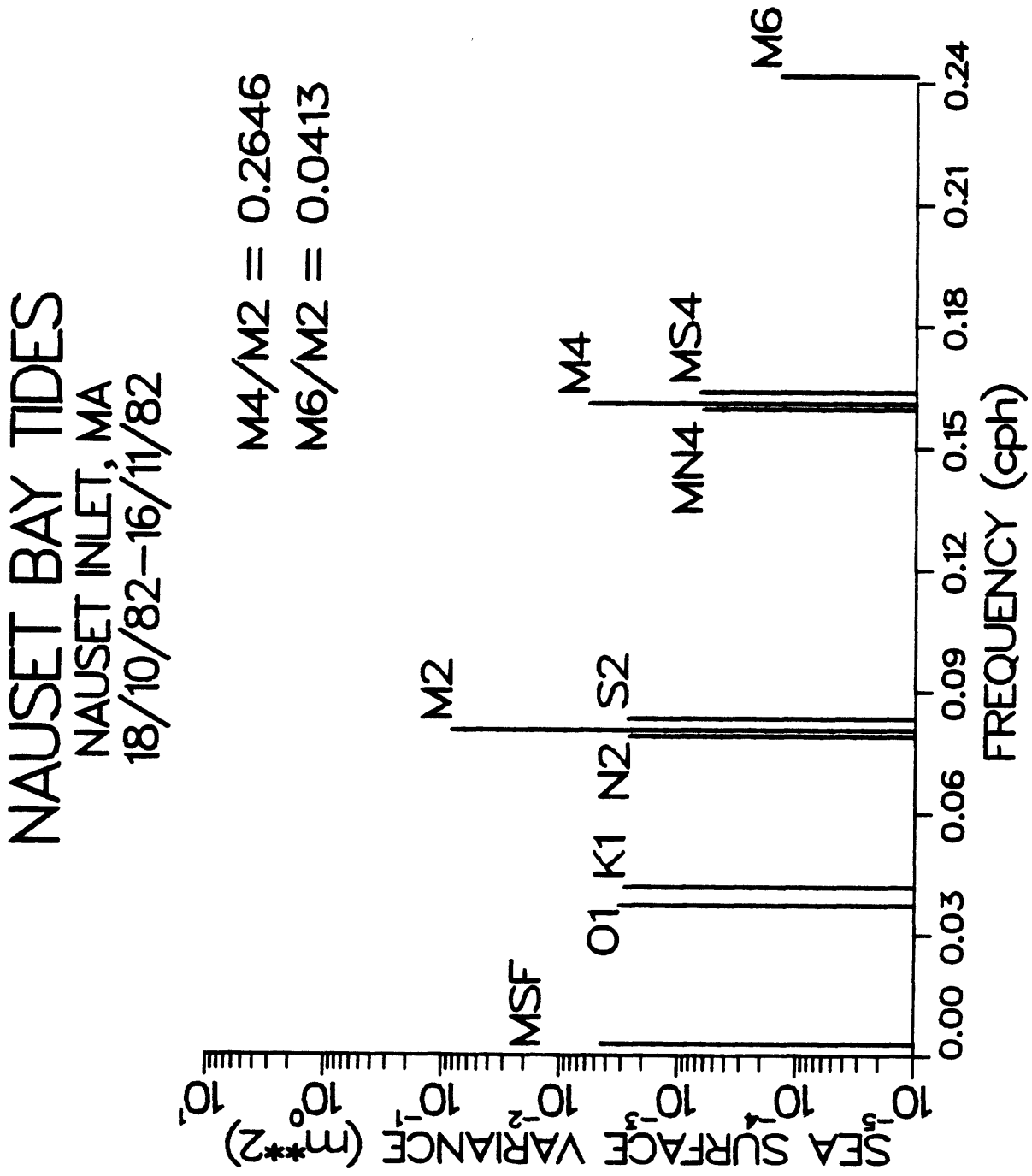

Figure 2b. Periodogram of tides within Nauset estuary. Note the growth of high frequency (>2 cpd) overtides and compound tides. The large M_4/M_2 ratio indicates strong distortion of the surface tide.

(Aubrey and Speer, 1983). The harmonics of M_2 are larger than compound tides produced by interaction among constituents.

Field observations (e.g., Boone and Byrne, 1981; Aubrey and Speer, 1983) and theoretical work (e.g., Kreiss, 1957; Dronkers, 1964; Pingree and Griffiths, 1979) have shown that the interaction of M_2 and its first harmonic, M_4, explain the general features of observed tidal asymmetries. The type of tidal distortion (e.g., flood dominant versus ebb dominant) depends on the relative phasing of M_4 to M_2. Defining the M_2 and M_4 constituents (sea surface or velocity) as

$$A_{M_2} = a_1 \cos(\omega t - \theta_1)$$

$$A_{M_4} = a_2 \cos(\omega t - \theta_2)$$

the $M_2 - M_4$ phase can be written:

$$\phi = 2\theta_1 - \theta_2.$$

The magnitude of tidal distortion is determined by the rate of harmonic growth and is indicated by the ratio of M_4 to M_2 amplitudes:

$$M_4/M_2 = a_2/a_1$$

An important problem is determining the estuarine characteristics which contribute to non-linear tidal response. This study investigates the mechanics of M_2 propagation in channels with dimensions similar to those described previously. The one-dimensional equations of motion (cross-sectionally averaged) are numerically integrated for various examples of idealized estuarine channels. Although this is clearly a simplification of the actual physical problem, the above discussion shows that insight can be gained from this approach.

Boundary forcing for the problem consists of the M_2 constituent. Harmonics present in the solution will, therefore, be entirely locally generated within and confined to the model channel. This situation is compli-

cated in the case of actual inlet/estuarine systems by the presence of shallow features, ebb tide deltas, seaward of the inlets. Finite amplitude effects on the ebb tide delta produce harmonics of M_2 which enter the estuary through the inlet. Field evidence (e.g., Boone and Byrne, 1981; Aubrey and Speer, 1983) suggests that phase and/or amplitude characteristics of M_4 can change dramatically through the inlet. The input spectrum is strongly modified by the estuarine geometry. Estuarine response solely to M_2 forcing is, therefore, an important part of the tidal asymmetry problem. In principle, the modeling can include an input spectrum consisting of the other important astronomical constituents (e.g., O_1, K_1, S_2, N_2). However, the most general features of the estuarine channel response to tidal forcing are revealed by considering M_2. Ter-diurnal compound constituents (e.g., MK_3, MO_3) do not produce any asymmetry and quarter-diurnal compound constituents (e.g., MS_4, MN_4) have smaller amplitudes than M_4.

3. Model Formulation

3.1. Governing Equations

In this section, we develop the equations of motion for one-dimensional flow in a well-mixed water column, and apply them to cross-sections of typical estuarine channels (figs. 3 and 4). A trapezoidal geometry is used to represent estuarine channels where the width generally contracts with decreasing depth. We consider the tidally driven problem and focus on cases where sea level fluctuations, a, are of the same order as the water depth, h. This is usually the case in these estuaries (e.g., Kjerfve, 1975).

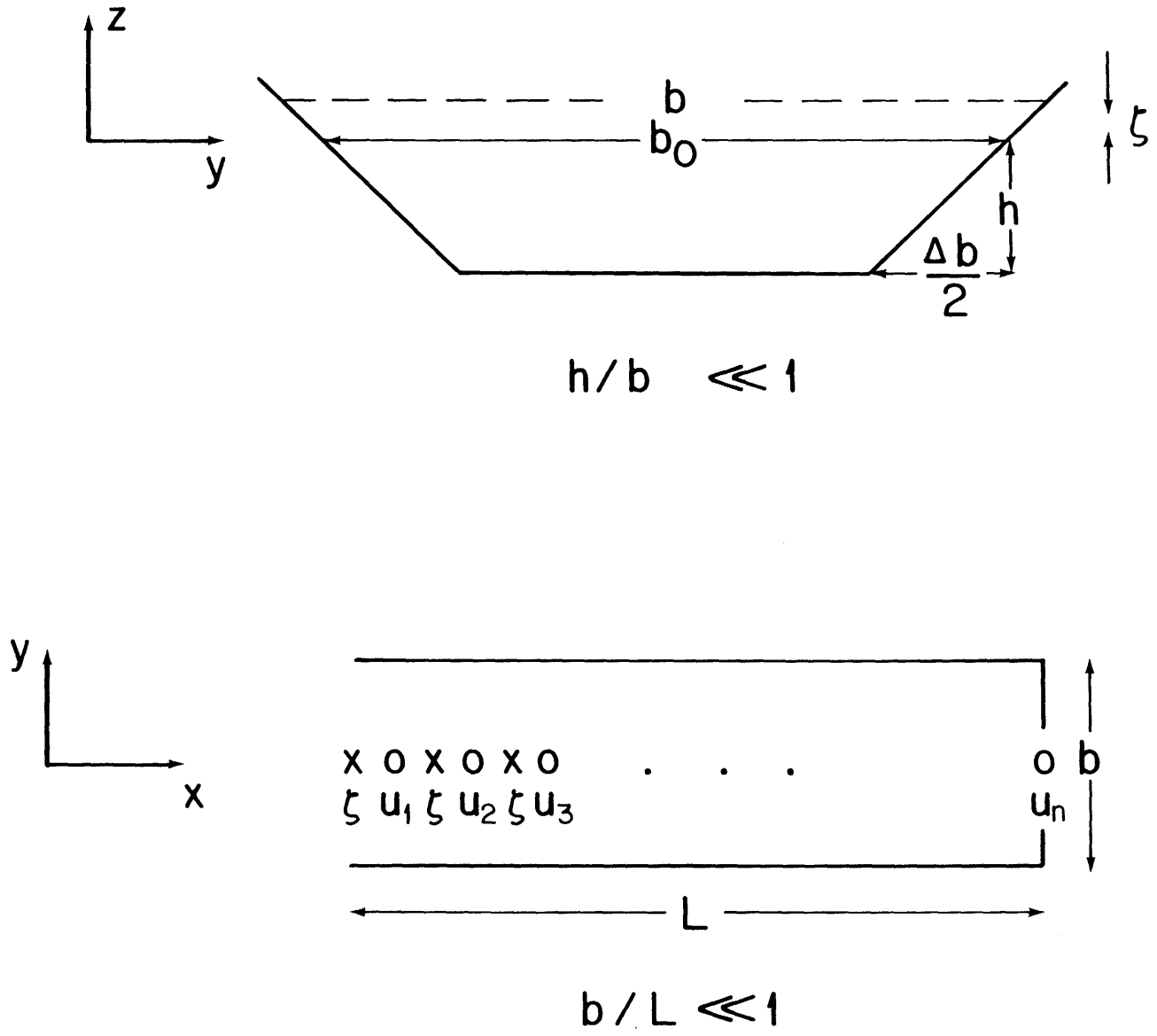

Figure 3. Channel geometry used in model runs and staggered numerical grid employed along channel.

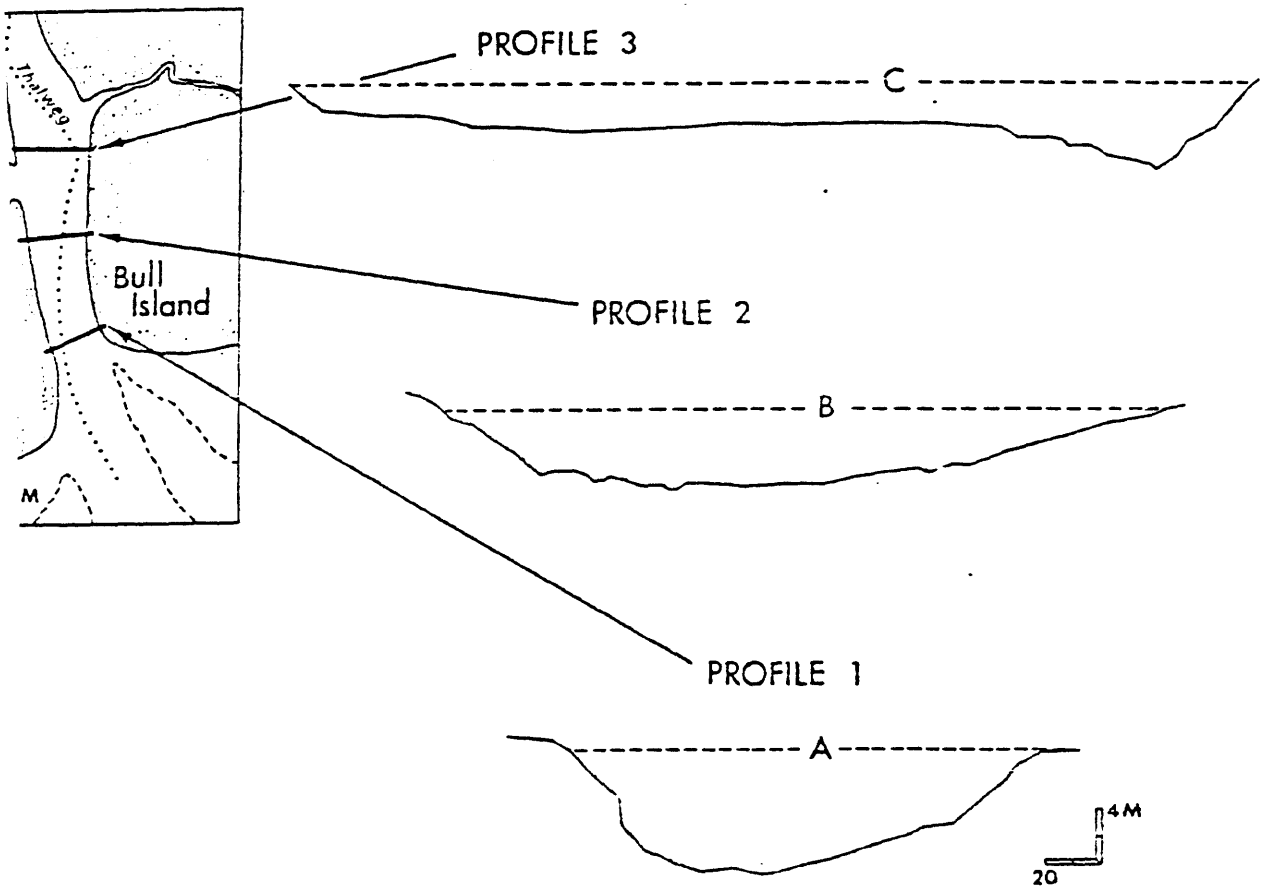

Examples of channel cross-sections

Figure 4. Typical estuarine channel cross-sections from Price Inlet, S.C. (taken from FitzGerald and Nummedal, 1983).

The following assumptions are made:

1) hydrostatic pressure

2) level sea surface across channel

3) small horizontal aspect ratio, $h/b \ll 1$

4) long narrow estuary, $b/L \ll 1$

Assumption one simplifies the z-momentum equation to:

$$p = \rho g(\zeta - z) \tag{1}$$

Assumption two simplifies the y-momentum equation:

$$\zeta = \zeta\ (x,t) \tag{2}$$

Clearly, in real estuaries, these assumptions will be violated locally. Channels with large bedforms and shallow depths may depart from purely hydrostatic conditions. Strong channel curvature (e.g., flow around bends) may violate assumption two. This two-dimensional effect is generally localized, affecting secondary circulation, shear stress and sediment transport patterns in the vicinity of the bend (Smith and McLean, 1983). This work examines the response to tidal forcing of the entire estuarine channel. Assumptions 3 and 4 hold for many estuaries of interest.

The model dynamics will be expressed in terms of cross-sectional flux, $U(x,t)$, cross-sectionally averaged velocity, $\bar{U}(x,t)$, and sea surface elevation, $\zeta(x,t)$. Defining the velocity vector $\vec{q}(u,v,w)$, the governing equations are:

$$\frac{\partial u}{\partial x} + \frac{\partial v}{\partial y} + \frac{\partial w}{\partial z} = 0 \tag{3}$$

$$\frac{\partial u}{\partial t} + \frac{\partial}{\partial x}u^2 + \frac{\partial}{\partial y}uv + \frac{\partial}{\partial z}uw = -\frac{1}{\rho}\frac{\partial p}{\partial x} + \frac{1}{\rho}\left[\frac{\partial \tau_{zx}}{\partial z} + \frac{\partial \tau_{zy}}{\partial y}\right] \tag{4}$$

Equation (3) is integrated vertically over the water column and horizontally

across channel (i.e., $\int_{-b_1-h}^{b_2}\int^{\zeta} dzdy$) to yield

$$\frac{\partial A}{\partial t} + \frac{\partial}{\partial x} U = 0 \tag{5}$$

$A(x,t)$ = cross-sectional area of channel

$$U = \int_{-b_1-h}^{b_2}\int^{\zeta} udzdy = \bar{U} \cdot A$$

For a trapezoidal channel,

$$\frac{\partial A}{\partial t} = b \frac{\partial \zeta}{\partial t}$$

$b(x,z)$ = channel width at depth, z.

Continuity becomes

$$\frac{\partial \zeta}{\partial t} + \frac{1}{b} \frac{\partial}{\partial x} U = 0 \tag{6}$$

The same integration on x-momentum yields after considerable algebra (Appendix 1):

$$\frac{\partial U}{\partial t} + \frac{\partial}{\partial x} \frac{U^2}{A} = -gA \frac{\partial \zeta}{\partial x} - \frac{\tau_b}{\rho} P \tag{7}$$

τ_b = average shear stress on solid boundaries
P = wetted perimeter

The derivation of equation (7) requires assumptions to integrate the advective and frictional terms. The form of the advective term in (7) depends on small cross-sectional variability in velocity. This, in turn, requires gentle changes in cross-section along channel. A momentum factor (e.g. Dronkers, 1964) may be introduced to account for non-uniformity in velocity across the channel. For the purposes of this study, a momentum factor was not used. The friction term in (7) includes sidewall friction by considering channel sidewalls in the wetted perimeter. The problem is closed mathematically by formulating friction as follows:

$\tau_b = \rho f |\bar{U}| \bar{U}$

f = dimensionless friction factor

In the formalism of cross-sectional discharge, U, bottom friction takes the form,

$$\tau_b = \rho \frac{f |U| U}{A \bullet A} \qquad (8)$$

This form is one commonly used by modelers to parameterize the inherently non-linear effects of bottom friction (e.g., Owen, 1980; Uncles, 1981). Other investigators use the Chezy/Manning expression (e.g., Pearson and Winter, 1976, 1977; Teubner and Noye, 1978), although these are quadratic forms as well. A number of shortcomings exist in this formulation of friction. The quadratic form is strictly valid for steady flows. Additionally, if surface gravity waves are present, a constant friction coefficient does a poor job of representing bottom friction (Grant and Madsen, 1979). Surface gravity waves are potentially important near the inlet and may considerably enhance the tidal bottom friction in this location. However, this is a complication which will not be treated in the model. The modeling will examine tidal propagation in the absence of waves.

Controversy exists as to whether a quadratic form accurately models the generation of tidal harmonics. In particular, it is felt that odd harmonics of the fundamental frequency are over-emphasized (Prandle, 1980). Snyder et al. (1979) found that a combination of quadratic and linear friction was required to reproduce M_4 and M_6 observations in a shallow gulf. Other investigators have had success modeling the M_2, M_4 interaction utilizing a quadratic friction (e.g., Pingree and Maddock, 1978; Pingree and Griffiths, 1979). This numerical study is not an attempt to reproduce a

set of field observations but rather to examine the types of tidal asymmetry produced by different estuarine geometries. A quadratic friction term is adequate for the purposes of this study.

Equations (6) and (7), together with the form of bottom friction specified in (8), constitute the equations solved by the numerical model. Principal non-linear effects in these equations enter through quadratic friction, advection of momentum and through tidal interactions with estuarine geometry in the continuity equation. By varying channel geometry and friction characteristics, the interplay of these terms in distorting the tidal signal is examined.

3.2. Inclusion of Tidal Flats

An important physical characteristic of these systems is the presence of tidal flats exposed at low tide. Tidal flats can occupy a significant fraction of the total estuarine surface area (e.g., FitzGerald and Nummedal, 1983). They can be incised with shallow channels which are active during only a portion of the tidal cycle. This type of geometry is particularly prevalent around the inlet mouth where they are termed marginal flood channels (Hayes, 1975). Obviously, a one-dimensional model cannot handle the presence of several distinct channels across a channel section. Throughout most of the estuary, however, tidal flats serve mainly to store water as opposed to transporting momentum. Bottom friction substantially weakens the velocity as water moves away from the main channel onto the flats. This suggests approximating the effect of tidal flats by including them solely in the continuity equation. This idealization will neglect dissipation of the tide as water flows across the flats, as well as the dissipative effect of low velocity fluid draining into the ebbing channel flow from tidal flats during falling tide. Dronkers (1964)

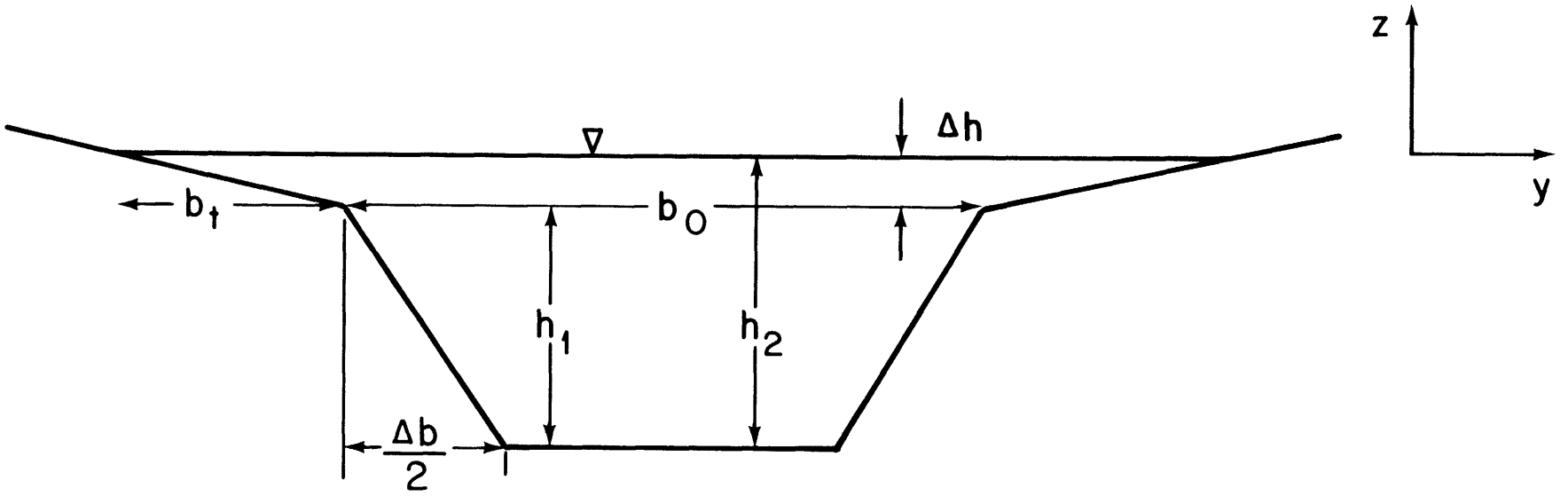

Figure 5. Channel geometry with tidal flats included.

suggests a procedure for including lateral inflow (discussed below). Consideration of flats solely as reservoirs has been utilized successfully before in model applications (e.g., Teubner and Noye, 1978; Boon and Byrne, 1981).

A model estuarine channel is composed of a momentum transporting portion of maximum width, b_o, and a storage region of initial width, $2b_t$ (fig. 5). The slope of the storage region, $\tan\theta$, is equal to $\Delta h/b_t$ where Δh represents the difference between total channel depth and the depth at width b_o. The presence of the tidal flats enters through the continuity term, $\frac{1}{b}$ $\partial U/\partial x$, where b is the total width including flats. The dissipative effect produced by water on the flats entering the main channel is modeled as follows.

The lateral inflow of tidal flat water into the main channel per unit length of the channel is equal to $(b_T-b_o)\ \partial\zeta/\partial t$, where b_T is the total width of the channel. The acceleration of this water in the main channel unit area equals:

$$\bar{U}\ (b_T-b_o)\frac{\partial\zeta}{\partial t}$$

or

$$\frac{U}{A}\ (b_T-b_o)\frac{\partial\zeta}{\partial t} \qquad (9)$$

This term will carry a positive sign on the right hand side of (7). Using continuity, we can rewrite (9) as

$$\frac{(b_T-b_o)}{b_T}\ \frac{U}{A}\ \frac{\partial U}{\partial x} \qquad (10)$$

showing that this term is quadratic in transport. It has the effect of acting like additional friction. Unless $b_T>>b_o$ this term is insignificant compared to the advective term. For most cases, the modeling ignores this dissipative effect. The preceeding derivation can also be obtained by retaining lateral inflow terms in momentum and continuity (Appendix I).

3.3. Boundary Conditions and Initial conditions

Equations (6) and (7) constitute an initial-boundary value problem. Initial conditions are taken as:

$$U(x,0) = 0$$
$$\zeta(x,0) = 0$$

The strong frictional effects in the models quickly damp out initial transients, making these convenient initial conditions. Boundary conditions include a condition of no flux into solid boundaries and a specified tidal forcing at the channel open boundary,

$$U(L,t) = 0$$

$$\zeta(0,t) = a \cos \omega t$$

3.4. Numerical Scheme

The numerical integration of equations (6) and (7) is carried out with an explicit time-stepping finite difference model (e.g., Teubner and Noye, 1978; Prandle, 1980; Uncles and Jordan, 1980). Sea surface and transport are spatially staggered with width and depth defined at sea surface grid points (fig. 3). Time derivatives are replaced by forward time steps and spatial derivatives by centered differences. The formal accuracy of the numerical scheme is approximately $O(\Delta t, \Delta x^2)$. An explicit finite-difference scheme was chosen because the relative simplicity and small size of the model domain made it easy to implement and inexpensive to run. Another popular scheme for tidal problems is the harmonic decomposition method (e.g., Pearson and Winter, 1976, 1977; Snyder et al., 1979; Le Provost et al., 1981; Uncles, 1981). This method recasts the time-dependent problem (hyperbolic equations) into a time-independent problem (elliptic equations). The resulting spatial problem is solved via finite differences or finite elements. An attractive feature of this method is that one solves directly

for the amplitudes and phases of tidal harmonics. It is particularly useful for large 2-D problems which are linear or weakly non-linear and for modeling a number of different constitutents. Non-linear effects are included either by analytical expansions for non-linear terms (e.g., Le Provost et al., 1976, Snyder et al., 1979) or by iterative approaches (e.g., Pearson and Winter, 1976). Strongly non-linear problems (such as those considered here) may converge slowly or not at all. In fact, Pearson and Winter (1976, 1977) found it necessary to include an artificial friction term to insure convergence in strongly non-linear coases. For this reason, as well as the ease of including non-linear terms, a time-stepping model was employed.

The continuous variables A, U and P are replaced by their discrete analogues over the space and time domain $x_j = j\Delta x$ and $t^n = n\Delta t$ for $j = 0,N$ and $n = 0,\infty$. The remaining variables, ζ and b, are replaced by a discrete set over $x_{j+1/2}$ and t^n for $j = 0,N$ and $n = 0,\infty$. Linear interpolation defines values of the discrete variables for all x and t. Defining the following operators:

$$N_j^n = N(x_j, t^n)$$

$$\Delta_t N_j^n = (N_j^{n+1} - N_j^n)/\Delta t$$

$$\Delta_x N_j^n = (N_{j+1}^n - N_j^n)/\Delta x$$

$$\delta_x N_j^n = (N_{j+1/2}^n - N_{j-1/2}^n)/\Delta x$$

$$\delta_x N_{j,1}^n = (N_{j+1}^n - N_{j-1}^n)/2\Delta x,$$

equations (6) and (7) are replaced by their discrete analogues:

$$\Delta_t \zeta_{j+1/2}^n + \frac{1}{b}{}_{j+1/2}^{n} \bullet \Delta_x U_j^n = 0 \qquad (11)$$

$$\Delta_t U_j^n + \delta_x D_{j,1}^n =$$

$$-gA_j^{n+1}\delta_x\zeta_j^{n+1} - f|U_j^n|U_j^n \bullet \frac{(P_j^n \quad)}{A_j^n \bullet A_j^n}, \qquad (12)$$

and $D_j^n = (U_j^n)^2/A_j^n$.

Mean velocity, $\bar{U}$, is defined: $\bar{U}_j^n = U_j^n/A_j^n$

The boundary and initial conditions become:

$$U_j^n = 0 \qquad j = N \tag{13}$$

$$\zeta_j^n = a \cos\omega(n\Delta t) \quad j = 1/2 \tag{14}$$

and $$U_o^n = U_1^n + b_{1/2}^n \cdot \Delta x \cdot \Delta_t \zeta_{1/2}^n$$

and $$U_j^o = \zeta_{j+1/2}^o = 0 \qquad j = 0,N. \tag{15}$$

The stability criterion governing the linearized numerical problem is the well-known CFL condition (e.g., Roache, 1972):

$$\frac{\Delta x}{\Delta t} > \sqrt{g h_{max}}$$

This condition states that information cannot be propagated faster than a "computational information speed" defined by the length and time scale of the model. The form of the advective term used in this numerical scheme can cause numerical instability under certain circumstances. The simple advective equation

$$\frac{\partial U}{\partial t} + c\frac{\partial u}{\partial x} \simeq 0,$$

c = advection speed

centered in space and forward in time (FTCS), is unstable. The instability in this equation can be removed by one-sided rather than space-centered differencing (Roache, 1972). It is also possible to stabilize the advective term in the FTCS scheme via the "angled derivative" approach (e.g., Flather and Heaps, 1975; Uncles and Jordan, 1980). This method performs a forward and backward sweep of the grid utilizing two different forms of the advective term, resulting in an advective term centered in space and time. Although the present study does not employ this scheme, the dissipation in the momentum equation overcomes any tendency towards advective instability.

The procedure in model runs was to time-step a particular experiment until a periodic solution was obtained. The amplitude and phase relationships of harmonics were determined by harmonic analysis of the solution. Sea surface and mean velocity were Fourier-analysed according to:

$$\zeta = \langle\zeta\rangle + \sum_n (A_n \cos n\omega t + B_n \sin n\omega t)$$

$$\bar{U} = \langle\bar{U}\rangle + \sum_n (C_n \cos n\omega t + D_n \sin n\omega t)$$

$\langle\ \rangle$ = tidally-averaged quantity

$n = 1 : M_2$

etc.

$n = 2 : M_4$

Additionally, the terms in the equations of motion were harmonically analysed to examine mechanisms for particular cases of non-linear tidal distortion (e.g., Prandle, 1980).

3.5. Model Comparison with Linear Solution

Although the general form of the numerical scheme described above has been employed successfully, it was tested against a linear solution for tidal propagation in a channel. The approach taken was to solve the full model equations (with a modified form of friction) for a case expected to be approximately linear. This solution was then compared to a solution of the linearized equations which are, of course, only valid in a weakly non-linear case. Such a case occurs when $a/h \ll 1$ and when strongly time-variable geometry is excluded. The channel used for the comparison was 20 km long with constant width (200 m) and depth (20 m) forced by a tide with amplitude, 0.5 m. The ratio, a/h, equals 0.025 and cross-sectional area changes only 5% over a tidal cycle. The linearized equations governing motion in the channel are:

$$\frac{1}{b_o}\frac{\partial U}{\partial x} + \frac{\partial \zeta}{\partial t} = o \tag{16}$$

$$\frac{\partial U}{\partial t} = -gA_o\frac{\partial \zeta}{\partial x} - fU \tag{17}$$

b_o = channel width (constant)
A_o = mean channel area (constant)
f = linear friction factor (t^{-1})

The solution for sea surface subject to boundary conditions

$$U(L,t) = 0$$
$$\zeta(0,t) = H\cos\omega t$$

and initial conditions,

$$U(x,0) = \zeta(x,0) = 0,$$

is (Dronkers, 1964):

$$\zeta(x,t) = H\,\frac{A\cos\omega t + B\sin\omega t}{\cosh(s\sigma) + \cos(s\beta)} \tag{18}$$

where,

$$A = 2\left[\phi_1(L)\phi_1(x-L) + \phi_2(L)\phi_2(x-L)\right]$$

$$B = -2\left[\phi_1(L)\phi_2(x-L) - \phi_2(L)\phi_1(x-L)\right]$$

$$\phi_1(x) = \cosh(\tfrac{1}{2}s\sigma\tfrac{x}{L})\cos(\tfrac{1}{2}s\beta\tfrac{x}{L})$$

$$\phi_2(x) = \sinh(\tfrac{1}{2}s\sigma\tfrac{x}{L})\sin(\tfrac{1}{2}s\beta\tfrac{x}{L})$$

$$s = \frac{2L\omega}{C_o} \qquad C_o = (gh_o)^{1/2}$$

$$\sigma = \left[-0.5 + 0.5\left(1 + \frac{f}{\omega}^2\right)^{1/2}\right]^{1/2}$$

$$\beta = \left[0.5 + 0.5\left(1 + \frac{f}{\omega}^2\right)^{1/2}\right]^{1/2}.$$

The numerical model solves equations (6) and (7) with a linear friction for various grid spacings and time steps. The effect of different grid spacings, Δx, on the numerical/analytical comparison was examined (Table 1 and fig. 6). The maximum time step for a particular Δx was determined by the CFL condition. In addition, the size of the time step was varied for one particular value of Δx. Results (Table 1) show that differences

TABLE 1

Expt.	$\frac{\Delta X}{L}$[1]	$\frac{\Delta t}{T}$[2]	$\Delta 1$[3] ($\times 10^{-4}$)	$\Delta 2$[4] ($\times 10^{-4}$)
FDT1	.0125	0.84	3.24	5.62
FDT2	.0250	0.84	4.18	7.78
FDT3	.0500	0.84	6.72	13.34
FDT4	.0500	0.42	6.54	13.12
FDT5	.0500	0.21	6.48	13.00
[5]Numerical experiments	.0357	0.36-0.44		

1. Grid spacing divided by channel length.
2. Time step divided by time scale derived from the Courant condition ($T = \Delta X/\sqrt{gh}$).
3. Rms error over tidal cycle in sea surface for numerical solution compared to analytical solution normalized by tidal amplitude (50 cm) at 0.45 length of the channel.
4. Same as 3. but at 0.9 length of the channel.
5. Values of space and time steps for numerical experiments described later.

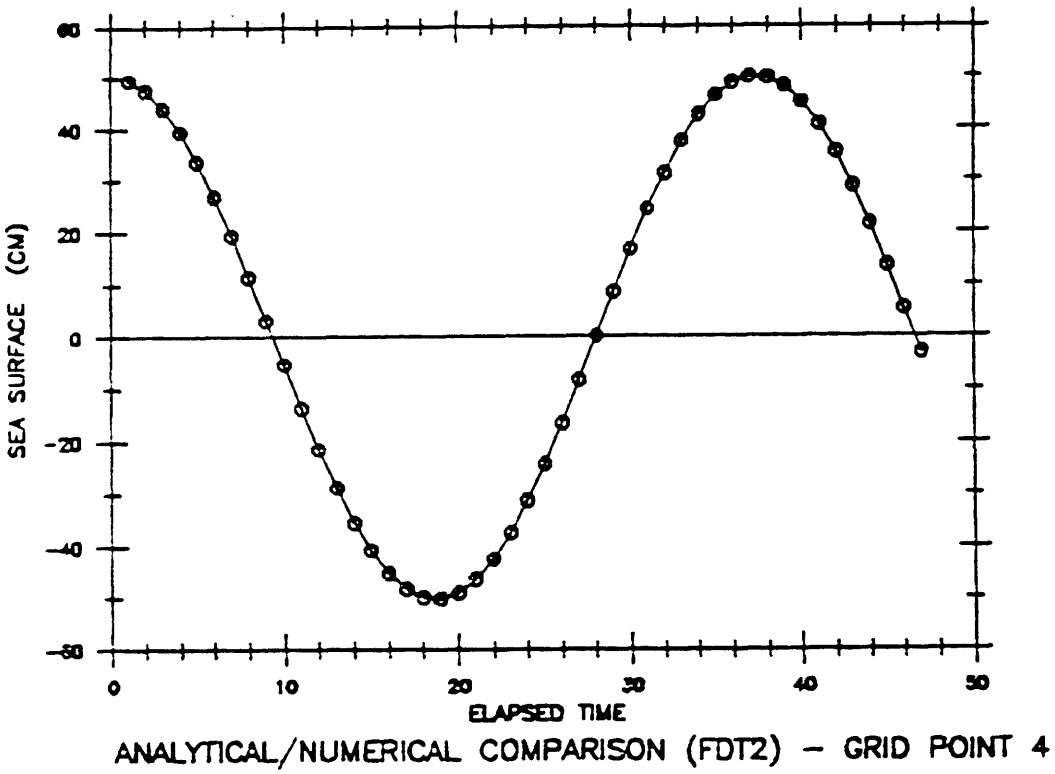

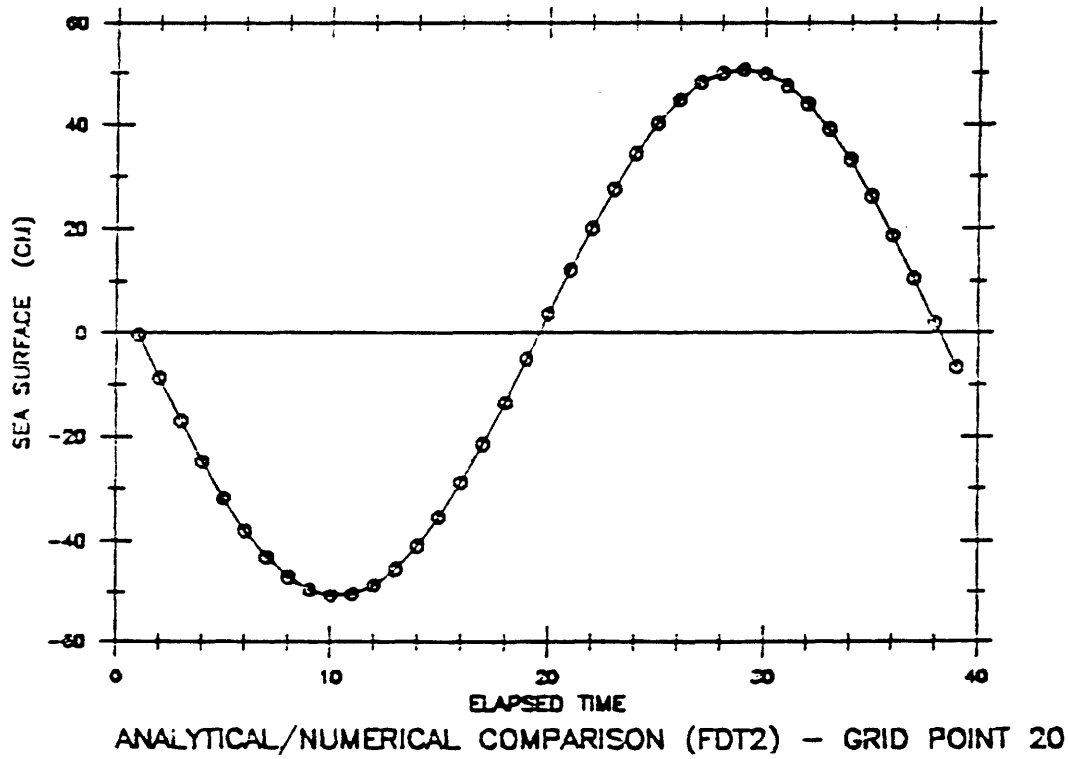

Figure 6. Comparison of linear analytical solution and numerical solution for example FDT2 (see table 1). The comparison is for sea surface at two grid points within the model channel.

between the numerical solution and analytical solution are small for the range of Δx and Δt values examined As can be expected, the numerical/ analytical differences decrease for decreasing Δx (increased spatial resolution of the channel) and, to a lesser extent, for decreasing Δt. A comparison of sea surface at two grid points for one of the examples (FDT2) shows good visual agreement in amplitude and phase (fig. 6). The model runs described subsequently have spatial and temporal resolution (Δx = 250 m, Δt = 15 s.) within the ranges studied in this section.

4. Numerical Experiments

4.1. Introduction

The numerical experiments fall into two general classes:

1) Tidal propagation in channels of constant mean width and depth, both with and without flats.

2) Tidal propagation in channels which represent features of the geometry of two real estuaries.

Each class was examined for the sense of tidal asymmetry, and for the phasing and rate of growth of the first harmonic (M_4).

The first class of numerical experiments is similar in philosophy to a number of analytical efforts which have examined aspects of tidal propagation in channels. Kreiss (1957) noted the occurrence of tidal current time and velocity asymmetries in estuaries. He studied the case of flood currents shorter in duration but reaching greater peak velocity than ebb (flood dominant), and explained this behavior as a result of advectional non-linearities and linear frictional effects. This work was extended by Gallager and Munk (1971) who demonstrated the effects of quadratic friction and an incident tide with many constituents. Quadratic friction introduced

odd harmonics into the solution at second order in a/h. Kabbaj and Le Provost (1980) utilized a complicated analytic decomposition of quadratic friction to include more accurately the effects of friction. These examples are limited to cases of simple constant width and depth rectangular channels, and the ratio $a/h \ll 1$. In fact, as previously discussed, natural estuarine channels tend to have widths which vary with depth. To include this feature, as well as cases where a/h is not constrained to be much less than one (again, a common feature of these estuaries), numerical integration of the equations is necessary.

The second class of experiments adds features characteristic of natural estuarine systems. These experiments compare two inlet/estuarine systems with different tidal responses. The two estuaries are Nauset Inlet, MA (fig. 1b) and Wachapreague Inlet, VA (fig. 1a). Nauset Inlet is characterized by strong harmonic growth, particularly of the M_4 constituent, and an asymmetry favoring longer ebbs than flood (e.g., Aubrey and Speer, 1983). Wachapreague Inlet has much weaker harmonic growth and an asymmetry favoring longer floods (e.g., Byrne et al., 1977; Boon and Byrne, 1981). Each estuary is modeled by an idealized channel which represents its basic geometry. These models are a combination of the features described in the first group of numerical experiments. The trade-off in effects of various geometries on the development of tidal asymmetries can be studied in these cases.

4.2. Parameters Studied in Model Runs

Referring to Figure 5, the following paramenters define the geometry of the problem:

h = total depth
h_2 = mean channel depth
h_1 = channel depth at width b_o
a = tidal amplitude
b_o = width of momentum transporting channel
Δb = difference between width at channel top and bottom
b_t = width of tidal flats at depth h_2
f = friction factor (parameterizes bottom roughness)
L = channel length

Non-dimensional parameters describing the geometry of model runs can be formed from this group. In most cases the channel length is held constant at 7 km, a characteristic length of these estuaries. The importance of non-linear terms in the equations of motion is indicated by the ratio a/h. Characteristic values of this parameter range from 0.1 to 0.5 for the estuaries of interest. An "amplitude dispersive" behavior in shallow water waves with a cascade of energy into harmonics of the fundamental frequency is anticipated for this range of values (e.g., Gallagher and Munk, 1971).

Variability in cross-sectional area and channel width over a tidal cycle is described by the ratios a/h and $\Delta b/b$. This is shown by considering expressions for cross-section and width for the channel depicted in Figure 3. The cross-section, A, and width, b, are given by:

$$A = A_0 + b_o \cdot \zeta \left(1 + \frac{1}{2} \frac{\Delta b}{b_o} \cdot \frac{\zeta}{h_2}\right) \tag{19}$$

A_o = channel area at mean depth h_2

$$b = b_o \left(1 + \frac{\Delta b}{b_o} \cdot \frac{\zeta}{h_2}\right) \tag{20}$$

Strong modulation of both channel area and width for non-rectangular geometries is possible if the ratio $\Delta b/b_o$ is large. No variability occurs in width, of course, for the rectangular case. For the non-rectangular case and a tidal motion given by

$$\zeta = a\cos\omega t,$$

cross-sectional changes will contain both the original frequency and its first harmonic at O(a/h). In fact, for a tidal motion containing many harmonics,

$$\zeta = \sum a_n \cos n\omega t \qquad a_1 >> a_2 >> a_n$$

a large number of interactions are possible, suggesting that time variable geometry may be an important source of harmonic growth. Modulation in channel geometry will have an important effect on both the non-linear continuity term and on the friction term. Because cross-sectional area and channel perimeter change at different rates over a tidal cycle, friction effects may be strongly modulated by geometry. The effects of friction are also dependent on the value of the friction factor used in model runs. Tidal propagation is studied, therefore, for a range of friction factors.

The geometry of the tidal flats is described by the slope of the storage banks,

$$\tan\theta = \Delta h / b_t \quad \text{where } \Delta h = h_2 - h_1$$

As mentioned earlier, the influence of tidal flats is introduced through continuity. Also the parameter (A_f/A_c) comparing the fractional change in the storage area versus momentum transporting portion of the channel describes the channel geometry with tidal flats:

$$\frac{A_f}{A_c} = \left(2 + \frac{a}{\Delta h}\right)\left(\frac{b_o}{b_t}\right)^{-1}$$

Other quantities of interest such as potential tidal prism and mean tidal current can be obtained from the geometric parameters. The potential tidal prism is the volume of water between high and low water the estuary would admit in the absence of tidal decay (or amplification). The reduction of potential tidal prism could be examined instead of the decay in tidal

range. In terms of tidal dynamics, these two points of view are equivalent. The mean current is defined as the potential prism divided by the product of channel cross-sectional area times one-half the tidal period (Swift and Brown, 1983). This quantity is defined assuming the absence of prism reductions (tidal decay) and tidal asymmetry.

In the following sections, the parameters are varied systematically to examine their effects on tidal distortion in the model channel. The role of channel geometry in producing distorted tides is explored by varying the ratios $\Delta b/b_o$ and a/h. Models with the same geometry are run with different values of the friction factor. Finally the effects of variable tidal flat area relative to channel area are studied.

4.3. Constant Mean Width/Depth Problems

4.3.1. Physical Considerations

Two types of geometry are considered in this section: channels with and without tidal flats. Harmonic growth depends on the balance between energy extracted from the fundamental frequency by non-linear friction, advection and continuity and the energy lost by friction. These problems have both a linearly decreasing potential prism and mean velocity down-channel because of the no-flow interior boundary condition (fig. 7). For these geometries, friction and advection of momentum will be strongest near the forcing boundary. Non-linear advection which scales with the channel length, L, will be relatively unimportant as an M_4 generation mechanism compared to friction in the model runs. In contrast to friction and advection, non-linear continuity will show only a slow decline (if any) down-channel. Near the interior boundary little change occurs in the growth of harmonics in sea surface and harmonics in velocity decrease to zero. Model runs reach an "equilibrium" phase relationship between M_2 and M_4 in both

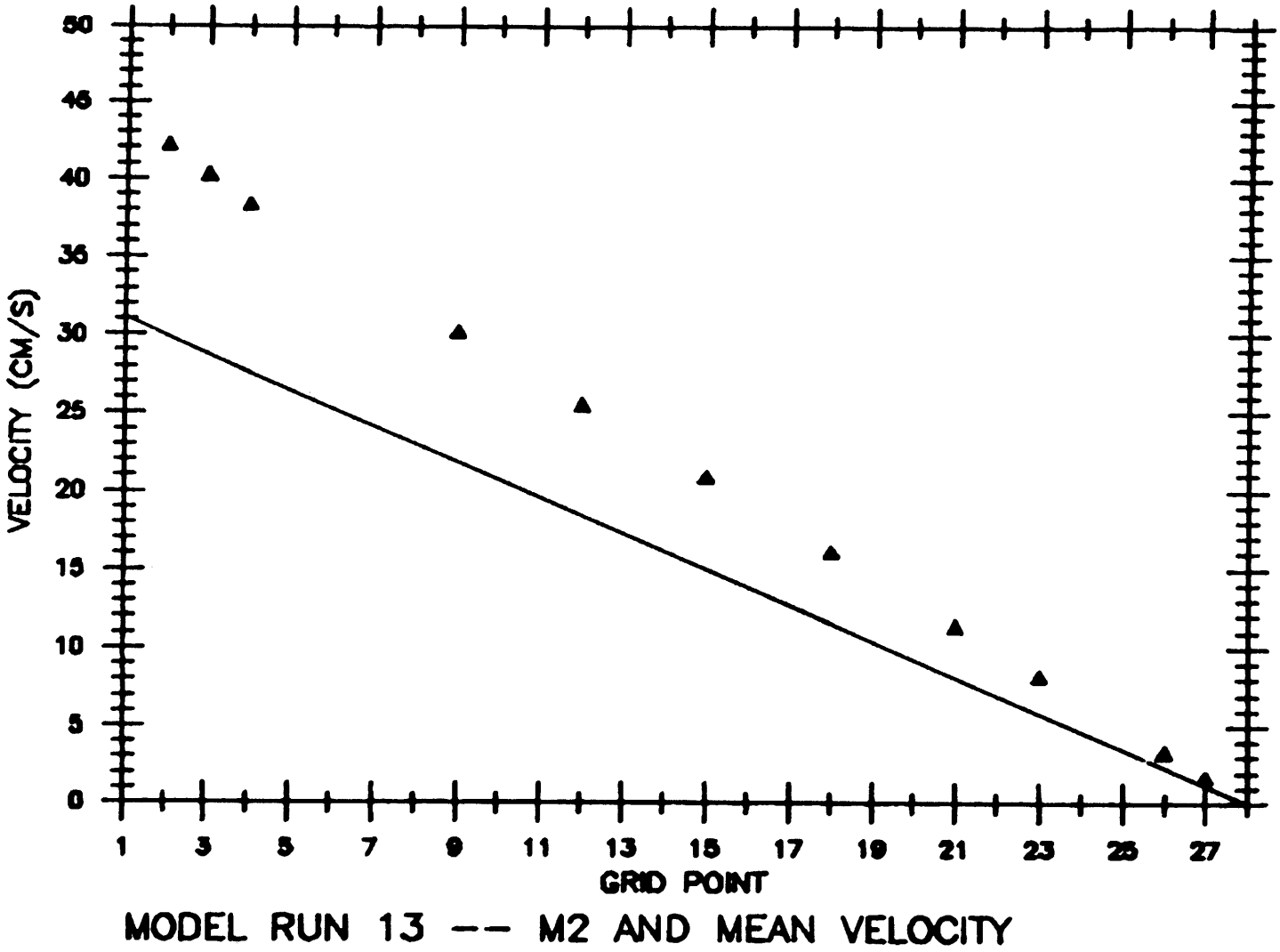

Figure 7. Comparison of mean velocity (calculated from potential prism) and M_2 velocity (calculated from model run) for numerical experiment 13.

sea surface and velocity (or transport) which is determined by the geometry and frictional characteristics of the channel. A representative model run (fig. 8) shows rapid adjustment in sea surface M_2-M_4 phase ϕ_ζ, near the forcing boundary followed by more gradual changes near the interior boundary. The ratio of sea surface M_4 to M_2 amplitude, $(M_4/M_2)_\zeta$, also increases rapidly near the forcing boundary before leveling off near the interior boundary.

Differences exist between the model behavior described above and that of natural estuarine channels. Cross-sectional area can vary widely along real channels producing large velocities well within the estuary. As a result, friction and advection will not necessarily show the monotonic downchannel decline exhibited by the models. The advective term, although relatively unimportant in the models, can become locally significant in natural channels due to rapid changes in geometry (e.g., flow around bends, sudden channel expansions). It can, in fact, dominate over friction as an M_4 generation mechanism in deeper channels with different geometries than those under consideration. Pingree and Maddock (1978) have shown, for example, that the advective term is more important that friction for M_4 generation in the English channel.

4.3.2. Numerical Experiments: channels without tidal flats

These experiments are organized in terms of increasingly time variable channel cross-sectional area as shown by the parameter, $a/h \cdot \Delta b/b_o$ (Table 2). This non-dimensional parameter is strictly geometrical, indicating how variable the channel cross-section area is over a tidal cycle. Since channel area enters into dynamical terms and the non-linear continuity term, a large value of this parameter can indicate the possibility of a

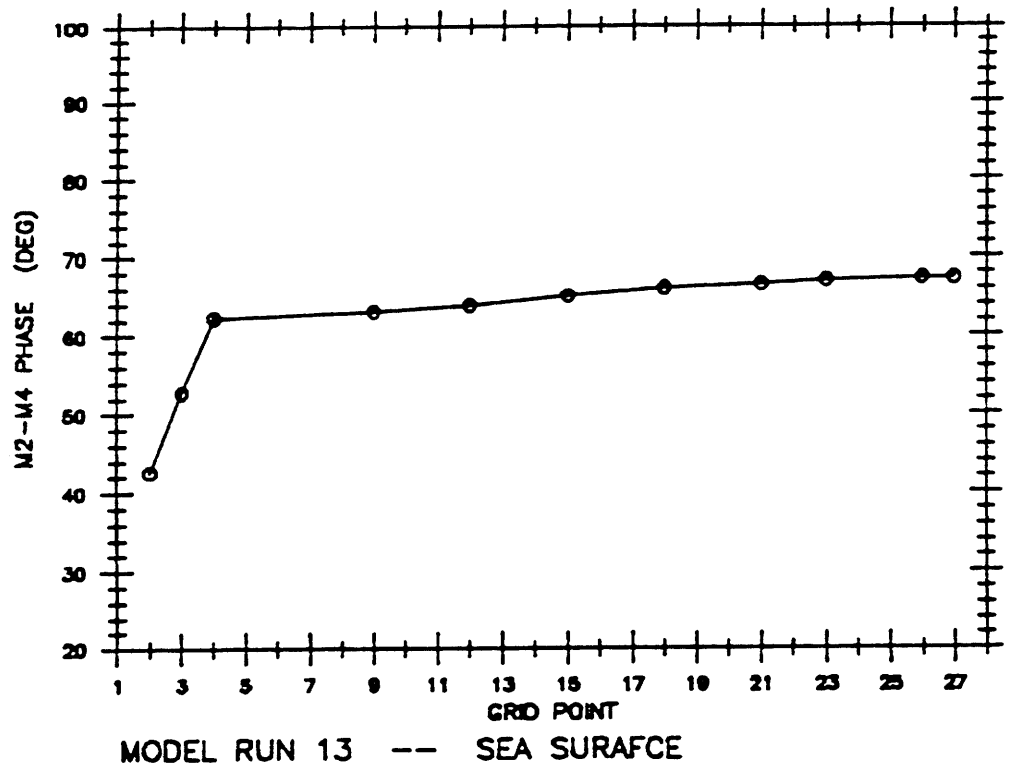

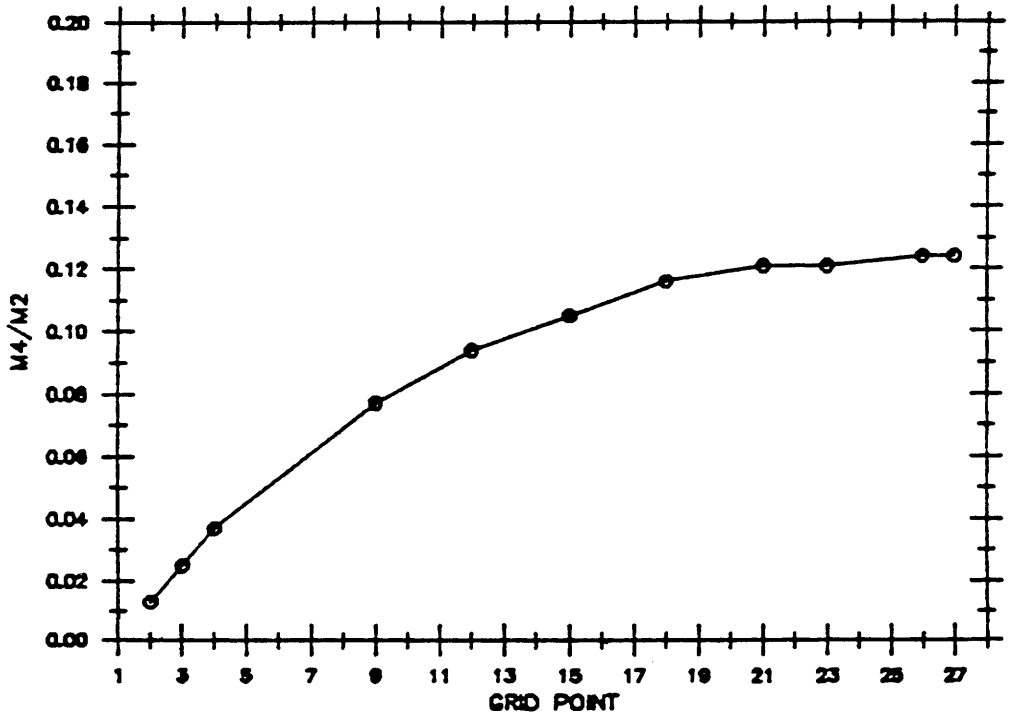

Figure 8. Typical pattern of M_4 growth in sea surface and relative M_2-M_4 phase in sea surface for a numerical experiment without tidal flats. Note the rapid phase adjustment within the first five grid points.

TABLE 2

Expt.	a/h	$\Delta b/b_o$	$a/h \cdot \Delta b/b_o$	f	M_4/M_2 [1]	M_4/M_2 [2]	ϕ_ζ [3]	ϕ_u [4]	%ΔH [5]
10B	.22	0	--	.0200	.005	.016	92	75	0
10	.32	0	--	.0200	.019	.065	81	50	0
10A	.32	0	--	.0020	.002	.010	117	84	0
10C	.39	0	--	.0200	.019	.065	79	55	0
10D	.46	0	--	.0200	.027	.092	74	48	0
22	.32	.20	.06	.0200	.021	.073	76	42	1
24	.32	.27	.09	.0200	.022	.076	75	38	1
24A	.32	.27	.09	.0100	.013	.046	85	59	0
24B	.32	.48	.15	.0200	.026	.093	72	26	4
13G	.20	.75	.15	.0200	.009	.031	85	56	0
13B	.26	.75	.20	.0200	.021	.074	78	31	3
13	.32	.75	.24	.0200	.037	.124	68	11	10
13E	.32	.75	.24	.0100	.026	.092	75	29	3
13F	.32	.75	.24	.0020	.008	.026	101	73	0
13A	.32	.87	.28	.0200	.044	.140	65	4	16
13C	.39	.75	.29	.0200	.040	.132	70	17	8
13D	.32	.94	.30	.0200	.050	.150	65	2	19
13I	.32	.94	.30	.0020	.014	.047	93	62	0
13J	.43	.75	.32	.0200	.056	.168	64	3	7

1. Sea surface amplitude ratio at grid point 4.
2. Sea surface amplitude ratio at grid point 26.
3. Sea surface M_2-M_4 relative phase at grid point 26.
4. Velocity M_2-M_4 relative phase at grid point 26.
5. % decline in tidal range at grid point 28.

strongly non-linear tidal response. It is not, however, a fundamental measure of the non-linearity of the long wave (or shallow water) equations. This is provided by the ratio of wave particle velocity, u, to wave phase velocity, c. For the case of long waves, this ratio equals a/h, the non-dimensional wave amplitude. The condition of linearity for long waves requires that $u/c \ll 1$. If the ratio is small, a large value of $\Delta b/b_o$ will have no impact on the non-linear development of the tide. Because a/h is large for these examples, channel geometry will influence the tidal response.

All these model runs produced time asymmetries characterized by a longer falling than rising tide. The maximum time asymmetry of this type for a given ratio, $(M_4/M_2)_\zeta$, is produced by an M_2-M_4 relative phase, ϕ_ζ, of + 90°. As can be seen in Table 2, ϕ_ζ ranges approximately 30° on either side of 90°. The sense of time asymmetry is determined by the M_2-M_4 phase and the magnitude, by the M_4/M_2 ratio. Results from the experiments show $(M_4/M_2)_\zeta$ depends strongly on geometry and friction characteristics of the channel. In general, more time-variable geometry and stronger friction produce larger M_4/M_2 ratios. The increase in this ratio is dominated by growth in M_4 as opposed to decrease in M_2.

These numerical examples also produce little decline in tidal range except for the cases of strongly time-variable channel cross-section area (e.g., experiments 13, 13A, 13D). This behavior is expected considering the linear problem (fig. 9). The linear solution shows friction in a rectangular channel is not effective in reducing tidal amplitude over short channel length scales. Modeling the large amplitude decay often seen in natural systems, therefore, requires a reasonable representation of channel geometry.

Mean velocity exhibits more variability in M_2-M_4 phase than does sea surface. If M_4 is in phase with M_2 in velocity, ($\phi_u \simeq 0°$), the case of short, strong floods versus long, slow ebbs occurs (e.g., experiments 13A, 13D). From a strict continuity argument, this situation results when falling tide exceeds rising tide in duration. The experiments approximating this particular phase relationship are characterized by strong friction and time variable channel geometry. In general, the experiments summarized in Table 2 show a tendency towards higher velocity floods than ebbs moving downchannel.

The tidal harmonic signature in velocity is more complicated than sea surface and hence is not summarized in Table 2. All cases showed greater harmonic growth in velocity than in sea surface (i.e., larger M_4/M_2 etc. ratios). Experiment 13 (fig. 10) shows that whereas M_4 steadily grows in amplitude for sea surface, it first increases and then declines in mean velocity. Initially, non-linear processes pump more energy into this harmonic than is removed by friction. Eventually, frictional effects and the constraint on velocity imposed by the interior boundary condition reduce its amplitude. The increase in $(M_4/M_2)_u$ is initially a result of both decay of M_2 and growth of M_4. Note also that higher harmonics in velocity (e.g., M_6, M_8) decline before M_4 begins losing energy.

The effect of channel geometry on sea surface response is clarified by three experiments (fig. 11) shown in order of increasingly trapezoidal geometry (i.e., larger cross-sectional variability over a tidal cycle). Each experiment has the same friction factor and tidal forcing (a/h = 0.32). Sea surface becomes increasingly non-linear as channel cross-sectional area becomes more time-variable. Both frictional effects and flow-geometry interactions produce this reult. Cross-sectional area contains a second

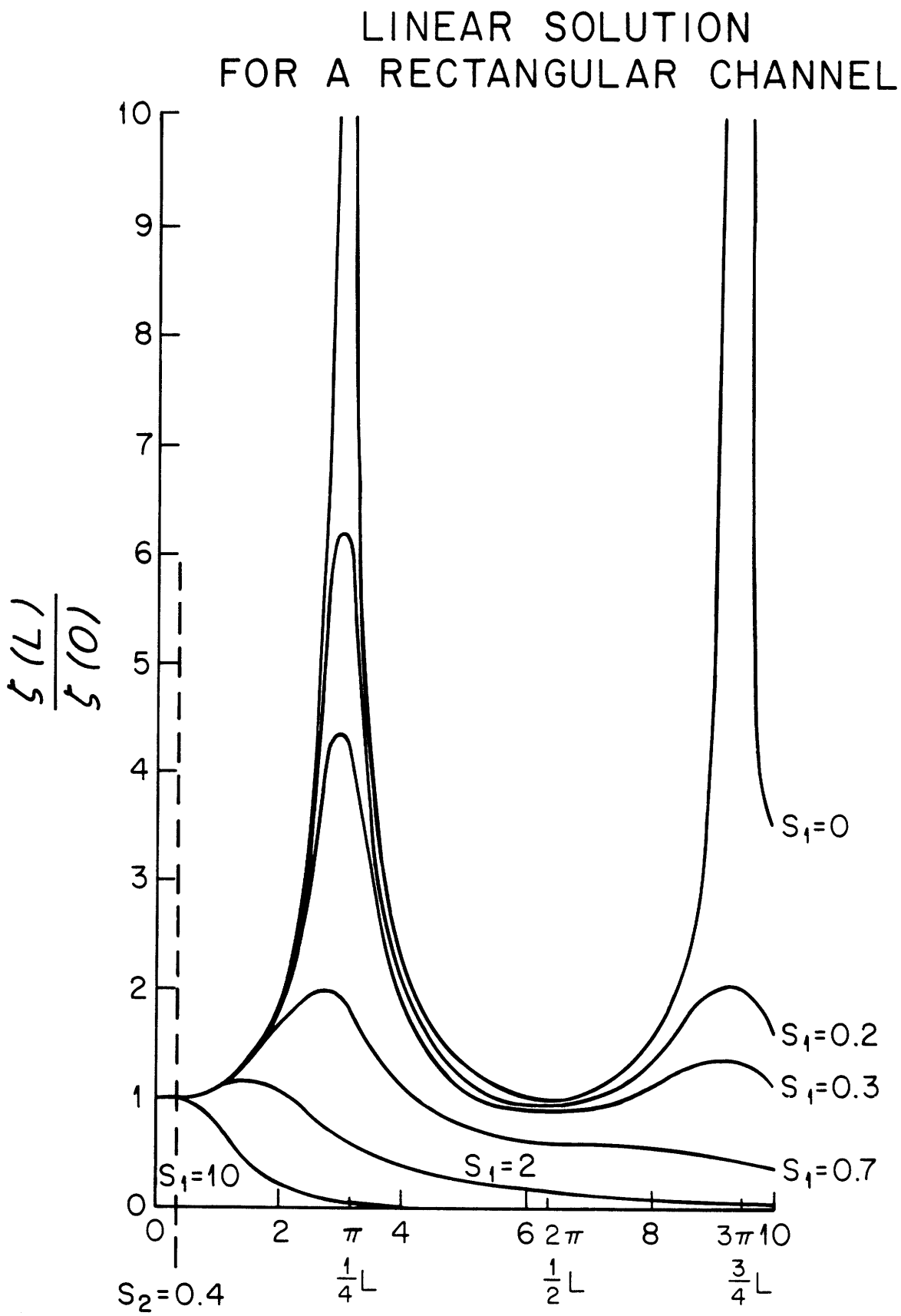

Figure 9. Linear analytic solution for tidal propagation in a rectangular channel (equation 18). The vertical axis represents sea surface amplitude at interior boundary normalized by the amplitude at the open boundary. S_2 is a non-dimensional channel length (=2kL). S_1 is a non-dimensional friction measure (=fT/2). The channel length scale for the model runs is marked as a dotted line.

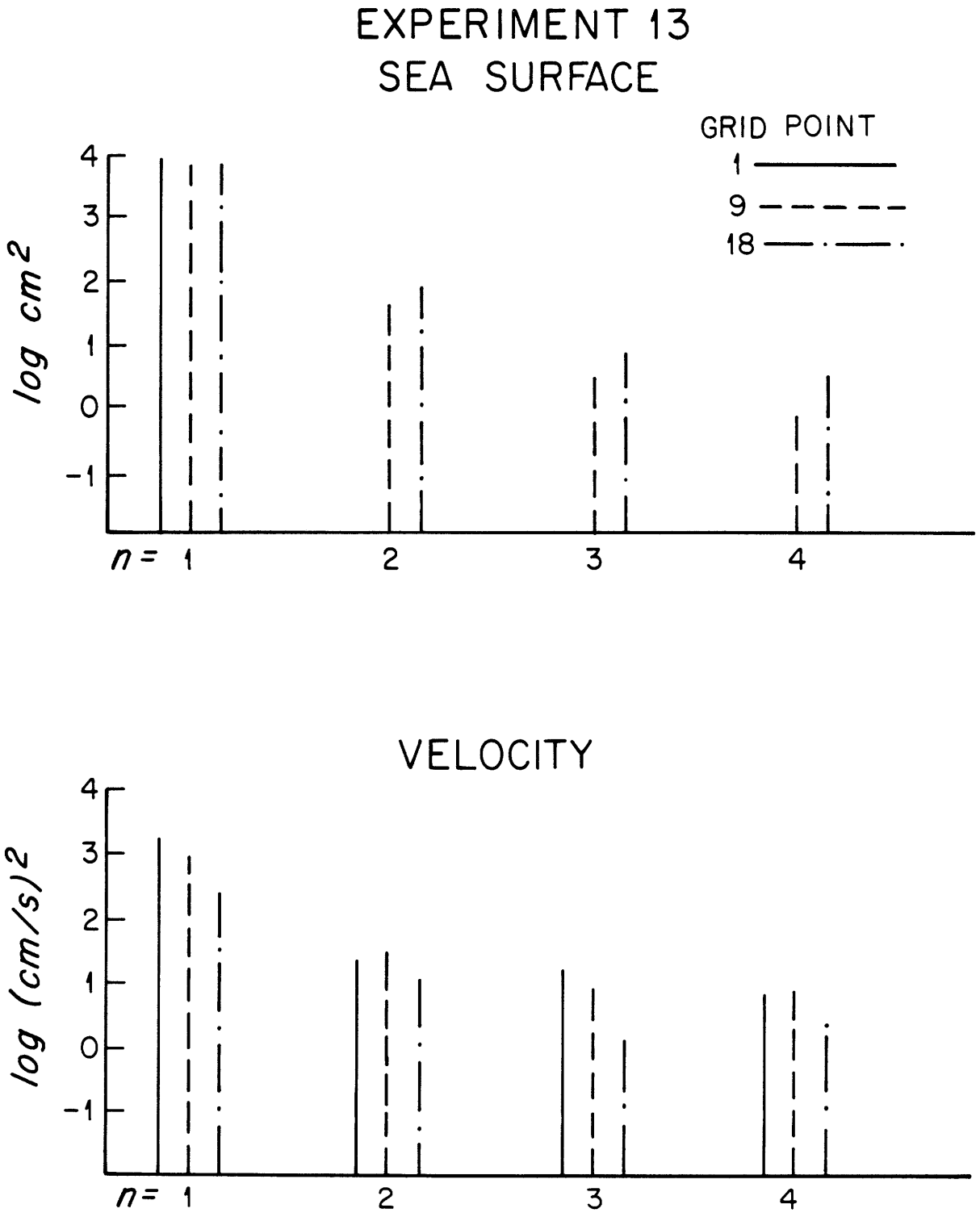

Figure 10. Periodogram derived from harmonic analysis of numerical solution for model run 13. Top panel is sea surface at three grid points, bottom is velocity at the same points. The numbers along the horizontal axis refer to M_2 and its harmonics (i.e. 1=M_2; 2=M_4; 3=M_6; 4=M_8).

harmonic term (equation 19) and width a first harmonic when the channel geometry is a trapezoid. The magnitude of these terms increases as $\Delta b/b_o$ increases. Also, velocity tends to be higher in the trapezoidal cases as a result of the way tidal prism and channel cross-sectional area combine. A calculation of the potential prism and mean velocity (as defined previously) for two of the cases (Table 3) illustrates the point. Higher velocities lead to larger values of friction (assuming f = constant) and hence more harmonic growth. The phase relationship between M_2 and M_4 in each case leads to falling tide exceeding rising tide in duration with the asymmetry increasing downchannel. The distortion of the tide at the model's interior boundary for three examples (fig. 12) shows the following: (i) the duration of rising tide decreases with increasing $\Delta b/b_o$; [For experiment 10, rising tide lasts 5 hr 40 m (fall: 6 hr 45 m), whereas for experiment 13D, the duration of rise is 5 hr 10 m (fall: 7 h 15 m). The latter value is comparable to time asymmetries observed in the field (e.g., Nauset Inlet, Aubrey and Speer, 1983a)]; (ii) the reduction in tidal range associated with increasingly trapezoidal geometry; and (iii) the tendency towards a small set up (tidally-averaged) in sea surface with increasingly trapezoidal geometry. This non-linear behavior has been noted before in channel models by Gallagher and Munk (1971) and is in accordance with the concept of a radiation stress (Longuet-Higgins and Stewart, 1964). The greater the dissipation of the tide, the larger the set-up in mean sea level at the channel interior boundary.

Since channel cross-sectional variability over a tidal cycle is also a function of a/h, increasing this ratio will lead to a more distorted tide. Sea surface line spectra for three different values of a/h (fig. 13) in cases where $\Delta b/b$ was held constant show enhanced non-linear transfers to

TABLE 3

POTENTIAL PRISM/MEAN VELOCITY

Expt.	potential prism[1] ($\times 10^6 m^3$)	grid point	mean velocity[2] (m/s)	M_2 velocity[3] (m/s)
Experiments without flats				
10	1.26			
		4	0.17	0.27
		12	0.12	0.18
13D	2.02			
		4	0.32	0.40
		12	0.22	0.26
Experiments with flats				
11	4.06			
		4	0.63	0.58
		18	0.23	0.23
14	4.72			
		4	0.63	0.55
		18	0.26	0.22

1. Potential prism (defined in text).
2. Mean velocity (defined in text).
3. M_2 velocity calculated from model run.

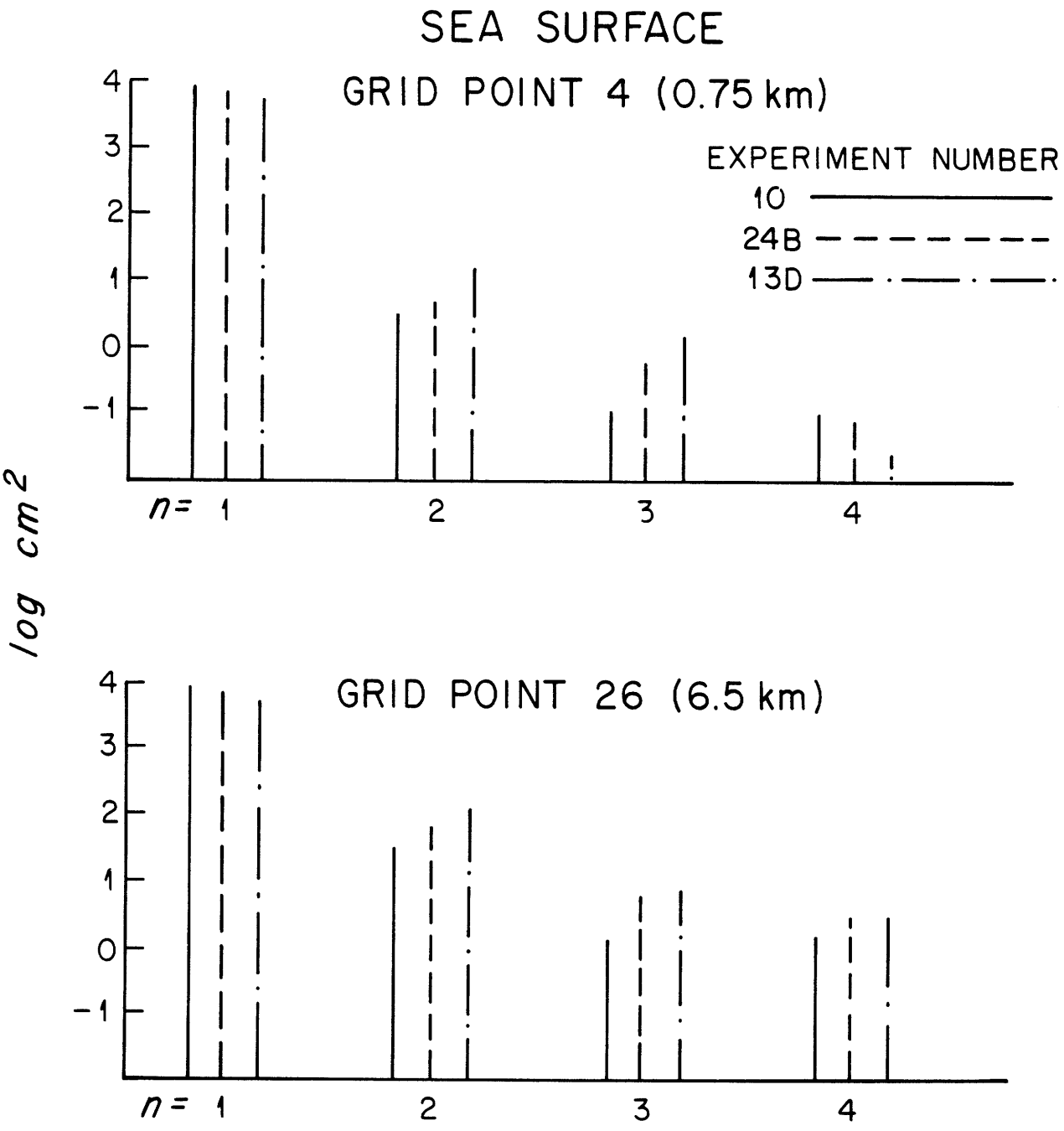

Figure 11. Periodogram of sea surface for three model runs at two different grid points. These experiments illustrate the effect of channel geometry on sea surface tidal distortion.

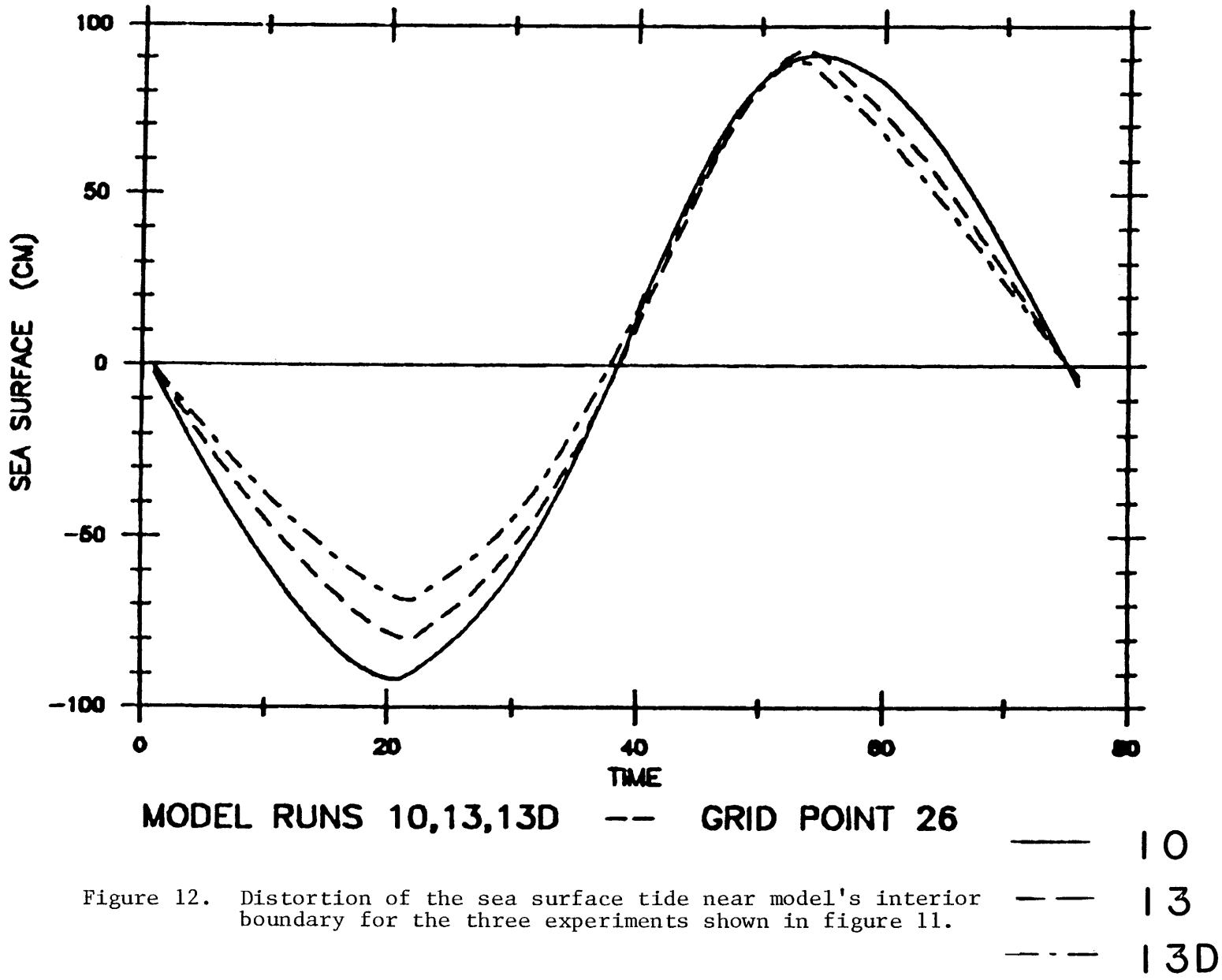

Figure 12. Distortion of the sea surface tide near model's interior boundary for the three experiments shown in figure 11.

all harmonics of M_2 as a/h increases. Experiment 13J had a larger tidal amplitude than the other two cases in which the ratio was increased by decreasing the mean depth. Similar to the geometry parameter $\Delta b/b_o$, larger values of a/h lead to stronger harmonics in cross-sectional area and width (equations 19, 20). As mentioned previously, it also indicates the importance of non-linear terms in the equations of motion. Finally, changing values of the parameter result in changes in mean velocity. This leads to increases in the magnitude of the advective term and particularly in friction. The first two examples admit approximately the same potential prism; however, mean cross-sectional areas decrease from 13G to 13. Mean channel velocities are larger in 13 than 13G, and more tidal distortion occurs in the former than the latter case. Experiment 13J admits a larger prism than the others and also has larger velocities. Comparing the results of experiments 24B and 13G (Table 2) emphasizes that a/h is the fundamental indicator of non-linearity in estuarine tidal response. The two experiments have approximately the same value of the geometry parameter, $a/h \cdot \Delta b/b_o$, however experiment 24B has the larger a/h ratio and the more non-linear tide. Channel geometry effects are only important if a/h is sufficiently large.

Most of the experiments were run with friction factors of $0(10^{-2})$. Numerical models of shelf and shallow sea circulation commonly use a coefficient of $0(10^{-3})$ (e.g. Flather and Heaps, 1975; Beardsley and Haidvogel, 1981), although this value is too low if surface gravity waves are present (Grant and Madsen, 1979). Estimates of friction factors in shallow estuaries with strong tidal flows, large bedforms and high sediment transport rates are of the order 10^{-2} (e.g., Swift and Brown, 1983; Aubrey and Speer, in prep.). Results of experiments with 3 values of f (.002,.02,.04), and the same geometry and forcing (fig. 14) show the effect of variable f. Friction

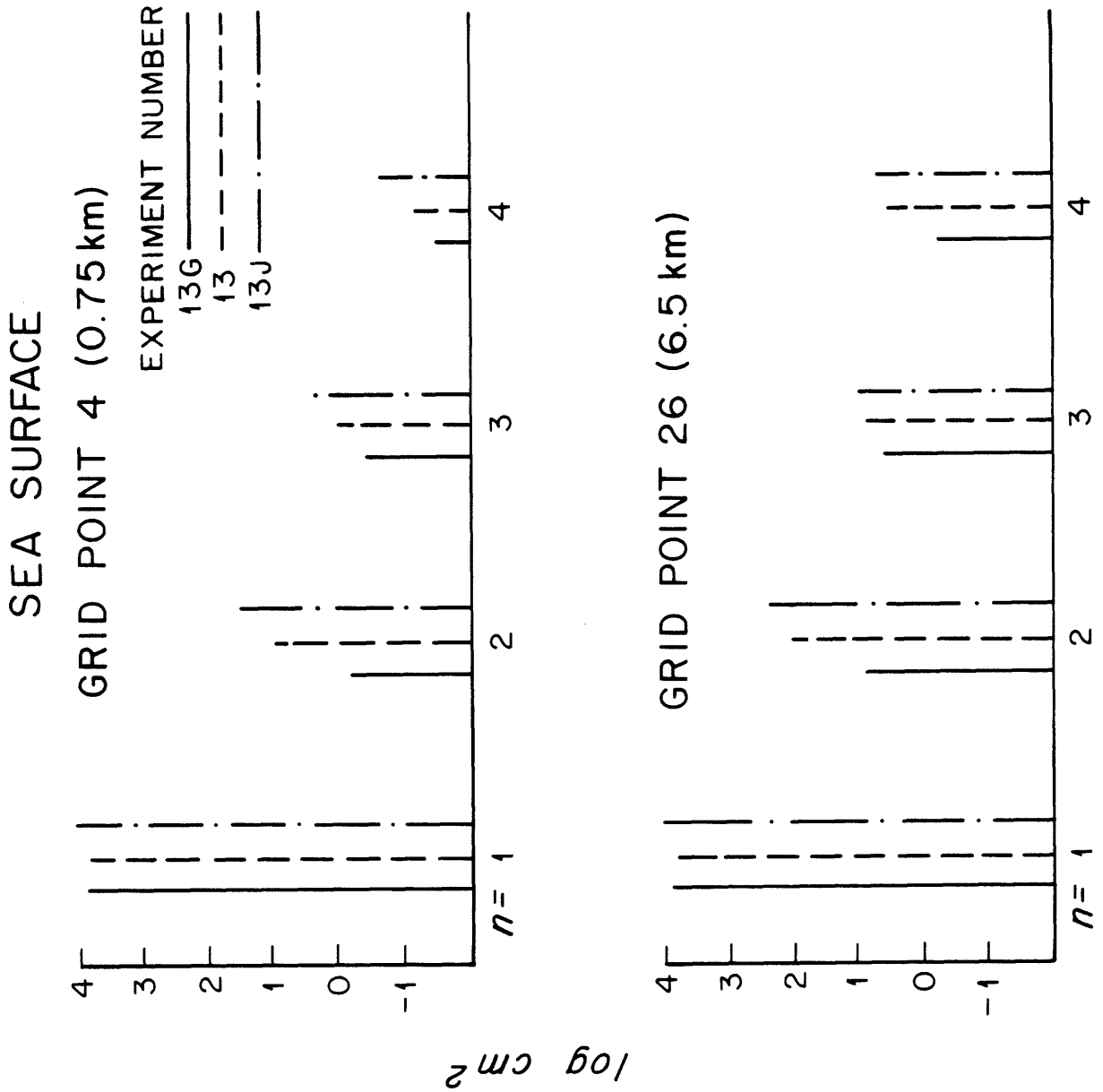

Figure 13. Periodogram of sea surface for three model runs at two different grid points. These experiments show the effect of increasing the parameter, a/h, on sea surface tidal distortion.

factors of $1\text{-}2\text{x}10^{-3}$ (commonly stated values) are too low for these systems when strong tidal flows are present. This level of friction does not produce any tidal decay and also causes negligible harmonic growth.

It has been stated that quadratic friction produces only odd harmonics (i.e., M_6) and that even harmonics (i.e., M_4) are produced by non-linear continuity and advection (e.g., Hamilton, 1977). Analytical models employing perturbation schemes to include quadratic friction find odd harmonics generated by friction to second order in non-dimensional wave amplitude when a time-invariant friction factor is used (e.g., Gallagher and Munk, 1971; Kabbaj and Le Provost, 1980):

$$\bar{U} = \varepsilon\cos\omega t \tag{21a}$$

$$\bar{U}|\bar{U}| = \tfrac{8}{3\pi}\,\varepsilon^2\,\{\cos\omega t + \tfrac{1}{5}\cos 3\omega t - \ldots\ldots\} \tag{21b}$$

where ε represents a non-dimensional measure of current amplitude. Higher order interactions (i.e., $0(\varepsilon^3)$) between the fundamental frequency and its harmonics are not calculated in analytical models. In fact, as Gallagher and Munk (1971) point out, the even harmonics can be modified considerably by higher order frictional interactions. The numerical results presented here and those of other numerical experiments (e.g., Pingree and Maddock, 1978; Prandle, 1980) show the importance of friction in generating both even and odd harmonics. This is important because even harmonics (M_4) produce the time asymmetries. Distortion of the tide at the model's interior boundary as a function of friction (fig. 15) shows a pattern similar to that produced by increasing the magnitude of the geometry parameter. Although increasing friction from .02 to .04 produces a more non-linear tidal response, it also leads to a decrease in the energy of the harmonics and a stronger attenuation of M_2 (fig. 14).

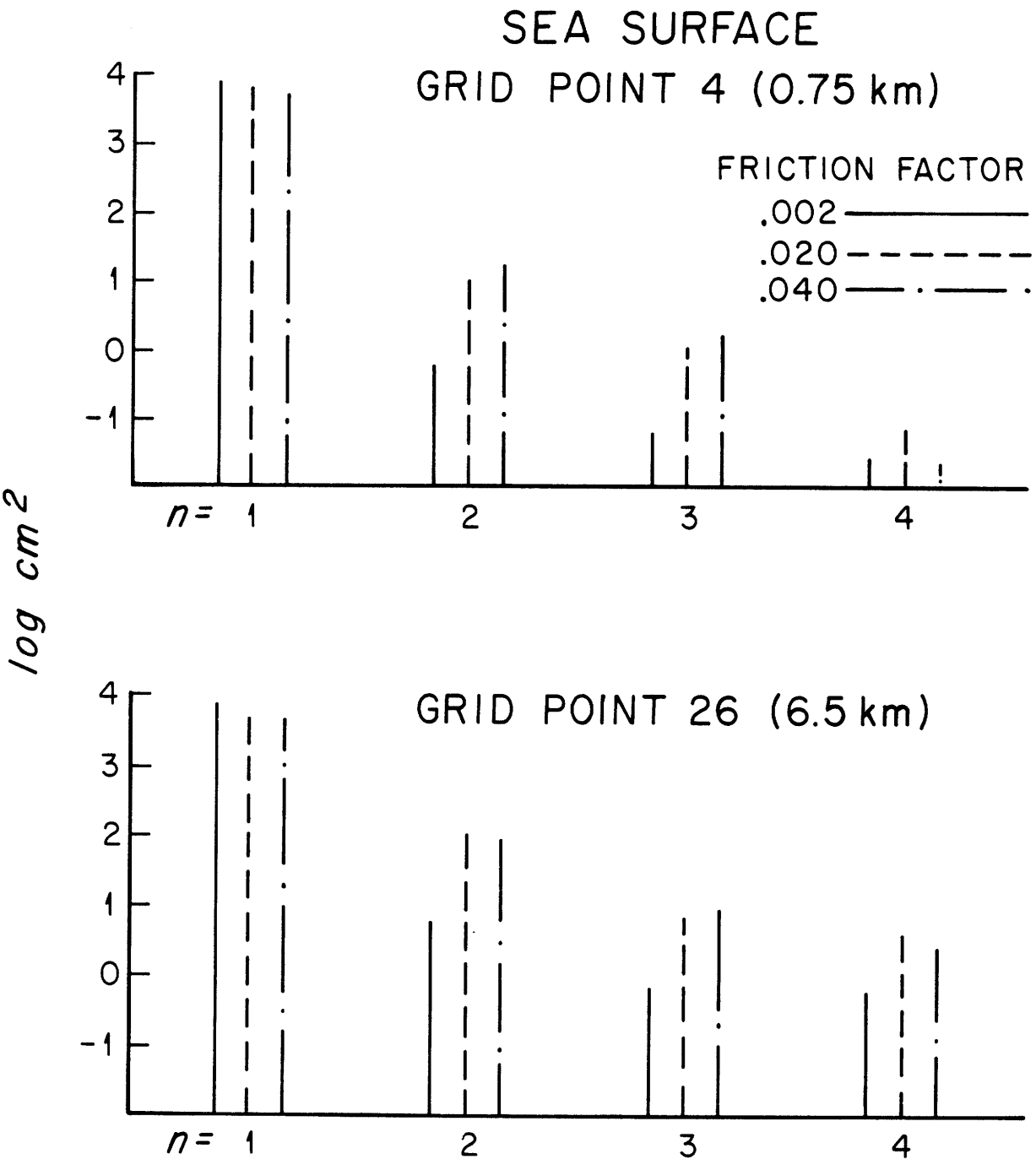

Figure 14. Periodogram of sea surface for three model runs illustrating the effect of increasing the friction factor on tidal distortion.

As stated previously, the mean velocity signal is more non-linear than sea surface in all these experiments (e.g., fig. 10). Friction and advection act directly on velocity to produce harmonics of M_2. Conceptually, the harmonic growth is transferred to sea surface via the term, $\frac{1}{b} \frac{\partial A \cdot \bar{U}}{\partial x}$. Since b has a constant term and oscillates dominantly at the M_2 frequency (equation 20), the effect of this term is to decrease the contribution of the higher frequencies in sea surface relative to mean velocity or transport. This is illustrated as follows:

$$\frac{1}{b} \frac{\partial}{\partial x} A \cdot \bar{U} = \frac{1}{b} \frac{\partial}{\partial x} U$$

with,

$$b = b_o + b_1 \cos(\omega t - \phi_1)$$

$$U = U_1 \cos(\omega t - \phi_2) + U_2 \cos(2\omega t - \phi_3)$$

$$\frac{1}{b} \frac{\partial U}{\partial X} = \frac{U_{1x}+U_{2x} + \ldots}{b_o+b_1}$$

$$= \frac{1}{b_o}(U_{1x}+U_{2x} + \ldots .)(1-\frac{b_1}{b_o}+. \ldots .)$$

Collecting terms of frequency ω,

$$\frac{U_{1x}}{b_o} \qquad (22a)$$

and terms of frequency 2ω,

$$\frac{U_{2x}}{b_o} - U_{1x} \cdot \frac{b_1}{b_o^2} \qquad (22b)$$

values from experiment 13 show that whereas the ratio of U_2/U_1 equals 0.27, the ratio of the 2^{nd} and 1^{st} harmonics of the continuity term (equations 22b, 22a) is approximately 0.13. The pattern in experiment 13 is similar to the others and shows that tidal distortion in velocity is stronger than sea surface.

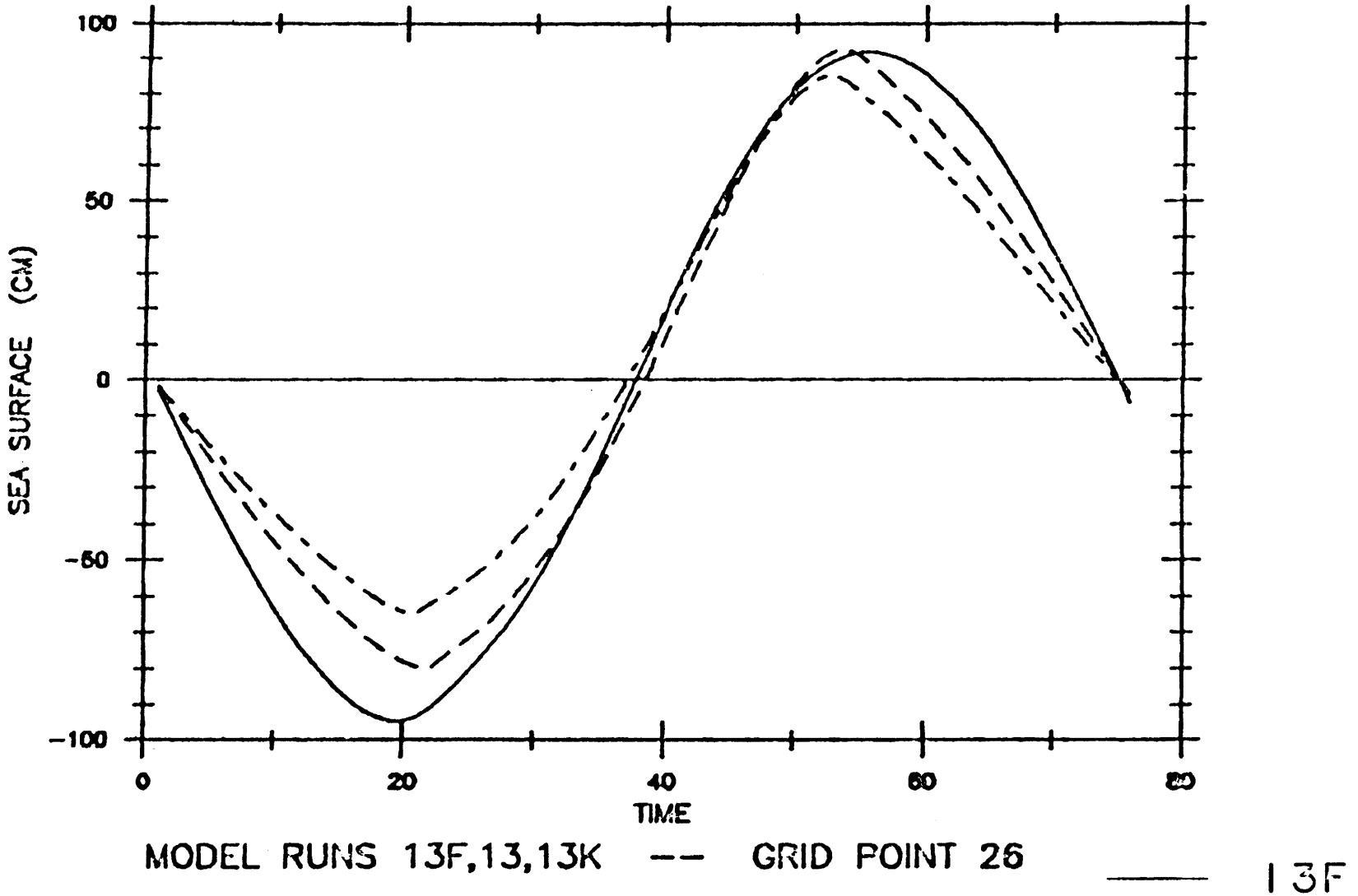

Figure 15. Distortion of the surface tide near the model's interior boundary as a function of friction for the experiments shown in figure 14. Experiment 13F has f=.002; 13 has f=.02; 13K has f=.04.

Similar to sea surface, increased channel cross-section variability, non-dimensional tidal forcing and friction lead to an increasingly distorted mean velocity signal. As the friction factor increases, ϕ_u shifts towards zero degrees (table 2). This phase relationship also requires strongly time-variable channel cross-sectional area (table 2). Increasing the geometry parameter, $a/h \cdot \Delta b/b_o$, while keeping friction constant increases the magnitude asymmetry and the duration of ebb (fig. 16). Note that velocity is non-dimensionalized by the maximum velocity developed in the model run. The experiments with a phase, ϕ_u, approximately zero are also the ones characterized by the strongest harmonic growth in sea surface and longest falling tides.

Three experiments (24,13,13D) were studied in more detail to examine the development of tidal asymmetries (tables 4, 5). These experiments focus on the effects of geometry (with strong friction) in producing tidal asymmetry. The tidal momentum balance is dominated by pressure gradient and bottom friction (fig. 17). Advection of momentum is not an important component of the balance and the temporal derivative is only important during the turn of the tide. This particular balance is characteritic of all the numerical experiments.

Non-linear terms in the equations of motion were Fourier analysed to provide phase and amplitude information. The form of the terms analysed in this section are (Appendix I):

$$f|\bar{U}|\bar{U} \cdot \left(\frac{P}{A}\right) \qquad \text{(friction)}$$

$$\frac{\partial}{\partial x}\bar{U}^2 \qquad \text{(advection)}$$

$$\frac{1}{b}\frac{\partial}{\partial x} A \cdot \bar{U} \qquad \text{(continuity)}$$

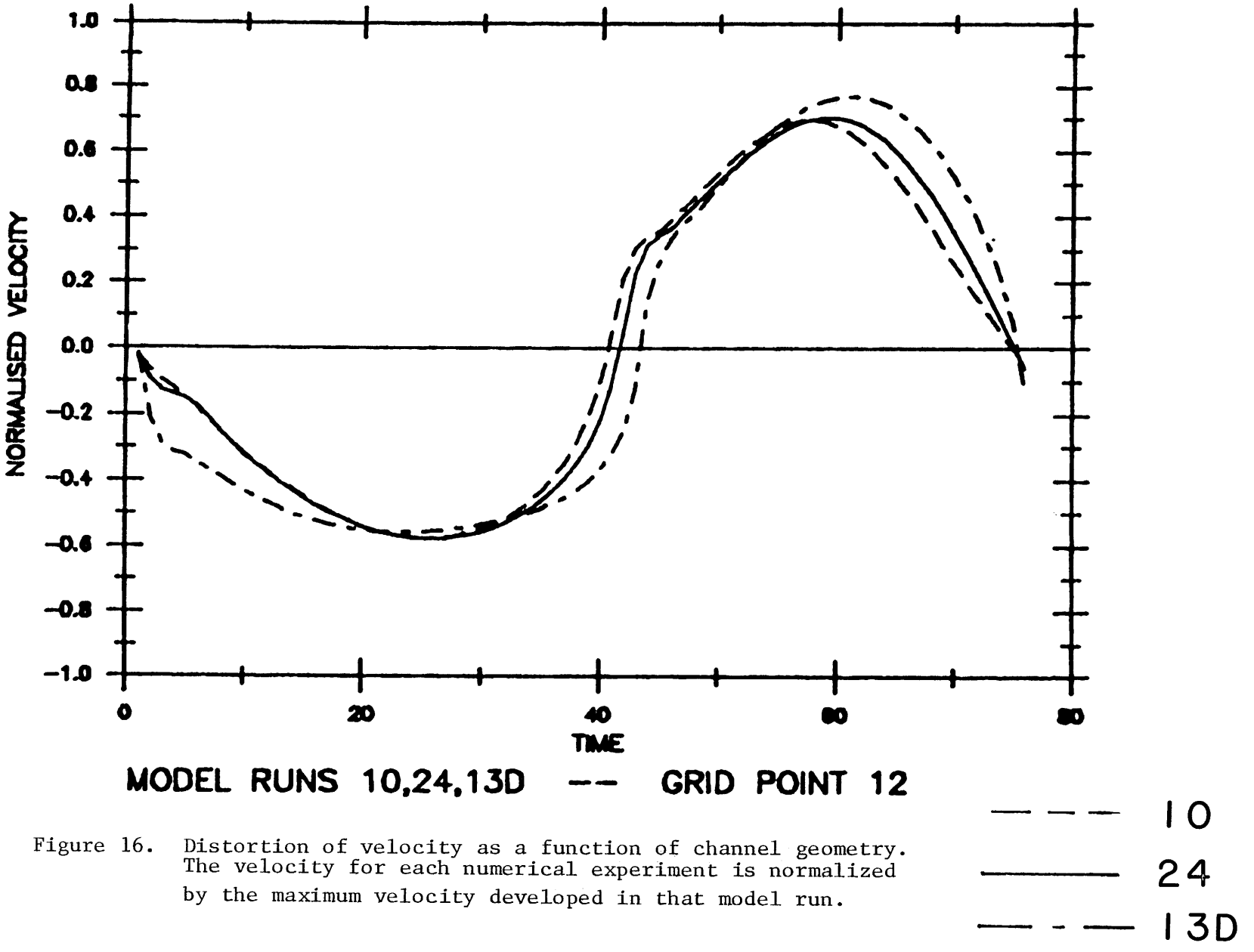

Figure 16. Distortion of velocity as a function of channel geometry. The velocity for each numerical experiment is normalized by the maximum velocity developed in that model run.

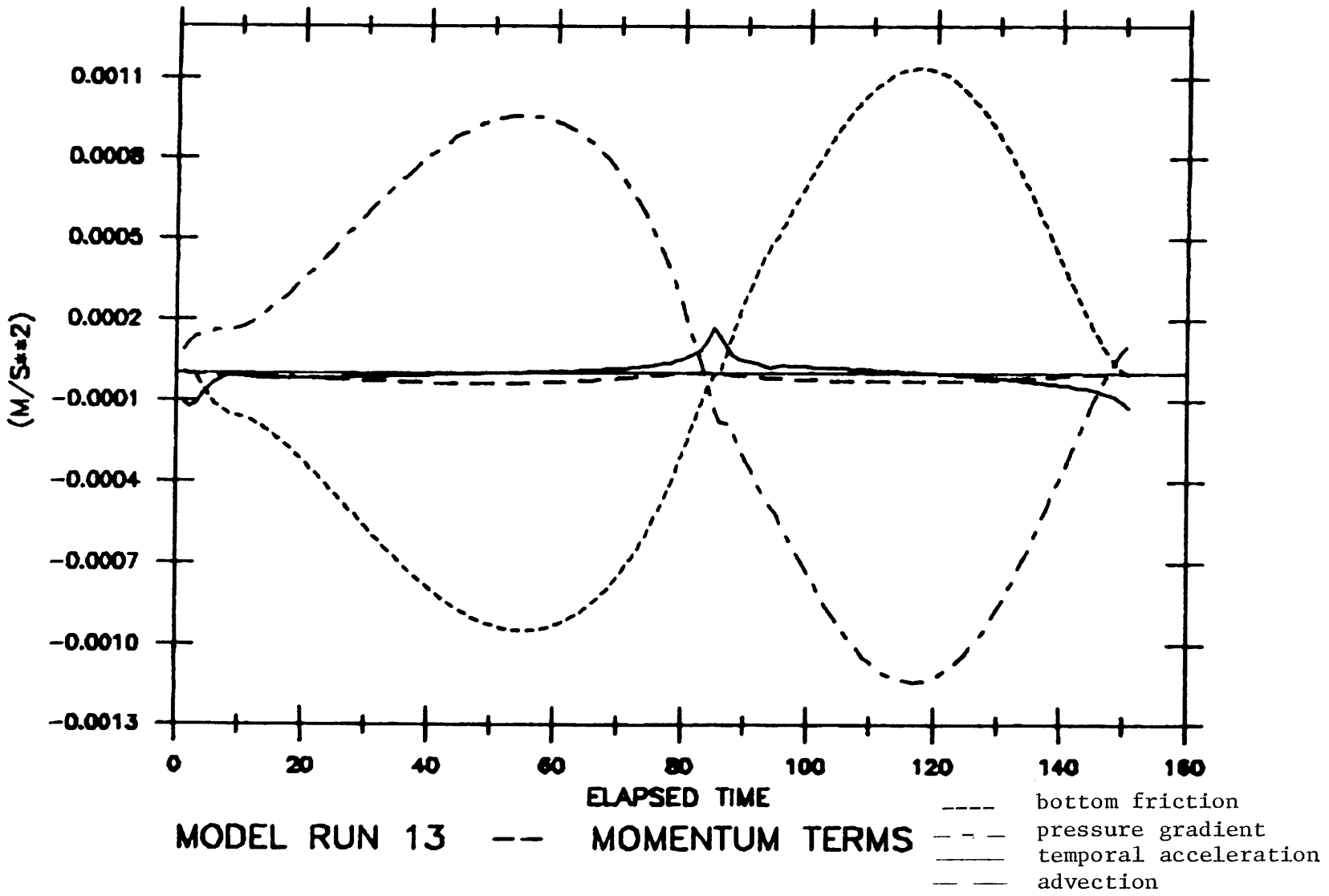

Figure 17. Tidal momentum balance for experiment 13 at grid point 6.

TABLE 4

FRICTION TERM

Expt.	Grid Location	km	$M_2(m/s^2)$	M_4/M_2	Relative Phase $M_2-M_4(°)$
24	2	0.5	8.35×10^{-4}	.294	90
	4	1.0	7.07×10^{-4}	.294	83
	12	3.0	3.16×10^{-4}	.311	66
	18	4.5	1.25×10^{-4}	.321	61
13	2	0.5	1.76×10^{-3}	.220	104
	4	1.0	1.43×10^{-3}	.206	84
	12	3.0	6.29×10^{-4}	.264	41
	18	4.5	2.52×10^{-4}	.299	33
13D	2	0.5	2.4×10^{-3}	.213	117
	4	1.0	1.84×10^{-3}	.178	85
	12	3.0	7.85×10^{-4}	.278	28
	18	4.5	3.21×10^{-4}	.333	20

TABLE 5

CONTINUITY TERM

Expt.	Grid Location	km	$M_2(m/s^2)$	M_4/M_2	Relative Phase $M_2-M_4(°)$
24	2	0.5	1.26×10^{-4}	.056	102
	4	1.0	1.25×10^{-4}	.075	121
	12	3.0	1.24×10^{-4}	.139	144
	18	4.5	1.24×10^{-4}	.162	149
13	2	0.5	1.24×10^{-4}	.138	97
	4	1.0	1.20×10^{-4}	.165	110
	12	3.0	1.14×10^{-4}	.256	130
	18	4.5	1.13×10^{-4}	.293	135
13D	2	0.5	1.22×10^{-4}	.172	99
	4	1.0	1.15×10^{-4}	.204	113
	12	3.0	1.05×10^{-4}	.304	130
	18	4.5	1.04×10^{-4}	.354	134

Harmonic analysis of the advective term confirms that it is small compared to friction and not an important driving mechanism for M_4 in these models. In general, the M_4 acceleration from friction is at least an order of magnitude larger than that from advection. This conclusion is not affected by changing geometry. Although the magnitude of the advective acceleration increases from 24 to 13D in response to the larger velocities in 13D, the relative importance of advection to friction does not increase. Tidal distortion is controlled, therefore, by friction and by tidal flow/geometry interactions.

The friction term is strongest in experiment 13D and weakest in 24 (table 4). This is a result of both the higher velocities in 13D and the smaller hydraulic radius, R (=A/P). For the three experiments at grid point 4, friction is larger during flood than ebb, reflecting the velocity asymmetry developed in these models (fig. 18). The hydraulic radius (fig. 18) varies more for experiment 24 than for 13 and 13D. Large variability in R arises in cases where channel width change with depth is small (i.e., channels are more "rectangular"). Despite lower velocities, experiment 24 (less variable geometry) has a larger frictional M_4/M_2 ratio than 13 and 13D. This behavior largely results from the greater variability in R in experiment 24.

The first order frictional M_4 generation represents interactions between tidal fluctuations in channel geometry at the M_2 frequency and frictional retardation of the M_2 tidal flow. Between the time of high water slack and peak ebb, friction is weaker than for the case of a constant mean R. This is especially true when R shows large variability, and is equivalent to a downchannel acceleration. Similarly, between low water slack and peak flood, friction will be stronger than for the case of constant mean R.

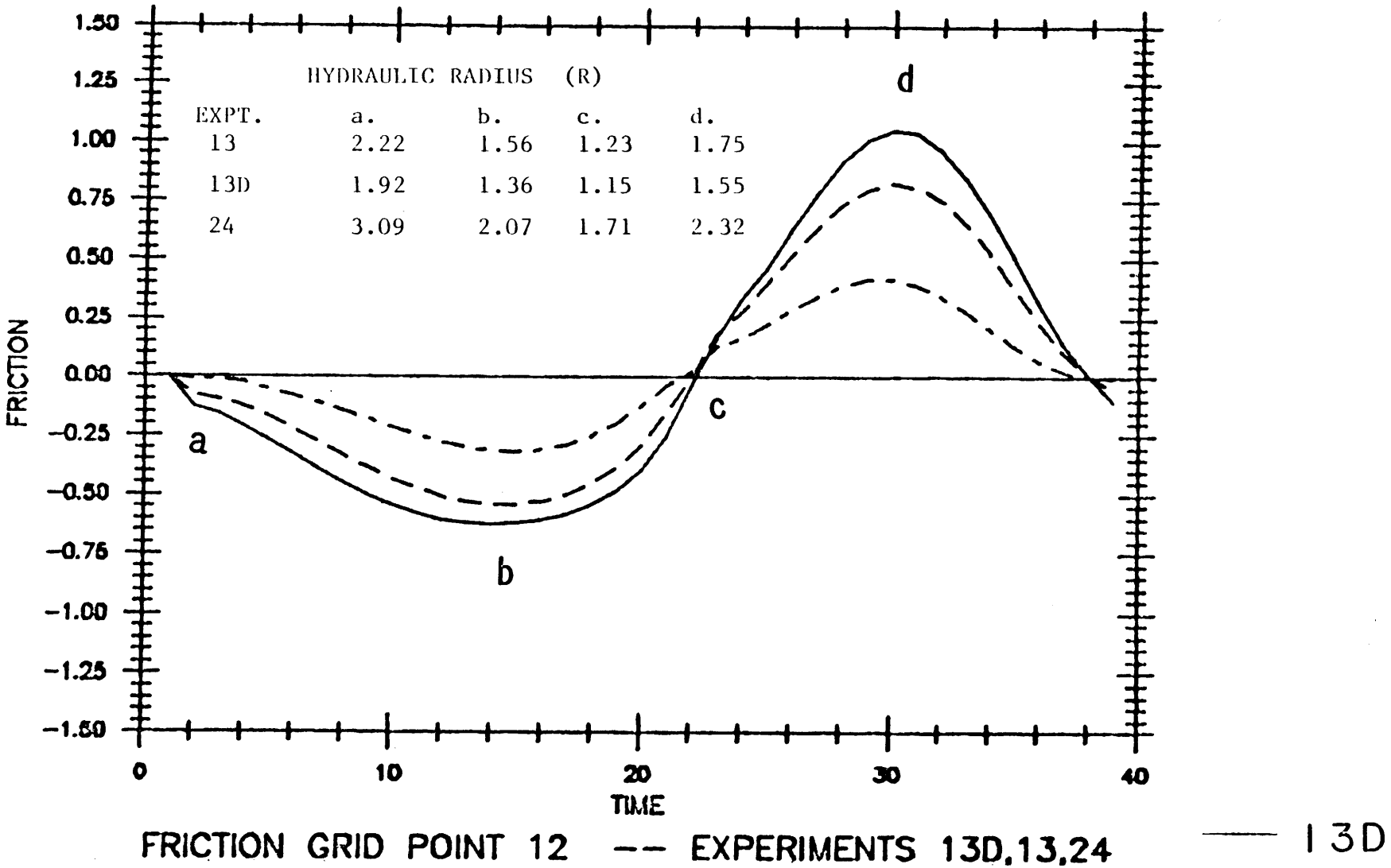

Figure 18. Tidal frictional oscillation for three experiments at grid point 4 (1 km). The form of friction represented in this plot is $(f/\bar{u}/\bar{u})/R$. Variation in the hydraulic radius, R, is shown on the plot.

This is again equivalent to a down-channel acceleration. Channel geometry (entering through R) modulates friction to produce an M_4 oscillation with peak down-channel accelerations between low water and maximum flood, and between high water and peak ebb. This qualitative explanation describes only the first order friction-geometry interaction. Other harmonics in velocity and geometry interact in a complex manner not readily described. These other interactions produce the different M_2-M_4 phase relationships observed in friction in the experiments. All three have similar phase relationships (~+90° - 100°) near the forcing boundary (table 4). Further downchannel, experiments 13 and 13D tend towards +20°, whereas experiment 24 reaches +60° (table 4).

Fourier analysis of the continuity term reveals a different behavior than the friction term. The magnitude of this term shows little decline downchannel, and in all three cases, harmonics of M_2 monotonically increase downchannel (table 5). In contrast to the friction term, experiments 13D and 13 are more non-linear than 24. This reflects the greater variability in channel cross-sectional area over a tidal cycle and greater tidal dissipation in the former two experiments.

The phase relationships in sea surface and velocity (ϕ_ζ, ϕ_u) observed in the model results are determined primarily by friction and continuity. In the examples described above and the experiments listed in Table 2, both terms drive the sea surface phase relationship to approximately +90° or less. Strong friction and time-variable geometry produce a sea surface phase of ~65° and velocity phase of ~0° as well as strong harmonic growth. Reducing friction (e.g. experiments 13 vs. 13E, 13F) for the same variable geometry changes phase relationships dramatically. Similarly, making the

geometry less variable while keeping the same friction (e.g. experiments 13 to 10) causes large phase changes. Both changes also have the effect of reducing harmonic growth.

4.3.3. Channels with Tidal Flats

These experiments include storage regions (tidal flats) with some of the channel geometries described in 4.3.2 (table 6). Compared to the previous experiments, an important effect of the storage regions is to increase the potential prism. Purely from continuity considerations, therefore, larger mean velocities are anticipated (table 3). Frictional effects will be enhanced resulting in greater dissipation of the tide. As in the previous examples, the potential prism and mean velocity linearly decrease downchannel. Again, friction and advection are strongest near the forcing boundary whereas the non-linear continuity term shows little downchannel decline.

The way in which tidal flats are introduced causes a discontinuity in the channel geometry with a sharp break between transported and stored fluid. This is reflected in velocity records where a distinct "break" in the record occurs as tidal flats first become covered (fig. 19). The hypsometric curve of two experiments (fig. 20) also emphasizes the break in the topography. Real estuaries, of course, have smoother hypsometric curves. The ratio, A_f/A_c, (table 6), indicates the change in tidal flats cross-sectional area versus channel area for a change in sea level. Three geometries from the first group of experiments (10, 13, 13A) were utilized in these experiments to assess the effects of tidal flats. The experimental results both in terms of phase and harmonic growth show a different

TABLE 6

Expt.	a/h	$\Delta b/b_o$	$a/h \cdot \Delta b/b_o$	tanθ	A_f/A_c	f	M_4/M_2 [1]	M_4/M_2 [2]	ϕ_ζ [3]	ϕ_u [4]	%ΔH [5]
11	.32	0		.0025	4.41	.0200	.073	.265	207	215	12
12	.32	0		.0025	4.41	.0100	.071	.242	217	225	2
11B	.32	0		.0050	2.60	.0200	.046	.166	209	223	4
11A	.32	0		.0075	2.00	.0200	.033	.114	213	231	2
25	.39	0		.0025	4.41	.0200	.068	.248	199	216	25
25A	.45	0		.0025	4.41	.0200	.080	.226	192	232	36
14A	.32	.75	.24	.00125	5.00	.0200	.072	.251	193	222	45
14	.32	.75	.24	.0025	2.75	.0200	.085	.175	182	279	30
14B	.32	.75	.24	.0025	2.75	.0100	.064	.174	193	236	13
14C	.32	.75	.24	.0025	2.75	.0075	.056	.171	199	230	7
17	.32	.75	.24	.0075	1.25	.0200	.055	.075	131	332	16
19	.32	.75	.24	.0075	1.25	.0100	.031	.053	144	310	8
17B	.32	.75	.24	.0150	0.62	.0200	.033	.085	81	345	7
23A	.28	.875	.245	.0075	1.08	.0200	.039	.060	128	329	14
23	.32	.875	.28	.0075	1.25	.0200	.064	.085	117	336	21
23B	.32	.875	.28	.0025	2.75	.0200	.089	.162	167	309	38

1. Sea surface amplitude ratio at grid point 4.
2. Sea surface amplitude ratio at grid point 26.
3. Sea surface M_2-M_4 relative phase at grid point 26.
4. Velocity M_2-M_4 relative phase at grid point 26.
5. % decline in tidal range at grid point 28.

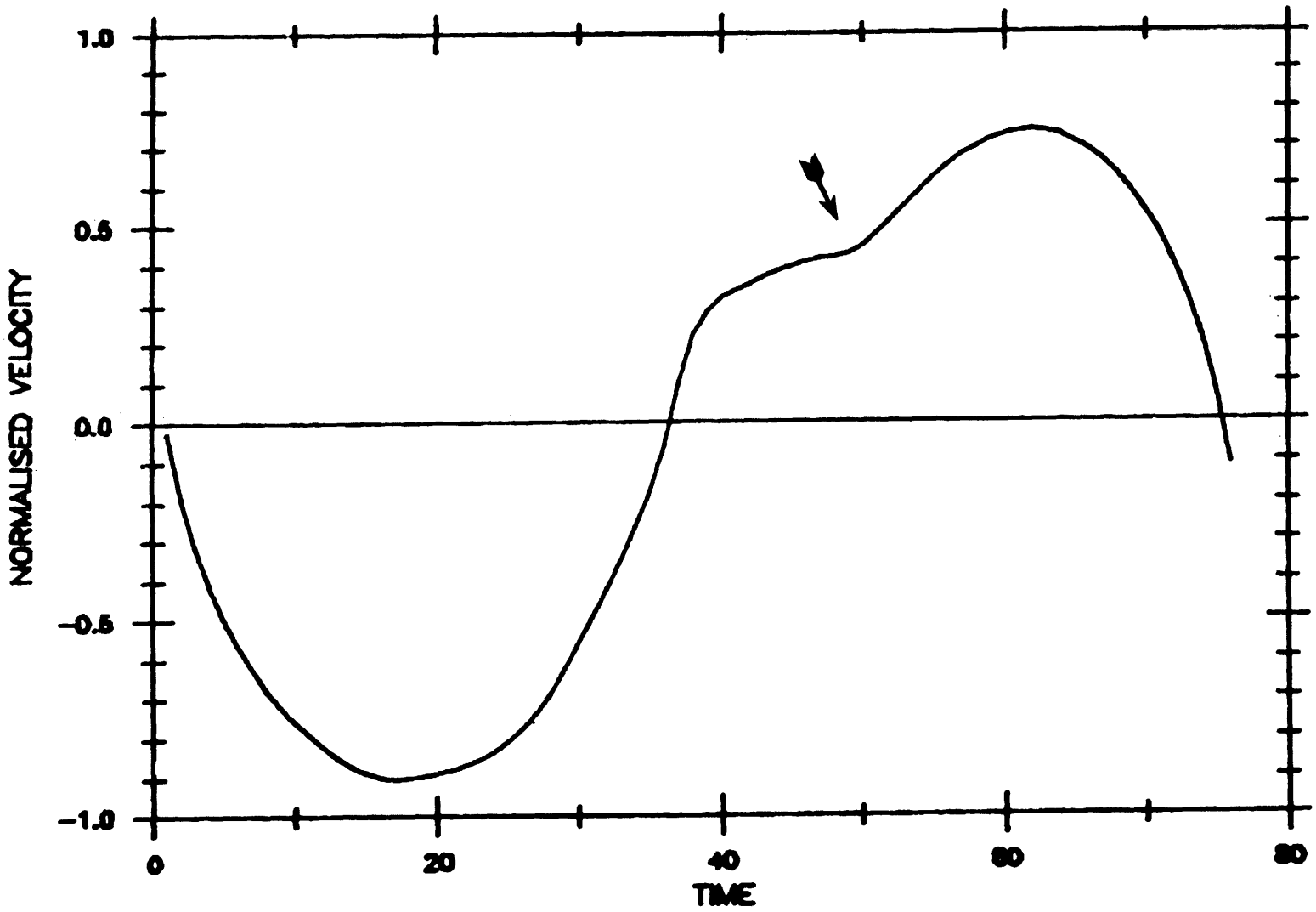

Figure 19. Velocity at grid point 4 from model run 11. The arrow refers to the point at which tidal flats become flooded at this location. Velocity is normalized by maximum velocity developed in the model.

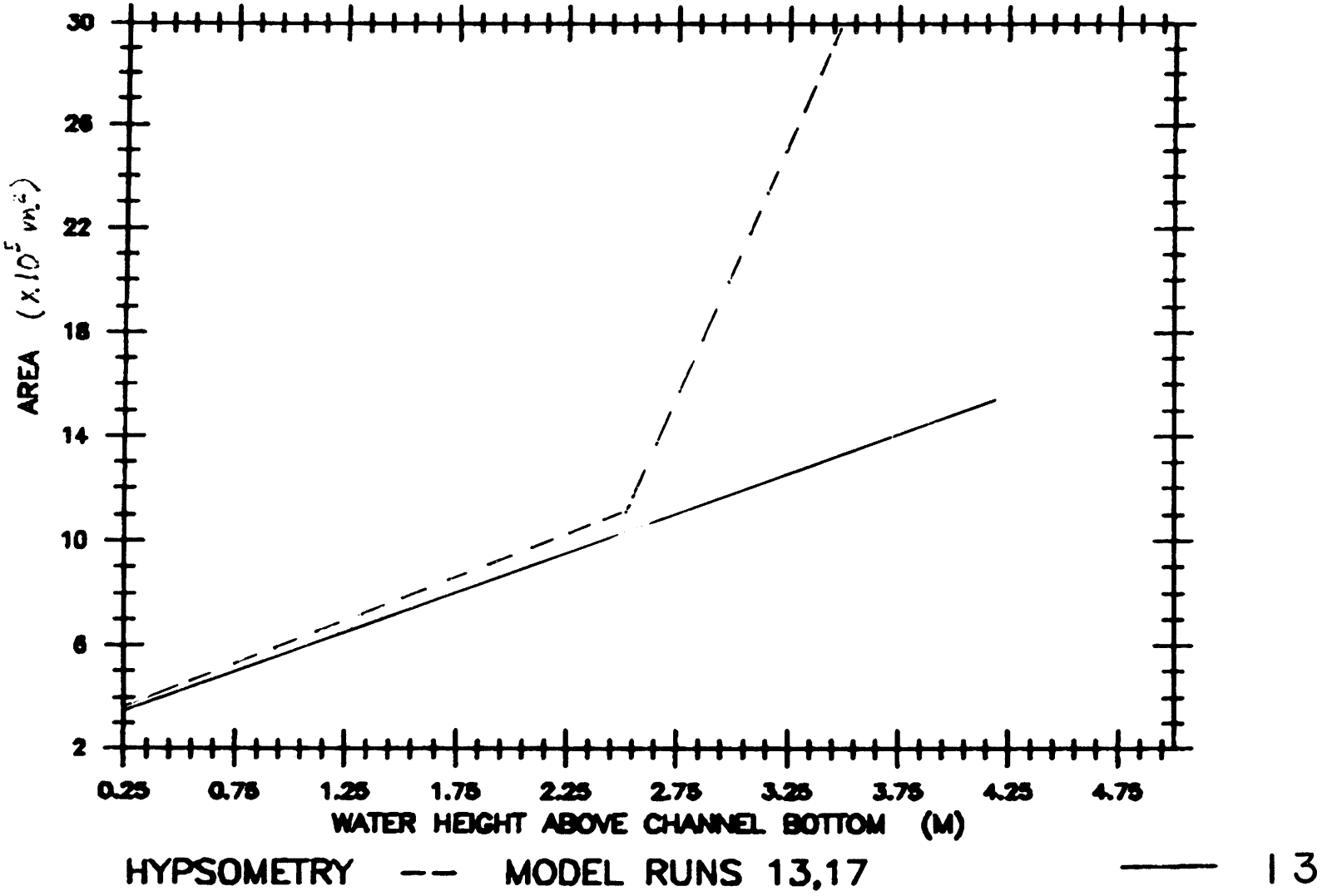

Figure 20. Hypsometric curves for model runs 13 and 17. The sharp break in the curve for 17 indicates the presence of tidal flats.

pattern than the previous examples. In general, patterns of harmonic growth are more complex for these cases (the complexities will be discussed later) but certain general trends can be derived.

In some of the experiments, the sea surface phase, ϕ_ζ, is greater than +180°. This phase relationship produces a longer rising tide than falling tide, and contrasts with the previous experiments. The channel characteristics include lower time-variability in channel cross-section and large values of A_f/A_c. Additionally, the results of experiments 14B and 14C versus 14 suggest that weaker values of friction can produce a longer rise even in cases of more variable geometry. In general, trapezoidal channels with relatively small tidal flats show phases, ϕ_ζ, between +100° and +180° indicating a longer falling tide. All these experiments show a greater adjustment in ϕ_ζ than the previous experiments. In every example, falling tide exceeds rising tide in duration near the forcing boundary (ϕ_ζ <180°). Where tidal flats are important, this inequality is reversed moving downchannel (compare fig. 8 with fig. 21). Thus, large storage regions adjacent to the channel can produce a duration asymmetry characterized by a longer rising tide.

Harmonic growth and particularly the relative phase of M_4 in sea surface depends on the size of tidal flats, time variability of channel geometry and the level of friction. The first six experiments listed in Table 6 involve rectangular (i.e. "weakly" time-variable) channels with different tidal flat areas and levels of friction. The geometry is similar to experiment 10 (table 2) which has a longer falling than rising tide ($\phi_\zeta \simeq +80°$). The addition of tidal flats to this channel geometry results in a longer rising tide (i.e. ϕ_ζ between 180° and 360°). As the channel geometry becomes more

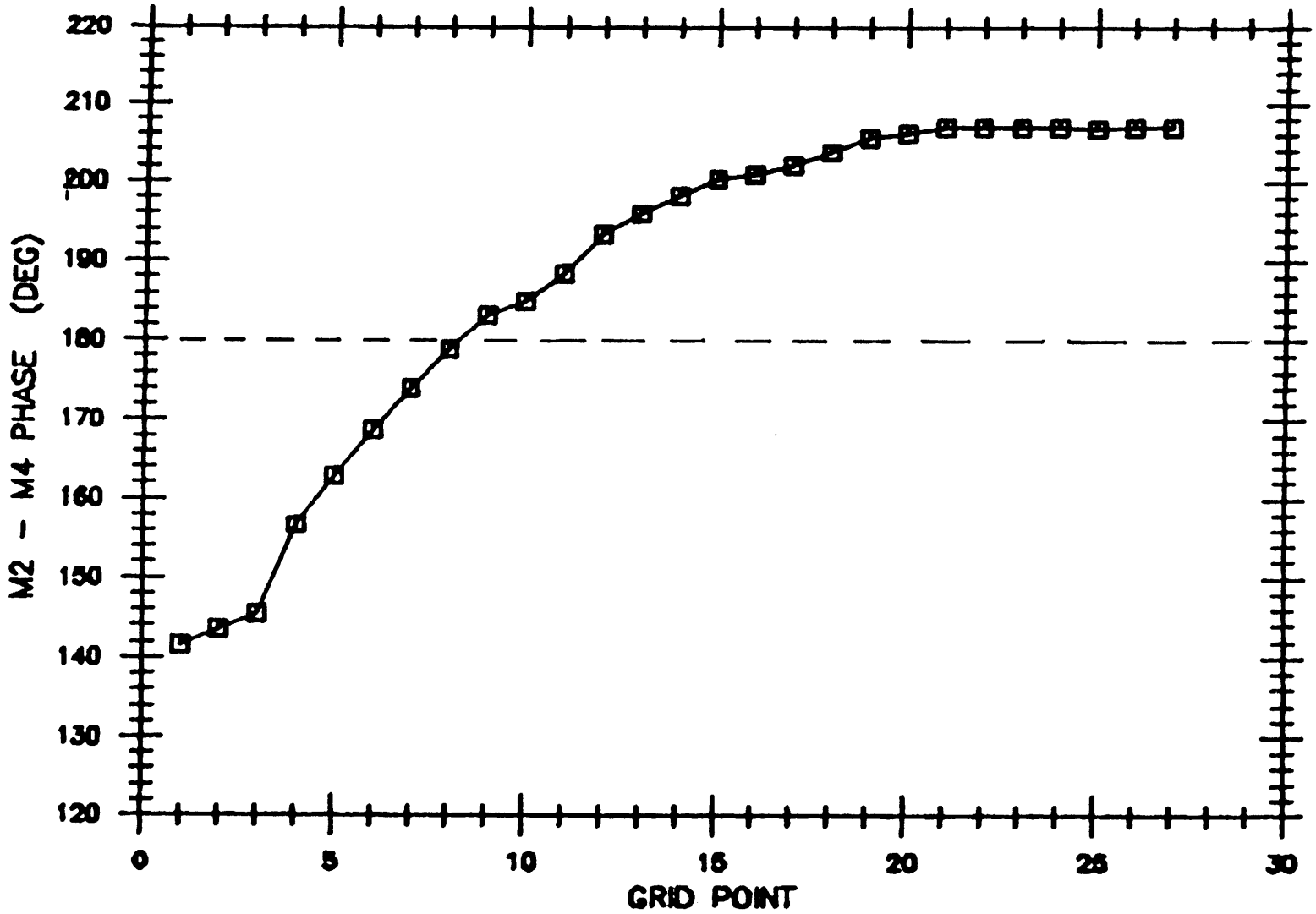

Figure 21. Adjustment in sea surface M_2-M_4 phase for model run 11 (compare with figure 8). Below the dashed line, time asymmetry is characterized by a longer falling tide; above the line by a longer rising tide.

time-variable (through larger a/h), the phase approaches 180°. For these experiments, a longer falling tide at the model's interior boundary does not occur. Adjustment in the phase of sea surface, ϕ_ζ, is much larger in these experiments than the ones in Table 2 (fig. 21). Because of this, the sense of time asymmetry changes moving downchannel.

A comparison of the surface tide at grid point 26 (fig. 22) show the different type of distortion present in experiment 10 (no tidal flats) and experiments 11, 11A (tidal flats). For 11 and 11A, the rise of water level slows as soon as the flats begin to flood (at -10 cm). This causes longer lags in high tide downchannel compared to channels without flats. As water floods the tidal flats, pressure gradients driving the flow relax and the rate of increase in velocity slows or can even temporarily reverse. This imparts a distinctive "kink" in model velocity records (figs. 19,23). This feature has been observed in velocity and pressure gradient records at Nauset (Aubrey and Speer, 1983), where it corresponds to tidal flat flooding. The velocity signal for grid ponts downchannel (e.g., grid point 18) includes not only the signature of tidal flat flooding but also reversals in the rate of velocity increase just after high and low water. These reversals are caused by pressure gradient fluctuations driving the weak flows in the model's interior. Note that these features are not present in high velocity regions of the grid (fig. 19). They do not appear to be directly related to tidal flat flooding and uncovering, however, the fluctuations become more pronounced with increasing tidal flat width. If the excursions in tidal flat width become too large for a given channel

$$b = b_o + b_t \cos\omega t$$

and

$$b_t >> b_o,$$

numerical instabilities develop at these points in the velocity records

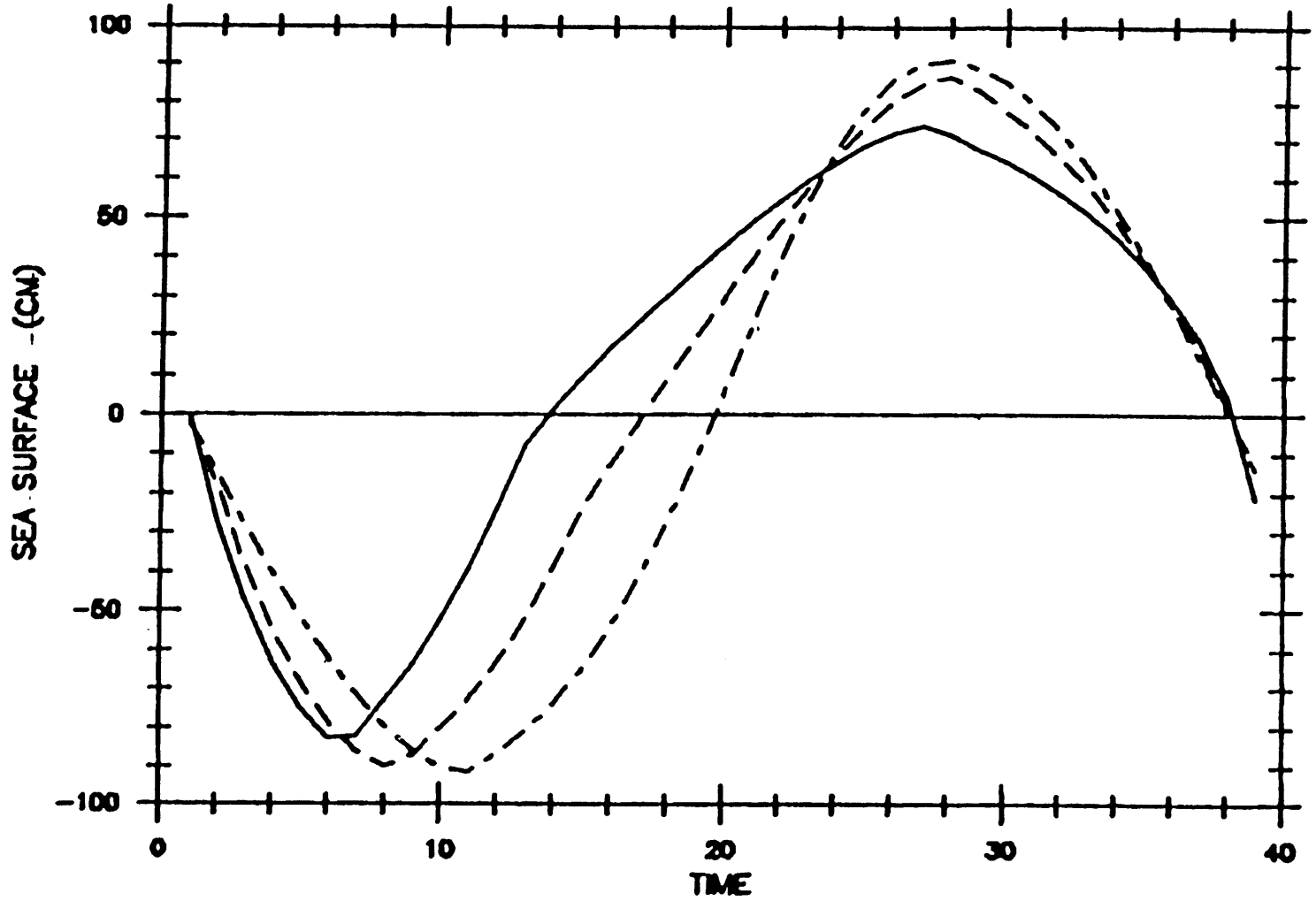

Figure 22. Distortion of the surface tide near the model's interior boundary as a function of tidal flat area for the same channel geometry (experiment 10 has no tidal flats; 11A and 11 increasing area of tidal flats).

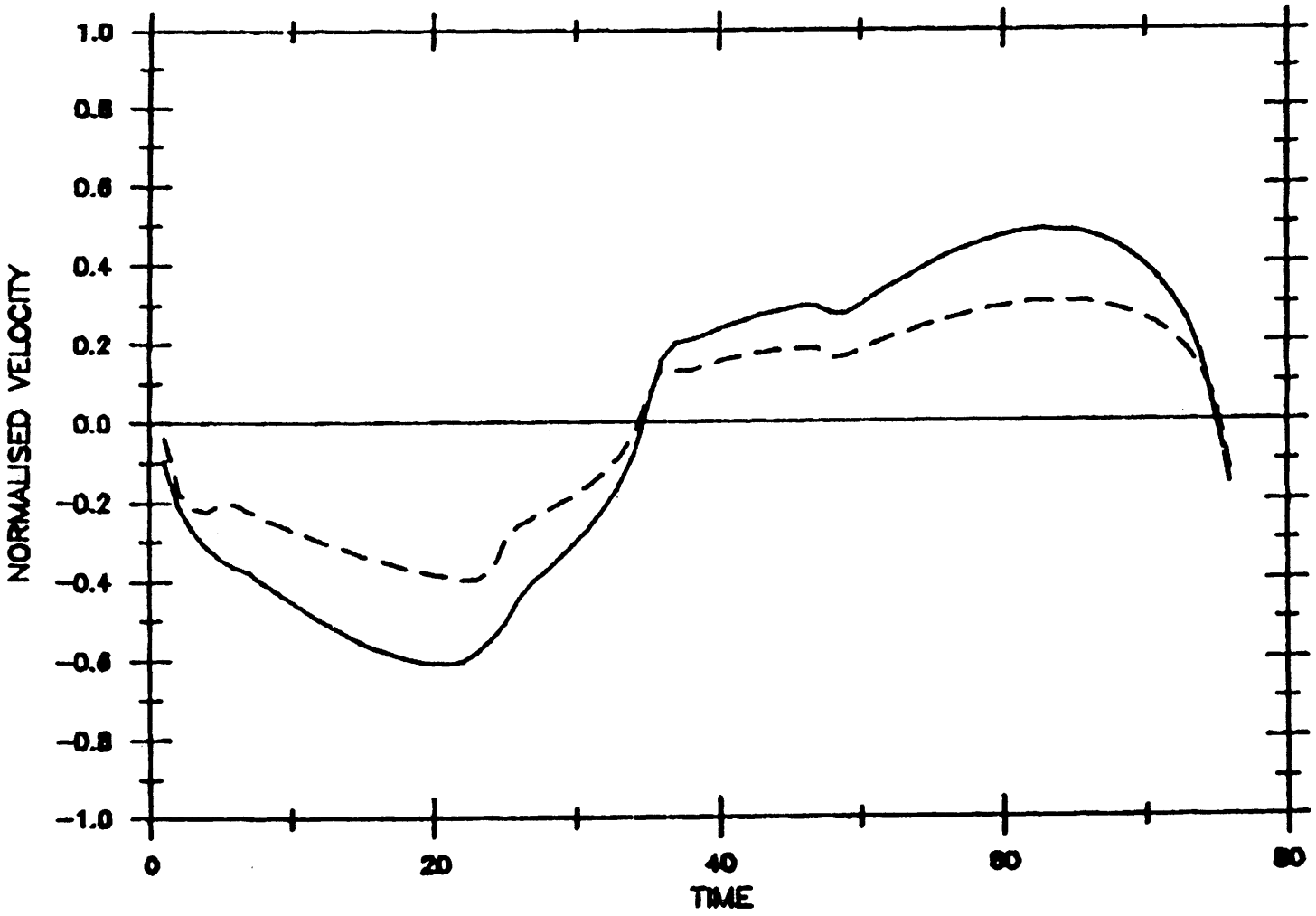

Figure 23. Velocity at grid points 12 and 18 for model run 11. The velocities are normalized as before.

and eventually contaminate the whole solution. A limit in the size of flats which can be included with a particular channel exists beyond which a non-physical solution is obtained.

The spectral structure of sea surface at grid point 26 (6.5 km) and velocity at grid point 12 (3 km) for experiments 10, 11, 11A shows that the tidal flats experiments have a more non-linear response (fig. 24). The effect of the large M_4 component in the tidal flats experiments is apparent in the time asymmetries of both sea surface and velocity. A strong third harmonic term is forced in both sea surface and velocity as well. The phasing of the third harmonic in velocity causes the flattening of the curve (fig. 23) during early flood. This corresponds in part to the onset of flooding of the tidal flats. The M_6 harmonic is more nearly in phase with sea surface M_2 and its effect is not as noticeable on sea surface records.

The strong harmonic growth is anticipated by the larger velocities associated with experiments 11 and 11A. However, generation of third harmonics is more vigorous for tidal flats experiments than for cases of channels without flats and with roughly equal velocities (e.g., experiment 13J, table 2). Examination of the harmonic structure of the primary non-linear forcing terms, friction and continuity for experiments 10 and 11A reveals the difference in non-linear response (table 7). With strong dissipation of both mean velocity and sea surface near the forcing boundary, the continuity term in 11A drives both a strong M_4 and M_6 constituent. This term is a weak source of non-linear forcing in experiment 10 (compare also with table 5). Conversely, the friction term in experiment 10, while having a smaller absolute magnitude, nevertheless is a more non-linear term as measured by the M_4/M_2 ratio.

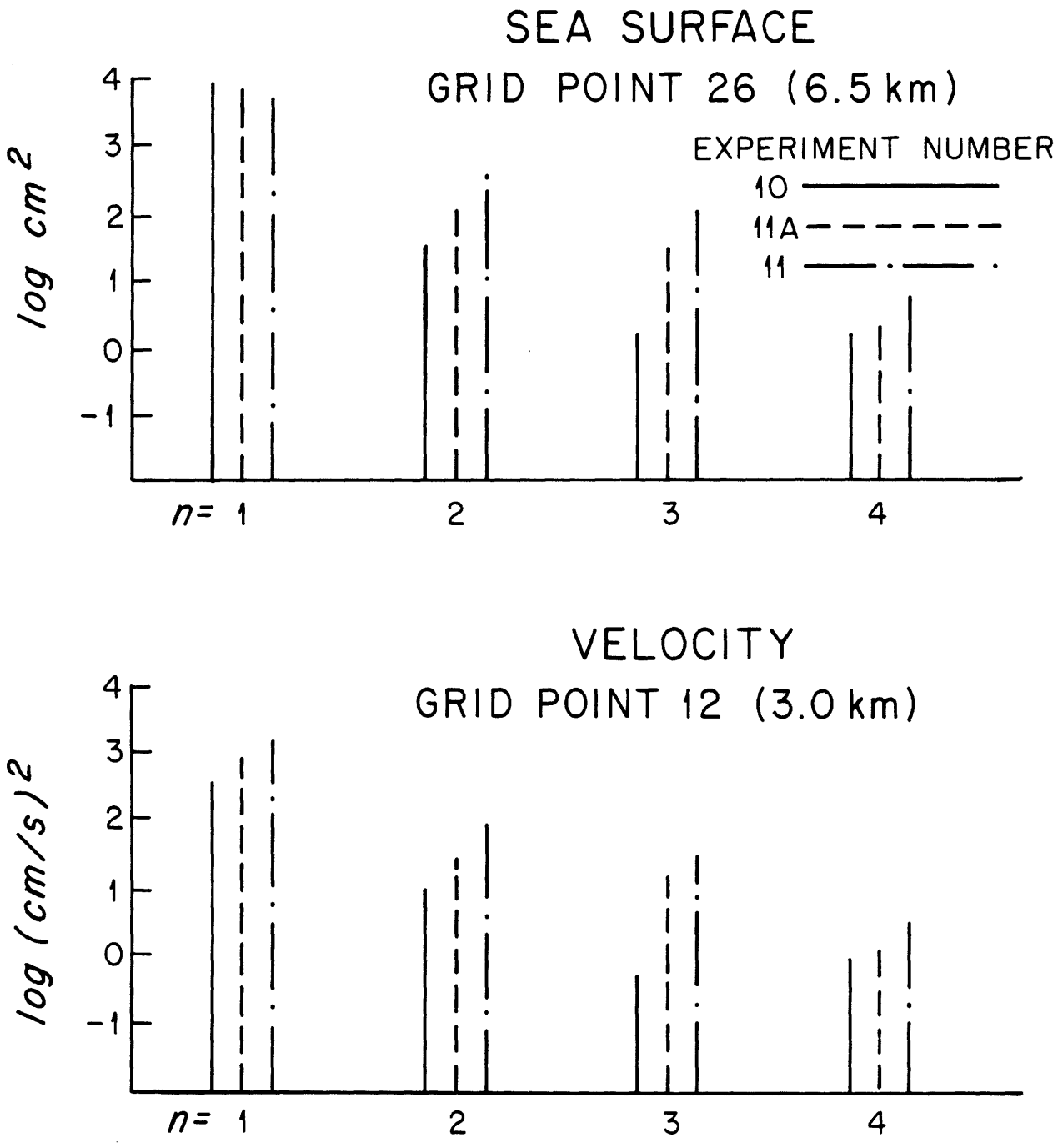

Figure 24. Periodogram of sea surface and velocity for three models showing the effect of increasing tidal flats area on the spectrum of the estuarine tidal response.

TABLE 7

CONTINUITY TERM

Expt.	Grid Location	km	$M_2(m/s^2)$	M_4/M_2	Relative Phase $M_2-M_4(°)$	
11A	2	0.5	2.46×10^{-4}	.446	.120	90
	10	2.5	2.32×10^{-4}	.330	.114	87
	15	3.75	2.31×10^{-4}	.302	.122	80
10	2	0.5	1.26×10^{-4}	.014	.005	139
	10	2.5	1.26×10^{-4}	.057	.019	159
	15	3.75	1.26×10^{-4}	.100	.033	165

FRICTION TERM

Expt.	Grid Location	km	$M_2(m/s^2)$	M_4/M_2	Relative Phase $M_2-M_4(°)$	
11A	2		1.8×10^{-3}	.244	.099	200
	10		9.8×10^{-4}	.209	.097	208
	15		6.1×10^{-4}	.200	.107	211
10	2		6.0×10^{-4}	.346	.072	87
	10		4.3×10^{-4}	.350	.071	79
	15		7.3×10^{-4}	.359	.077	71

The next group of experiments listed in Table 6 introduces the effects of more time-variable channel geometry with variable friction and tidal flat area. The channel geometry is essentially the same as that used in experiment 13 (table 2). Tidal asymmetries developed in these experiments reflect the conflicting effects of channel geometry in continuity and momentum tending to drive a longer falling tide and the presence of tidal flats in continuity driving a longer rising tide. As a result, a variety of channel responses including both types of time asymmetry are found. Again, an important point about these model runs is that sea surface phase adjustment between M_2 and M_4 can be substantial (fig. 25). This is particularly true of the experiments which involve a mixture of large tidal flats and strongly time-variable geometry (e.g., experiment 14). The important point is that the phase relationship does not level off quickly as in the experiments without tidal flats (fig. 8). The phase relationship of both sea surface and mean velocity shown in Table 6 is taken from near the interior model boundary and indicates the type of tidal asymmetry the model is developing.

In general, most of these experiments have a longer falling tide ($\phi_\zeta < 180°$), although the actual phase is quite different from experiment 13. The size of tidal flat area has an important effect on the type of tidal asymmetry. Sea surface at grid point 26 for experiment 14 shows little time asymmetry, although considerable distortion is present (fig. 26). If the amount of tidal flat area is increased, the example of a longer rising tide is found (experiment 14A). Conversely, as the area of tidal flats declines, the behavior of the model becomes more similar to experiment 13 as one would expect (compare experiments 17B and 13). A comparison of sea surface distortion for experiments 14A, 14 and 17B illustrates graphically

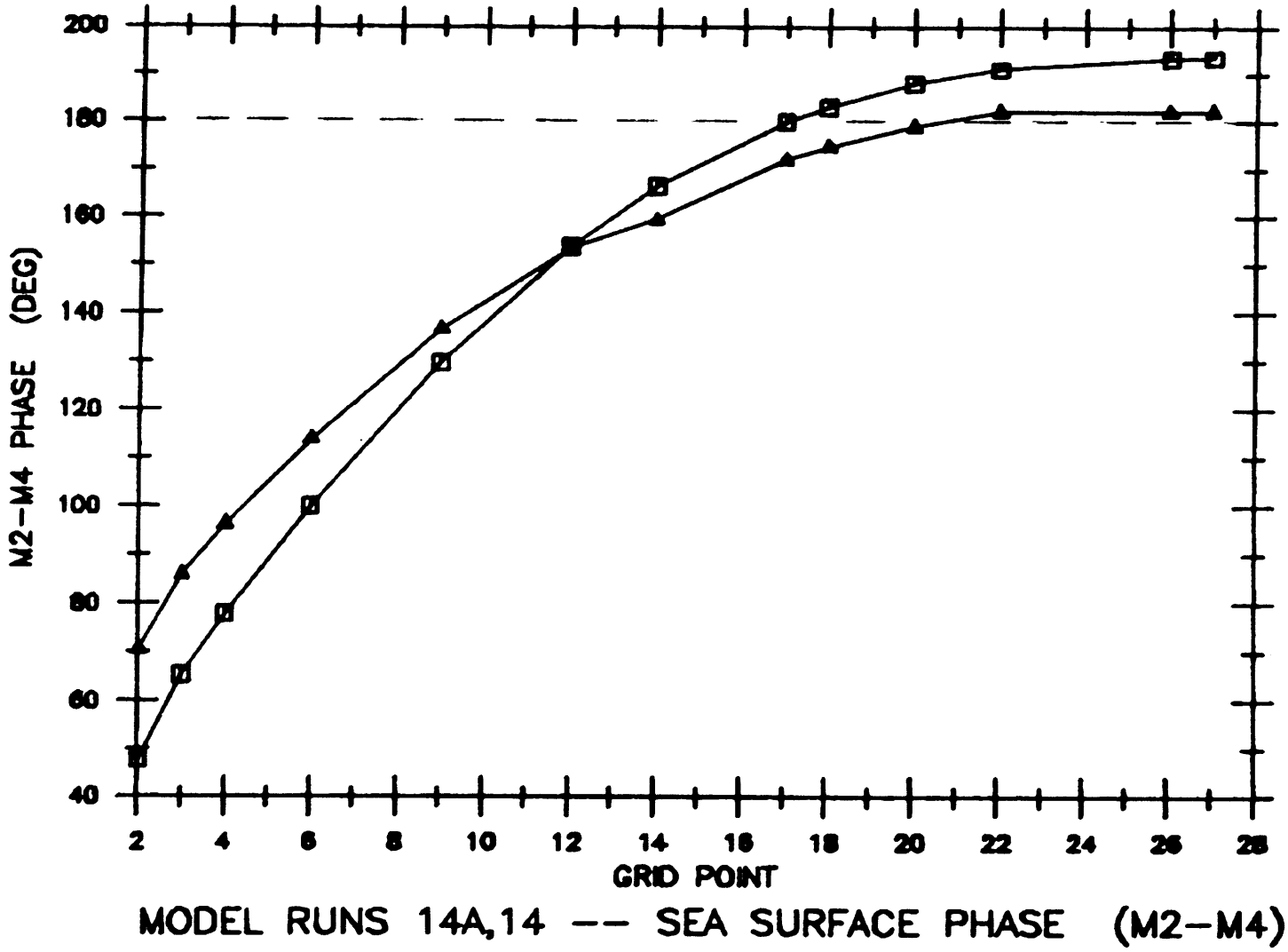

Figure 25. Adjustment in sea surface M_2-M_4 phase for model runs 14 and 14A.

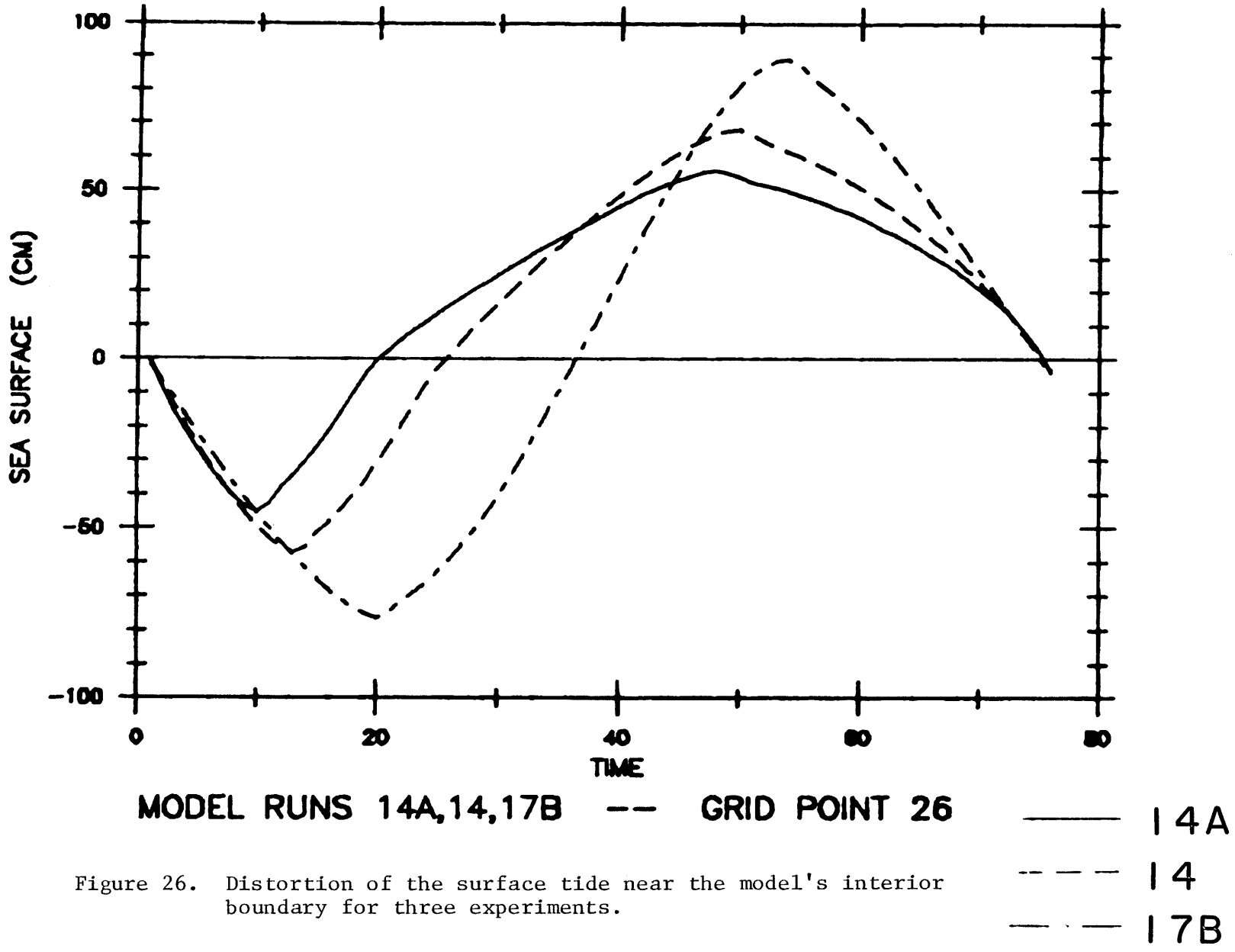

Figure 26. Distortion of the surface tide near the model's interior boundary for three experiments.

the effect of combining tidal flats with time variable channel geometry (fig. 26). The spectral structure of sea surface for these examples reveals the strong second and third harmonic growth driven by cases with extensive tidal flats (fig. 27).

The rate of harmonic growth in sea surface changes as the area of tidal flats decreases (fig. 28). The case of extensive flats (experiment 14A) shows strong growth of both M_4 and M_6. As the area decreases (e.g., experiment 17) harmonic growth is sharply reduced and, in fact, tends to decline downchannel (fig. 28). The exact reasons for this behavior are not clear, except that the competing non-linear effects of tidal flat flooding and time-varying channel geometry must be nearly in balance. With continuing decrease in tidal flat area (experiment 17B), the behavior begins to resemble experiment 13 both in terms of harmonic growth and phase (fig. 28 and table 6). The pattern of M_4 growth and decline exhibited in experiment 17 changes to one of steady M_4 growth. Non-linear effects associated with time-variable channel geometry dominate those associated with the presence of tidal flats for this experiment.

The final three experiments listed in Table 6 also emphasize the interaction of channel geometry and tidal flats. The larger ratio of $\Delta b/b_o$ indicates greater time-variability of channel geometry. The channel geometry is the same as experiment 13A (table 2). For these examples, the effects of variable channel geometry dominate the tidal response even if the tidal flat area is large (experiment 23A). The result is that all three examples have a tidal asymmetry characterized by a longer falling tide. Experiments 23A and 23 also display the previously observed pattern of initial M_4 growth and then decay representing conflicting effects from tidal flats and variable channel geometry.

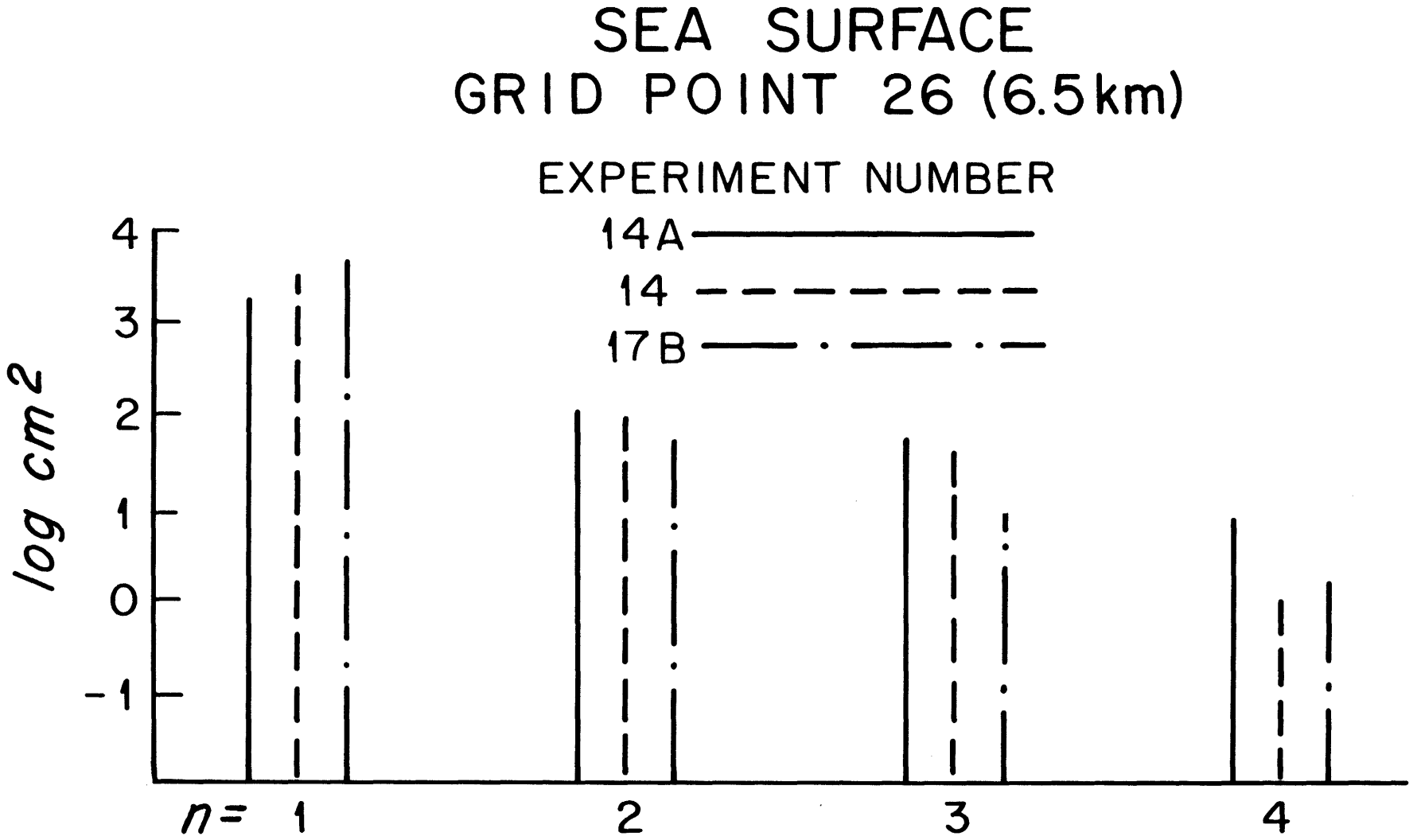

Figure 27. Periodogram of the surface tide for the grid point and three experiments shown in figure 26.

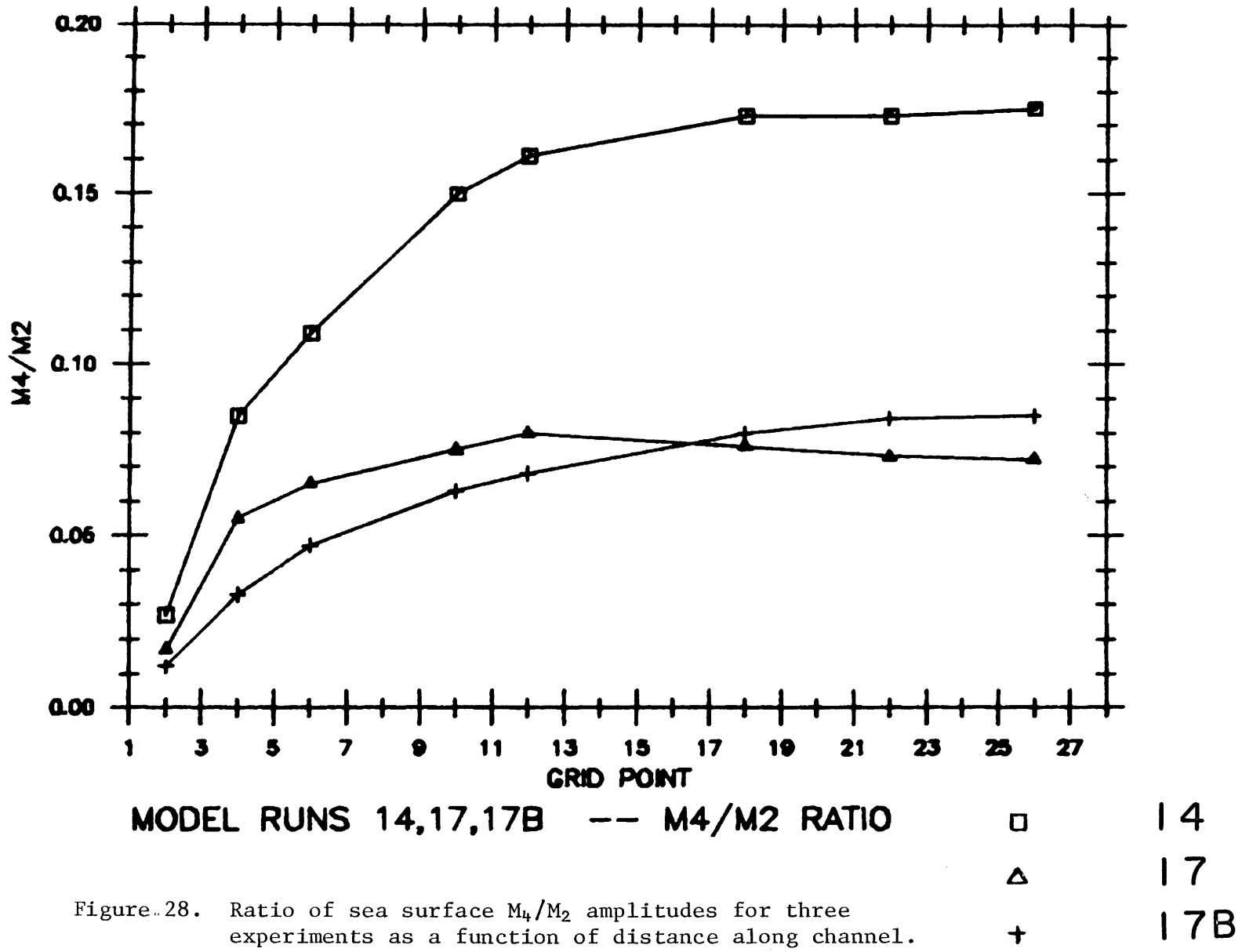

Figure 28. Ratio of sea surface M_4/M_2 amplitudes for three experiments as a function of distance along channel.

The magnitude of friction within a channel affects its tidal asymmetry, as seen by comparing experiments 14, 14B, 14C where the friction factor was reduced while the geometry remained the same. Harmonic growth in sea surface increases slightly with increasing friction and the amount of tidal dissipation increases dramatically. The M_2-M_4 phase of sea surface shifts from a nearly symmetrical tide in experiment 14 to a longer rising tide as the level of friction decreases (table 6).

4.4. A Comparison of Two Different Estuarine Geometries

The problems studied in the previous two sections identified important estuarine channel characteristics involved in different types of asymmetry and different rates of harmonic growth. The models considered in this section involve two different geometries based on estuaries found along the U.S. east coast. The first model idealizes the case of the main tidal channel at Nauset (MA). The second is approximately representative of an estuarine channel at Wachapreague inlet/estuary (VA). These numerical experiments do not attempt to model predictively or hindcast conditions at the estuaries in question. The complexity of these features cannot be reproduced adequately by one-dimensional models. Instead, the models are employed as diagnostic tools in the same spirit as the previous sections. Actual channel depths and widths are idealized and not reproduced exactly. Model results are discussed in terms of the form of tidal asymmetry and not in terms of exact matches with field data. The problems studied here combine elements of the models studied in the previous two sections.

Nauset and Wachapreague represent two different types of estuarine geometry with different tidal responses. Nauset Inlet is characterized by shallow (<3 m) tidal channels which lead to an unstable inlet with flood and ebb tide delta deposits (fig. 1b). Tidal flats along the main southern

drainage are located near the inlet mouth and consist of flood tide delta and barrier overwash deposits. The total extent of tidal flats is moderate in this system. Nauset is modeled by a channel of constant width and depth as these do not vary in any systematic way along the channel, and includes a region of tidal flats near the forcing boundary. The area of flats decreases linearly to zero moving downchannel. Wachapreague Inlet (fig. 1a) is characterized by deep (~5 m) tidal channels which terminate in broad shallow bays. The bays represent extensive tidal flat deposits with large changes in water surface area over a tidal cycle. The inlet itself is relatively stable and lacks flood tide delta deposits. Wachapreague is modeled by a deep channel with contracting width downchannel. Channel reaches near the interior boundary are bordered by large regions of tidal flats. Since these experiments do not represent exact matches between prototype and model geometry, an ensemble of runs, varying the geometry and friction parameters over plausible ranges for each estuary, was considered (table 8). A consistent estuarine response over a reasonable range of parameters is found in each case. Two particular cases (N1, W4) were selected to illustrate the contrasting features of estuarine tidal response for the two systems.

The models representing Wachapreague are characterized by a longer rising tide, stronger ebb flows and relatively weak harmonic growth (fig. 29). This result holds even if one allows for a trapezoidal channel geometry (table 8). The tidal response of the model is dominated by the presence of large tidal flat area and a relatively small a/h ratio (~0.11). Because of these factors, even strong friction (e.g., f = 0.020) is unable to produce a longer falling tide. If the model is run without the tidal flats, harmonic growth is weak and sea surface phase produces a longer falling tide (table 8). The effect of the tidal flats, as indicated by the previous

TABLE 8
NAUSET MODEL (L=7000 km)

Expt.	a/h	$\Delta b/b_o$	$a/h \cdot \Delta b/b_o$	AM[1]	AH[2]	f	M_4/M_2[3]	M_4/M_2[4]	ϕ_ζ[5]	ϕ_u[6]	%ΔH[7]
N1	.32	.88	.282	.143	.436	.0200	.030	.152	63	3.1	15
N2	.32	.88	.282	.143	.480	.0200	.024	.143	64	-2	16
N3	.32	.87	.280	.152	.403	.0200	.032	.155	63	-3	15
N4	.32	.87	.280	.154	.500	.0200	.033	.145	65	13	16
N5	.32	.875	.280	.225	.538	.0200	.036	.108	76	23	20
N6	.30	.73	.219	.153	.493	.0200	.016	.126	61	-16	21
N11	.29	.73	.212	.153	.493	.025	.017	.125	62	-16	25
N12	.32	.88	.282	.143	.436	.0100	.029	.127	70	11	5
N13	.25	.88	.220	.143	.390	.0200	.023	.119	65	2	10
N14	.32	.88	.282	.143	.436	.0050	.022	.088	80	32	0
			WACHAPREAGUE MODEL (L=5750 km)								
W1	.11	.87	.096	.191	.623	.0200	.012	.059	262	261	0
W1B	.11	.83	.091	.173	.732	.0100	.013	.066	271	262	0
W2	.11	.73	.080	.159	.570	.0200	.011	.067	261	258	0
W4	.11	.82	.090	.182	.609	.0200	.010	.051	265	261	0
W5	.11	.69	.076	.191	.623	.0200	.009	.042	272	264	0
W6	.11	.89	.098	.173	.595	.0200	.010	.050	264	260	0
W7	.13	.82	.107	.182	.640	.0200	.013	.062	260	261	0
W8	.11	.82	.090	.182	.609	.0100	.006	.028	286	266	0
W9	.13	.82	.107	.182	.640	.0100	.007	.036	280	265	0
W10	.11	.82	.090	.166	.582	.0100	.009	.041	269	273	0
WT	.11	.82	.090	0	0	.0200	.002	.006	97	80	0

[1] Ratio of surface area of tidal flats to total estuarine surface area at mean sea level.
[2] Ratio of surface area of tidal flats to total estuarine surface area at high tide.
[3] Ratio of sea surface M_4 and M_2 amplitudes at grid point 4.
[4] Ratio of sea surface M_4 and M_2 amplitudes at model's interior boundary.
[5] Relative sea surface M_2-M_4 phase at model's interior boundary.
[6] Relative velocity M_2-M_4 phase at model's interior boundary.
[7] Decline in tidal range at model's interior boundary.

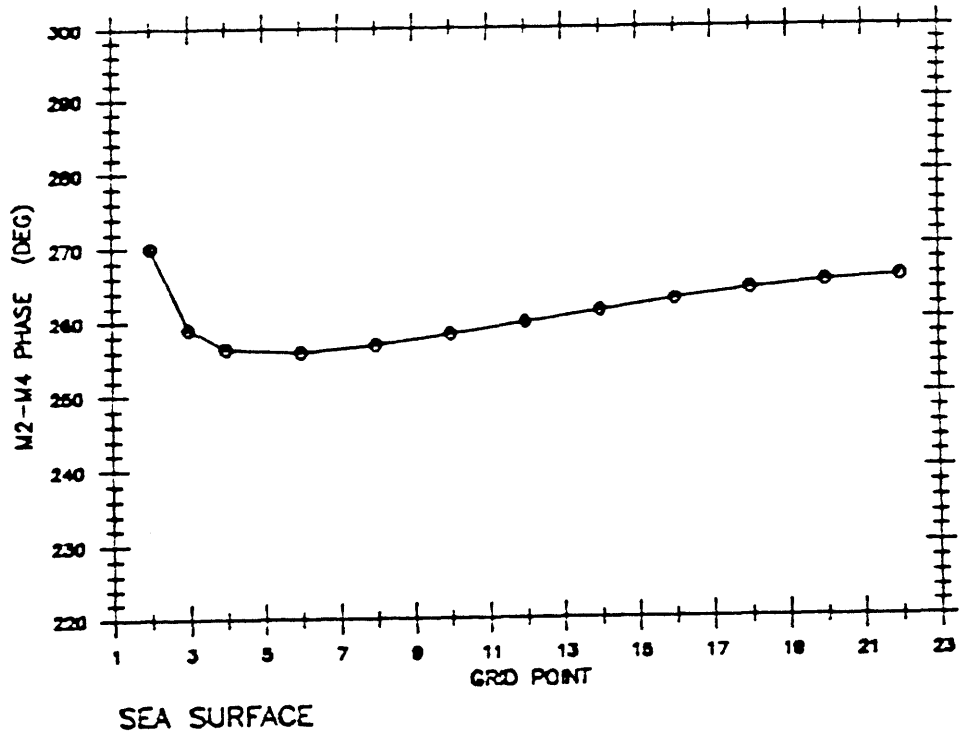

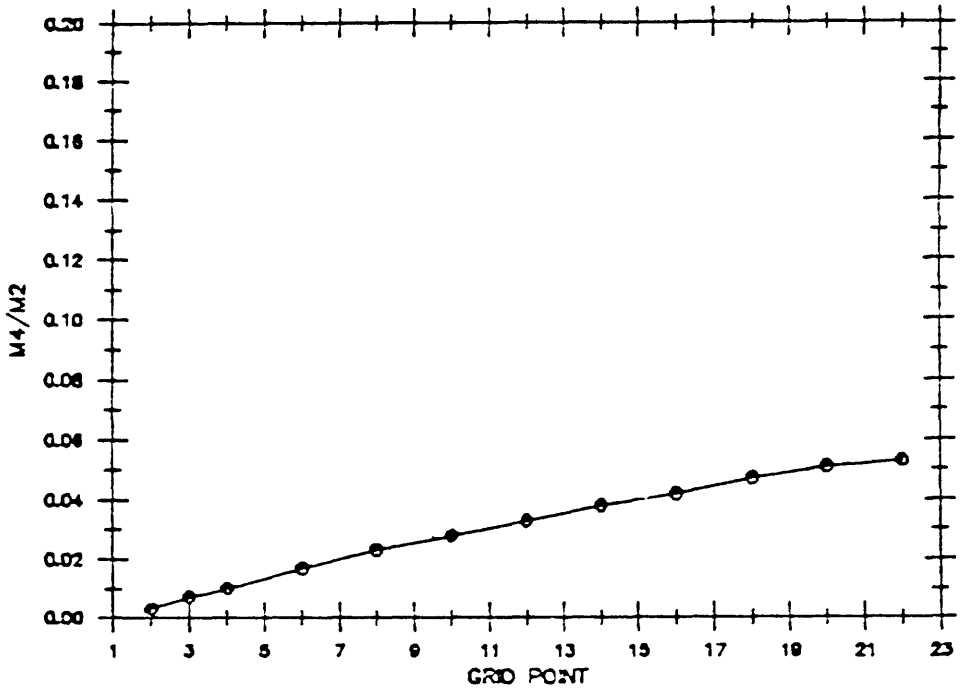

Figure 29. Summary of the tidal response of Wachapreague model W4. Top panel is sea surface M_2-M_4 phase adjustment. Bottom panel is ratio of sea surface M_4/M_2 amplitudes.

section, is to produce both greater harmonic growth and more important, a M_2-M_4 phase in sea surface (ϕ_ζ) producing a longer rise. For model W4 rising tide lasts 6 hours 25 minutes and falling tide 6 hours at the interior boundary. Actual field measurements at Wachapreague show $(M_4/M_2)_\zeta$ equals approximately 0.04 within the estuary (Boon and Byrne, 1981). Sea surface phase is approximately 200-220° producing a longer rising tide and stronger ebb currents. The simple model described in this section reproduces the general features of this tidal response by focusing on the "first order" estuarine characteristics of Wachapreague. These characteristics include deep tidal channels and large tidal flats at the distal reaches of the channels. Modeling phases and amplitudes exactly would require (among other factors) a representation of the non-linear hypsometric curve of real estuaries as Boon and Byrne (1981) point out. The model presented here employs a linear hypsometric curve.

The models representing Nauset display strong harmonic growth, a longer falling tide and stronger flood flows (fig. 30). The important factors determining its tidal response are the large a/h ratio (~0.30) which produces a strongly time-variable channel geometry and the moderate extent of tidal flats. The sea surface phase relationship (≃64°) indicates that the effects of channel geometry dominate the effects of tidal flats. A strong time asymmetry exists in model N1 with falling tide lasting 7 hours 15 minutes and rising tide 5 hours 10 minutes at the interior boundary. Field measurements at Nauset (Chap. 3) show $(M_2/M_4)_\zeta$ is approximately 0.20 and ϕ_ζ, 63°. Again, a simple representation of estuarine geometry has reproduced essential features of Nauset's tidal response. The important characteristics in this example are shallow tidal channels with moderate tidal flat area near the forcing boundary. The tidal distortion in sea

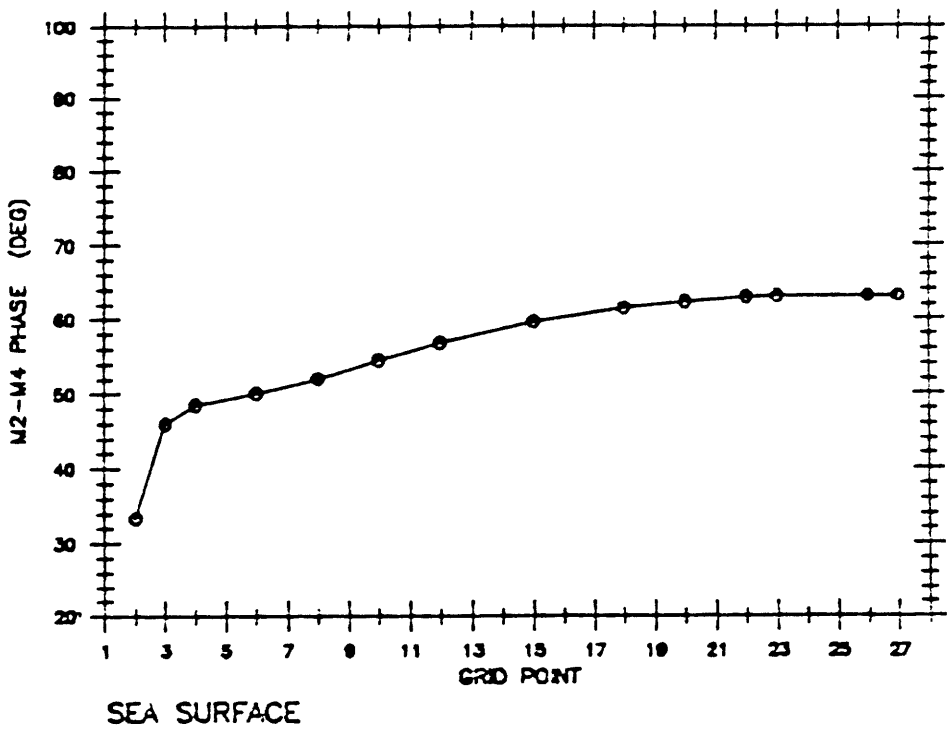

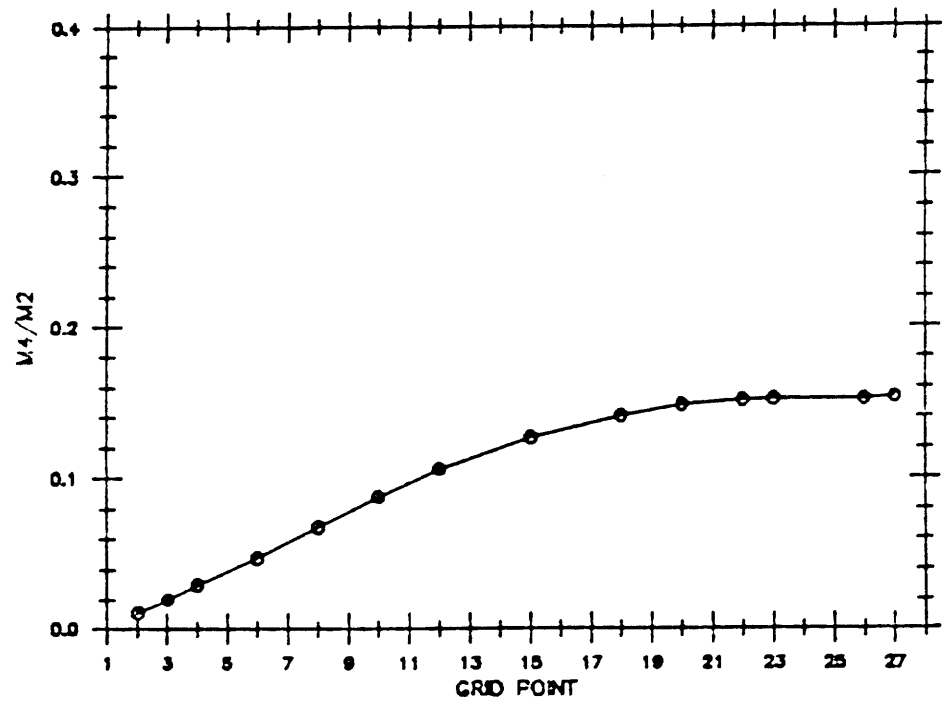

Figure 30. Summary of the tidal response of Nauset model N1. Panels are the same as for figure 29.

surface within the channel for both models clearly indicates the different time asymmetries developed (fig. 31). The mean velocity signal shows the tendency towards ebb dominant flows in the Wachapreague case and flood dominant in the Nauset case (fig. 32) although the distortion in both instances is not exceedingly large.

5. Discussion

Although the modeling is a simplified representation of estuarine tidal response, the results can be combined with field observations of asymmetry to suggest geometry characteristics producing different types of tidal distortion. Harmonic growth in both models and natural estuaries is a strong function of the non-linearity parameter, a/h. Channel geometry effects become important only when this parameter is relatively large (>0.1). In this case, representing channel geometry properly (i.e., contracting width with depth) has an important effect on both the rate of harmonic growth and on the phasing of harmonics.

Estuaries characterized by relatively large values of the non-linearity parameter ($\simeq$0.3) tend to have longer falling tides than rising tides (flood dominant). In addition to Nauset, Murrells Inlet which has approximately the same value of a/h, also has a longer falling than rising tide ($\phi_\zeta \simeq +90°$). The modeling indicates that large areas of tidal flats can change this behavior to a situation of a longer rising tide. If the channel geometry is strongly time-variable (i.e., $\Delta b/b_o=0$), the area of flats must be more extensive than if the channel were rectangular. It is difficult to put a number on the critical area of tidal flats which produces a longer rising tide because the modeling is not an exact representation of estuarine physics and field observations are sparse. However, most of the very shallow (a/h>~0.3) estuaries will be flood dominant. Deeper estuaries

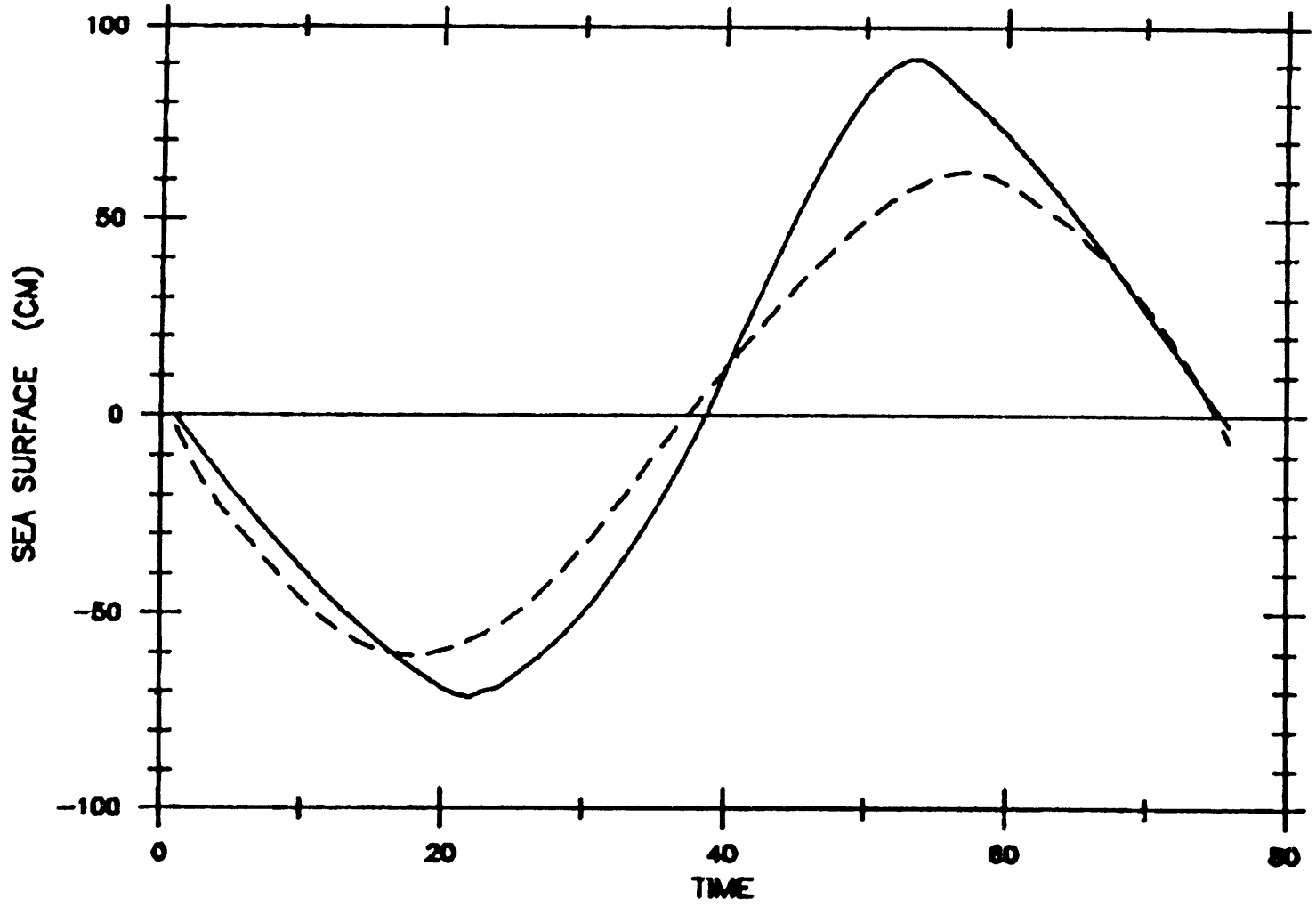

Figure 31a. Distortion of surface tide at grid point 20 for model runs N1 and W4.

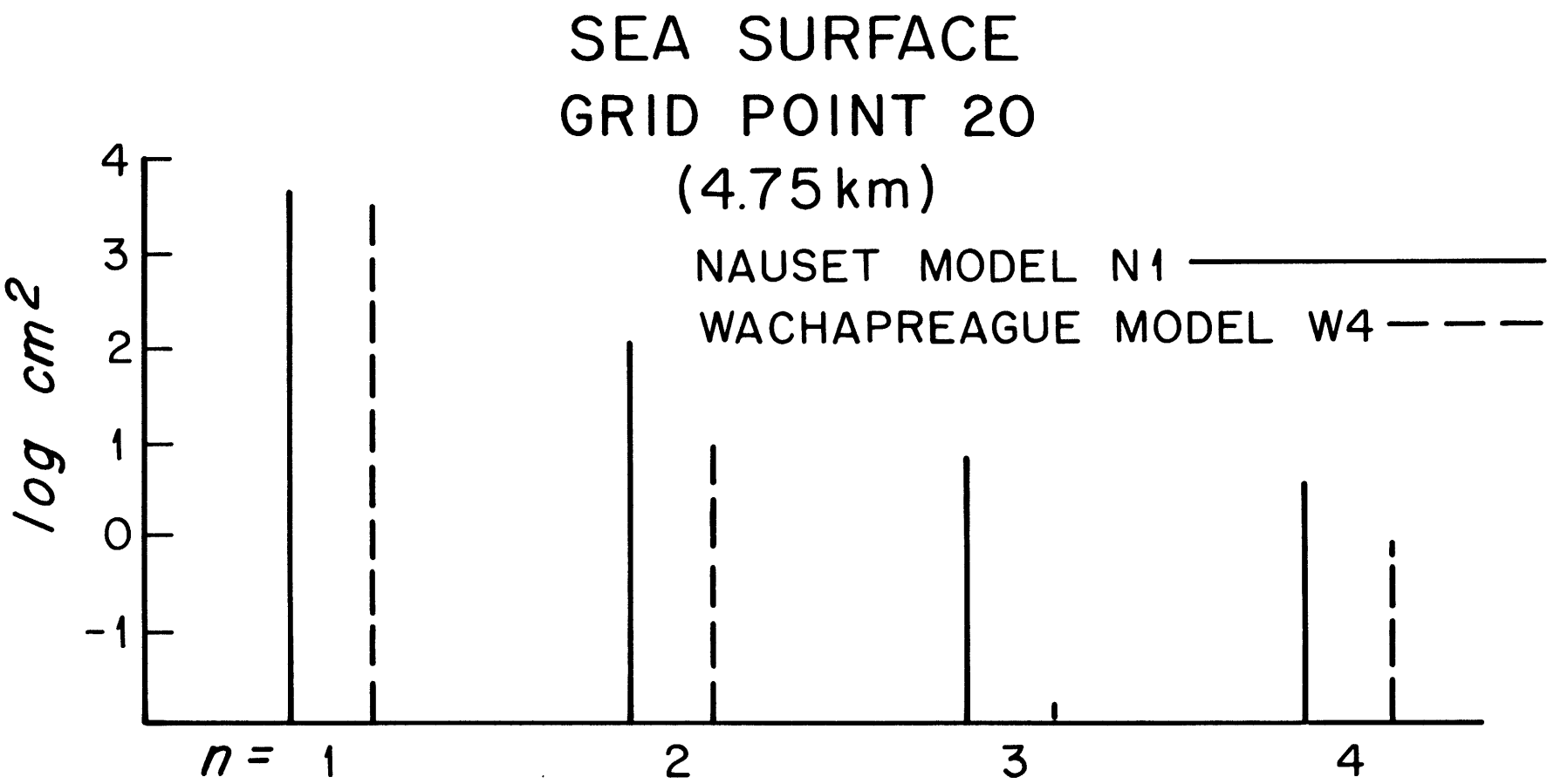

Figure 31b. Periodogram of sea surface at grid point 20 for model runs N1 and W4.

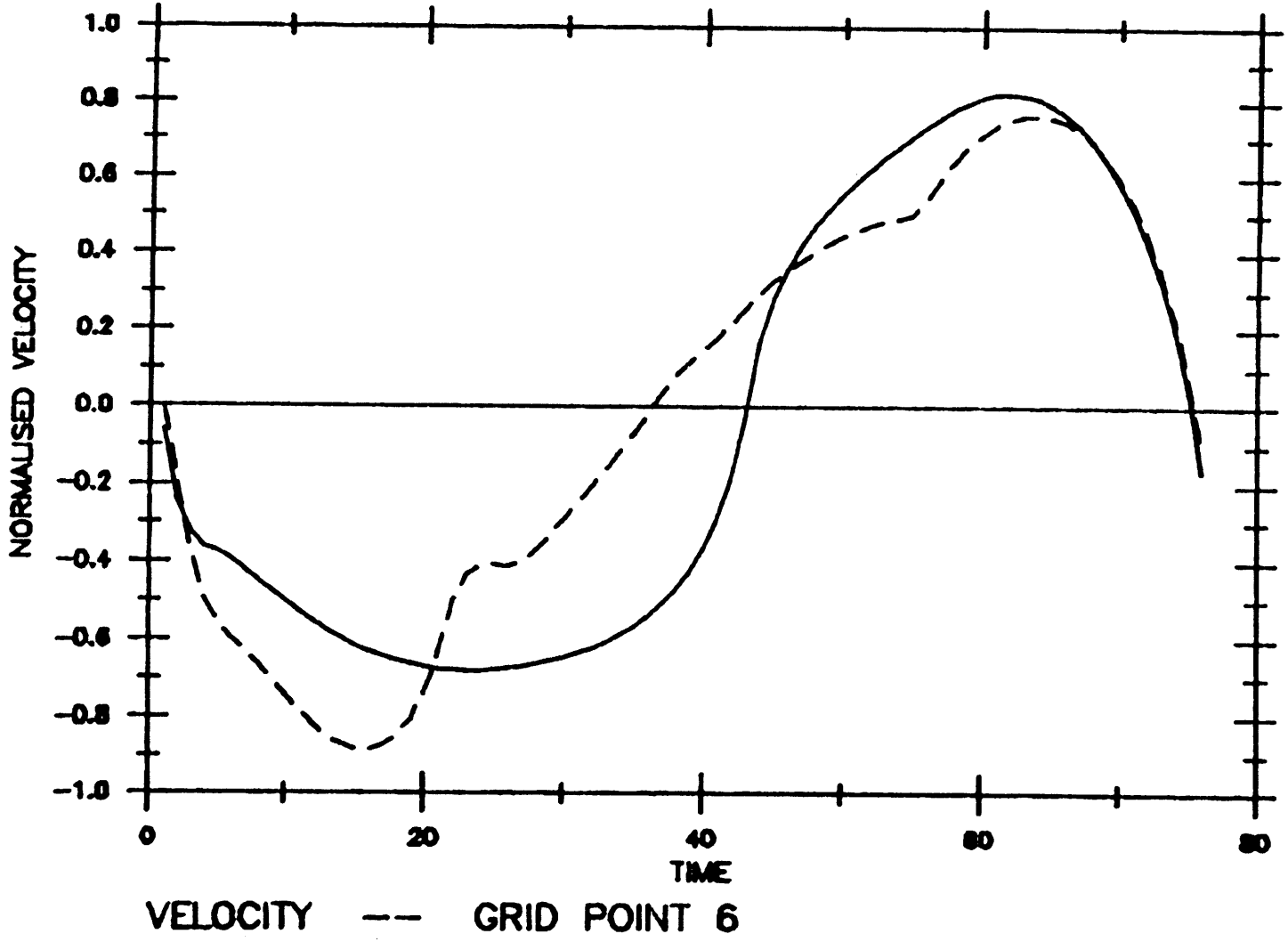

Figure 32. Velocity at grid point 6 for model runs N1 and W4.

——— Nauset model N I

— — Wach. model W4

(a/h ~0.1-0.2) without flats will develop a weak tendency towards flood dominance. The presence of even moderate tidal flat area can reverse this time asymmetry. Natural estuaries characterized by a longer rising tide (e.g., North Inlet, SC; Price Inlet, SC; Wachapreague, VA) have relatively small values of the non-linearity parameter (~0.1) and extensive regions of tidal flats. Price Inlet and Wachapreague Inlet, in fact, contain approximately five times as much water in flats as in channels (Byrne et al., 1975; FitzGerald and Nummedal, 1983).

Some investigators of shallow inlet/estuarine systems have suggested that the variation of estuarine surface area relative to channel cross-sectional area controls duration asymmetries (Nummedal and Humphries, 1978; FitzGerald and Nummedal, 1983). This argument is stated utilizing a spatially integrated form of the continuity equation:

$$\frac{dh_b}{dt} = \frac{A_c}{A_b} \cdot \bar{U}$$

h_b = sea surface level in estuary

A_c = inlet channel cross-sectional area

A_b = area of estuary at h_b

$\bar{U}$ = mean channel velocity.

The spatial integration requires estuarine water level to be everywhere horizontal. In this equation the rate of sea level change is proportional to A_c/A_b. The ratio is a maximum at low tide and a minimum at high tide in estuaries with large changes in surface area (i.e. extensive tidal flats). Consequently, it appears that the water surface in the estuary adjusts more rapidly to the ocean tide at low water than high water. The channel is said to be more "efficient" in its exchange of water at low than high tide. Essentially, duration asymmetries are explained solely by continuity

effects, neglecting momentum considerations. A_c/A_b ratios for the experiments with and without tidal flats exhibit different patterns: channels without flats have a maximum at high and a minimum at low tide; channels with flats show the opposite trend (table 9). Nonetheless, several of the latter experiments have longer falling tides than rising tides. These experiments are characterized by strong frictional and time-variable channel geometry effects entering both momentum and continuity equations. In addition, field results show that Nauset Inlet is characterized by a longer falling tide (Aubrey and Speer, 1983) and yet A_c/A_b is a minimum at high tide. Clearly, momentum effects cannot be ignored in all cases. Shallow frictionally dominated channels develop significant pressure gradients which make an analysis by the continuity equation incomplete. This "continuity" approach is best suited for estuaries which consist largely of an open bay that oscillates up and down with a level surface in response to tidal forcing.

Although the modeling focused on the estuarine response to M_2 forcing, the effects of harmonics introduced in the boundary conditions were studied. The question is how important is estuarine geometry in determining tidal distortion versus harmonics entering the estuary through the inlet. Tidal harmonics can be generated on ebb-tide deltas, shallow platform shoals located oceanward of the inlet. The field evidence which exists suggests that phase relationships and amplitudes of harmonics can be strongly modified as the tide propagates into the estuary (Boon and Byrne, 1981; Aubrey and Speer, in prep.). At Nauset, pressure sensor records from the ebb-tide delta indicate different sea surface M_2-M_4 phase than within the estuary (ϕ_ζ ebb delta $\simeq 30°$; ϕ_ζ estuary $\simeq 63°$). The implica-

TABLE 9

A_c/A_b RATIOS

Expt. 13

High tide	$A_c/A_b = 3.2 \times 10^{-4}$
Mean water level	$A_c/A_b = 2.5 \times 10^{-4}$
Low tide	$A_c/A_b = 1.8 \times 10^{-4}$

Expt. 11

High tide	$A_c/A_b = 5.9 \times 10^{-5}$
Mean water level	$A_c/A_b = 2.2 \times 10^{-4}$
Low tide	$A_c/A_b = 2.7 \times 10^{-4}$

Expt. 17

High tide	$A_c/A_b = 1.3 \times 10^{-4}$
Mean water level	$A_c/A_b = 1.8 \times 10^{-4}$
Low tide	$A_c/A_b = 1.8 \times 10^{-4}$

tion is that estuarine geometry is a strong control of tidal asymmetry, and dissipation within the inlet proper may isolate internal harmonic generation from external forcing.

Two different values of ϕ_ζ (64°, 179°) in the boundary condition and the geometry of experiment 13 (table 2) were used to study the problem in a model estuarine channel. One of the phase relationships is compatible with the channel geometry as determined by the runs with M_2 forcing. Introduction of a small amount of M_4 (M_4/M_2 = .033) at a compatible phase in the forcing boundary condition eliminates the phase adjustment and results in slightly greater M_4 growth (fig. 33). The phase, ϕ_ζ, at the model's interior boundary is close to that of experiment 13. In contrast, the same amount of M_4 introduced at a phase, ϕ_ζ, of 179° produces a different result. The M_2-M_4 phase changes dramatically, approaching the value of experiment 13 near the model's interior boundary, and the amplitude of M_4 first declines before growing downchannel. Thus the channel geometry in the model runs exerts an important control on tidal asymmetry regardless of the presence of harmonics in the boundary condition.

The implications of tidal asymmetry for estuarine sediment transport are clear. Although sediment transport represents a complex flow/boundary interaction, large-scale patterns of estuarine transport are controlled by tidal asymmetry. Flood dominant estuaries will show net up-estuary transport if the asymmetry is sufficiently pronounced. If sediment supply is adequate, therefore, these systems may gradually fill over time. The process of shoaling likely will accelerate the flood dominant tendencies of the of the estuary. Eventually, the reduced tidal prism from infilling can lead to inlet shoaling and possibly closure. By contrast, deeper systems with tidal flats may represent more stable estuarine systems with ebb dominant currents able to flush entering sediments.

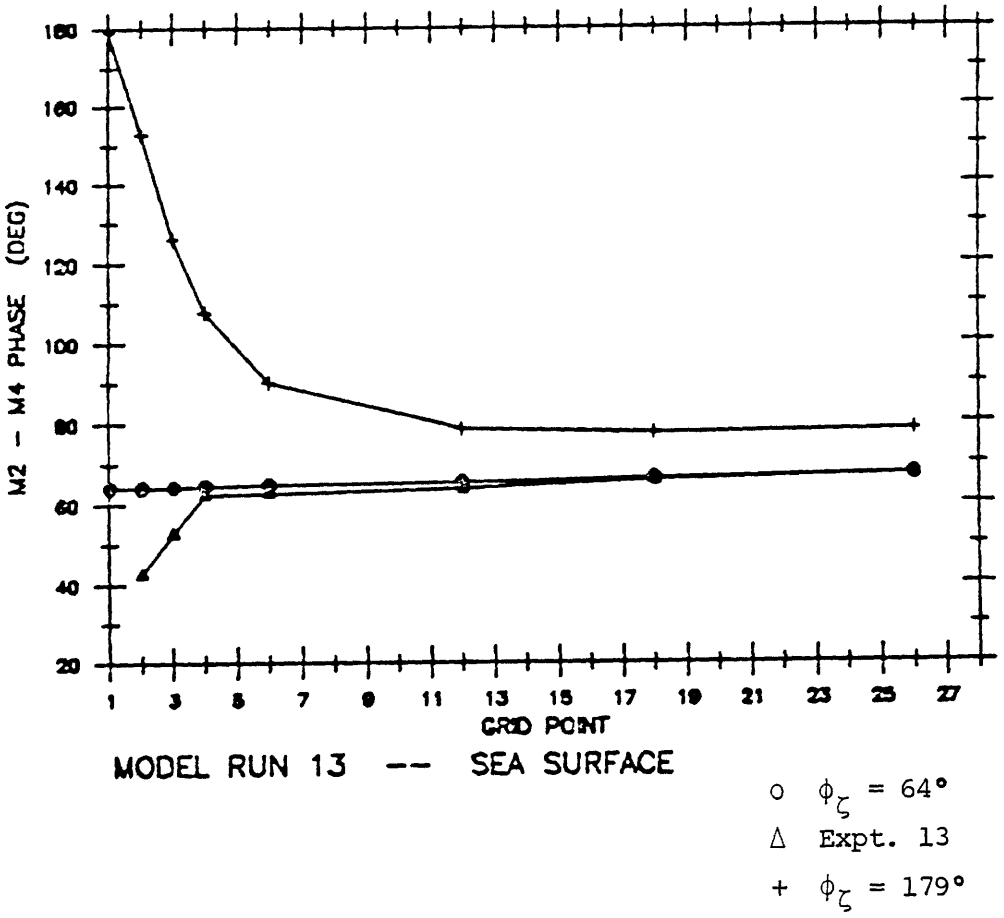

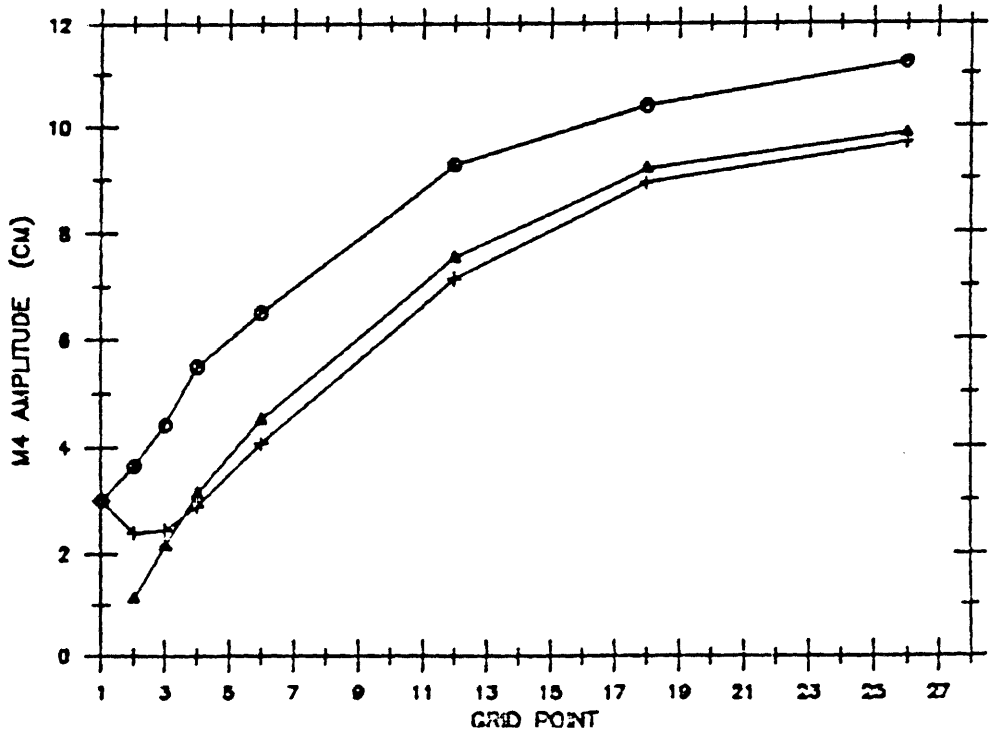

Figure 33. Model run 13 with three different values of sea surface M_2-M_4 phase at forcing boundary.

6. Summary

1). Numerical integration of the one-dimensional equations is employed to study M_2 tidal propagation in long, narrow channels typically found in shallow estuaries along the U.S. east coast. Tidal flats are frequently found along the estuarine channels. Numerical results indicate that channels without tidal flats develop a time asymmetry characterized by a longer falling tide. This asymmetry becomes more pronounced with larger friction factors and increasingly time-variable channel cross-sectional area. Currents associated with this time asymmetry tend to be stronger during flood than ebb. These estuaries can be termed flood dominant.

2). Addition of tidal flats to these channels can produce the case of a longer rising tide and stronger ebb currents (ebb dominant). This time asymmetry develops if the tidal flat area is large enough to overcome the effects of time-variable channel geometry. Channels with relativey small values of a/h and rectangular cross-sections require smaller tidal flat area to produce an ebb dominant asymmetry. Weaker values of friction with tidal flats can also drive the time asymmetry towards a longer rising tide.

3). The general features of tidal channels in shallow estuaries can be represented with simple geometries. Despite the physical complexity of these systems, essential features of the estuarine tidal response in sea surface can be recovered from simple models. This is illustrated by modeling idealized representations of tidal channels at Nauset Inlet, MA and Wachapreague Inlet, VA. Over a range of geometry parameters and friction factors which could characterize these estuaries, reasonable agreement in M_4/M_2 amplitude ratios and M_2-M_4 phasing in sea surface is demonstrated.

4). Field observations and model results suggest that the shallowest estuaries ($a/h>0.3$) generally will be characterized by longer falling tides and stronger flood currents unless extensive tidal flats are present. Deeper systems ($a/h\sim0.1-0.2$) with tidal flats will likely have longer rising tides and stronger ebb currents. Sediment transport patterns in flood dominant estuaries will be directed up-estuary with consequent channel shoaling if sediment supply is adequate. Ebb dominant estuaries may represent more stable configurations with stronger ebb currents able to flush sediments entering the estuary through the inlet.

5). The models considered here provide only qualitative information on the effects of tidal flats. To include these effects more accurately, the modeling must be extended to two dimensions (depth-integrated). Two-dimensional models solve the full momentum and continuity equations over the flats as well as in the channel. This enables the impact of flats in momentum to be more carefully evaluated. Allowing greater cross-sectional area variability along channel and the possibility of channels in the tidal flats also requires a two-dimensional model. Given sufficient spatial resolution of estuarine geometry, two-dimensional models can also more accurately include regions where the advective term is of importance (e.g., channel bends, channel constrictions). Future efforts will be directed towards this type of modeling.

REFERENCES

Aubrey, D.G. and P.E. Speer, 1983. Sediment transport in a tidal inlet. Woods Hole Oceanographic Institution Technical Report, WHOI 83-20, 130 pp.

Aubrey, D.G. and P.E. Speer, submitted. Updrift migration of tidal inlets.

Beardsley, R.C. and D.B. Haidvogel, 1980. A simple numerical model for the wind-driven transient circulation in the Middle Atlantic Bight. Jour. Phys. Ocean.

Boon, J.D., III and R.J. Byrne, 1981. On basin hypsometry and the morphodynamic response of coastal inlet systems. Marine Geology, v. 40, p. 27-48.

Byrne, R.J., J.T. DeAlteris and J.P. Sovich, 1977. Recent history and response characteristics of Wachapreague Inlet, VA. Final report to ONR Geography Programs, VIMS, Gloucester Pt., VA, 127 pp.

Dronkers, J.J., 1964. Tidal Computations in Rivers and Coastal Waters. North Holland Publishing Company, Amsterdam, 516 pp.

FitzGerald, D.M. and D. Nummedal, 1983. Response characteristics of an ebb-dominated tidal inlet channel. Jour. Sed. Pet., v. 53, p 833-845.

Flather, R.A. and N.S. Heaps, 1975. Tidal computations for Morecambe Bay. Geophys. Jour. Roy. astr. Soc. v. 42, p. 489-517.

Gallagher, B.S. and W.H. Munk, 1971. Tides in shallow water: spectroscopy. Tellus, v. 23, p. 346-363.

Grant, W.D. and O.S. Madsen, 1979. Combined wave and current interaction with a rough bottom. Jour. Geophys. Res., v. 84, p. 1797-1808.

Hamilton, J., 1978. The quarter-diurnal tide in the English Channel. Geophys. Jour. Roy. astr. Soc. v. 53, p. 541-552.

Hayes, M.O., 1975. Morphology of sand accumulating in estuaries: an introduction to the symposium. In L. Eugene Cronin (ed.), Estuarine Research, v. 11, Academic Press, p. 3-22.

Kabbbaj, A. and C. Le Provost, 1980. Non-linear tidal waves in channels: a perturbation method adopted to the importance of bottom friction. Tellus, v. 32, p. 143-163.

Kjerve, B., 1975. Velocity averaging in estuaries chartacterized by a large tidal range to depth ratio. Est. Coast. Mar. Sci., v. 3, p. 311-323.

Kreiss, H., 1957. Some remarks about nonlinear oscillations in tidal channels. Tellus, v. 9, p. 53-68.

Le Provost, C., G. Rougier and A. Poncet, 1981. Numerical modeling of the harmonic constituents of the tides, with application to the English Channel. Jour. Phy. Ocean. v. 11, p. 1123-1138.

Longuet-Higgins, M.S. and R.W. Stewart, 1964. Radiation stress in water waves - a physical discussion with applications. Deep Sea Res., v. 11, p. 529=562.

Nummedal, D. and S.M. Humphries, 1978. Hydraulics and dynamics of the North Inlet, 1975-1976. G.I.T.I. Report 16, US Army Coastal Engr. Res. Cent., 214 pp.

Pearson, C.E. and D.F. Winter, 1976. Computation of tidal flow in well-mixed estuaries. Jour. Hydraulics Div., ASCE, v. 102, p. 367-377.

Pearson, C.E. and D.F. Winter, 1977. On the calculation of tidal currents in homogenous estuaries. Jour. Phys. Ocean., v. 7, p. 520-531.

Pingree, R.D. and L. Maddock, 1978. The M_4 tide in the English channel derived from a nonlinear numerical model of the M_2 tide. Deep Sea Research, v. 26, p. 53-68.

Pingree, R.D. and D.K. Griffiths, 1979. Sand transport paths around the British Isles resulting from M_2 and M_4 tidal interactions. Jour. Mar. Biol. Ass., v. 59, p. 497-513.

Prandle, D., 1980. Modeling of tidal barrier schemes: an analysis of the open-boundary problem by reference to AC circuit theory. Est. Coast. Mar. Sci., v. 11, p. 53-71.

Roache, P.J., 1972. Computational Fluid Dynamics, Hermosa Publishers, Albuquerque, 434 pp.

Smith, J.D. and S.R. McLean, in prep. A model for meandering streams.

Snyder, R.L., M. Sidjabat and J.H. Filloux, 1979. A study of tides, set-up and bottom friction in a shallow semi-enclosed basin. Part II: Tidal model and comparison with data. Jour. Phys. Ocean., v. 9, p. 170-188.

Swift, M.R. and W.S. Brown, 1983. Distribution of tidal bottom stress in a New Hampshire estuary. Report No. : UNH-MP-T/DR-SG-83-2, Univ. of New Hampshire, 40 pp.

Uncles, R.J. and M.B. Jordan, 1980. A one-dimensional representation of residual currents in the Severn Estuary and associated observations. Est. Coast. Mar. Sci., v. 10, p. 39-60.

Uncles, R.J., 1981. A note on tidal asymmetry in the Severn estuary. Est. Coast. Mar. Sci., v. 13, p. 419-431.

Teubner, M.D. and B.J. Noye, 1978. Tidal and thermal propagation in a tidal estuary. In J. Noye (ed.), Numerical Simulation of Fluid Motion, North-Holland, Amsterdam, 580 pp.

APPENDIX I

EQUATIONS OF MOTION FOR ONE-DIMENSIONAL FLOW

I.1. Introduction

The channel geometry considered in this derivation is a narrow and shallow channel with a well-mixed water column (fig. I.1). The axes are as shown in the figure and the geometry suggests that the longitudinal velocity component, u, will be much greater than the lateral, v, and vertical, w. The derivation assumes that changes in width and cross-sectional area are gradual in the longitudinal direction. The dynamics will be expressed in terms of the volume flux, U(x,t), cross-sectionally averaged velocity, $\bar{u}(x,t)$, and surface elevation, $\zeta(x,t)$. The derivation presented below follows Dronkers (1964), Madsen (unpub. MIT class notes) and Brown and Trask (1980).

I.2. Continuity Equation

The continuity equation for an incompressible fluid is:

$$\frac{\partial u}{\partial x} + \frac{\partial v}{\partial y} + \frac{\partial w}{\partial z} = 0 \qquad (1)$$

This equation is integrated over the cross-section shown in Figure I.1.

$$\int_{-b_1}^{b_2} \int_{-h}^{\zeta} \left| \frac{\partial u}{\partial x} + \frac{\partial w}{\partial y} \right| dz dy = 0 \qquad (2)$$

In the following, the integrals $\int_{-b_1}^{b_2}\int_{-h}^{\zeta} dz dy$, $\int_{-b_1}^{b_2} dy$ and $\int_{-h}^{\zeta}$ are denoted $\langle \ldots \rangle$, $\{\ldots\}$ and $\tilde{\ldots}$ respectively. Evaluation of the integrals in (2) requires repeated use of Liebnitz' rule:

$$\left\langle \frac{\partial u}{\partial x} \right\rangle = \frac{\partial}{\partial x}\langle u \rangle - \frac{\partial b_2}{\partial x}\tilde{u}_2 - \frac{\partial b_1}{\partial x} u_1 + \left\{ u(-h)\frac{\partial(-h)}{\partial x} - u(\zeta)\frac{\partial \zeta}{\partial x} \right\} \qquad (3a)$$

$$\left\langle \frac{\partial v}{\partial y} \right\rangle = \tilde{v}_2 - \tilde{v}_1 + \left\{ v(-h)\frac{\partial(-h)}{\partial y} - v(\zeta)\frac{\partial \zeta}{\partial y} \right\} \qquad (3b)$$

$$\left\langle \frac{\partial w}{\partial z} \right\rangle = \{ w(\zeta) - w(-h) \} \qquad (3c)$$

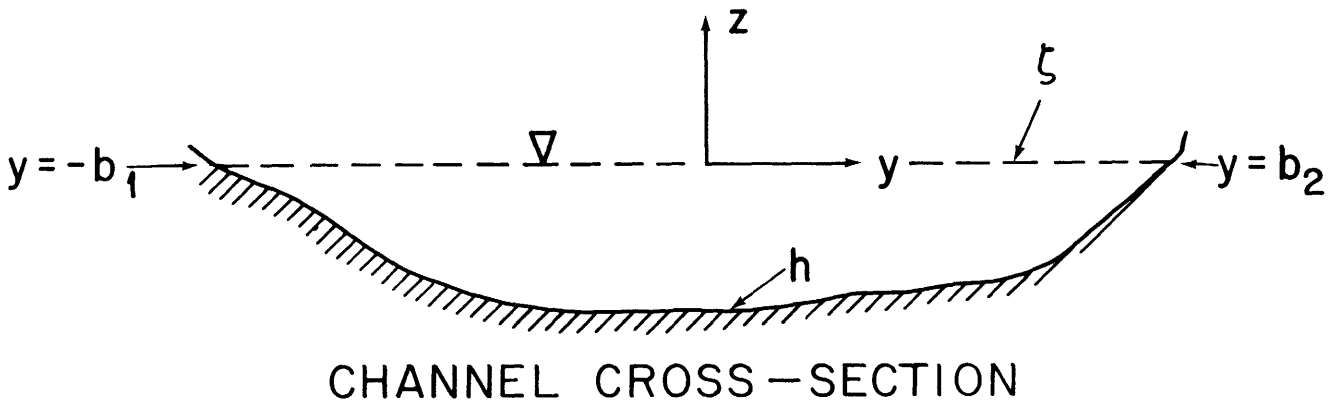

CHANNEL CROSS-SECTION

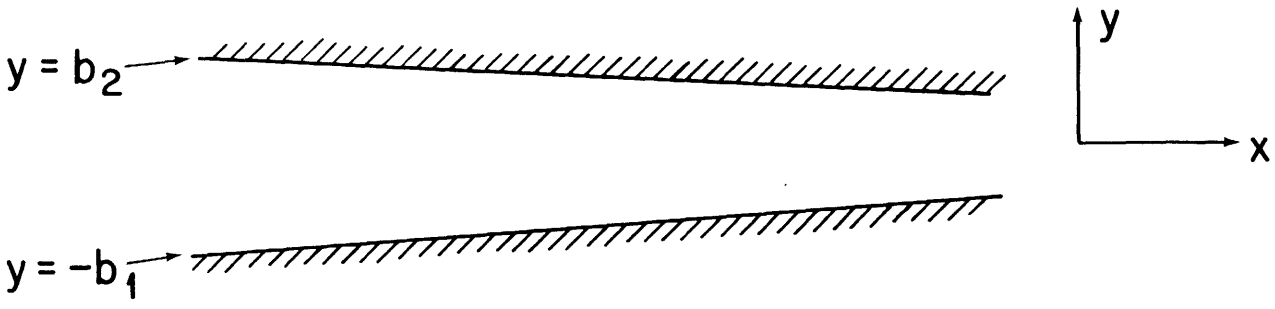

PLAN VIEW

Figure I.1. Channel geometry and coordinate system.

The subscripts 1,2 refer to conditions at $y=-b_1, b_2$ respectively. To simplify these integrals, kinematic surface and bottom boundary conditions are applied:

$$\frac{D\zeta}{Dt} = w(\zeta) \tag{4a}$$

$$\frac{D(-h)}{Dt} = w(-h) \tag{4b}$$

and the integrated continuity equation becomes:

$$\frac{\partial}{\partial x}\langle u\rangle + \left\{\frac{\partial \zeta}{\partial t} - \frac{\partial(-h)}{\partial t}\right\} + \tilde{v}_2 - \frac{\partial b_2}{\partial x}\tilde{v}_2 - \tilde{v}_1 - \frac{\partial b_1}{\partial x}\tilde{v}_2 = 0 \tag{5}$$

The integral $\left\{\frac{\partial \zeta}{\partial t} - \frac{\partial(-h)}{\partial t}\right\}$ can be rewritten using the Liebnitz rule as,

$$\frac{\partial}{\partial t}\{\zeta - (-h)\} - \frac{\partial b_2}{\partial t}(\zeta - (-h))_2 - \frac{\partial b_1}{\partial t}(\zeta - (-h))_1 \tag{6}$$

and utilizing kinematic side boundary conditions,

$$\frac{Db_2}{Dt} = v(b_2) \tag{7a}$$

$$\frac{Db_1}{Dt} = v(b_1) \tag{7b}$$

the integrated continuity equation can be written:

$$\frac{\partial}{\partial x}\langle u\rangle + \frac{\partial}{\partial t}\{\zeta - (-h)\} = 0 \tag{8}$$

Defining,

$\langle u\rangle = U = \bar{u}\bullet A$ $\qquad$ A = cross-sectional area

$\{\zeta - (-h)\} = A$

continuity becomes

$$\frac{\partial}{\partial x} U + \frac{\partial A}{\partial t} = 0 \tag{9}$$

For the trapezoidal cross-section shown in figure I.2,

$$\frac{\partial A}{\partial t} = b\frac{\partial \zeta}{\partial t} \qquad b = \text{channel width} \tag{10}$$

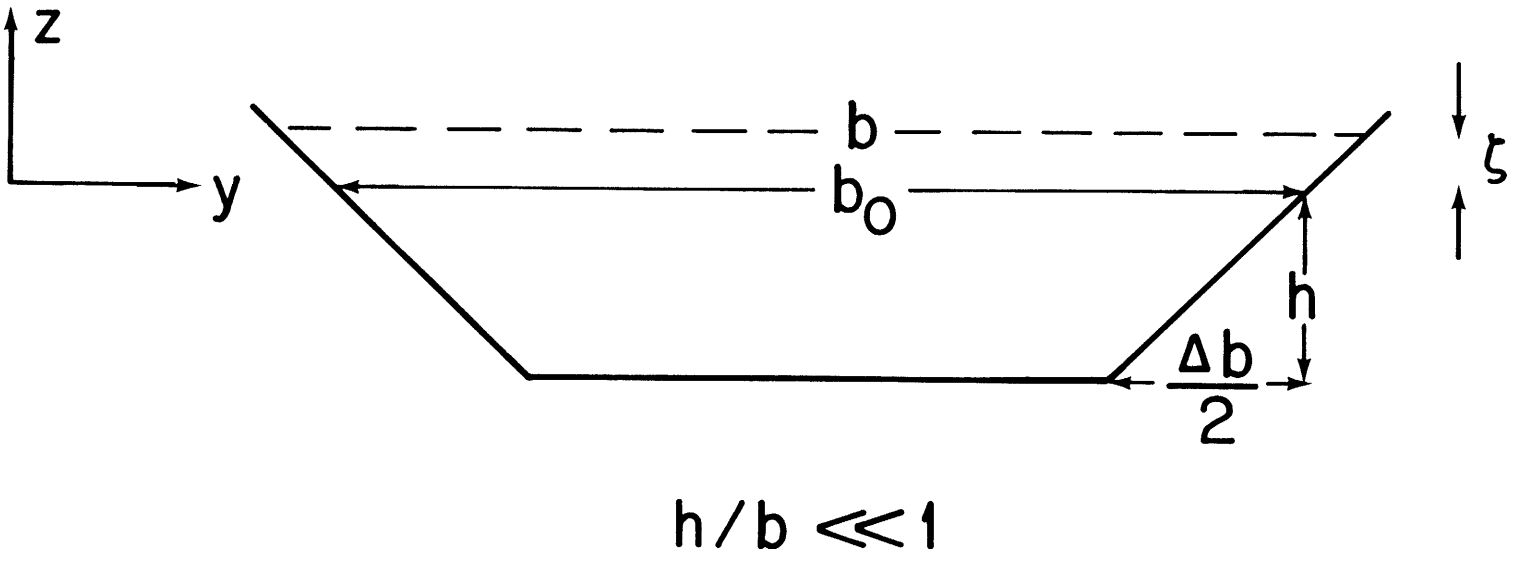

Figure I.2. Trapezoid used to represent channel cross-section.

The forms of continuity considered in the numerical model result from substituting (10) into (9):

$$\frac{\partial U}{\partial x} + b\frac{\partial \zeta}{\partial t} = 0 \tag{11a}$$

$$\frac{\partial A \bullet \bar{u}}{\partial x} + b\frac{\partial \zeta}{\partial t} = 0 \tag{11b}$$

Note that the derivation does not account for lateral inflow from side channels.

I.3 Momentum Equation

The geometry of the problem, asumptions of gradual change in cross-section in the longitudinal direction and hydrostatic pressure distribution allow us to state the y- and z-momentum equations as:

$$\zeta = \zeta(x,t) \tag{12}$$

$$p = \rho g(\zeta - z) \tag{13}$$

The x-momentum equation is

$$\frac{\partial u}{\partial t} + u\frac{\partial u}{\partial x} + w\frac{\partial u}{\partial y} = -\frac{1}{\rho}\frac{\partial p}{\partial x} + \frac{1}{\rho}\left(\frac{\partial \tau_{xx}}{\partial x} + \frac{\partial \tau_{yx}}{\partial y} + \frac{\partial \tau_{yz}}{\partial z}\right) \tag{14}$$

Adding to (14), $u(\nabla \bullet \vec{v})$, where $\vec{v}(u,v,w)$ is the velocity vector, and substituting (13) in (14), x-momentum becomes

$$\frac{\partial u}{\partial t} + \frac{\partial u^2}{\partial x} + \frac{\partial uw}{\partial y} = -g\frac{\partial \zeta}{\partial x} + \frac{1}{\rho}\left(\frac{\partial \tau_{xx}}{\partial x} + \frac{\partial \tau_{yx}}{\partial y} + \frac{\partial \tau_{yz}}{\partial z}\right). \tag{15}$$

The velocities in (15) are time averaged over an interval long compared to turbulent time scales but short compared to tidal time scales. The shear stresses, τ, represent both viscous forces and stresses arising from advection of momentum by turbulent velocity fluctuations (Reynold's stresses).

It has been assumed in deriving (15) that the coriolis term is not important in a narrow tidal channel. This assumption is valid if the Kelvin number, $K_E = fb\,(gh)^{-1/2}$, is much smaller than unity. For the estuarine system of interest, b~200 m, h~4 m, f~10^{-4}s, and K_E~10^{-3}.

The momentum equation (15) is integrated over the channel cross-section. This integration yields for the total derivative $\frac{Du}{Dt}$,

$$\left\langle \frac{Du}{Dt} \right\rangle = \frac{\partial}{\partial t}\langle u\rangle + \frac{\partial}{\partial x}\langle u^2\rangle - \{u(\zeta)(\frac{\partial \zeta}{\partial t} + u(\zeta)\frac{\partial \zeta}{\partial x} + v(\zeta)\frac{\partial \zeta}{\partial y} - w(\zeta)\}$$

$$+\{u(-h)(\partial(\frac{-h}{\partial t}) + u(-h)\partial(\frac{-h}{\partial x}) + v(-h)\partial(\frac{-h}{\partial y}) - w(-h)\}$$

$$-\int_{-h}^{\zeta} u_2(\frac{\partial b_2}{\partial t} + u_2\frac{\partial b_2}{\partial x} - v_2)dz - \int_{-h}^{\zeta} u_1(\frac{\partial b_1}{\partial t} + u_1\frac{\partial b_1}{\partial x} - v_1)dz. \qquad (16)$$

The third and fourth integrals vanish by applying kinematic boundary conditions on the free surface and on the channel bottom. If, in addition, no lateral inflow takes place, the last two integrals vanish due to kinematic conditions on the channel side. Therefore,

$$\left\langle \frac{Du}{Dt} \right\rangle = \frac{\partial}{\partial t}\langle u\rangle + \frac{\partial}{\partial x}\langle u^2\rangle \qquad (17)$$

The integral $\frac{\partial}{\partial x}\langle u^2\rangle$ can be written as:

$$\frac{\partial}{\partial x}\langle u^2\rangle = \frac{\partial}{\partial x}\,Km\,\frac{U^2}{A} \qquad (18)$$

$$Km = \text{momentum coefficient} = \left\langle \frac{u^2}{U \cdot \overline{u}} \right\rangle \sim O(1)$$

The momentum coefficient accounts for the deviation from constant velocity over the cross-section and allows the advective term to be written directly in terms of the volume flux, U. For gentle variation in cross-sectional area, Km is taken equal to unity and,

$$\langle u^2\rangle = \frac{U^2}{A}$$

The acceleration term becomes, therefore,

$$\left\langle \frac{Du}{Dt} \right\rangle = \frac{\partial U}{\partial t} + \frac{\partial}{\partial x}\frac{U^2}{A} \qquad (19)$$

This derivative can be expressed in terms of the mean velocity, $\bar{u}$, by manipulating the definitions of U and A:

$$\frac{\partial}{\partial t}\langle u\rangle = A \cdot \frac{\partial \bar{u}}{\partial t} + A \cdot \bar{u}\frac{\partial \bar{u}}{\partial x} - \frac{\partial}{\partial x}\left(\frac{1}{A}\langle u^2\rangle\right) \tag{20}$$

Dividing through by A and substituting in (17) yields:

$$\left\langle \frac{Du}{Dt} \right\rangle = \frac{\partial \bar{u}}{\partial t} + \bar{u}\frac{\partial \bar{u}}{\partial x} + \frac{1}{A}\frac{\partial}{\partial x}\left(\langle u^2\rangle - \frac{\langle u\rangle^2}{A}\right) \tag{21}$$

The third term in (21) accounts for the deviation from constant velocity over the cross-section and will be small under the same conditions that Km approximates unity.

Assuming a gentle lateral and depth-wise variation over the cross-section, the pressure term in (15) can be integrated:

$$-\left\langle g\frac{\partial \zeta}{\partial x}\right\rangle = -gA\frac{\partial \zeta}{\partial x} \tag{22}$$

The shear stress terms are integrated after neglecting the term $\frac{\partial \tau_{xx}}{\partial x}$. This requires the assumption of slow longitudinal variations in channel geometry. Integration of the remaining terms yields

$$\left\langle \frac{1}{\rho}\left(\frac{\partial \tau_{xy}}{\partial y} + \frac{\partial \tau_{xz}}{\partial z}\right)\right\rangle = \tilde{\tau}_{xy,\,2} - \tilde{\tau}_{xy,\,1} + \{\tau_{xz}(\zeta)\} - \{\tau_{xz}(-h) - \frac{\partial}{\partial y}(-h)\tau_{xy}(-h)\} \tag{23}$$

The first two integrals represent sidewall friction if channel sidewalls are vertical. The channel geometry under consideration (fig. I.1) does not have steep lateral boundaries and the sidewalls will be considered part of the channel bottom boundary. Thus the first two integrals are neglected. For the case of a rectangular channel, the lateral stresses which scale as h are unimportant compared to the bottom stresses which scale as b.

The third integral represents a surface wind stress and will be taken as zero for the tidal problems under consideration. The final integral can be shown to be equivalent to an average shear stress on the solid boundary times the wetted perimeter:

$$\{\tau_{zx}(-h) - \frac{\partial}{\partial y}(-h)\tau_{xy}(-h)\} \simeq - \tau_b \cdot P \tag{24}$$

τ_b = average shear stress
P = wetted perimeter.

The momentum equation is closed mathematically by writing shear stress in terms of mean velocity, $\bar{u}$, or volume flux, U:

$$\tau_b = \rho f |\bar{u}| \bar{u} \tag{25a}$$

$$\tau_b = \rho f \frac{|U|U}{A \cdot A} \tag{25b}$$

Combining (25) and (22) with (21) or (19) yields the final form of the momentum equation:

$$\frac{\partial U}{\partial t} + \frac{\partial}{\partial x}\frac{U^2}{A} = -gA\frac{\partial \zeta}{\partial x} - f\frac{|U|U}{A \cdot A} \cdot P \tag{26a}$$

$$\frac{\partial u}{\partial t} + \bar{u}\frac{\partial \bar{u}}{\partial x} = -g\frac{\partial \zeta}{\partial x} - f\frac{|\bar{u}|\bar{u}}{A} \cdot P \tag{26b}$$

I.4 Tidal Flats

The effect of lateral inflow from tidal flats on the continuity and momentum equations can be included in a more systematic manner than shown in Chapter 4. If lateral inflow into the main channel occurs, the kinematic side boundary conditions (7a,b) do not vanish and the continuity equation (11a) is rewritten:

$$\frac{\partial U}{\partial x} + b\frac{\partial \zeta}{\partial t} + q_E = 0 \tag{27}$$

q_E = lateral inflow per unit length of channel
b = width of momentum transporting channel

The amount of inflow (or outflow) caused by tidal changes in sea surface is given by:

$$q_E = (b_T - b)\frac{\partial \zeta}{\partial t} \tag{28}$$

b_T = total width of channel including flats

substituting (28) into (27), the equation of continuity becomes

$$\frac{\partial U}{\partial x} + b_T\frac{\partial \zeta}{\partial t} \tag{29}$$

which is the same as equation (6) in Chapter 4.

Similarly for momentum, the retention of lateral inflow terms in (26b) allows the equation to be written

$$\frac{\partial \bar{u}}{\partial t} + \bar{u}\frac{\partial \bar{u}}{\partial x} + (u_E - \bar{u})q_E = -g\frac{\partial \zeta}{\partial x} - f\frac{|\bar{u}|\bar{u}}{A} \cdot P \tag{30}$$

u_E = longitudinal velocity component of lateral inflow

If the lateral inflow from tidal flats has approximately zero velocity, $u_E \simeq 0$, and substituting (28) and (29) into (30) yields:

$$\frac{\partial \bar{u}}{\partial t} + \bar{u}\frac{\partial \bar{u}}{\partial x} + \bar{u}\frac{(b_T - b)}{b_T}\frac{\partial U}{\partial x} = -g\frac{\partial \zeta}{\partial x} - f\frac{|\bar{u}|\bar{u}}{A} \cdot P \tag{31}$$

In terms of discharge, U, momentum is written

$$\frac{\partial U}{\partial t} + \frac{\partial U^2}{\partial x}\frac{}{A} + \frac{(b_T - b_o)}{b_T}\frac{U}{A}\frac{\partial U}{\partial x} = -gA\frac{\partial \zeta}{\partial x} - f\frac{|U|U}{A \cdot A} \cdot P \tag{32}$$

where the lateral inflow term can be compared to equation (10) in Chapter 4.